Advances in Electrochemical Science and Engineering

Volume 2

VCH

Advances in Electrochemical Science and Engineering

Volume 1

G. P. Evans, The Electrochemistry of Conducting Polymers
R. Kötz, Photoelectron Spectroscopy of Practical Electrode Materials
T. Iwasita-Vielstich, Progress in the Study of Methanol Oxidation by *In Situ, Ex Situ* and On-Line Methods
Der-Tau Chin, Theory and Experimental Aspects of the Rotating Hemispherical Electrode
J. Winnick, Electrochemical Separation of Gases
V. Brusic et al., Electrochemical Aspects of Thin-Film Storage Media

Advances in Electrochemical Science and Engineering

Volume 2

Edited by Heinz Gerischer
and Charles W. Tobias

Contributions from

C. Deslouis, B. Tribollet, Paris
A. Hammou, Saint Martin d'Hères
G. L. Richmond, Eugene
S. Trasatti, Milan

VCH

Editors:
Prof. Dr. Heinz Gerischer
Fritz-Haber-Institut der MPG
Faradayweg 4–6
D-1000 Berlin 33

Prof. Charles W. Tobias
Dept. of Chemical Engineering
University of California
Berkeley, California 94720, USA

Published jointly by
VCH Verlagsgesellschaft mbH, Weinheim (Federal Republic of Germany)
VCH Publishers Inc., New York, NY (USA)

Editorial Director: Karin von der Saal
Production Manager: Claudia Grössl

British Library Cataloguing-in-Publication Data
Advances in electrochemical science and engineering: Vol 2. –
(Advances in electrochemical science and engineering)
I. Gerischer, H. II. Tobias, C.W. III. Series
541.3
ISBN 3-527-28273-4

Deutsche Bibliothek Cataloguing-in-Publication Data
Advances in electrochemical science and engineering :
Weinheim ; Basel (Switzerland) ; Cambridge ; New York, NY : VCH
ISSN 0938-5193
Erscheint unregelmäßig. – Aufnahme nach Vol. 1 (1990)
Vol. 1. (1990) –

Printed on acid-free and low-chlorine paper

Composition: K+V Fotosatz GmbH, D-6124 Beerfelden
Printing: strauss offsetdruck GmbH, D-6945 Hirschberg 2
Bookbinding: Wilh. Osswald + Co., Großbuchbinderei, D-6730 Neustadt/Weinstr.
Printed in the Federal Republic of Germany

Distribution:
VCH, P. O. Box 101161, D-6940 Weinheim (Federal Republic of Germany)
Switzerland: VCH, P. O. Box, CH-4020 Basel (Switzerland)
United Kingdom and Ireland: VCH (UK) Ltd., 8 Wellington Court, Wellington Street, Cambridge CB1 1HZ (England)
USA and Canada: VCH Suite 909, 220 East 23rd Street, New York, NY 10010-4606 (USA)

ISBN 3-527-28273-4 (VCH, Weinheim)
ISBN 1-56081-139-0 (VCH, New York)
ISSN 0938-5193

Preface

Of the four chapters presented in this volume two address topics of great technological importance, and two concern novel experimental techniques for the study of electrode surfaces and reaction kinetics.

S. Trasatti provides a detailed review of the advances in the production of cathodes with favorable characteristics for the manufacture of electrolytic hydrogen. A careful analysis is given of performance characteristics on the basis of electrode reaction kinetics and catalysis.

H. Hammou outlines the thermodynamic concepts and rate processes relevant to solid oxide fuel cells. Recent advances in materials research concerning electrical properties, and stability at high temperatures, are thoroughly reviewed. The most promising hardware developments are described, along with problems to be resolved.

G. L. Richmond contributes an authoritative summary of the theory and applications of second harmonic generation by a laser beam reflected from an electrode surface. This powerful new in-situ technique yields information on the structural and electronic properties of electrode surfaces.

C. Deslouis and B. Tribollet present the theoretical basis and state of the art of a novel technique for kinetic analysis, in which the mass transfer rate to a rotating disk electrode is modulated. The capabilities and limitations of this technique are demonstrated along with illustrations of typical applications.

Heinz Gerischer
Charles W. Tobias

Contents

List of Contributors

C. Deslouis
U.P.R. 15 du C.N.R.S.
Physique des Liquides
et Electrochimie
Université Pierre et Marie Curie
Tour 22, 4 Place Jussieu
75252 Paris Cédex 05
France

A. Hammou
Laboratoire d'Ionique
et d'Electrochimie
du Solide de Grenoble
ENSEEG-INPG
Domaine Universitaire-BP 75
38402 Saint Martin d'Hères
France

G. L. Richmond
Chemical Physics Institute
University of Oregon
Eugene, Oregon 97403
USA

Sergio Trasatti
Department of Physical Chemistry
and Electrochemistry
University of Milan
Via Venezian 21
20133 Milan
Italy

B. Tribollet
U.P.R. 15 du C.N.R.S.
Physique des Liquides et
Electrochimie
Université Pierre et Marie Curie
Tour 22, 4 Place Jussieu
75252 Paris Cédex 05
France

Advances in Electrochemical Science and Engineering
Edited by Heinz Gerischer and Charles W. Tobias

Electrocatalysis of Hydrogen Evolution: Progress in Cathode Activation

Sergio Trasatti

Department of Physical Chemistry and Electrochemistry, University of Milan,
via Venezian 21, 20133 Milan, Italy

Contents

1 Introduction

Electrolytic hydrogen liberation at the cathode is one of the reactions most frequently occurring in industrial cells. While it is the wanted reaction in water electrolysis [1–4], hydrogen is formed as a by-product in the chlor-alkali process [5, 6] and in chlorate production [7], which are among the most intensive electrochemical processes. Nevertheless, problems of cathode activation started to be tackled intensively not earlier than about 15 years ago [8–13]. The reasons for this are to be sought in the fact that hydrogen evolution is a reaction giving relatively few problems compared to other major industrial processes, such as anodic chlorine and oxygen evolution; moreover, hydrogen production has not raised any major technological interest in recent years.

In the case of chlorine evolution the replacement of graphite electrodes with DSA® (Dimensionally Stable Anodes) was forced by the need to avoid an inefficient technological situation [14, 15]. In the case of oxygen evolution, its high inefficiency bears on the whole economy of electrolytic cells quite substantially, very often more so than the wanted reaction taking place at the cathode of the cell [16]. On the other hand, corrosion under impressed current poses material problems related to the electrode working as an anode, so that the alleviation of anodic problems is usually given higher priority in industry.

With the solution of most problems concerning anodes after the introduction of DSA®, and especially with the advent of membrane technology in the chlor-alkali industry [17], and with the increasing cost of electric power, the relative inefficiency of cathodes has remained one of the most outstanding factors of energy dissipation [18]. In the case of water electrolysis, the high cost of electrolytic hydrogen production [19] calls for intensive improvement by working at higher temperatures with more efficient electrocatalysts [20]. Actually, this is the primary application that orients research in the direction of improving hydrogen electrocatalysis.

In principle, improving the efficiency of cathodes is not as acute a technological necessity as that of anodes [21]. Traditional cathodes for industrial applications have long been iron or mild steel [1, 7, 22]. However, these materials do not withstand the more severe conditions of high caustic concentration and higher temperature which derive from the development of most stringent conditions of water electrolysis, and of membrane cells in the chlor-alkali industry. Under similar circumstances, Ni is mostly used to replace the above materials [23, 24]. Incidentally, it is to be mentioned that while most of the fundamental research on metals, especially precious metals, is based on data for acid solutions, strongly alkaline solutions are technologically more common (e.g., conventional water electrolysis, chlor-alkali cells, etc.), acid environments being restricted to a few specific applications (e.g., electrolysis of strong acids and SPE (solid polymer electrolyte) water electrolysis). Therefore, cathodes for caustic solutions are more in demand than those for acid solutions. On the other hand, at the high current densities used as a rule in technological applications, the intense alkalinization of the cathode solution is a normal occurrence.

It is interesting that Ni is not more active than iron (or mild steel) [25, 26], but its use is forced by the need for stability. The competition between activity and stability, taking into account the economy of the whole process, is the "leit-motiv" accompanying the application of materials in industry. Lately, the need for health safety has also become one of the guiding factors in the technological development [27, 30].

Ni can be taken as the reference material against which all other materials should be evaluated. On the average, the operating overpotential of untreated Ni electrodes is about 0.4 V at 0.2 A cm^{-2} [5]. Beyond Ni, we deal with "activated cathodes", which in fact derive from the idea of activated anodes such as the DSA®. By activated electrodes we mean that the surface has been subjected to some treatments aimed at increasing its catalytic activity. This can be a treatment which modifies the surface structure and the morphology of the base metal, but more often the treatment is aimed at coating the base metal with a more active material [31].

Several reasons are behind the ideas of activation: (i) A thin layer or a microdeposit of active but expensive materials enables to keep costs down to an acceptable level; (ii) Some materials would be highly resistive if used in bulk form; (iii) Certain materials are not suitable to prepare solid electrodes and need to be supported; (iv) The support can be made of materials inert to the working conditions, so that even a destruction of the active layer won't produce a collapse of the structure; (v) An activated electrode offers more flexible mechanical solutions.

A wealth of investigations have been carried out during the past 15 years in the direction of cathode activation. A number of them remain of exclusive fundamental interest, while only a few prospective solutions have indeed found practical application. The main reason is that cathode activation must be really cost effective to be applied, since it is not strictly needed to solve major technical problems otherwise hampering the process (as it is the case with anodes).

The search for new electrode materials is expected to be guided by the fundamental understanding of the factors governing the activity. In electrochemistry, this branch of the discipline is known by the name of "electrocatalysis". Strictly speaking, electrocatalysis is the science devoted to the relationship between the properties of materials and the electrode reaction rate. The scope of electrocatalysis as a science is to establish a predictive basis for the design and the optimization of electrocatalysts.

In the case of hydrogen evolution, the theory of electrocatalysis on single individual metals was established about thirty years ago [32, 33]. However, no decisive advances have been made since then from the point of view of the theory of composite materials. It is probably for this reason that a great deal of applied research has been conducted thus far following the always convenient approach of "try and see". In one case [34], it has been explicitly reported that more than 400 different materials have been tested in a few years with the purpose of finding the best one.

It is thus evident that a survey of all the work carried out so far on cathode activation is necessary to try to organize the matter in a way useful to establish a guide for more focused future research. It is in fact clear that if the 60's and the 70's were the years of anodes [35], the 80's and 90's have been and will be devoted to the development of cathodes, including those for oxygen reduction [36, 37] which will not be considered here.

The purpose of this chapter is to review the work carried out during the past 10–15 years and to subject to scrutiny the advances really made. The question is whether these advances can be rationalized in terms of existing theory, or whether they point the way to new predictive basis to be established in the future. This chapter is not meant to be a handbook of numerical data. The essential purpose is to give a broad view of the state of the art of facts, trying to analyze the factors which may be important in guiding to the development of new cathodes. This chapter is inspired by technologically oriented concepts rather than by purely fundamental views. Nevertheless, emphasis will be placed on the relationship between fundamental knowledge and practical achievements.

1.1 Previous Work

Only two general reviews [38, 39] entirely devoted to the hydrogen evolution reaction have appeared after the start of the development of cathode activation [40]. In several other cases, hydrogen evolution has been discussed within the general frame of electrocatalysis [4, 41–47] or kinetics of electrode reactions [48, 49]. However, only one of the two reviews mentioned above discusses electrocatalytic aspects with literature coverage up to the late 70's, when the field of cathode activation was at the beginning of its development.

This chapter will preferentially review the literature of the past 10 to 15 years; earlier papers will be recalled where necessary for the discussion.

2 Analysis of Major Issues

In this section, some general aspects emerging from the survey of the literature, common to all classes of electrode materials and essential to properly evaluate the performance of cathodes, will be illustrated and discussed.

2.1 Electrocatalysis

The voltage ΔV applied across an electrolysis cell can be expediently split into several contributions:

$$\Delta V = \Delta E + \sum \eta + \Delta V_{\Omega} \; . \tag{1}$$

ΔE is the thermodynamic cell voltage depending on the nature of the electrode reactions, $\sum \eta$ is the total overpotential and represents the surplus of electrical energy required to drive the process at a practical rate and to overcome mass transfer resistances. $\Delta V_{\Omega} = IR$ is the ohmic drop in the interelectrode gap, the electrode structure and the connecting circuits. It is evident that electrocatalysis, operating on *the part of η that depends on the nature of the electrode material, is just one of the* ways by which the rate of an electrochemical process can be enhanced [50]. Other means involve engineering aspects relevant to the cell as a whole. Since the aim of electrocatalysis in industrial applications is to contribute to reducing the voltage ΔV applied across an electrolysis cell so as to reduce the operational costs, the concept of electrocatalysis is broader when applied in the technological field. In a general sense, a reduction in ΔV is obtained either by increasing the true surface area, or by reducing the overpotential. In other words, the evaluation of electrode materials is accomplished by comparing the *apparent* current density at a given electrode potential or, more commonly, by comparing the overpotential at a given apparent current density. It is evident that an increase in surface area will produce a more favorable electrode performance as much as a reduction in overpotential. In fact, one of the procedures adopted in practice to activate a cathode is precisely increasing its surface area [50, 51].

While the reduction of ΔV related to an increased surface area has a decisive practical impact, it is clear that this cannot be strictly considered as an electrocatalytic effect, unless the variaton of the electrode surface area also involves a modification of the nature of the surface active sites, which may sometimes be the case. Two factors have therefore to be considered in evaluating a new material: geometric factors and electronic factors.

Another point to be considered is what parameters are really important for the evaluation of the electrocatalytic activity. It is well known that, apart from mass transfer and ohmic loss problems, the overpotential can be related to the reaction rate by the (Tafel) equation:

$$\eta = b \ln (I/I_0) \ , \tag{2}$$

where b is the so-called *Tafel slope* and I_0 the *exchange current.* The exchange current density (j_0), as a rule based on the geometric (apparent) surface area ($j_0 = I_0/S$), is often used to compare the activity of electrodes [33, 52, 53]. However, since the aim of the use of new materials is to reduce the applied voltage at practical current densities, the comparison of exchange currents may be often misleading. At low overpotentials, electrodes with high j_0 and large Tafel slopes may be more active than electrodes with low j_0, but as a rule they become less active at high overpotentials (Fig. 1). Further, the Tafel slope may increase as the current density is raised, as a consequence of a modification of the rate determining step and/or of the surface conditions of the electrode (cf. Section 2.7). In both cases, an electrode very active at low overpotentials becomes less active at higher overpotentials. Nevertheless, the (nominal) exchange current extrapolated from the high η range is higher than the j_0 obtained from the low overpotential section of the polarization curve. On the other hand, while the apparent j_0 is an extensive quantity, i.e., it depends on the extension of the true surface area, the Tafel slope b is an intensive quantity, i.e., it is not influenced by the surface area. Thus, if a procedure of electrode activation results in a change in Tafel slope, electronic factors are certainly responsible for that. However, if it results in a parallel shift of the Tafel line, it might imply a true change in j_0, but this can only be verified after adequate correction for the real surface area.

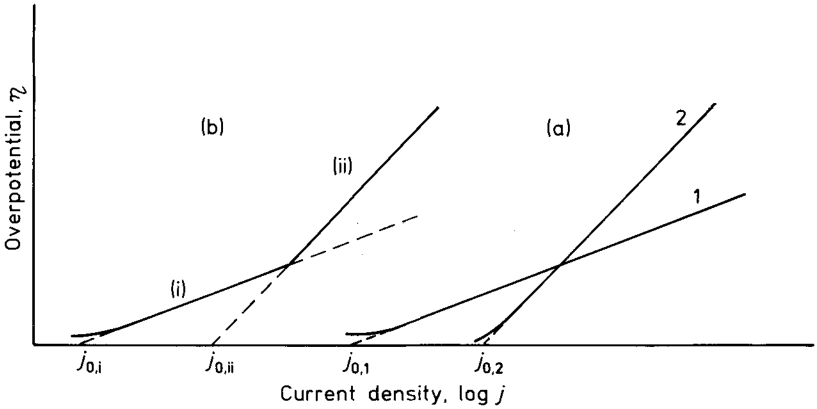

Fig. 1. Sketch showing (a) Tafel lines with different slopes and exchange currents for two different electrocatalysts, and (b) the observable two-section Tafel line in case, e.g., of change in r.d.s. for a single electrocatalyst.

2.2 Electrocatalytic Activity

Hydrogen evolution is the only reaction for which a complete theory of electrocatalysis has been developed [33]. The reason is that the reaction proceeds through a limited number of steps with possibly only one type of intermediate. The theory predicts that the electrocatalytic activity depends on the heat of adsorption of the intermediate on the electrode surface in a way giving rise to the well known "volcano" curve. The prediction has been verified experimentally [54] (Fig. 2) and the volcano curve remains the main predictive basis on which the catalytic activity is discussed [41, 55].

The volcano curve is based on the performance of simple metals, and the heat of adsorption is the factor which turns out to be responsible for the change in activity from metal to metal. However, the difficult issue from a theoretical point of view is the identification of the properties of metals which govern the magnitude of the adsorption heat. A number of correlations have been proposed, based on different electronic or structural properties of metals [56–65]. The aim has been to establish a "reactivity scale" from which predictions on the behaviour of unknown materials could be made. It appears that the correlation between the electron work function and the activity of metals for hydrogen evolution is very likely to be the most reliable [54, 66], since it has been verified several times by different authors independently [57, 62, 67].

The search for correlations has even produced simply statistical approaches based on a combination of several properties of metals [68, 69]. It has been ascertained that the electrocatalytic activity of metals is a periodic function of the position of the metal in the Mendeleev Table [38, 70–72]. A strict correspondence is observed between two different periods (Fig. 3) indicating that metals in the same group occupy the same relative position in the various periods [60]. Since all properties of metals

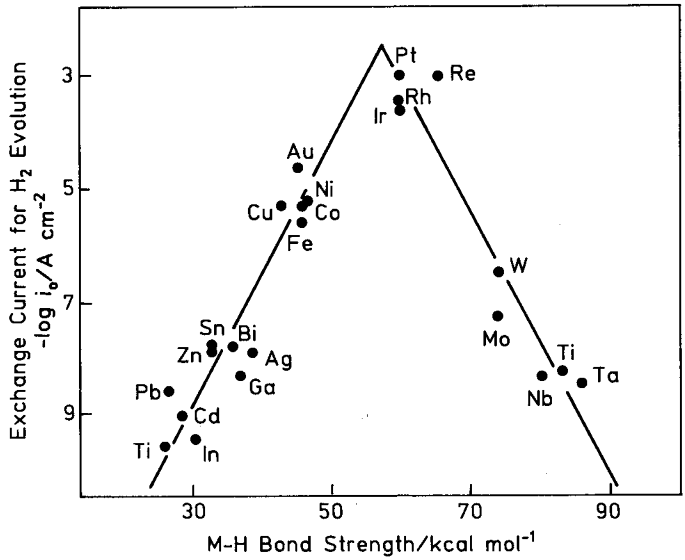

Fig. 2. Experimental "volcano"-shaped curve for hydrogen generation on metals. From ref. 54, by permission of Elsevier Sequoia.

follow the same pattern [73], correlations with varied properties are not surprising. The difficult task is to find out which properties may be considered as the *primary* factor on which the activity depends.

If correlations do exist for simple metals, predictions are much more difficult for composite materials. On the other hand, cathode activation has two aims: (i) to replace active but expensive materials with cheaper ones, and (ii) to enhance the activity of cheaper materials so as to approach or even surpass that of the more expensive catalysts. In the case of pure metals there is little hope to find a new material satisfying the above requirements since in the "volcano" curve each metal has a fixed position which cannot be changed. Therefore, activation of pure metals can only be achieved by modifying its structure so as to enhance the surface area (which has nothing to do with electrocatalysis in a strict sense), and possibly to influence the mechanism and the energetic state of the intermediate in the wanted direction. This includes the preparation of rough surfaces but also of dispersed catalysts. Examples will be discussed later.

From a true catalytic point of view, what is looked for are so-called "synergetic effects", i.e., a reciprocal influence between two or more components so as to obtain a material whose activity exceeds that of the pure components [74]. This usually involves intimate electronic interaction between the various components so that their electronic structures become profoundly modified. It is well possible that a metal deprived of part of its valence electrons may behave as the element on its left in the Periodic Table [75]. However, the theory of "synergetic effects" is still in its infancy in electrochemistry. Predictions for a bimetallic catalyst with two *non-interacting* sites obtained by combining two metals with different adsorption energies are that

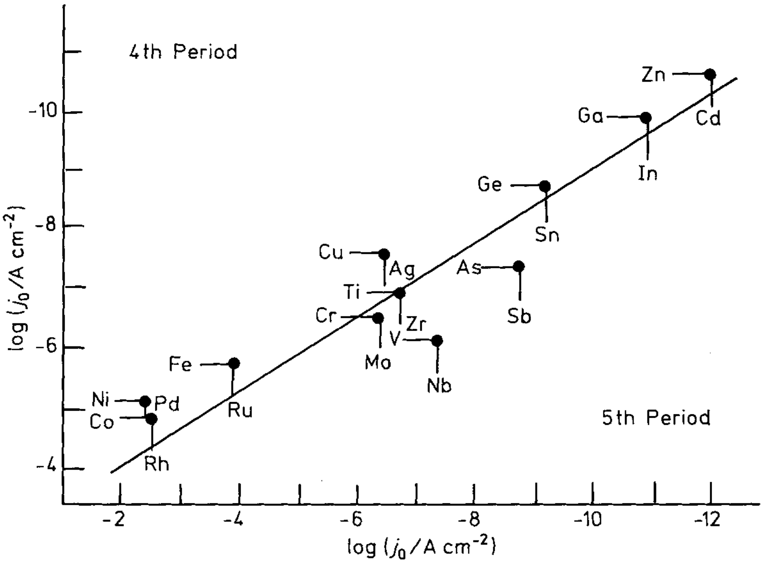

Fig. 3. Correlation between the exchange current for the hydrogen reaction on the metals of the 4th Period and that on the metals of the 5th Period. After ref. 60, by permission of Plenum Press.

no enhancement of the activity is to be expected [76]. However, theory for interacting sites is lacking on account of that the nature of the interaction between the sites is unknown.

Relationships or correlations which can help to guide in the choice of the way to proceed are rather uncertain. It seems that the only possibility to obtain an enhancement of the activity is to combine two or more elements giving rise to synergism. However, *linear* activity-property correlations gathering all metals in one group cannot help in this task. In fact, such correlations do not offer any guide to the prediction of synergistic effects (synergism implies activity above the one expected from the simple linear combination of the two pure components). If metals split into different groups giving separate correlations, synergism can be expected if metals from different groups are combined. For example, d-metals and sp-metals are grouped in two parallel linear correlations as the activity for hydrogen evolution is plotted against the work function [54, 66]. A combination of a metal of a group with a metal of the other group with almost the same catalytic activity may result in an alloy of intermediate work function. However, there is no easy way to know *a priori* how the electron work function varies with composition and if the activity is enhanced or depressed at intermediate compositions. This is because the electron work function does not enter as a primary parameter in the rate equation [66]. In fact, predictions of this kind have never been attempted.

The heat of adsorption of the intermediate remains the most straightforward parameter on which we can base our reasoning. Therefore, the "volcano" curve is the relationship which in principle can guide in making predictions. Miles [72] suggested in 1975 that a combination of two metals from the two branches of the volcano curve could result in enhanced activity [9]. But this implies of course that a direct correlation exists between composition and heat of hydrogen adsorption. The same approach was suggested by Jakšić [77, 78] who showed that a combination of Ni or Co with Mo can result in a substantial enhancement of the activity for hydrogen evolution [79].

Predictions based on the "volcano" curve do not show any general validity since only a few combinations give more active materials. In particular, it is to be noted that Ni, Co and Fe appear on the right branch of the volcano curve if the ΔH_{ad} measured in the gas phase is used [54]. Thus, they would be on the same branch as Mo. They appear on the left branch of the curve [66] if the heat of adsorption is derived *in situ* from electrochemical measurements [80]. This indicates that these metals are modified by hydrogen discharge, probably because of hydrogen absorption which renders the surface adsorption bond weaker. The same possibility has been pointed out for Pt [81]. Thus, the verification of the prediction based on the "volcano" curve does not appear to be entirely convincent.

Jakšić has tried to propose a predictive basis for the hydrogen reaction beyond the "volcano" curve. The idea is based on Brewer-Engel's theory [82] for bonding in metals and intermetallic phases. According to this theory, a maximum in bond strength and stability of the intermetallic phases is expected as a metal lying at the beginning of a transition period in the Periodic Table (e.g., Ti or Zr) is combined with

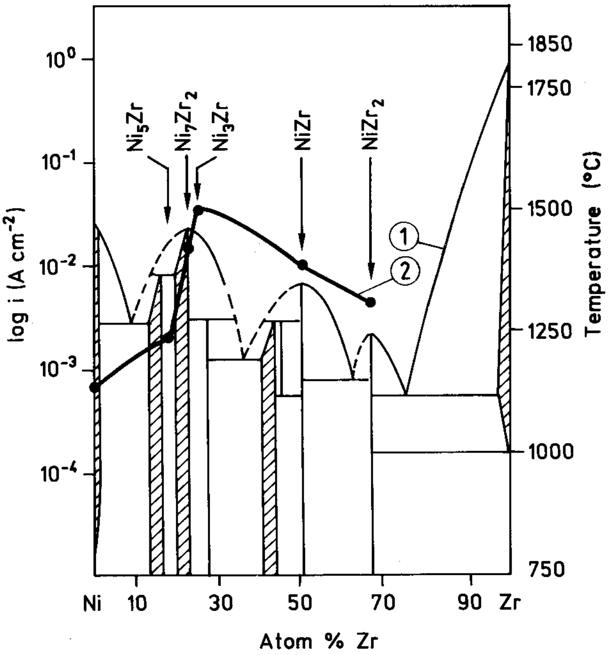

Fig. 4. Activity of various intermetallic phases of Ni and Zr for electrolytic hydrogen evolution. The phase diagram is also shown. From ref. 83, by permission of Elsevier Sequoia.

a metal at the end of a transition period (e.g., Ni) [73, 77, 79]. This implies that part of the electrons of the metal with partly filled d-bands is shared with the metal with almost empty d-orbitals [73, 83]. According to the theory, this would result in very stable systems, such as $MoCo_3$, WNi_3, $MoNi_3$, $LaNi_5$ etc. According to Jakšić, an enhanced electrocatalytic activity for hydrogen evolution is consistently observed with these intermetallic compounds (Fig. 4).

The theory of Brewer-Engel is for bulk solids, while electrocatalysis is governed by the properties of the surface. On the other hand, correlations between activity and bulk properties are not uncommon [84–87], as a consequence of the fact that the surface is the boundary of the bulk of the phase and manifests at least in a relative scale the properties of the phase itself. It is to be mentioned that an observation correlating the activity for hydrogen evolution with an intermediate phase formation was made long ago by Ohtani [88]. However, the verification of the theory calls for a separation of geometric from electronic effects. This aspect is not completely clarified in every investigation in the literature. It is not uncommon that as the real surface area is accounted for, the apparent enhancement of the catalytic activity disappears [89, 90]. This was established long ago by Kolotyrkin and Frumkin [91] for smooth and spongy Pb. This does not imply that this is the case for all systems, but simply that this kind of ambiguity needs to be removed in many instances.

It thus appears that there may be a basis for some predictions which can guide in the selection of components for composite materials, but the theoretical basis for discussions goes always back to the principles of the volcano curve in the sense that a relative increase or decrease in activity is customarily explained by recurring to the features of such a curve [92]. Therefore, a theory is needed to describe the dependence of the adsorption strength of hydrogen on the electronic properties of composite materials. However, before a sound theory can be proposed, it is necessary that the experimental picture be freed from the many obscurities, ambiguities and irreproducibilities due to the scarce characterization of the surface of various materials, and to the insufficient identification of various factors which can influence electrode kinetics.

2.3 Surface Characterization

In the case of solid electrodes, knowledge of the real surface area is a prerequisite for the proper evaluation of the activity with respect to other samples from the same laboratory, or for the comparison of results from different laboratories. It is very difficult to determine the real surface area because there are no unique techniques applicable to all materials. When the surface area determination is lacking, an evaluation in terms of synergetic effects can only be ambiguous.

Although many of the results in the literature are still insufficiently characterized from this point of view, in general the need for a surface area determination is largely felt. Sometimes BET values are given, but the BET area may not correspond to the electrochemically active one especially if supported catalysts are used or inert components are part of an admixture [93]. Determinations based on capacitance are also ambiguous [94] because there exists no absolute reference for many materials and there is no potential at which the capacitance is the same even among different crystal faces of a metal [95]. However, relative measurements for different samples of the same materials are acceptable.

The best approach is normally an *in situ* determination based on voltammetry or charging curves, usually within the hydrogen adsorption region [96]. It is of course necessary to know the actual value of θ_H for absolute determinations, but the method is practicable on a relative basis. The method becomes absolute only in a few cases, in particular for Pt electrodes [97] for which the catalytic activity per metal atom, which is the parameter really needed to evaluate electrocatalytic effects, can be calculated [98]. Sometimes, results are reported relative to the surface area measured on the basis of the limiting current for a redox reaction [99], but what is obtained is only the macroscopic surface in which asperities of a height higher than the diffusion layer thickness can only be accounted for.

Whenever composite materials are used, the surface composition becomes an essential parameter to assess the actual electrocatalytic activity. The dominating role of surface composition in electrocatalysis was stressed by Frumkin et al. long ago [100]. This is especially the case with not well-defined compounds such as sulphides, carbides, etc. This task is undoubtedly tougher since the equipment for surface analysis is not an ordinary tool in electrochemical laboratories. As a matter of fact, the surface of electrodes remains insufficiently characterized in most instances, so that no more than a phenomenological observation can be made. In the cases where surface analysis has been carried out, it has usually opened new horizons to the understanding of the electrocatalytic action of materials [101, 102]. In some instances, the surface analysis has been essential to show that synergetic effects were only apparent [103].

Surface characterization includes also the study of the modification of a surface under cathodic load or after some pretreatments. The presence of residual surface oxides can explain some observations otherwise inexplicable. Activation *in situ* usually results in composite structures which are difficult to identify by X-ray, and may contain metallic and non-metallic components. Particularly crucial is the case of the surface structure of glassy metals or amorphous alloys.

The field of cathode activation, as well as that of anode activation, requires the use of complementary physical techniques to evaluate systems otherwise difficult to understand. Electrochemical techniques are sufficient to evaluate the kinetic parameters and the state of intermediates, especially if digital acquisition of open-circuit potential-decay transients, coupled with computer processing of the data, is used [104–106]. But the chemical and physical characterization of the surface remains essential. The literature shows that such an approach is becoming more accepted, so that there are hopes that the real situation of a number of systems will become clarified in the near future.

2.4 Stability

In a technological perspective, electrocatalytic activity is not the only requirement for a cathode. The electrode must be stable under the working conditions, i.e, ΔV should not drift with time. In practice, the choice of a material is based on a balance between activity, overall efficiency and stability. The test of cathode stability is thus an essential step in applied research [107]. Presently, the problem of the stability of cathodes appears to be more stringent than for activated anodes [34].

The most outstanding source of instability, which from an academic point of view may be difficult to realize, is the corrosion that can arise at open circuit when a cell is shut down for maintenance or other reasons [108]. The cathode can simply corrode, or can be oxidized. In the latter case, the residual oxide can be deleterious for the catalytic activity since it may remain unreduced even under cathodic load. Therefore, cathode materials usually contain additives whose function is to reduce the consequences of shut-downs [109]. Laboratory experiments should thus include also this kind of test if a complete analysis of the material is to be done [105, 108, 110]. If the cathode corrodes, some cathodic protection may need to be maintained during shut-downs [7], which is of course to be accounted for in the evaluation of the economic efficiency.

Under the term "stability", modifications that the electrode may undergo during its performance are also included such as the formation of hydrides as a consequence of hydrogen penetration into the cathode material [111]. This appears to be a very general phenomenon [81, 112, 113–116]. In the case of metals the process of hydrogen dissolution has been shown to depend on crystal structure, the number of valence electrons, and the atomic volume of metal and hydrogen [117]. "Metallization" of the dissolved hydrogen has been pointed out [118]. Hydrides are the cathodic analogues of oxides. While metals are always covered by oxides during oxygen evolution, cathodically most of them form hydrides which thus become mediators of hydrogen evolution. The reason why oxides are active for oxygen evolution is to be sought in the particularly favorable interaction of intermediates for oxygen evolution with the oxide surface [16, 119]. Likewise, there is evidence that the formation of hydrides may be one of the main reasons for the high activity of some cathode materials [120]. However, in other cases, hydrogen absorption may be deleterious. This is believed to be the case of Ni and Co, whose overpotential for hydrogen evolution increases at the beginning of electrolysis [121, 122].

While anodic oxide formation may be precursor to anodic dissolution [123], in that metal ions become surrounded by a water-like environment which reduces the energy required for them to leave the lattice, the formation of hydrides can result in the phenomenon of hydrogen embrittlement [124]. Hydrogen usually penetrates through the lattice interstices [125] thus causing an expansion of the crystal. Internal bursts or blisters may result if large amounts of hydrogen collect in localized areas [126]. The metal may become mechanically fragile and in some cases, such as $LaNi_5$, the structure of the material may literally collapse to a powder [127]. It has been pointed out that the "explosion" of the material can be prevented by operating at relatively high temperature and moderate current density so that the internal fugacity of H_2 gas (depending on overpotential) is maintained below the equilibrium H_2 pressure [128]. Additives are usually introduced into the cathode material to reduce the effects of hydrogen embrittlement. For example, Ti, which is largely used as a support for anodes, has limited uses as cathode or as a support for cathodes [129] precisely for its tendency to absorb hydrogen with mechanical deterio-

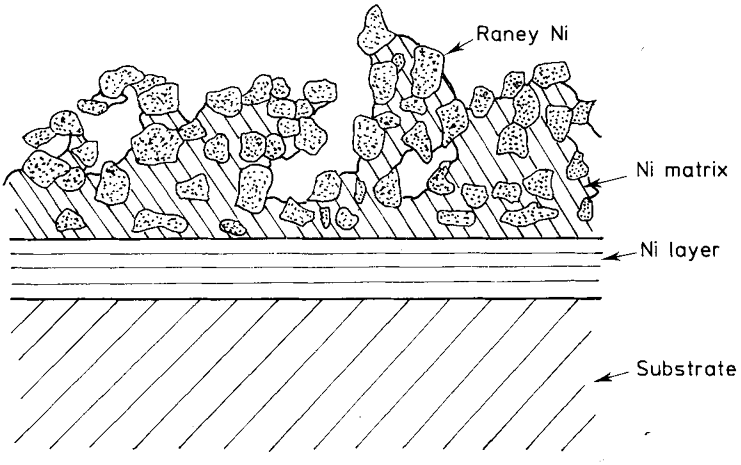

Fig. 5. Sketch showing the structure of a co-deposit of Raney Ni in a Ni matrix. After ref. 137, by permission of the International Association for Hydrogen Energy (IAHE).

ration [130–132]. However, the rate of hydrogen absorption can be controlled by modifying the surface of the metal with foreign metals [133]. With the addition of 0.2% Pd, Ti has been used industrially as a cathode for chlorate cells [134].

Raney metals, in particular Raney Ni, can be pyroforic in air because of the large amount of H dissolved [135]. Some additives are used to alleviate this problem [136], although other solutions have also been proposed. For instance, Raney-Ni can be incorporated into a Ni matrix so that the heat of H_2-O_2 recombination is dissipated through the metal [17, 137, 138] (Fig. 5).

Modifications of the chemical nature of the catalyst under cathodic load are also possible. Sulphides can be reductively dissolved with liberation of H_2S [139]. Oxides can be progressively reduced with loss of the specific activity [140]. In the latter case, an additive can be used to diminish the rate of reduction. Intermetallic compounds or alloys may exhibit preferential dissolution of one of the components during cathodic performances in concentrated alkali [141].

2.5 Methods of Preparation

The method of preparation is the most crucial and usually the least controllable variable, so much that it is usually taken as the last chance to explain any inconsistent behaviour. Unfortunately, this remains the least understood parameter, but also the most open one to originality and inventiveness. It is hard to list all methods, also because in many cases details have been left purposely obscure. However, to a first approximation, cathodes can be coated with an active layer by (i) electrodeposition [142], (ii) thermal decomposition [143], (iii) flame and plasma spraying [144–146], (iv) *in situ* activation [147, 148]. Cathodes may also be prepared from the powder of the active components by means of a suitable binder [20, 149], or by pressing and sintering [150]. "Pigmented" surfaces have also been prepared. This can be accomplished by dispersing the active component in a Watts (Ni) bath; the electrodeposited layer will consist of a Ni matrix incorporating the active component [151]. In principle, ion implantation is also expected to result in a "pigmented" surface.

Different methods of preparation usually result in cathodes with different activity. In some cases, the authors have directly compared different preparation procedures [141]. However, the same procedure may produce different results in different laboratories. This is not surprising, since this has been the case also with activated anodes. Only by identifying the factors responsible for the electrocatalytic activity, and by finding suitable conditions to control them during the preparation, it will be possible to standardize procedures and perhaps to establish some standards for reference.

The activity of cathodes may differ also for different *activation* procedures applied to the surface. In other words, electrodes as prepared may be inactive, or insufficiently active, and a sort of *etching* is needed before they exhibit the expected activity. The activation usually involves the removal of a *passivating* layer formed during the preparation. This is the case of Ti or Zr containing intermetallics [89, 152]. The surface is initially passive due to a TiO_2 or ZrO_2 overlayer, and can be activated by means of HF. The duration and the procedure of the pretreatment will influence the final activity by producing a surface of different composition.

In other cases, thermal decomposition is used to prepare the active layer which is then activated either by a high temperature treatment in H_2 atmosphere, or by *in situ* reduction under cathodic load. It has been reported that for molybdate-activated cathodes the latter procedure is less satisfactory than the former [153]. Thus, temperature, procedure of preparation and activation are all crucial parameters which can dramatically influence the final activity.

A further parameter is the nature of the support. In some cases, no effect has been observed, in other cases the effect of the support is evident, or even essential as in the case of disperse catalysts. As for the *in situ* activation achieved by dissolving the precursor in the working solution, the activity depends not only on the concentration of the species in solution, but also on the potential where activation is performed [147]. *In situ* activation is very attractive, since no separate coating formation is needed with all its labour cost. However, its applicability is in practice strongly subjected to the conditions of electrolysis, since precursors might interact with electrolysis products, or they might turn out to be unwanted impurities in the solution at the outset. Furthermore, while the presence of the precursor in solution can in principle be a guarantee against the deterioration of the active layer, maintaining its concentration in solution poses problems.

2.6 Poisoning

While poisoning of anodes is rare in view of the strongly oxidizing conditions existing on their surface, poisoning of cathodes is routine in technology. When investigating new electrode materials, tests of stability in the presence of poisoning impurities should always be included.

Organic substances are obvious poisons for hydrogen evolution (inhibitors) [154], but the most common poisons for industrial cathodes are the metallic species present in solution as a result of corrosion of the cell hardware and of other components of the electrochemical reactor. As a matter of fact, the most common impurity is Fe coming from the steel employed in manufacturing cells, which can be cathodically deposited on the active layer [34, 155]. Other impurities which have been considered are Cr, Ni, Hg and Cu [156, 157]. In other cases, and under different conditions, S [158–160] and CO [161] have also been considered as poisons for Pt.

The poisoning effect depends on the nature of the cathode. If the main impurity is Fe, it is expected to have negligible effects on mild steel, while it can result in activation with Ni or Ti cathodes [34, 162] (Fig. 6). It may even prevent the large increase of η with time observed with Ni at least on the laboratory scale [163]. With more

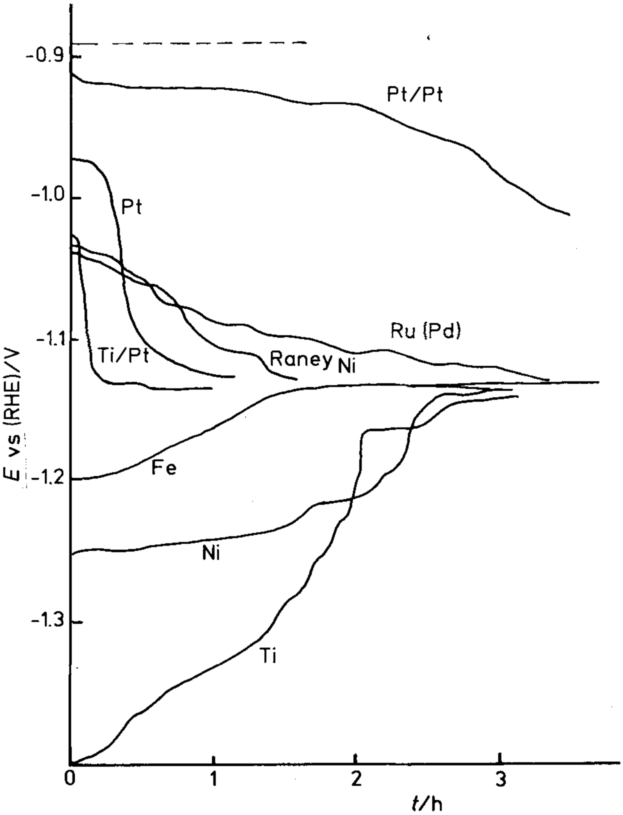

Fig. 6. Variation with time of the potential of hydrogen evolving cathodes at 3 kA m^{-2}, 90 °C, in 33 wt% NaOH, in the presence of 10 ppm Fe impurities in solution. (– – – –) Reversible potential. After ref. 162. This paper was orginally presented at the Spring 1984 Meeting of the Electrochemical Society, Inc. held in Cincinnati, Ohio.

active cathodes the presence of Fe is very deleterious. Since it cannot be avoided under technological conditions, it is necessary to design cathodes which are resistant to poisoning. Two possibilities are offered. Poisoning is reduced if the cathode surface is very rough and porous (es. Pt black, Raney metals, bonded $LaNi_5$, etc.) [149, 162] simply because the active surface is much larger than the diffusion front. This is also what is observed in the case of organic impurities [164]. The capacity of porous layers to slow down diffusion phenomena are exploited also in other cases, such as electrolysis of sea water to H_2 and O_2 [165], and chlorate and hypochlorite reduction [7, 166]. However, porosity offers a simple physical barrier whose features depend on the morphology of the active layer only.

More interesting from a fundamental point of view is the observation that the efficiency of poisoning depends also on the physical structure of the deposited impurity; this is in turn governed by the nature of chemical interaction between the impurity and the electrode surface. In other words, a different mechanism of deposition may result in a structure of the deposit which does not inhibit the active surface substantially. Thus, in the case of Pt electrodes, it has been observed that if the impurity content is around 14 ppm Fe, the cathode may even be activated since small crystallites of iron are formed [167].

In the case of oxides or sulphides, poisoning has been observed to be very weak [99, 168]. One reason is that these materials, especially oxides, are usually obtained as porous layers [169, 170]. But another, more exciting explanation is that metal deposition on non-metallic surfaces is more difficult than on metals, since the bond formed between the surface and deposited metal atoms is weaker [168]. Therefore, no underpotential deposition takes place, which pushes the potential range of impurity deposition to more cathodic potentials. If deposition takes place, it occurs at a high overpotential, and the resulting discharged particles form clusters rather than monolayers, thus leaving most of the active surface uncovered.

Poisoned cathodes can be recovered by dissolving the deposited iron. While this cannot be easily carried out *in situ*, a combination of *in-situ* activation with molybdate and poisoning by Fe can result in enhanced activity as a result of Fe-Mo interaction on the electrode surface [171].

Other impurities which can be present in industrial solutions are silicates coming from the dissolution of asbestos in diaphragm cells [34]. Although this may no longer be a problem, since asbestos is being replaced owing to its toxicity, and since cathode activation is not an economic solution for diaphragm cells in view of the poorer quality of the alkali produced, it is interesting to note that silicates inhibit hydrogen discharge on Raney Ni [172]. An inverse linear correlation between log j and log c (c = silicate concentration) has been observed. However, the conclusion is that the effect does not consist simply of blocking active surface sites, since an increase in the Tafel slope as the silicate concentration is increased is also observed. Thus, a redistribution of adsorbed hydrogen with different adsorption energies is probably involved.

Gas bubbles can also deactivate the electrode surface by forming a physical curtain [173, 174]. While bubble movement may enhance *in situ* mass transfer resulting in an increase of the current [175–178], the blocking effect of bubbles can distort measured parameters by introducing a sizable ohmic drop [179–183]. Bubble effects call primarily for engineering solutions, such as adequate electrolyte flow rate and optimized cell design, but they can also be related, though indirectly, to electrocatalysis, since the wetting of the surface depends on the electrode material.

2.7 Reaction Mechanism

The mechanism of hydrogen evolution is classically based [33, 184, 185] on a primary discharge step:

$$H^+(aq) + e \rightarrow H_{ad} \tag{3}$$

followed by either a recombination reaction:

$$H_{ad} + H_{ad} \rightarrow H_2 \tag{4}$$

or an ion+atom reaction (electrochemical desorption):

$$H_{ad} + H^+(aq) + e \rightarrow H_2 \ . \tag{5}$$

If the steps are strictly consecutive and one is the rate determining step (r.d.s.), theory [186] predicts (at 25 °C) a Tafel slope of 120 mV for reaction (3), of 30 mV for reaction (4) and, provided the coverage by the intermediate (H_{ad}) is potential-dependent (i.e., θ_H is small), 40 mV for reaction (5) being rate determining. If θ_H is high, a limiting current is expected if reaction (4) and a Tafel slope of 120 mV if reaction (5) is rate determining.

The above assumptions have remained unchanged for several decades. This mechanism has been shown to explain also the dependence of the Peltier effect on the nature of the metal [187]. The nature of the intermediate has been rarely disputed. The suggestion [62, 188] that reaction (5) might involve as an intermediate, $(H_2^+)_{ad}$, has not received any definite experimental confirmation [53, 189], although in one case it has been adopted [96]. In the case of alkaline solutions, it has been claimed [190–192] that the intermediate of the primary discharge is probably Na_{ad}:

$$Na_a^+ + e \rightarrow Na_{ad} \tag{6}$$

followed by:

$$Na + H_2O \rightarrow NaOH + H_{ad} \ , \tag{7}$$

which would replace reaction (3). Reaction (6) is indeed possible because of underpotential deposition [193], but the deposition potential should depend on the nature of the cathode surface since it is determined by the difference between the electron work function of the deposited metal and that of the support [66, 194]. On the other hand, the presence of alkali metals has been detected on various metals (e.g., Ni) during hydrogen discharge in alkaline solution [195, 196]. These adsorbates can be produced in a side-reaction at higher current densities [195], although adatoms have been detected at as low overpotentials as 0.1 V [190].

Apart from the case illustrated above, steps different from (3) to (5) have rarely been suggested, which emphasizes the simplicity usually envisaged in the hydrogen reaction. The possibility that the various steps proceed at comparable rates, rather than with a single r.d.s., has also been suggested and theoretical calculations have been carried out [197, 198]. This would explain the curvature of the Tafel line observed in some cases [199]. However, a Tafel slope of ca. 60 mV has been sometimes observed. This is not straightforwardly predicted by steps (3) to (5), unless activated adsorption according to Temkin's mechanism is postulated [186]. This is not unlikely, especially with transition metals, but it is difficult to envisage with weakly adsorbing materials. Thus, the possibility of slow surface diffusion (or rearrangement) of adsorbed intermediates:

$$H^+ (aq) + e \rightarrow H^*_{ad} \tag{8a}$$

$$H^*_{ad} \rightarrow H_{ad} \tag{8b}$$

has been suggested. This would imply that the intermediate produced in step (3) may not be the catalytically active one. The existence of "inert" and "active" adsorbed hydrogen has recently been postulated on the basis of IR surface investigations [200].

Tafel slopes different from the usual ones may also result if the r.d.s. proceeds *barrierless* (i.e., with $\alpha = 1$) (or quasi-barrierless [201]). Thus, hydrogen evolution with *barrierless* discharge – step (3) – or *barrierless* electrochemical desorption – step (4) – as the r.d.s., is expected to occur with a Tafel slope of 60 and 30 mV, respectively [202]. This behavior has been reportedly observed with Hg [203] , Bi [204], Ag [205], and Au [206]. However, such an experimental observation takes place only under very special conditions and cannot have any relevance to practical electrolysis.

Theoretical developments [207–209] have also included a comparison between the intermediate formed in the H_2 evolution promoted by photoemission, and that resulting at electrodes [206, 210, 211]. The conclusion has been that the two intermediates are in different states, the former corresponding to a hydrated unadsorbed hydrogen atom. Potential energy curves have also been derived and the activation energy of some of the steps calculated [212, 213]. The role of partial charge transfer has been analyzed [214]. The state of hydration of the proton has some importance in determining the energetics of the whole reaction. In particular, by comparing the discharge behavior of the fully protonated $H_9O_4^+$ and the H_3O^+ present in pure CF_3SO_3H, Conway [215–217] has concluded that the reaction rate, with allowance for double layer and concentration effects, is one to two orders of magnitude higher in the former case. The author suggests from these data that frequency factors can be as important as activation energies in determining the rate of proton transfer from different sources. Many more vibrational and librational modes are available for $H_9O_4^+$. These studies emphasize the problem of the correct description of the molecular mechanism of activation of the reaction of proton discharge; other pieces of evidence suggest that they are based on the model of solvent reorganization rather than on bond stretching [218, 219].

The relevance of a discussion of the reaction mechanism in the context of cathode activation for technological applications is obvious. Most of the traditional electrode materials exhibit Tafel slopes close to 120 mV at practical current densities. This can be interpreted [186] either as a retarded discharge, or as a slow electrochemical desorption under conditions close to saturation coverage with adsorbed hydrogen. In some cases a lower Tafel slope ranging 40 to 60 mV is observed at lower overpotentials. This is interpreted as slow electrochemical desorption at low θ_H, or slow discharge under Temkin adsorption conditions. A Tafel slope of 30 mV is seldom observed, mostly with expensive precious metals in acid solutions [38, 168] (with the notable exception of Re [220]). Incidentally, the exchange current density of step (3) on Pt in aqueous solution has been recently determined [221], by means of the galvanostatic transient method, to be 0.42 A cm^{-2} at pH = 0. This is regarded as one of the most rapid elementary reactions.

It is the purpose of electrocatalysis to design materials capable of evolving hydrogen with low Tafel slopes. Since catalytic metals usually adsorb hydrogen rather strongly, a Tafel slope of 120 mV is the most probable occurrence at high current densities. Thus, the situation for hydrogen is in principle less favorable than for Cl_2 and O_2 evolution. In the latter cases [16, 222], Tafel slopes of 40 mV (or even less) can be observed over several decades of current up to ca. 1 A cm^{-2}. This indicates that a moderate adsorption strength is operative for the intermediates with DSA® electrodes. The same target should be achieved with electrocatalysts for hydrogen evolution. However, the mechanism giving a 30 mV Tafel slope is not especially favorable, since it evolves naturally to a limiting current as the overpotential is increased and the hydrogen coverage rises. If the efficiency of H-H recombination is increased too much, it is probable that electrochemical desorption becomes the rate determining step. The task should be to maintain the low slope up to high current densities, which should be achieved by appropriately modulating the M-H adsorption strength. This is precisely what is pursued as an elemental electrocatalyst (a metal) is alloyed with others, or combined with non-metals (as in sulphides, oxides, carbides, etc.). It is clear that the most important parameter in this discussion is the heat of adsorption of the intermediate, which in turn will depend on the electronic and structural properties of the catalyst surface. Unfortunately, the theoretical description of the surface bond is still insufficient for composite materials; it is therefore necessary to recurr to experimental and conceptual correlations.

Normally, as a metal atom is surrounded by an environment differing from the bulk metal, its adsorption properties change. This is what happens as a metal hydride is formed, or as a metal adsorbs hydrogen in solution. The effect of the solvent giving rise to a lower adsorption strength is well documented [223] and should always be kept in mind when discussing electrolytic hydrogen evolution. It is at the base of the so-called *hydridic* nature of the M-H bond on electrodes as envisaged by Barclay [224] and verified by the present author [225] on the basis of available data. This opens the problem of the adsorption heat which should be adopted to build up a "volcano curve". Strictly speaking, it should be the adsorption heat in solution as it can be estimated *in situ* with electrochemical techniques. Adoption of such an adsorption heat can distort the volcano curve or even reverse one of the branches [225].

Since in most cases adsorption heats are not available experimentally, other parameters can be correlated with the activity, e.g., the calculated heat of hydride formation. Under similar circumstances a volcano curve can still be obtained for example for intermetallic compounds of Ti [53] (Fig. 7), or a linear correlation with the activation energy can be found [226] (Fig. 8). These correlations still point to the existence of volcano-shaped relationships with a maximum around an estimated value

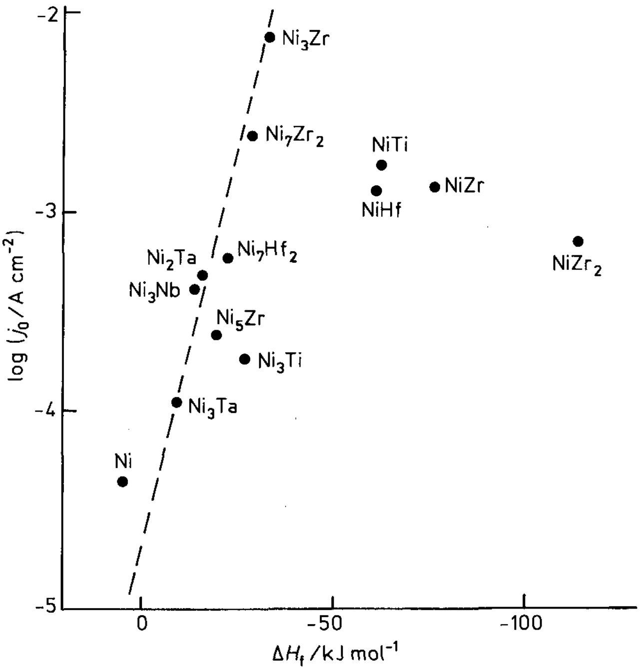

Fig. 7. "Volcano"-shaped curve for a series of Ni intermetallic compounds, obtained by plotting the activity for hydrogen evolution (j_0 in 9.2 M NaOH at 80 °C) against the calculated enthalpy for the formation of the related hydride (ΔH_f). (– – – –) Theoretical [17] straight line of (1/2.303 RT) slope. From ref. 53, by permission of IAHE.

for the M-H interaction [53] of the same order of magnitude as that for the apex of the volcano curve for metals [33, 54]. Thus, it appears that in order to obtain a Tafel slope of ca. 40 mV over several current decades, the adsorption of hydrogen on the catalytic surface should be lower than on such pure metals as Ni or Fe. This seems to be the case with oxides of Ir and Ru which show very favorable properties also in the case of hydrogen evolution [227], but not for many intermetallic compounds or alloys for which the Tafel slope persists around 120 mV although the apparent exchange current is substantially higher [228].

2.8 Effect of Temperature

Since hydrogen evolution is an activated reaction, an increase in temperature can only be kinetically beneficial. However, in many cases the Tafel slope has been observed not to increase linearly with T (i.e., $RT/\alpha F$) but to increase at a lower rate or even to remain constant [229–232]. This has stimulated much discussion [233–240] about the fundamental significance of such an "*anomalous*" behaviour which has been interpreted in terms of a partly potential dependent entropy of activation as op-

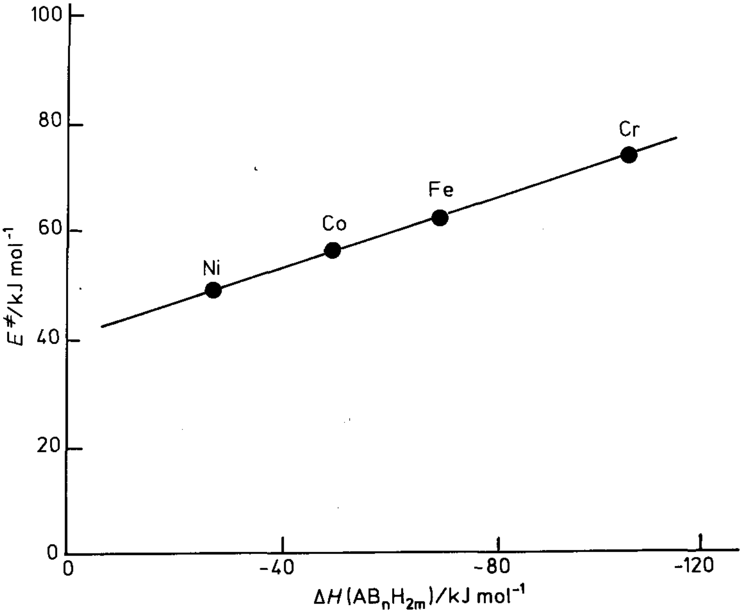

Fig. 8. Relationship between the activation energy for hydrogen evolution (1 M KOH, 30 °C) on LaM_5 and the enthalpy of hydride formation calculated by means of equation (12) (later on in Section 4.7). The nature of M is specified by the points. After ref. 226, by permission of Elsevier Sequoia.

posed to the classical theory of constancy in $\Delta S^{\neq}$ [241]. A modified quantum theory of electrochemical proton transfer has been proposed [242] to account for the "anomalous" temperature effect.

Although anomalous temperature effects involve very basic aspects of electrochemical kinetics, this topic is of relevance also to the practical situation in technology. In fact, it is necessary to know what one should expect (as a reference event) as the temperature of the cell is raised, which is always relevant in technology. Intensive electrolytic processes are not carried out at room temperature, first of all because, due to the intense heating of the solution by the current, room temperature in it could be maintained only by removing heat from cell (which would be impractical), and secondly because such self-heating is exploited to accelerate the reaction rate by reducing the overpotential. Thus applied studies always report Tafel lines over a wide temperature range.

The situation does not appear to be settled. Contrary to claims that the classical Tafel slope is probably an exception rather than a rule [239], the correct increase in Tafel slope has often been observed [243–245] also with catalytic metals [246, 247]. Measurements in frozen electrolytes with solid electrodes have not shown [232] any discontinuity in the dependence of b on T (whatever it may be), while a sharp discontinuity has been observed [234] as the melting temperature of Hg is crossed. On the other hand, the Tafel slope has been observed even to decrease with temperature [146, 248, 249]. It seems obvious that in such extreme cases a change in mechanism and/or in the electrode surface state is probably responsible for the decrease in *b*. In other words, the temperature not only raises the reaction rate on account of the activation energy, but it can also *catalyze* some modifications in the nature of the surface active sites. It is here necessary to stress that, for instance, sintering effects of Raney metals can be induced by an increase in temperature [250]. It is essential to take into account that an increase in temperature accelerates not only the steps of the hydrogen reaction, but also all other reactions which can proceed in parallel, including surface segregation in alloys and oxide reduction on passive surfaces.

Krishtalik and co-workers [251, 252] have convincingly shown for a few cases that if all possible interfering factors, including double layer effects, are avoided (or properly accounted for) and the experiments are conducted under controlled conditions of surface purity and stability, the anomalous effect does not appear. This does not mean that the interpretations offered for the anomalous effect are wrong (some discussion has indeed been provoked by the existence of different points of view [239]), but that any explanation should be applied only to data which have been positively freed from any other spurious effect. In the case of hydrogen evolution on catalytic metals and alloys, for which experimental evidence exists that the state of the surface can drift under cathodic conditions, the certainty that it remains the same at different temperatures has not yet been convincingly reached. This may explain why the anomalous temperature effect does not show any systematic variation with the nature of the electrode surface, which should indeed be expected considering that all other parameters of the hydrogen reaction do show it.

Sometimes very low Tafel slopes are claimed (<15 mV) [99, 253]. It seems difficult to interpret such an observation in terms of a specific mechanism. It is more probable that anomalously low Tafel slopes are the result of a combined thermal activation of the reaction and of the electrode surface state, resulting in a reaction rate limited by the diffusion of molecular hydrogen away from the electrode. Supersaturation of the electrode ad-layer by the evolved gas can also play a decisive role [254, 255]. This phenomenon has been amply discussed in the case of Cl_2 evolution on oxide electrodes [256], but the same idea can be applied to the case of H_2 evolution [257, 258].

3 Factors of Activity Enhancement

In what follows, some of the approaches proposed to enhance the electrocatalytic activity of cathodes for H_2 evolution will be scrutinized. Although the investigations reported are of fundamental interest, they should help to gain insight into the factors responsible for the activity of industrial electrodes.

3.1 Surface State

A morphological modification of the surface state without addition of foreign materials can result in an enhancement of the apparent activity of cathodes. This includes the mere increase in surface area which is normally achieved in practice by sandblasting electrodes [137, 259]. This is as a rule the first operation, both for activated anodes (support of Ti or Ni) and for activated cathodes (support of Ni or mild steel), it is done before proceeding to the coating step. Alternatively, as in the case of Ni, the metal can be co-deposited with ultrafine particles of silicon carbide to form a rougher composite surface [260]. The idea of roughening the electrode surface to enhance its activity is an old trick [261].

The effect of roughening is usually reported just to correspond to an increase in surface area. A thorough investigation [262] of the nature of the active sites on evaporated films of Ni has led to conclude that the mechanism does not change, with the activity being proportional to the number of active sites. However, different observations have also been made. Mechanically renewed surfaces show an increase in activity for both catalytic (Ni) [247] and non-catalytic metals (Zn) [263]. The increase in activity corresponds to a decrease in activation energy, which suggests that the M-H adsorption bond is modified by the mechanical treatment. In some cases, it has been reported that for freshly generated surfaces the activity enhancement is not stable. A decay is observed [264] in the case of Fe–Cr alloys, but the steady state activity remains higher anyway. It is intriguing that the final enhanced activity is independent of composition, while on the initial surfaces as well as on the just created surfaces the activity varies linearly with composition.

Enhancement of the activity of Ag has been observed upon continuous potential cycling [265], as well as with more complex potential sequences including potential holding at some cathodic values [266] and pulsating overpotential [267]. The enhancement cannot be explained only in terms of surface area increase, so that the creation of especially active Ag sites has been postulated [266].

Coldly worked Ni annealed at different temperatures has not shown [268] any electrocatalytic effect in acid solution while a drop has been observed in alkali as annealing is carried out above a given temperature. This has been interpreted as a support to the mechanism in which Na_{ad} is the intermediate (cf. steps (6) and (7) above). However, a characterization of the state of the surface, which may differ in alkalis and in acids, is lacking.

Smooth Pt and Rh electrodes have been compared [105, 269] with electrodeposited layers to investigate the effect of roughness (which may be of the order of 10^3). While electrodeposited Pt absorbs hydrogen and bright Pt does not, no surface area effect has been observed as for hydrogen evolution. This indicates that the internal surface (pores) of rough electrodes does not work because of exclusion due to gas formation. Thus, the porosity of the active layers also needs to be characterized. It has been shown that in the case of Raney Ni [270] this can be conveniently done by means of impedance measurements [271].

While no effects of simple roughness (except surface area effects) has been observed for the electrocatalytic activity of Ni, the situation appears to differ with mild steel for which a decrease in Tafel slope has been observed in the low overpotential range [272] (Fig. 9). An investigation of the effect of temperature and NaOH concentration has suggested [273] that in fact this may be related to the appearance, at low overpotential, of surface oxides, whose reduction leads to the break in Tafel line. Again, these results warn against interpreting certain apparent Tafel slopes only in terms of kinetic mechanisms.

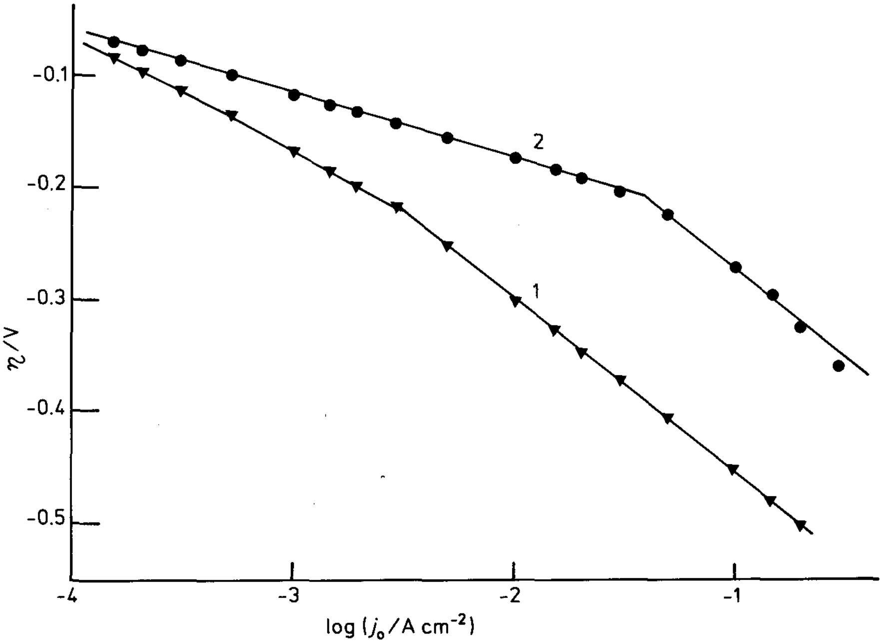

Fig. 9. Effect of electrode roughening on hydrogen evolution on mild steel in 10 M NaOH, 75 °C. (*1*) Smooth electrode; (*2*) Roughened electrode. After ref. 272, by permission of Pergamon Press.

A relative decrease in Tafel slope has been observed with steel subjected to thermal treatments leading to different microstructures [274]. In this case an effect can indeed be expected because of the possible formation of different phases or different proportions (martensite vs ferrite) of phases (Fig. 10). An effect of the size of grains has been observed on the Tafel slope.

While effects of film thickness have also been reported [275], metal-support interactions seem to be important in governing the properties of the overlayer. For instance, Ni chemically deposited on MgO has shown in particular higher resistance to oxidation as a consequence of electronic interactions with MgO [276].

It has already been mentioned that one of most used forms of Ni is Raney Ni which is obtained from Ni-Al or Ni-Zn alloys by leaching Al or Zn in alkaline solution. However, the properties of the resulting electrocatalyst appear to depend on the nature of the precursor [135]. Methods of application of the alloys are various [135]. A particularly convenient one is the so-called LPPS (low pressure plasma spray) [146]. Raney Ni prepared in this way has shown that lower Tafel slopes can be obtained, thus suggesting a real electrocatalytic effect (Fig. 11). On such highly porous Ni it is possible that the proportion of particularly active sites (at the edges and peaks of crystallites [262] increases considerably. However, the effect of temperature on the Tafel slope is more than anomalous [248] suggesting indeed some temperature-induced surface modifications. In fact, recrystallization phenomena are observed which can be minimized by means of small additions of Ti, Mo or Zr. The

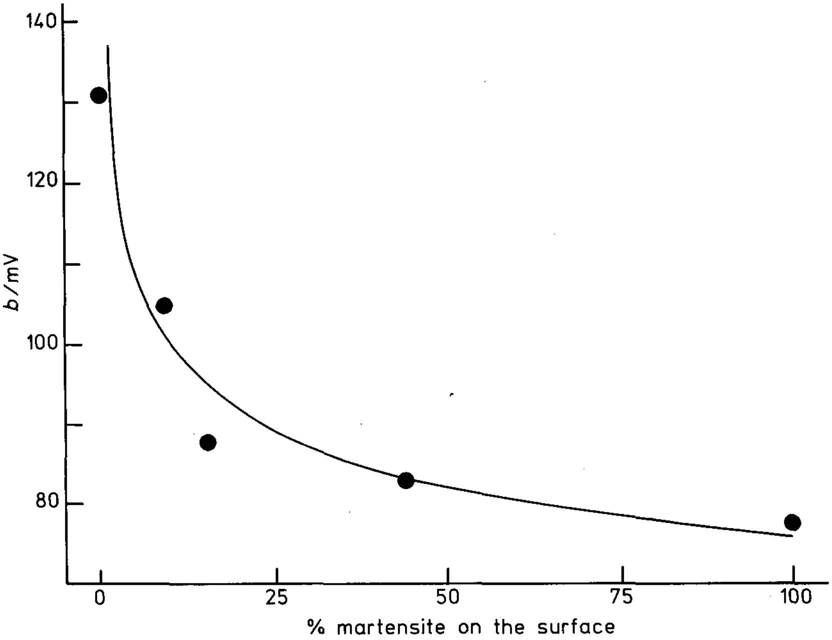

Fig. 10. Effect of the martensitic content of dual phase AISI-SAE 1008 steel on the Tafel slope for hydrogen evolution. After ref. 274, by permission of the publisher, the Electrochemical Society, Inc.

roughness factor can be as high as 10^3. The first commercial electrodes of Raney Ni have been reported to reduce the hydrogen overpotential by about 0.1 V at 0.2 A cm^{-2} [277], but much more effective reduction is achieved with specially structured electrodes (ca. 0.3 V) [34, 137].

Mechanical strain of Pd and Pt has been observed [278] to give rise to overpotential variations. Such an effect has been studied to gain insight into the factors responsible for the relationship between surface modifications and electrocatalytic activity. The analysis has shown that, of the various factors scrutinized including the possible variation in the interatomic distance, the most probable one is a change in ionic specific adsorption.

Ion implantation is often recommended as an efficient tool to enhance electrocatalysis either by disrupting the surface structure of the catalyst or by placing active atoms on an inactive (or less active) matrix. The latter possibility (which links this section with Section 3.3 devoted to adatoms) offers also a way to the use of extremely small amounts of active but expensive materials. In order to investigate the effect of surface damages, self-implantation or ion beam bombardment is the most appropriate approach. Implantation of Ni on Ni has led to a modest enhancement of the surface area, but not to electrocatalytic effects [279]. On the other hand, Pt bombarded with neutrons has shown an increase in the activity for hydrogen evolution [280]. However, it has been suggested that this is not related to the formation of surface defects, but rather to the effect of the radioactivity induced on the electrode and on the electrolyte.

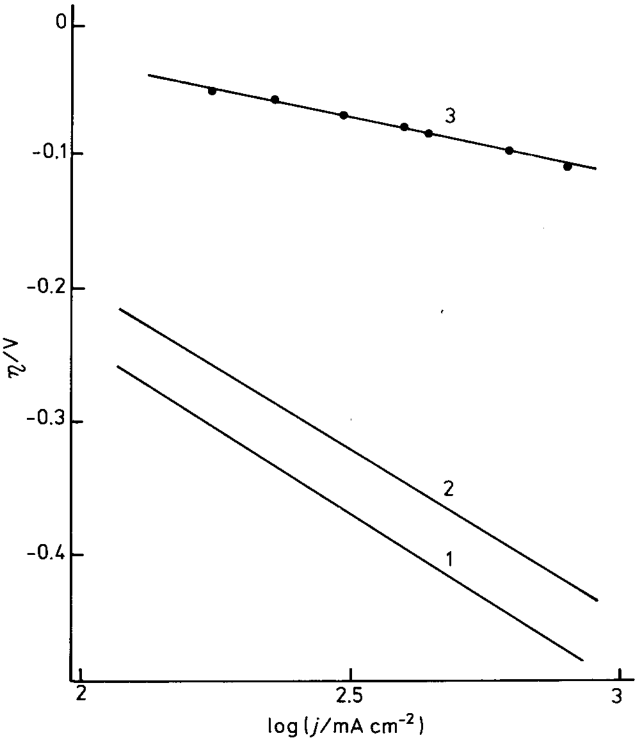

Fig. 11. Raney Ni (3) compared to untreated (1) and sandblasted Ni (2) for hydrogen evolution in 35 wt% NaOH at 90 °C. After ref. 137, by permission of IAHE.

Ion implantation of an active metal on an inactive (or less active) support is obviously expected to lead to electrocatalytic effects. This is clearly the case of various catalytic metals implanted on glassy carbon [281], but the results for Pt-implanted Fe are less obvious. No effect has been reported in one case [279], some effect in another case [282], depending on the dose. According to the latter authors, a dose of 10^{16} atoms per cm^2 produce a coverage of about 2% and imparts to Fe an activity similar to that of smooth Pt. It seems reasonable that in this case the effects are closely dependent on the dose as well as on the energy of the implanted ions, and that a comparison between results of different investigations may not be straightforward. In any case, the implantation of foreign elements couples the field of surface state modification to the field of application of adatoms (see later).

3.2 Single Crystal Faces

Investigations on single crystal faces are obviously not of *direct* interest in technology, but they are essential to again insight into the role of the surface structure. In fact, the nature and structure of surface sites are precisely defined on crystal planes, while they can be only roughly envisioned on crystallite faces [262].

A large part of the investigations on single crystal faces has been devoted to the study of the dependence of underpotential hydrogen adsorption on the crystallographic orientation [283–287]. Irrespective of the possible differences among the various authors, these studies have clearly indicated that the crystallographic orientation has a dramatic influence on the forms and the energy states of adsorbed hydrogen. In particular, as seen in voltammetric curves, at low hydrogen coverage the energy of interaction on Pt single crystal faces varies in the order $(111)>(100)>(110)$. However, as the coverage increases, the heat of adsorption decreases and the difference between the three main faces almost vanishes [288, 289]. Moreover, anions interfere with hydrogen adsorption [290, 291], which might explain some of the discrepancies often found in the literature.

Investigations of hydrogen evolution on single crystal faces are sparse and almost entirely by the Soviet school. The literature up to 1984 has been reviewed by the present author [292] and need not be reexamined in detail here. The evidence is that despite major effects at low θ_H, the crystallographic orientation has a minor influence on the electrocatalysis of hydrogen; the variation with the electron work function, Φ, or the potential of zero charge, $E_{\sigma=0}$, of the crystal face is however negligible compared to the variation over the same range of Φ [54] or $E_{\sigma=0}$ [293] exhibited by a large group of polycrystalline metals (Fig. 12).

Since 1984, only a few additional papers have appeared. These confirm the minor influence of the crystallographic orientation for Pt [294], Ni [295], and Ag [199] single crystal faces. Particularly detailed is the investigation carried out by Hamelin and Weaver [296] who have compared the activity of hydrogen evolution for seven faces of Au including some of high index. It is intriguing that the activity is higher in the presence of Li than in the presence of Na in the electrolyte. On the main faces the activity varies in the sequence $(111)<(100)<(110)$ but altogether the activity spans a factor of ca. 3.5 fold over a range of $E_{\sigma=0}$ of about 0.3 V (Fig. 13). Over the same range of $E_{\sigma=0}$ for polycrystalline metals the activity is observed to change by three orders of magnitude [293]. The conclusion of the authors has been that adsorbed hydrogen is stabilized on surfaces of higher step density, i.e., atoms of lower surface coordination number give stronger M-H bonds. However, this does not seem to be the conclusion of quantum-chemical calculations of H adsorption on single crystal faces of Ag [297]. On the other hand, it agrees with the suggestion that sites for H adsorption on Ni are atoms at the edges or summits of crystallites [262].

Investigations on single crystal faces of Ni have also indicated that well-defined faces give higher Tafel slope than the polycrystalline surface, and that the adsorption of hydrogen also depends on the crystal face [295].

Studies on single crystal faces have indicated that, on the whole, the crystallographic orientation has a minor influence on the electrocatalytic activity. Of the possible explanations which can be offered [292], a reasonable one is that the high coverage with adsorbed hydrogen far from equilibrium smoothes down the differences in ΔH_{ad} from face to face. Actually, quantum chemical calculations reproduce more closely the situation at $\theta_H \to 0$, which does not usually correspond to the real situation under cathodic load. Another possibility is that the hydridic

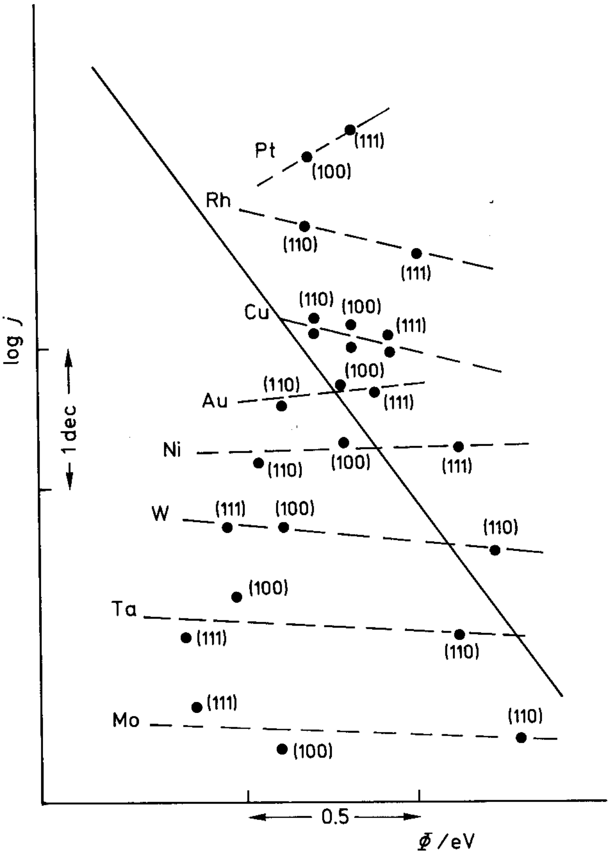

Fig. 12. Activity of single crystal faces of a number of metals for electrolytic hydrogen evolution as a function of the electron work function. (———) Relationship found with polycrystalline metal surfaces [54]. Adapted (updated) from ref. 292, by permission of Elsevier Sequoia.

nature of the M-H bond on electrodes (i.e., the competition with solvent adsorption) almost compensates the differences that would exist for the bare metal surface [223]. It is to be stressed that results with single crystals do not disagree with the weak effect in general observed with various surface treatments. Therefore, electronic factors seem to prevail over structural factors. Nevertheless, there are indications that very active sites can be obtained with atoms in a very low coordination state.

3.3 Adatoms

Unlikely ion implantation, adatoms can be deposited *in situ* on the cathode surface at underpotential. The mechanism of adsorption, its potential dependence and the state of the adsorbed atoms has been widely discussed in the literature [66, 193, 194,

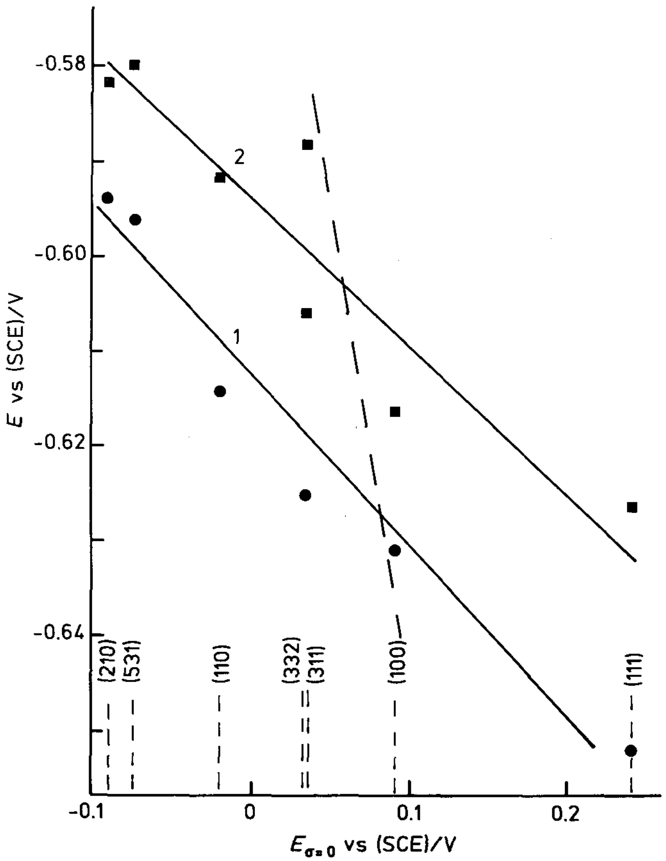

Fig. 13. Activity (measured as electrode potential at a given current density) for hydrogen generation on various Au single crystal faces as a function of the respective potential of zero charge. Electrolyte: (1) 0.09 M $LiClO_4$+0.01 M $HClO_4$; (2) 0.09 M $NaClO_4$+0.01 M $HClO_4$. (– – – –) Relationship found with polycrystalline metals [293]. Adapted from ref. 296, by permission of Elsevier Sequoia.

298]. In respect to ion implantation, the choice of metals to be deposited *in situ* is however, limited to the elements which can be deposited in the underpotential region. This restricts the choice mostly to post-transition sp-metals.

It is invariably reported that adatoms of Pb, Tl, Se, Sn, etc. on Au, Pt, Ir or Ag always give rise to deactivation of the surface for H_2 evolution [299–303]. The mechanism has been investigated especially by Motoo et al. [304] who have related the activity to the structure of the overlayer. Deactivation is mainly attributed to blocking of the surface active sites, so that it can be followed as a function of surface coverage by adatoms (Fig. 14). This turns out to provide an elegant approach to identifying the mechanism of hydrogen evolution [302, 303]. If the rate determining step involves only one active site, a linear decrease of j with θ_M is observed, otherwise

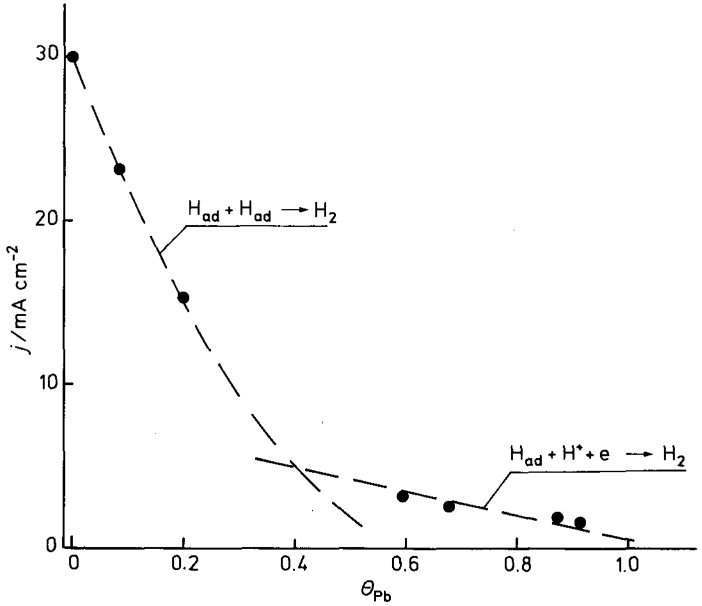

Fig. 14. Activity of Pt for hydrogen evolution in 1 M $HClO_4$ as a function of the coverage with underpotential deposited Pb. A change in mechanism with Pb coverage is indicated. After ref. 303, by permission of Pergamon Press.

the pattern is more complicated, usually with an abrupt drop in activity at $\theta_M \simeq 0.5$ if hydrogen atom recombination is the rate determining step [304].

Motoo [305] has also been able to show that an order-disorder transition in the overlayer can affect the activity of the surface (this may be related to the homogeneous adatom surface distribution vs cluster, or island formation), and that the electrocatalytic activity depends solely on the surface structure and not on bulk properties. The latter point has been demonstrated [306] by noting the similarity in the behavior of Au on Pt and of Pt on Au. Limited synergetic effects have been observed in both cases.

The study of inactive adatoms on noble (precious) metals has little impact on the practical problems of cathode activation for two reasons: (i) deactivation is the more common occurrence; (ii) adatoms are not stable in the absence of ions in solution where a finite level of precursors must be maintained, which in fact corresponds to the approach of *in situ* activation. The presence of ionic *impurities* in solution may pose serious technical problems. Studies of adatoms activation of Raney Ni, a material of current use in technology, can have a greater practical impact. It is interesting that the adsorption of Cd or Pb normally results in a sizable enhancement of the catalytic activity of Raney Ni [307–312]. The Tafel slope of the Raney Ni used by these authors is reported to decrease to ca. 30 mV as the catalyst is first soaked in a solution of the nitrates of the above metals [307, 308] (Fig. 15). The electrocatalytic activity is observed to increase slowly with time of adsorption as well as of polarization.

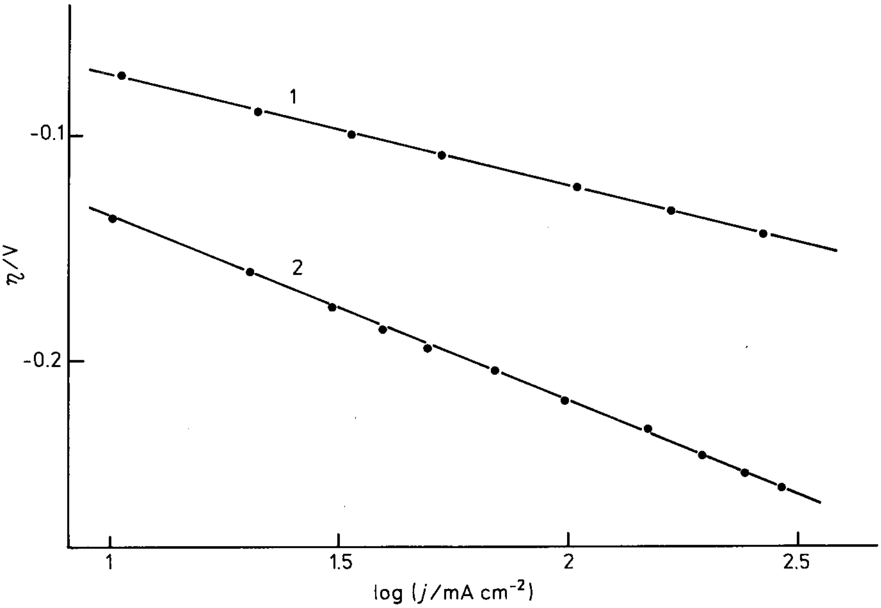

Fig. 15. Effect of adatoms on hydrogen evolution (6 M NaOH). (1) Pure Raney Ni; (2) Raney Ni after dipping in a 0.5 M solution of $CdSO_4$. Adapted from ref. 309, by permission of Plenum Press.

The explanation offered is that the electronic state of Cd or Pb on Ni is different depending on the polarization potential, and reaches steady-state conditions with slow partial charge transfer from the Ni surface to the ad-ions. The results show that adsorption of the ad-ions gives rise to displacement of preadsorbed hydrogen [307] with creation of new adsorption sites of more favorable adsorption energy [310]. This results in a change of mechanism. It is interesting that in the case of Ti [313] and Sn [314] adsorbed on Ir the activity continues to increase for some time at constant coverage, which indicates that the electronic state of the adatoms changes slowly with time compared to the rate of adsorption. It is thought that the modification is in the direction of slow *metallization* of ad-ions since the charge originally carried by them is unfavorable to hydrogen ion discharge. On the other hand, it is precisely the removal of electrons from the neighbouring metal atoms the cause of the creation of new active sites.

Results with Raney Ni and Ir show that the presence of adatoms does not exert only a blocking effect in the case of hydrogen evolution, but that partial charge transfer is the main mechanism by which new (or different) sites are created [314, 315] (Fig. 16). It is to be mentioned that the nature of the anion is also important [316] as the electrode is loaded with the precursor by soaking. The maximum effect has been observed with $Cd(NO_3)_2$ [311], with $Pb(NO_3)_2$ second [308]. Some evidence that a mechanism involving NO_3^- reduction may be responsible for the activation of Raney Ni has been offered [311]. Using $CdSO_4$ no effect has been observed on smooth Ni by other authors [26].

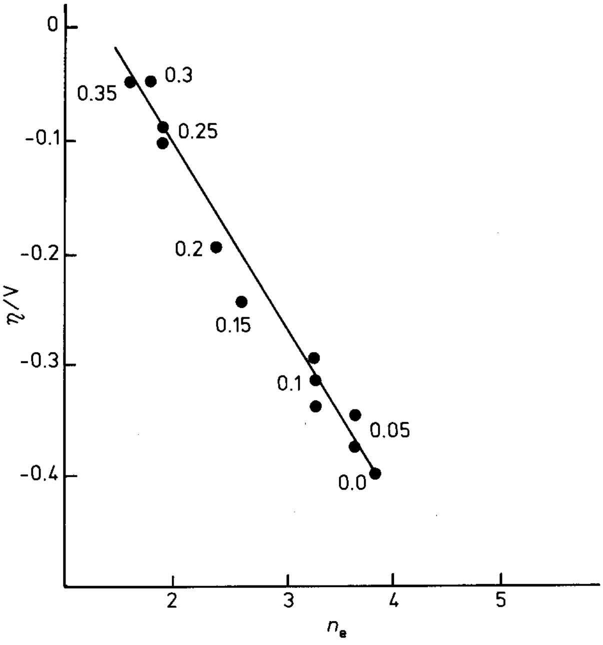

Fig. 16. Effect of adatoms on hydrogen evolution (0.5 M H_2SO_4). Dependence of overpotential of an Ir electrode on the degree of charge transfer (in units of electronic charge) to adsorbed Ti ions. Figures by the points indicate the adsorption potential. Adapted from ref. 313, by permission of Plenum Press.

The importance of electronic interaction as the basic mechanism leading to synergetic effects is also suggested by results showing that the simultaneous underpotential deposition of Cd and Tl on Ag(111) results in an enhancement of the hydrogen evolution rate while inhibitory effects are shown by the two kinds of adatoms separately [317].

3.4 Dispersed Microcrystals

On the way from adatoms to bulk solids there exist two intermediate structures: microcrystals and thin films. Both can be used to modulate the electrocatalytic properties with a modest expenditure of active materials.

The form of dispersed catalyst is especially suited for work with precious metals; no such stringent limitation in the amount of material is needed with other less expensive materials. On the other hand, finely subdivided catalysts are necessary for use in the SPE (solid polymer electrolyte) technology [10, 318–320]. When dealing with dispersed catalysts, the degree of dispersion (particle size effect) and the nature

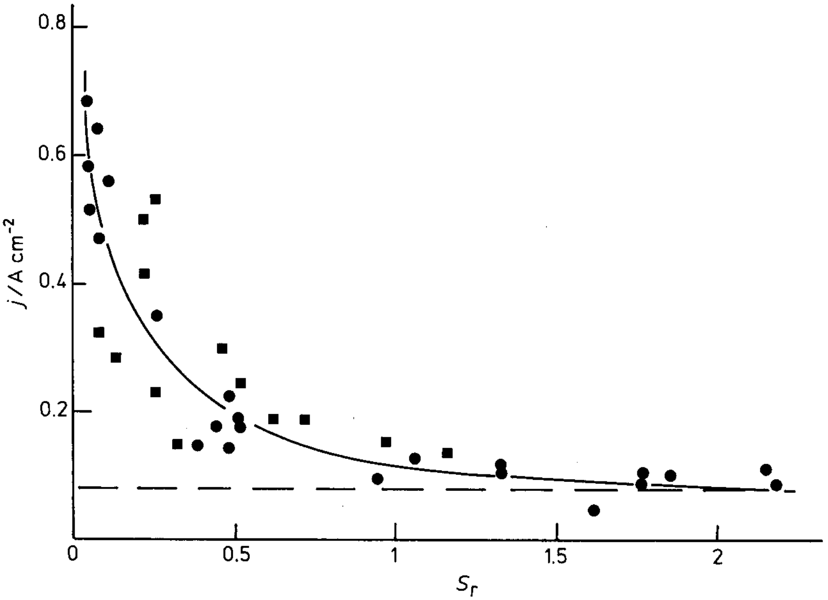

Fig. 17. Activity for hydrogen evolution (0.5 M H_2SO_4) of Pt microdeposits on unoxidized (●) and thermally oxidized (■) valve metals (Ti, Ta, Nb, Zr) as a function of particle size (decreasing with decreasing parameter S_r). (– – – –) Pure Pt. Adapted from ref. 326, by permission of Pergamon Press.

of the support (metal-support interaction) play paramount roles. Intensive studies have been devoted to the properties of microdeposits of metals notably by Kinoshita and Stonehart [321–325], and by Bagotskii, Vassiliev et al. [315, 326–330].

Details about preparation and characterization of dispersed microcrystals can be found in review chapters [322] and will not be dealt with here. All investigations indicate that the properties of microcrystals differ considerably from those of bulk metals (and from those of adatoms and thin films as well) [328], and that they can also be influenced by the nature and texture of the support. In particular, microdeposits of precious metals on various inert supports (Ti, Ta, Zr, Nb, glassy carbon etc.) exhibit enhanced electrocatalytic effects as evaluated per metal atom, while the mechanism of H_2 evolution remains the same [329], and the enhancement increases as the crystallite size decreases [326, 331] (Fig. 17). However, while this is the case with Rh, Pt, Os and Ir, Pd shows only an insignificant increase, whereas for Ru even a drastic decrease is observed [315, 332]. Thus, the effect of crystal size on the catalytic activity appears to depend on the nature of the catalyst (without any relation with the crystal structure group) [330].

It is very intriguing that as the particle size decreases below a critical value, its properties are so modified that new features appear [331]. Thus, the well-known two forms of hydrogen present on massive Pt become in fact three, and the amount of the third one increases as the particle size decreases [323]. The well-known ability of Pd to dissolve large amount of hydrogen disappears as the crystallite size decrease below about 2.5 nm [333]. Techniques of observation at high resolution are needed for these investigations [322]. TEM and STM are particularly suitables.

The electrocatalytic effect of small crystallites is attributed to the metal-support interaction [326, 330], a well known and widely discussed topic in catalysis [334]. In particular, since precious metals have high electron work functions, electrons are injected from the support into the crystallites thus modifying considerably the electron density which becomes a function of the crystal size. The fact that the effect of different supports is not visible [335] can be explained in terms of a large $\Delta\Phi$, so that the variations between different supports are very small [326]. However, in the case of carbonaceous supports, different preparations of the support may result in sizable effects because the morphology of the overlayer can be influenced [336].

As the particle size decreases, the ratio between the number of atoms at the surface to those in the bulk increases with a parallel decrease in the average coordination number for the metal atom, which is also expected to be a factor of electrocatalysis. It has been calculated for Pt that the minimum size of a crystallite (cluster) for all atoms to be on the surface is 4 nm, corresponding to a specific surface area of $280\ \mathrm{m^2\ g^{-1}}$ [322] (note that this is larger than the critical particle size where absorption of H atoms disappears on Pd) [333]. It is also interesting that dispersed catalysts can in turn influence the electronic properties of the support so that an interesting combination of sites with varied properties can result [330]. At low catalyst loadings, spillover of intermediates is also possible.

It has already been mentioned that "pigmented" cathodes can be prepared by codepositing, for instance, nickel together with small amounts of activating substances [151]. Such a structure may resemble a dispersed catalyst on an active surface (Ni), and the particle size can play a role. No detailed studies are presently available in this direction. "Pigmented" catalysts are suitable for application in chlor-alkali cells or other technologies. However, dispersed (powdered) catalysts are necessary in the SPE technology presently available for water electrolysis and, hopefully, soon also for other processes. In the case of SPE technology, the catalyst must be porous and therefore dispersed, and the degree of dispersion has to be optimized [337].

3.5 Modified Electrodes

The term "modified electrodes" encompasses a broad variety of electrode materials obtained by attaching a monomolecular layer of a specific compound on the surface of a conducting solid [338]. In electrocatalysis, modified electrodes are common in the field of oxygen reduction, where carbon materials can be modified for example by attaching layers of macrocycles. Modified electrodes are very common in the field of molecular or supramolecular electrochemistry, especially in the organic area.

For hydrogen as well as for oxygen evolution, where current densities are very high, modified electrodes are uncommon. Actually, adatom activated surfaces may fall into this category although they are not customarily included there, and in any case the use of the term becomes only a semantic question. To the knowledge of the present author, only very few investigations have been carried out with classically modified electrodes for H_2 evolution. In particular, cobalt porphyrins have been suggested as possible active agents for this reaction [339, 340]. The support has been glassy carbon. However, the H_2 evolution rate has been found to be very low, while the stability of the overlayer is insufficient. Nevertheless the catalyst is claimed to be potentially very active, and if incorporated into Nafion, it can become very stable. The problem is thus confined to finding a suitable support [340].

The mechanism of action of some Co porphyrins has been investigated [339]. It has been suggested that Co(I) is responsible for the reduction of water so that a sort of surface redox catalysis is operative. The principle of the activity is not very different from that of composite solid materials, e.g., oxides. Various solvents have been tested, and it has been found that the catalyst is especially active in neutral solution since the redox potential of the Co(II)/Co(I) couple approaches the potential of the H^+/H_2 couple.

A different kind of modification, which actually links this category of electrodes with surface alloys (discussed later), is that obtained by depositing a polymeric array of oxometalates (silicotungstate or phosphosilicomolybdate) on a metallic or nonmetallic support [341–343]. The activation can be accomplished *in situ* by dissolving in solution a small amount of $H_4SiW_{12}O_{40}$ or $H_4PW_{12}O_{40}$ (or other derivatives of the tungstic and molybdic acids) [344, 345] and polarizing cathodically [346]. During the first moments a drastic enhancement of the H_2 evolution reaction is observed, while a film is formed on the electrode surface. Later, oxometalates entrapped in polymeric matrices have also been used [347–350]. Alternatively, it has been shown that the above catalyst can be co-deposited with Ni from a Watts bath to form a "pigmented" surface [352].

In both cases, the enhancement of the electrode activity has been documented (Fig. 18). However, the characterization of the former electrodes in particular, although carried out with both electrochemical [352–355] and physical techniques [356], still appears insufficient. It is likely that Si and W are on the surface, but the amount of Si is minor, and the state of oxidation of both is unknown. It is not improbable that some forms of oxides may be present. Voltammetry shows that the active material exhibits a number of redox transitions close to the hydrogen evolution potential, and it is probably a form a surface redox catalysis which actually takes place. The active sites are thus provided by the surface redox centers.

The mechanism of hydrogen evolution has been briefly investigated both in acid [357] and in alkaline solution [358]. The kinetic parameters observed suggest that the mechanism remains the same in both media. Since the Tafel slope has been found to be around 120 mV (on glassy carbon as a support), the surface does not appear to be especially catalytic. The exchange current density is reported to be indeed remarkably high (about 10^{-2} A cm^{-2}), but due to the high Tafel slope the expected overpotential cannot be less than 0.25 V at 1 A cm^{-2} even though no further complications should arise. It has been reported [342, 354] that the same catalytic activity is achieved with different supports. This indicates that no overlayer-support interaction is operating, and that the overlayer is catalytic. However, the electrocatalytic activity has been assessed on the basis of the exchange current [342], which does not account for the fact that at high current density a material with low Tafel slope can easily surpass these modified electrodes. It is to be mentioned that the *in situ*

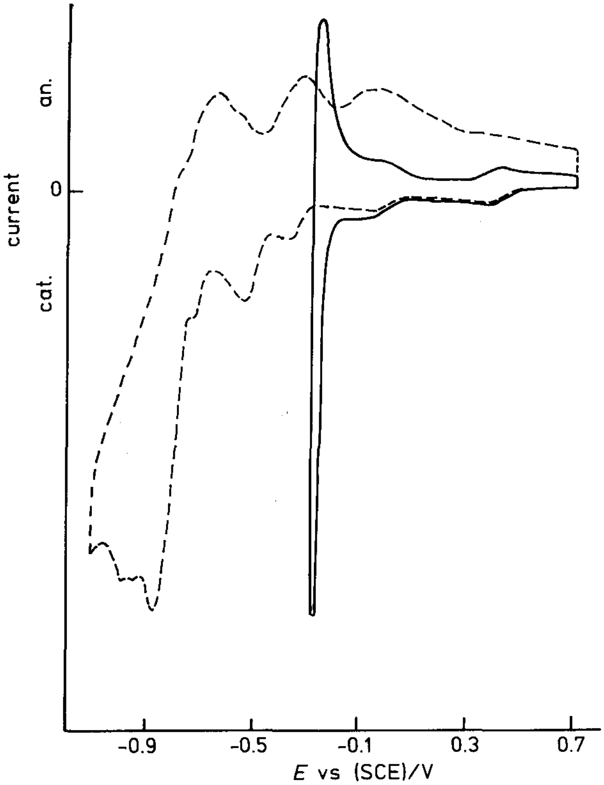

Fig. 18. Voltammetric curves showing the activation of glassy carbon (– – –) for hydrogen evolution in 0.5 M H_2SO_4 by *in situ* modification with α_1-$P_2W_{12}MoO_{62}K_6$ (———). After ref. 344, by permission of Elsevier Sequoia.

deposited material appears to be stable both in acid and in alkaline solution, which makes in principle these electrodes interesting especially for hydrogen evolution at low pH for which the options are very limited (e.g., borides and carbides).

Stability tests have shown [359] that these modified surfaces can be stable for more than 3000 hours. It is interesting that no deactivation has been observed in the presence of metallic impurities in solution. An activation of the surface has even been observed, which is to be related to the decrease in Tafel slope brought about by the deposition of small metal particles [167]. This is rather a proof that the original surface is not especially active for H_2 evolution (cf. Section 4.6).

The "pigmented" electrode has shown a more marked electrocatalytic effect [351]. The Tafel slope in acid solution decreases substantially with respect to pure Ni. The decrease in overpotential is substantial even with respect to Pt. SEM analyses have shown that the surface is very rough and that no apparent damage issues from a prolonged electrolysis. The considerable roughness of the surface may be the source of the observed resistance towards the deactivating action of Cd and Hg impurities in solution.

The catalytic activity of these oxometalates is well documented [360, 361]. An inactive surface of TiO_2 becomes an efficient catalyst for H_2 evolution as it is *derivatized* with silicotungstic acid [362, 363]. However, while real electrocatalytic effects seem likely for a pigmented Ni surface in view of the lower Tafel slope observed (which can also be due to some activation of the Ni itself), these are not completely established for the surface of pure oxometalates: surface area effects could be entirely responsible for the apparent activation. The real surface state of these electrodes deserves to be further investigated since these materials might fall into the category of amorphous phases.

4 Specific Materials

A more specific discussion will now be devoted to classes of materials which have been used more often in practical applications. Separation into groups has normally been quite a straightforward operation. Some ambiguity may remain between alloys and intermetallic compounds. While the metallurgical definition is quite clear, the assignment of some materials to either group used for electrochemical investigations can be a perplexing task. As a rule, materials have been classified as intermetallics as their nature resulted clearly from the context of the given paper. However, while this is only a problem of classification, a possible misplacement of a material cannot detract from the validity of the discussion.

The analysis will start with some discussion of Fe and Ni electrodes which are still the most economic and largely used technological materials.

4.1 Iron and Mild Steel

The hydrogen evolution reaction on pure Fe and on steels has been investigated in great detail because of its relevance to corrosion problems. No detailed discussion will be given here. A specific review has recently appeared in the literature [364].

H_2 evolution can proceed on Fe surfaces both in acidic and in alkaline solution. However, the metal is more appropriate for alkaline solutions although it cannot withstand high caustic concentrations and high temperature. The Tafel slope is usually around 0.12 V [365–368] pointing to either the primary discharge or electrochemical desorption as the rate determining step. The coverage with hydrogen reaches intermediate values [368–370], but penetration beneath the surface has been pointed out [371, 372].

No particular difference in mechanism is observed between iron and steels, but the way Fe is prepared (e.g., its purity) bears on the activity [368, 373]. The discharging particle is H^+ in acids and H_2O in alkalis. In buffered solutions [374] the acid component of the buffer probably participates in the reaction mechanism, at least beyond a critical concentration. The effect of pH has been investigated over the complete pH range [366, 371]. Both “anomalous” [230] and “normal” [366] effects of temperature on the Tafel slope have been reported.

The mechanism of hydrogen evolution has been investigated by impedance measurements [371] and hydrogen-tritium kinetic isotope effects [375]. The effect of halides dissolved in solution has been studied [372, 376]; these ions increase the overpotential in the sequence $Cl^- < Br^- < I^-$. Adsorption isotherms for halides have been derived. They conform to the Temkin adsorption model with partial charge transfer. The lateral interaction between adsorbed particles has been calculated. It is higher for Br^- than for I^- and increases with overpotential on account of the weakening in the metal-halide bond. Thus, halides are substantial poisons for hydrogen evolution on iron. Poisons also include metal ions such as Cd^{2+}, Zn^{2+}, and Mn^{2+} [26].

The mechanism may change from acids to alkalis in some cases [365]. This may be related to the higher sensivity of the Fe surface to oxidation in alkaline solutions [365, 367]. Actually, the corrosion of Fe proceeds also under moderate cathodic load [368]. Impedance measurements have suggested that the classical mechanisms of hydrogen evolution is probably inadequate to describe the situation on Fe [377]. A surface diffusion step with spillover of hydrogen to sites with lower M-H energy has been suggested. Adsorption of CN^- interferes with such a diffusion.

A new mechanism has been proposed to account for the role played by surface oxides [372, 375], where the rate determining step is the reduction of surface oxides:

$$FeOH + H^+ + e \rightarrow Fe + H_2O \tag{9}$$

followed by the chemical reduction of water due to the very active bare surface metal sites:

$$Fe + H_2O \rightarrow FeOH + 1/2\,H_2 \ . \tag{10}$$

The inhibiting effect of halides is explained not in terms of an effect on the M-H bond but rather as an influence on the M-OH bond strength and on the degree of coverage with oxidized sites. The degree of poisoning depends also on the mechanical treatment of the surface [372, 373]. On an electropolished electrode the coverage by hydrogen becomes affected at a higher halide concentration than on a mechanically renewed surface. On the other hand, electrochemically polished electrodes show a higher overpotential than those mechanically polished.

The metal-water interaction has also been suggested [373] to play a role in determining the extent and strength of hydrogen adsorption. The metal-water interaction is potential dependent; in particular it decreases as the potential is made more cathodic. Thus, pseudo-capacitances were observed at higher overpotential than 0.3 V because of the appearance of a considerable amount of adsorbed hydrogen.

4.2 Nickel

Nickel is certainly the material most widely used for cathodes and activated cathodes. Various procedures have been suggested to modify the structure of the surface and its morphology with the aim to increase the surface area and to possibly enhance the electrocatalytic activity [51].

4.2.1 Smooth Nickel

The mechanism of H_2 evolution from acids and bases was investigated long ago [378]. The Tafel slope is invariably around 120 mV while the surface is heavily covered with adsorbed hydrogen. The r.d.s. is normally the primary discharge of H^+ in acids and of H_2O in alkaline solution. An alternative mechanism has been suggested [379] for caustic solutions according to which H_{ad} is formed from the chemical reaction of H_2O with electrodeposited alkaline metals (cf. steps (6) and (7) above). Evidence has been provided [190] to support this mechanism, but arguments against have also been offered [378]. However, the details of the mechanism do not seem to change the general picture.

The activity of Ni cathodes decreases under prolonged cathodic load [380, 381]. This is primarily due to absorption of hydrogen which can reach quite considerable concentrations [382]. The diffusivity of H in Ni has been measured [383]. However, the mechanism does not appear to change on deactivated electrodes [380]. An increase in temperature appears to conform to the kinetic predictions in some cases [378], but at temperatures above 80 °– 100 °C, a dramatic activation is observed [380, 384] which must be related to some modifications occurring on the electrode surface.

Oxides are always present on the surface of transition metals in alkaline solution. At open circuit they are intermediates in the mechanism of corrosion. The resistance of Ni towards corrosion in base is better than Fe or mild steel, especially at high caustic concentration and high temperature [23, 24]. The role of surface oxides in the cathodic range of potentials depends on the conditions of their formation. Thus, a reducible layer of hydroxide $Ni(OH)_2$ or even oxohydroxide NiOOH has been found [385] to be beneficial for the electrocatalytic activity. It has even been claimed [386] that some good performances are specifically due to the formation of oxide layers during the preparation (Fig. 19). An activation of the Ni surface by the application of anodic current pulses has been reported [387] to be beneficial owing to the formation of $Ni(OH)_2$ layers. This has been confirmed by impedance studies of the mechanism [388].

Surface oxides are easily reducible if formed at low anodic potentials but they can become deactivating if formed at higher potentials, as during a cell shut-down. For the latter case, specific remedies have been suggested. For example, if a metal hydride capable of absorbing large amounts of hydrogen is introduced into the cathode structure, it can be charged on cathodic load and discharged during shutdowns thus protecting the Ni surface from anodic oxidation [109, 389, 390]. Due to the presence of surface oxides which are anyway difficult to reduce quantitatively, the effect of temperature on the kinetic parameters is difficult to interpretate in terms of established concepts [391].

The adsorption of H on Ni around the reversible potential can be estimated by charging curves, potentiodynamic curves, and impedance measurements [96, 382, 392, 393]. The heat of adsorption decreases as the coverage increases, but the

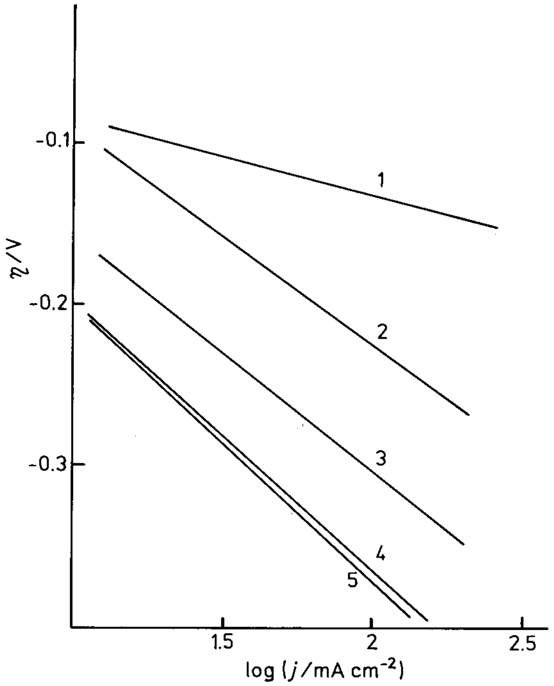

Fig. 19. Tafel lines for hydrogen evolution in 30 wt% KOH, 80 °C, on plasma-sprayed Ni cathode coatings reduced under H_2 atmosphere for 30 min at different temperatures. (1) Electrode as prepared; (2) Reduced at 200, (3) 300, (4) 400, (5) 500 °C. After ref. 386, by permission of Chapman & Hall.

coverage is close to saturation of E_{rev}. This enables the true surface area to be determined from the charge spent to ionize the adsorbed hydrogen. A capacitance value of 260 $\mu F\,cm^{-2}$ [96] or of 1120 $mF\,cm^{-2}$ [382] (depending on the procedure of calculation) has been suggested as a basis for surface area determinations. The amount of adsorbed hydrogen increases with increasing temperature as expected for an activated process. Comparison between gas phase and solution shows that water molecules occupy some of the sites otherwise covered by hydrogen [393]. However, hydrogen preadsorbed in the gas phase is not displaced as the sample is immersed in solution [394]. This indicates an interaction between two adsorbing sites. However, the amount of hydrogen adsorbed in solution is lower than in the gas phase [93] (Fig. 20); this fits in with the predictions based on the position of Ni on the hydrophilicity scale of metals [223].

The amount of adsorbed hydrogen decreases in the presence of halide ions [395, 396]. This is due to a decrease in the M-H adsorption energy induced by ion-specific adsorption with partial charge transfer. The decrease in M-H bond strength results in an increase of overpotential. The effect is lower for Cl^- and higher for I^-. However two joint effects are operative: one due to electronic modifications, and the other one of an electrostatic nature related to a change in the local electric potential

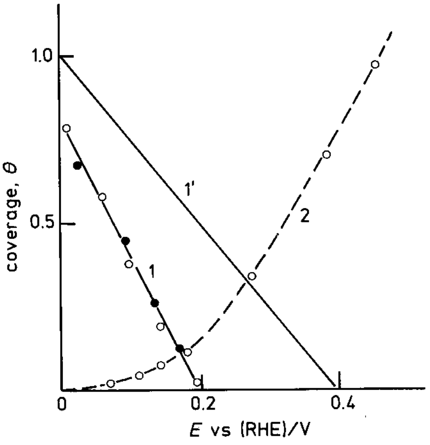

Fig. 20. Coverage of Ni with adsorbed hydrogen (1,1') and with adsorbed oxygen (2), in the gas phase (1') and in alkaline solution (1, 2). (●) Dispersed Ni; (○) Compact Ni. After ref. 93, by permission of Elsevier Sequoia.

(ϕ-effect). With Cl^-, the latter is more important than the former. The reverse is the case with I^-. The overpotential decreases as the acid concentration increases and the effect is observed to be stronger in HCl than in H_2SO_4 solutions. A ϕ-effect is invoked in this case as well [397]. However, a possible role of the decrease in the dielectric permittivity of the solution at high ionic concentration has also been pointed out [398].

4.2.2 Raney Ni

With the aim to enhance the apparent current density of Ni cathodes, several surface treatments have been proposed to increase the surface area. The simplest procedure, and therefore the one of routine, consists in sandblasting the surface. The Tafel line turns out to be shifted towards higher currents without changes in its slope [137]. Sandblasting is a common operation also prior to proceeding to the further activation of cathodes (or anodes) [259]. The aim is to provide a support of larger surface area and to ensure better adhesion of the overlayer.

Since improvements achievable with bulky electrodes are limited by the structure of the electrode itself, sintered, porous, Teflon bonded, or phosphate-bonded Ni electrodes have been proposed [386, 391, 399, 400]. A mere increase in surface area is observed without any change in Tafel slope. The same is the case with Ni wiskers in spite of their very large surface area and small particle size [401, 402]. A decisive modification of the kinetic pattern is indeed obtained as Raney Ni is used [93, 403] (see Fig. 11). This form of Ni is well known also in the field of hydrogenation catalysis. As an electrocatalyst it was proposed by Justi et al. [404] long ago. Raney Ni is obtained by allowing Ni with a component (usually Al or Zn) which is then leached away in caustic solution. The dissolution of the soluble component leaves a porous structure with a very high surface area and particularly active metal sites [135, 406]. However, there is evidence that not all of the "inner" surface of Raney Ni works under intense hydrogen evolution [51, 135]. Moreover, under long-term cathodic load, the structure of the electrocatalyst may change with extensive sintering and recrystallization phenomena leading to progressive deactivation [405].

Raney Ni is normally unstable in air immediately after it is charged with hydrogen. Various remedies have been proposed to alleviate this shortcoming, including the co-deposition of pulverized Raney Ni in a Ni matrix which can disperse the heat produced [137], and the controlled anodic ionization of the adsorbed hydrogen before the use of the Raney material [135].

Variants of preparation have been proposed [135, 248] including sintering [391] or co-electrodeposition of the precursors [138, 407], and "*aluminization*" of the surface of Ni at high temperature whose nature has a definite effect on the resulting electrocatalytic activity [408]. The main features of Raney Ni have been evaluated, including the pore size distribution and the real surface area [93, 135]. It has been found that the composition of the precursor alloys and their particle size have important influence on the adsorption properties of the resulting Raney metal, hence on its electrocatalytic properties [409].

Raney Ni evolves hydrogen exhibiting a two-section Tafel line [93, 248, 406, 408]. At low overpotentials b is around 40 – 60 mV, at high overpotentials it is close to 120 mV. The Tafel slope of the first section is usually observed to decrease with increasing temperature, which suggests the probable occurrence of a change in the surface state.

Raney Ni with additives is also used [77, 276]. In particular, valve metals are added to stabilize the catalyst structure [102, 410, 411], thus decreasing the recrystallization and sintering which always takes place as the solution temperature is raised [412] (which points to the high energy state of such an electrode structure). In this respect, potential cycling has also been observed to be detrimental since it can induce recrystallization [407]. This is probably the reason why surface oxidation may be deleterious with Raney structures [390] while it normally results in improved electrocatalytic properties with bulk Ni electrodes [386]. However, after prolonged cathodic load resulting in deactivation, Raney Ni electrodes can be reactivated (temporarily) by means of anodic sweeps [405].

Various metals can be prepared in Raney form [410, 413, 414]. In particular Co, Fe and Ni – Co have been compared with Ni. While in one case the presence of Co has been found detrimental [407], in another synergetic effects have been claimed for Raney Ni – Co alloys [415]. Alloy compounds will be discussed later on.

More complex structures have been designed to meet special technological requirements. A cathode developed by the Japanese chlorine industry [416] consists of a layer of Ni electrodeposited on steel, covered by a second layer of Ni co-deposited from a bath containing dispersed active charcoal, with on top a layer of an electroplated Ni – S alloy to impart better mechanical strength thus avoiding erosion of the active layer by evolving hydrogen. The sandwich-like sequence is repeated several times. Although sulfur is partly leached away during cathodic operation, the protecting layer is not destroyed and does not have any adverse effect on the performance.

This cathode (called TWAC) exhibits a low Tafel slope up to a few kA m^{-2} so that the reduction in overpotential, compared to the traditional cathodes, reaches 0.2 V at 3 kA m^{-2} which is almost the same as that achieved with a Rh-activated cathode. The resistance to poisoning by Fe impurities is also improved; this is probably related to its exceptionally high surface area, the roughness factor being of the order of 10^4.

4.3 Interstitial Compounds (Carbides)

Ni or steel, although as active in acid as in alkaline solution, are not suitable materials for strongly acid environments, such as water electrolysis by SPE or with a SO_2-depolarized anode, or electrolysis of HCl and H_2SO_4 solutions.

Precious metals are natural candidates under similar circumstances, and carbides have been proposed to replace the more expensive precious metals [417]. Typical carbides are those of W [418, 419], although some Cr [420] and Ti [419, 421] carbides have also been investigated.

Carbides were first proposed as anodes for H_2 ionization in electrochemical power sources [422]. The higher activity of WC with respect to W for H_2 evolution was discovered about forty years ago [423], but the first practical proposals for the use of carbides as cathodes are found only recently under the influence of research aimed at the development of more efficient water electrolyzers [424]. More recently, aqueous suspensions of WC have been proposed to catalyze H_2 formation in the presence of the reduced form of a redox relay that is continuously generated through a photochemical reaction [425].

WC is intrinsically not very active since the exchange current for smooth electrodes is of the order of 10^{-6} A cm^{-2} [423, 426]. Two Tafel slopes are usually observed, ca. 50–60 mV at lower overpotentials, and ca. 120 mV in the high overpotential region [418, 419, 426, 427]. However, the overpotential for WC is much lower than for TiC and is stable with time [423]. The activity appears to depend on the carbon content, increasing with some departure from the stoichiometric ratio [92, 428] (Fig. 21). Cr_3C_2 and Cr_7C_3 show similar patterns, with the former apparently slightly more active than the latter [427, 429]. The mechanism proposed is slow discharge or slow electrochemical desorption under Temkin adsorption conditions. The active sites are suggested to be the metallic atoms. It is interesting to note that a regular behavior has been observed for the effect of temperature on the Tafel slope in both sections of the Tafel line [426].

The WC electrode has been suggested [92] to lie on the ascending branch of the volcano curve. As the carbon content departs from stoichiometry (deficit), the M–H bond strength increases with a shift of the activity to higher values. However, no maxima have been observed on the anodic charging curves, which suggests that the coverage with adsorbed hydrogen is probably low [430]. Anodic ionization of H_2 is however preceded by an adsorption step.

Surface oxides play a paramount role in imparting the electrocatalytic activity to W carbides [92, 426–429]. W is known to be covered by a thin oxide layer which

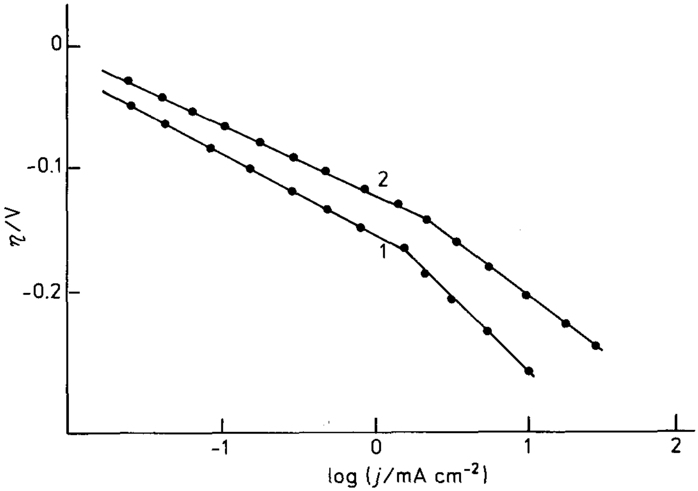

Fig. 21. Effect of carbon deficit on hydrogen evolution in 0.5 M H_2SO_4, 20 °C, on W carbides. (1) WC; (2) $WC_{0.9}$. After ref. 92, by permission of Plenum Press.

is reduced only with difficulty. If W electrodes are pretreated cathodically they become more active than WC. Electrodeposited W has been shown to behave similarly to electroplated Ni [431]. Thus, W oxides deactivate the electrode surface for H_2 evolution. Carbon stabilizes W towards oxidation; the higher the carbon content the higher such a stabilization, but the carbon content itself has an adverse effect on the electrocatalytic activity. As a C deficit is present, not only the susceptibility to anodic oxidation, but also the electrocatalytic activity increases. Therefore, the departure from stoichiometry must be limited. However, the stoichiometric surface is more corrodible than the non-stoichiometric surface.

Since WC is intrinsically not very active, special electrode structures have been aimed at increasing the surface area. In particular, Teflon-bonded WC electrodes show enhanced activity which, however, depends on the details of preparation [424]. WC prepared by carburizing WO_3 [432] incorporated into bonded graphite powder [433] has shown the highest activity (Fig. 22). It has been found [433] that the most active electrodes consist of an oxide-free layer of hexagonal WC with particle size ranging 10–20 nm. WC cathodes containing unreacted WO_2 or other tungsten oxides have been found to be correspondingly less active. Long-term tests have shown a loss of a few percent of the active layer.

Results concerning other interstitial compounds are sparse. The hydrogen overpotential on non-stoichiometric TiN_x increases with the N content [434]. These materials are thus less active than pure Ti. The Tafel slope is about 120 mV independent of N content. Decrease in M–H bond strength with N content has been suggested. Hydrogen penetration has also been observed.

Nickel boride (Ni_2B) has been quoted sometimes as an excellent electrocatalyst in alkaline solution [3, 10, 400]. However, there exists only one paper describing a practical stability test [107]. A patent filed in 1974 describes the electroless formation

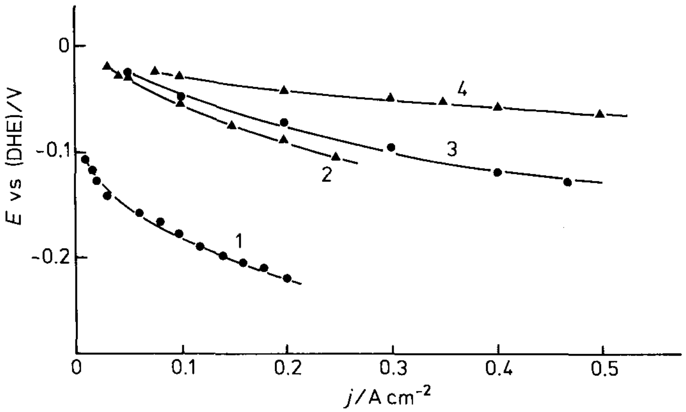

Fig. 22. Current-overpotential curves for hydrogen evolution in concentrated H_2SO_4 on differently prepared WC cathodes. (1) Teflon-bonded powder; (2) Teflon-bonded powder pressed onto glided Ti; (3, 4) Powder pressed onto graphitic support (in two different conditions). After ref. 432, by permission of IAHE.,

of Ni_2B layers [435]. The structural state of the compound mentioned above has never been explicitly specified. No further results have apparently been published since 1982.

Nickel boride with the same composition as the above one has been investigated in the amorphous state (see Section 4.8). Borides and nitrides of other transition metals, in particular the valve metals Zr, Nb, Ta, and W, have not shown any interesting activity for hydrogen evolution [436].

4.4 Sulfides

Studies of hydrogen evolution on sulfur activated cathodes appeared for the first time (but see ref. 74) in the late 70's in connection with the development of advanced water electrolyzers [11, 12, 437, 438]. More recently, cathodes of this kind have been developed for chlor-alkali cells [439]. That sulfur compounds can catalyze hydrogen evolution has been clearly observed with non-catalytic metals such as Hg [440, 441].

The compound most commonly used is NiS_x, whose composition is variable. But FeS_x, CoS_x, and $NiCoS_x$ (formally $NiCo_2S_4$) have also been proposed. Methods of preparation are varied. They go from electrodeposition in the presence of a sulfur compound (thiourea, sulfite, etc. [25, 442]), to electroless coating in the presence of dithionite [443, 444], to "pigmented" electrodes (obtained by electrodepositing NiS_x dispersed in a Ni bath) [151], to sulfidization of the related oxide [445]. As expected, the activity of the resulting catalyst is largely dependent on such details of the preparation procedure as composition of the bath, thickness of the active layer, nature of the support, etc.

Although these electrodes are customarily referred to as sulfides, they are of a broadly varied composition; strictly speaking they can even be regarded as amorphous materials [442]. In fact, X-ray analysis has shown that NiS_x is poorly crystalline and that some crystallinity is achieved only as the sulfur content is higher than a critical value (ca. 30%) [439]. The crystalline compound has then be identified as Ni_3S_2 [446]. Usually, the sulfur content is much lower than the stoichiometric one [442, 444, 446, 447], i.e., only a minor part, if any, of the metal can be really present as a sulfide. The composition can also differ between the bulk and the surface where there may be a sulfur-rich layer which passivates to some extent the electrode [139, 448].

The activation of Ni or mild steel with sulfurized layers is well documented [93, 443, 447, 449]. The Tafel slope is usually low, of the order of 40–60 mV, while the amount of hydrogen adsorbed by the surface increases compared to the non-sulfurized metal. The activity can equal that of Raney Ni, and a Raney Ni electrode activated with sulfur can be very active. The activity is largely increased by raising the temperature [25, 443]. However, the Tafel slope decreases as the temperature rises, which indicates some other kind of activation.

In the light of common parallelisms between catalysis and electrocatalysis, it is interesting to note that Co and Mo are used in catalytic processes of hydrodesulfurization [450]. The activity of sulfide electrodes changes with time [439, 442, 446]. Normally, there is an initial period during which the overpotential decreases, then it increases again or levels off at a constant activity. The initial improvement is interpreted in various ways but it is generally attributed to some stabilization of the electrode surface (Fig. 23). It seems that a hydride phase is formed initially [442].

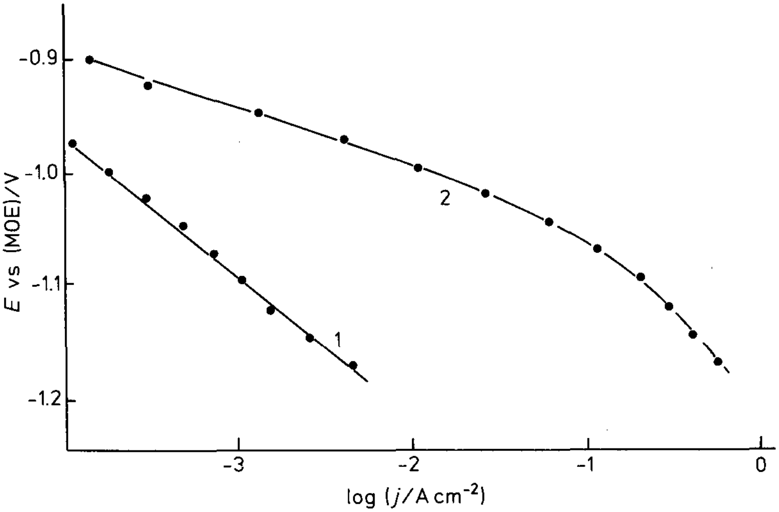

Fig. 23. Current-potential (MOE = mercury oxide electrode) curves for hydrogen evolution in 1 M NaOH on an electrolytically prepared NiS_x electrode. (1) Initial behaviour; (2) After stabilization. After ref. 442, by permission of Pergamon Press.

This has been proven by showing that anodic activation re-establishes the initial behaviour. This is also the case with CoS_x [451]. However, the composition of the catalyst changes with time with a constant loss of sulfur [151, 439, 444]. This loss of sulfur has even been invoked as a possible source of activation since it corresponds to leaching out of unbonded and passivating sulfur. The loss of sulfur is readily detected in acid solutions since H_2S is evolved, whereas sulfur is leached out as S^{2-} in alkaline solution [441, 445, 448].

It is interesting that the loss of sulfur does not correspond to a steady decrease in activity. It is well possible that the leaching of sulfur results in a structure resembling that of Raney Ni. The kinetic pattern is in fact the same. Some remedies have been proposed to slow down such a weight loss. For instance, it has been shown [151] that a small addition of MoS_2 co-deposited with NiS_x in a Ni matrix can apparently alleviate the problem.

Another source of deactivation is the usual presence of metallic impurities, in particular Fe, in technical solutions [25, 151, 446]. Fe is deposited on NiS_x and can produce deactivation, but the effect is reduced on account of the larger surface area and the semimetallic nature of the surface. The addition of MoS_2 is reported to result in an improvement in this direction as well. Ni impurities have been found not to deactivate NiS_x electrodes.

NiS_x has been observed to behave better than CoS_x and FeS_x. The decrease in overpotential can be as high as 0.3 V with respect to Ni [25, 151]. $NiCo_2S_4$ (formal composition) has been found to operate at -0.1 V vs DHE, at a current density of $1\ A\ cm^{-2}$ and has been tested successfully for several thousand hours [444, 452]. At open circuit a bluish coloration of the solution indicates that some Co is leached out since it becomes anodic with respect to Ni. A small continuous cathodic protection would be necessary. Teflon-bonded $NiCoS_x$ electrodes have been found to be immune from Fe poisoning; this has been attributed to the precipitation of FeS_x on the electrode surface due to the presence of sulfur in solution leached out from the surface. This condition will not be realized in a continuously flowing solution.

4.5 Oxides

In previous sections it has been mentioned that surface oxides may sometimes catalyze and sometimes inhibit the hydrogen evolution reaction. As a matter of fact, DSA-type electrodes developed for Cl_2 evolution and based on oxide coatings have been industrially applied to hydrogen evolution in recent times. Patents have been filed claiming low Tafel slope, insensivity to poisons and long-term stability [453–455].

Anodic Ni oxides catalyze H_2 evolution if they are not formed at too high potentials, otherwise they may depress the activity [93, 385, 449, 456]. Insulating layers are normally inefficient for hydrogen evolution [457, 458]. It is interesting to note that semiconductors can reduce the overpotential for hydrogen evolution on Hg and the effect increases as the semiconductor band gap decreases [459]. This is in line with the observation that a passivated Nb electrode is not an efficient electrocatalyst for H_2 evolution [460] whereas $Sr_xNbO_{3-\delta}$, which is a metallic conductor, evolves H_2 with a low Tafel slope [461]. Investigations on Na_xWO_3 were carried out about 20 years ago [462]. These materials showed a dependence of the electrocatalytic activity on x with a maximum at about 0.7. The Tafel slope was observed to be 120 mV, rising to 180 mV at higher current densities. The exchange current was in the range of 10^{-5} to 10^{-4} A cm^{-2}. However, most of the activity was attributed to traces of Pt (about 100 ppm) present in the solid [463]. No further developments appear to have occurred in the direction of the application of these materials as hydrogen cathodes.

Several studies have addressed the mechanism of hydrogen evolution on passive metals or bulk semiconducting oxides. Even on Ti the activity improves with the oxygen content as Ti–O alloys are formed. A maximum is observed around 30% oxygen [464]. The Tafel slope is somewhat larger than 120 mV. However, on cathodically treated TiO_2 hydrogen can be evolved with 60 mV slope in the presence of residual TiO_2. An increase in oxide thickness depresses the catalytic activity [465].

The above systems cannot have any impact on the technology of cathode activation but they are useful for gaining insight into the details of the mechanism [466, 467]. During the cathodic load, hydrogen penetrates into the oxide which is thus progressively reduced resulting in a variation of its properties. The penetration is likely to be promoted and assisted by the strong electric field which develops across the solid phase [468, 469].

The stability of oxides with respect to reduction is often a kinetic problem. In the case of RuO_2, the main component of DSA®, although thermodynamics predicts that it should not be stable under hydrogen evolution [470], this is not the case. Under prolonged cathodic load the oxide appears to be stable and no bulk reduction can be detected [168]. This phenomenon is probably related to the fact that proton penetration into RuO_2 cannot be assisted by any electric field since the oxide is a metallic conductor [471]. Nevertheless, RuO_2 can be reduced in a hydrogen atmosphere at high temperature [472]. A correlation between the reducibility of metal oxides in hydrogen and the strength of the oxygen bond in their surface layer has been proposed [473].

The first investigation of H_2 evolution on RuO_2 was carried out by the present author about 20 years ago [474]. A Tafel slope of 60 mV was observed indicating higher activity than Ni and steel, but research in this direction was not pursued further over the next fifteen years. More recently, studies have shown that RuO_2 [168, 227], and also IrO_2 [475], evolves hydrogen with a Tafel slope of 40 mV from both acid and alkaline solutions and that the low Tafel slope extends up to current densities of 0.2–0.3 A cm^{-2} where a transition to a higher Tafel slope is apparent [476]. It is clear that such an electrode is among the most active materials for H_2 evolution. But DSA® are not inexpensive since they contain precious metals and alternatives are being investigated. An interesting oxide system is $Sr_xNbO_{3-\delta}$, a metallic conductor, which also exibits a Tafel slope of 40 mV (for $x > 0.95$) which extends to high current densities [461]. The electrocatalyst is suitable for acid solutions and shows an anodic current after hydrogen evolution which may indicate some hydrogen absorption. Whether hydrogen is trapped only at the surface is unclear. In the case of RuO_2 and IrO_2 no hydrogen absorption is observed [475, 477].

The state of the surface is a unique feature of oxide electrodes. The hydration of surface sites is responsible for a particular mechanism giving a fractional reaction order with respect to H^+ which results from a pH dependent electric potential at the reaction site [478]. A discussion of the structure of the oxide-solution interface has been given by the present author [479]. Single crystals of IrO_2 do not show any tendency to adsorb hydrogen on account of their hydrophobic surface [480], whereas useful insight into the relationship between nature of active sites and mechanism of hydrogen evolution can be gained with RuO_2 single crystals [481]. No kinetic studies of H_2 evolution have been carried out thus far on oxide single crystal faces.

Spinels provide another possibility for oxide cathodes [8]. Patents have been filed covering the thermally prepared spinels of Ni, Co, Fe and Mn [482]. However, very few details are available. Pure Co_3O_4 is easily reduced cathodically with dramatic changes of its properties [483]. Additives are necessary to slow down the cathodic reduction [8]. Studies in the field of catalysis can guide in the search for additives. Among others, La, Zr and Al are expected to be the most efficient ones [484, 485]. No data are presently available to test this prediction.

By and large, all oxide electrodes need to be stabilized since some reduction takes always place during long-term use. ZrO_2 has been proposed as an additive for RuO_2 based electrodes [253]. Solid state chemistry investigations suggest that the presence of small amounts of La_2O_3 together with ZrO_2 strengthens the action of the latter [472]. Actually, DSA® never consist of pure RuO_2; they contain valve metal oxides (usually TiO_2) and certain structure stabilizers. The nature of the additives is often unknown since compositions are developed in industrial laboratories rather than in academic institutions. For instance, a porous NiO_x based electrode has been developed by Asahi, which is claimed to resist current reversals and high cathodic currents [140]. The base electrode has been found to drift towards higher overpotentials with the progressive reduction of the oxide. For this reason a more advanced cathode contains a suitable additive.

Since RuO_2 and IrO_2 are usually prepared by thermal decomposition of suitable precursors on an inert support, the morphology of the active layer is very like that of a compressed powder [486]. The surface area plays an important role since the roughness factor can be between 10^2 and 10^3. However, the low Tafel slope observed is a clear indication of electrocatalytic effects and the high surface area is the factor which extends the low Tafel slope to much higher current densities. Thus, the combination of these two factors renders these oxides very efficient electrocatalysts for H_2 evolution.

The surface area is a function of the temperature of preparation of the oxides [169, 486]. Thus, the apparent electrocatalytic activity decreases with increasing temperature of calcination (which is usually in the range 350 °– 500 °C) [227, 475]. However, if the calcination is carried out at too high temperature, the electrode surface is deactivated probably as a consequence of some dehydration, and the observed Tafel slope can be very high [487]. The important relationship between the acid-base properties of an oxide surface in solution and its electrocatalytic properties has been pointed out by the present author [488].

Phenomena of pore exclusion may occur with gas evolving reactions on very porous electrodes. This is the case with Raney-Ni electrodes for which a proportional increase in activity does not correspond to an increase in porosity [135]. Quite interestingly, no pore exclusion is observed [227, 475] with RuO_2 and IrO_2. The activity even increases upon hydrogen evolution (self-activation) indicating that surface reduction promotes the wetting of surface regions otherwise excluded [477]. This has been attributed to the higher hydrophilic character of a partly reduced oxide surface. The evolution of gas is thought not to take place directly in the pores, but the internal walls still work via fast proton transfer along the surface OH groups (something like a surface Grotthus mechanism).

Since the oxide structure is not reduced, the following mechanism has been proposed [475]:

$$-\overset{|}{\underset{|}{\mathrm{M}}}-\mathrm{OH}+\mathrm{H}^+ + \mathrm{e} \leftrightarrow -\overset{|}{\underset{|}{\mathrm{M}}}-\mathrm{OH}_2 \tag{11a}$$

$$-\overset{|}{\underset{|}{\mathrm{M}}}-\mathrm{OH}_2+\mathrm{e} \rightarrow -\overset{|}{\underset{|}{\mathrm{M}}}-\mathrm{H}+\mathrm{OH}- \tag{11b}$$

$$-\overset{|}{\underset{|}{\mathrm{M}}}-\mathrm{H}+\mathrm{H}_2\mathrm{O} \rightarrow -\overset{|}{\underset{|}{\mathrm{M}}}-\mathrm{OH}+\mathrm{H}_2\ . \tag{11c}$$

The second reaction is the rate determining step. This mechanism predicts the observed Tafel slope of 40 mV; the fact that the same slope extends to high current densities indicates that the reaction proceeds with low H_{ad} coverage. The increase in Tafel slope at even higher current densities may indicate that the first step becomes rate determining. The same mechanism apparently holds also in alkaline solutions.

An interesting composite activated cathode based on RuO_2 has been developed for use in chlor-alkali cells [489]. The cathode consists of a first thermal layer of RuO_2 on a Ni support, modified by a second layer made of electroless Ni. This activated cathode permits a saving of 250 mV overpotential compared to smooth Ni. It is intriguing that although observations by SEM show a "cracked-mud" like layer of Ni, RuO_2-like behavior is obtained (Fig. 24). Electroless Ni without RuO_2 underneath does not show activation. It is clear that the electrode works through the cracks. The modified electrode is much more stable than pure RuO_2; it maintains its performance over long time periods (tests reached almost 2.5 years without any apparent failure), while it is unaffected by Fe impurities in solution.

RuO_2 has been proposed to "modify" indium tin oxide electrodes used in storage photoelectrolysis devices [490]. RuO_2 has been reported to increase the electocatalytic activity of the system while the optical transparency is not compromised even at relatively high catalyst loads. Acceleration of photocatalytic H_2 evolution in mixed solvents upon deposition of RuO_2 on TiO_2 single crystals has also been reported [491].

RuO_2 has been found to be an efficient catalyst also for H_2 evolution assisted by light [492–495]. A dispersion of RuO_2 in aqueous solution decomposes water in the presence of a suitable sensitizer. However, it has been observed [496] that the ac-

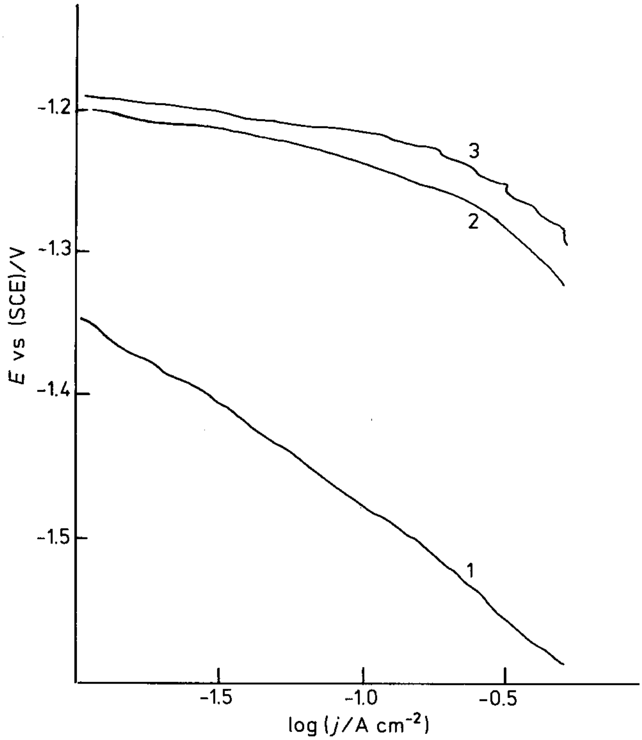

Fig. 24. Current-potential curves for hydrogen evolution in 35 wt% NaOH at 85 °C. (1) Electroless Ni coating; (2) Thermally prepared RuO_2; (3) RuO_2 with electroless Ni coating. After ref. 489, by permission of Elsevier Sequoia.

tivity of the catalyst depends on the producer, i.e., on the procedure of preparation, and its efficiency reaches a maximum only after the oxide has been appropriately prereduced, in line with the mechanism proposed above. Thus, consistent pictures are obtained from completely independent fields.

Oxide electrodes have been observed to be almost immune from poisoning effects due to traces of metallic impurities in solution [99]. This is undoubtedly due primarily to the extended surface area. It can be anticipated that the calcination temperature must have a sizable effect. But in addition, a different mechanism of electrodeposition must be operative. Chemisorption on wet oxides is usually weak because metal cations are covered by OH groups [479]. As a consequence, underpotential deposition of metals is not observed on RuO_2, although metal electrodeposition does takes place. However, electrodeposited metals give rise to clusters or islands and not to a monomolecular layer like on Pt. Therefore, the oxide active surface remains largely uncovered even if metallic impurities are deposited [168]. Thus, the weak tendency of oxides to adsorb ions, and its dependence on the pH of the solution is linked to their favorable behavior observed as cathodes in the presence of metallic impurities.

It has been suggested [497] that if oxide cathodes are doped with the oxide of the metal present in solution as an impurity, the electrodes become immune with respect to that specific impurity. Such a "homeopathic" approach is certainly intriguing, but it should be documented with some more evidence that clarifies the state of the dopant and its role during impurity adsorption.

4.6 Metallic Alloys

Alloying two (or more) metals has long appeared as the most straightforward way of achieving electrocatalytic activation. The study of solid solutions over the whole composition range has been often used as a means to gain insight into the relationship between electrocatalytic activity and electronic structure [498]. Interestingly, no major effects have ever been observed with bulk alloys. Smooth correlations between activity and composition have mostly been reported [56, 499]. Recent investigations with Pd-Ag [500–502] and Pd-Au [503] alloys have shown that a modest activity maximum probably exists around 60% Pd but this composition does not fit in with the idea of relevance of the often overemphasized "percentage of d-character" [63], which is thus ruled out as playing an important role [56, 504].

Studies with adatoms and microcrystals have clearly shown that the electronic structure of these systems are profoundly different from those of the corresponding bulk material. Electrocatalytic activation can be expected only as the structure of the material is substantially changed (cf. Raney metals). The case of DSA® has shown how widely the properties of a material can be varied as it is obtained in a poorly crystalline, dispersed, non-stochiometric form.

It is difficult to trace back the origins of cathode activation, since it is certainly linked to the observation of electrocatalysis by ionic species. However, one of the first examples of cathode activation for technological applications seems to be the use of molybdenized graphite to enhance amalgam decomposition in chlor-alkali industry [504]. It appears that the proposal of Mo-based materials as cathode activators has taken origin from that specific case. Thus, Mo-based alloys either electrodeposited [142], or thermally prepared [505], or added *in situ* [147, 148], have constituted the main objective of research during the past fifteen years [13, 34, 145, 402]. The basic promoter is an alloy of Ni and Mo, but variants have been proposed and tested [506–509], consisting in additions of small amounts of V, Ti, W, Cd, Re or, as a third component, Fe, Co, Cr, Cu, etc. In addition to this group of materials, Ni–Fe [510] and Co–Mo [511] have also been investigated. Actually, Co–Mo has been among the first systems proposed as a means to further enhance the activity observed with molybdenized graphite [512, 513].

Various methods have been suggested to deposit a thin active layer of material on a support. Those most commonly employed are: (i) electroplating; (ii) thermal decomposition; (iii) *in situ* formation. "Pigmented" Ni matrixes have also been proposed [508]. As one can expect, a range of activation has been observed; the electrochemical and mechanical stability is also varied. As for the nature of the active material, it seems clear that Ni–Mo based materials show superior qualities. The

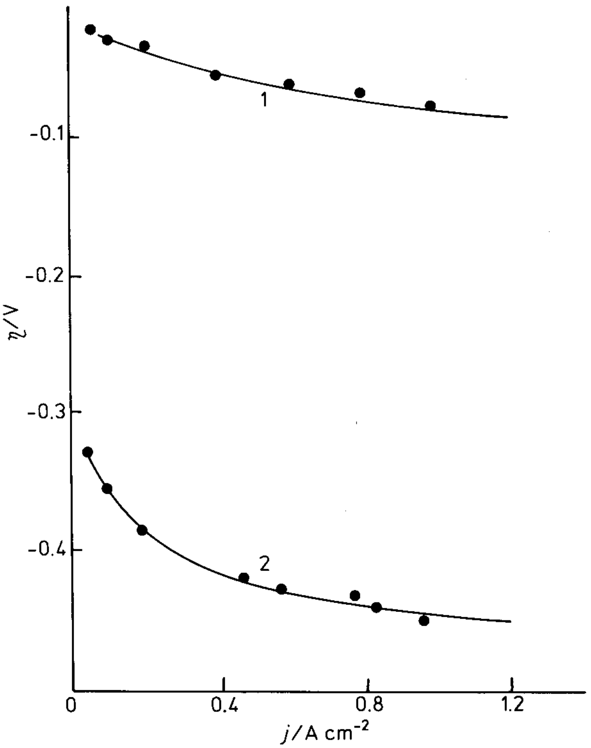

Fig. 25. Current-potential curves for hydrogen evolution in 5 M KOH at 70 °C. (1) 80 mesh Ni screen coated with thermally prepared Ni+Mo coating; (2) 80 mesh Ni screen. After ref. 505, by permission of IAHE.

Ni–Fe alloy is also interesting. However, the activity enhancement has recently been found to be only due to a larger surface area [514].

Increase in surface area has been invoked to explain the apparent enhanced activity also in the case of *in situ* activation with molybdate [515, 516]. Synergetic effects have been explicitly ruled out. As molybdates are deposited from a technical solution, a co-deposit of Mo and Fe is in fact formed, but the Tafel slope remains the same as for pure Ni [147, 517]. The same is the case of Ni–Mo *bulk* alloys [518].

As Ni–Mo mixed layers are prepared by thermal decomposition of suitable precursors, clear synergetic effects are observed (with a maximum around 30% at Ni [73]). The Tafel slope decreases to 40 mV and extends to very high current densities so that the overpotential has been reported to be only 70–90 mV at 1 A cm^{-2} (Fig. 25), formally implying an exchange current close to 10 mA cm^{-2}, three orders of magnitude higher than that for bulk Ni. While part of the activity is to be related to the large surface area, synergetic effects are manifested by the change in the reaction mechanism [5, 153, 505, 519].

A change in mechanism with respect to bulk Ni has been observed also with electrodeposited alloys of Ni–Mo containing only 1% of Cd. Two Tafel slopes are ob-

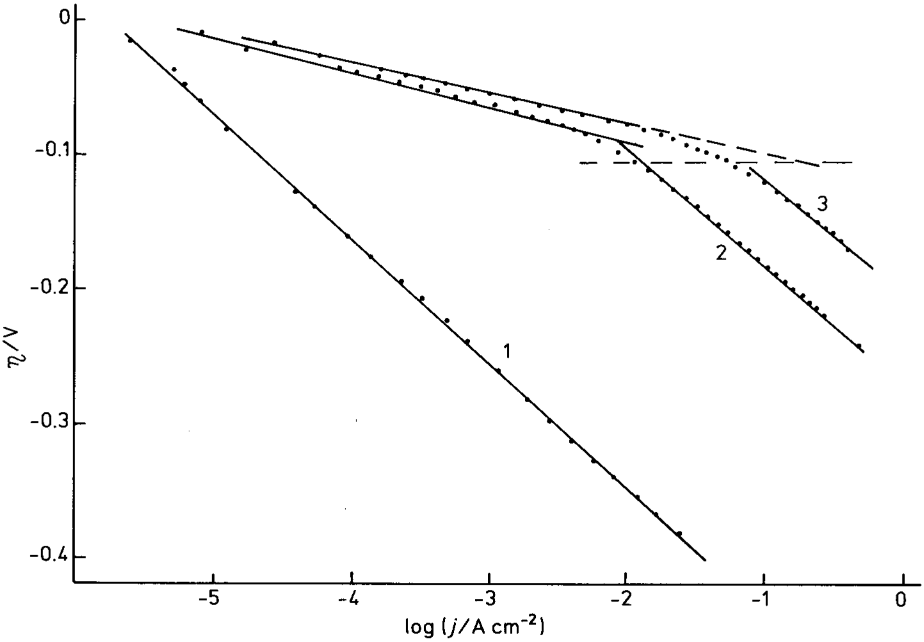

Fig. 26. Current-overpotential curves for hydrogen evolution in NaOH solution on (1) Ni and (2, 3) electrodeposited Ni(79)Mo(20)Cd(1) coatings. Temperature: (1, 2) 25 °C; (3) 80 °C. (– – – –) Transition potential. After ref. 521, by permission of IAHE.

served, and the current density where the lower *b* (ca. 40 mV) changes into the higher one (close to 120 mV) increases as the temperature is increased (Fig. 26). It is interesting that the measured BET surface area can account for the difference in activity with respect to Ni in the high overpotential range. Thus, it appears that the reaction step determining the rate on Ni is not catalyzed on Ni–Mo–Cd. Nevertheless, another parallel step is enhanced. The energetics of H adsorption on Ni and Ni–Co–Cd is in fact very different. Higher coverages, increasing with temperature, are observed with the alloy [518, 520–522].

Other additives do not appear to be as decisive. The replacement of Mo with some Fe does not activate the Ni–Mo alloy. Fe appears to control the pore size distribution [523, 524]. The addition of 0.1–0.2% of V produces a maximum beneficial effect at some [Mo]/[V] ratio around 80 [525]. The effect is however modest; nevertheless, better performance are claimed for these alloys than for Raney Ni. Investigations of several co-deposits on mild steel have shown [507] that the electrocatalytic (as well as the stability) sequence is Ni–Mo > Raney Ni > Ni–Co > Ni–Fe > Ni–Cr > Ni.

In view of the importance of the structure and composition of the active layer, several investigations have focussed on the optimization of the plating procedure and on the analysis of the coating. Mechanisms have also been proposed showing that metallic alloys are formed through steps involving intermediate oxides of Mo [142, 525–527].

It seems established that the thermal procedure gives rise to oxides as precursors of the active alloy [153, 523, 528]. This has been demonstrated in the case of La – Mo coatings [143]. The precursors can then be reduced *in situ* or pre-reduced in H_2 atmosphere before use [153, 415, 519]. The latter procedure appears to give more efficient results [153]. Various methods of preparation have been compared by Divisek et al. [141]. They have shown that the thermal method is superior to electroplting, but not for the case of Ni – Mo – Cd alloy which seems to possess special properties.

The origin of the activity of Ni – Mo – Cd coatings has been investigated by Conway and co-workers using a data acquisition and processing approach which enables overpotential decays to be investigated in the ms range [104, 521]. X-ray analysis has shown that the coating is poorly crystalline, very likely amorphous [520]. They have found that the cathodic behaviour can be explained in terms of the formation of a hydride phase at low overpotentials [522]. Thus, Cd either imparts to the alloy the ability of absorbing hydrogen resulting in more favorable surface conditions, or it modulates the properties of the hydride which also forms on Ni and Ni – Mo. Once more, the properties of the hydride phase appear to be of outstanding importance for the electocatalytic activity of cathodes, as much as the properties of the oxide phase are crucial for anodes [119]. However, lower surface oxides are probably of some importance also in the case of hydrogen evolution, as discussed in a previous sections. A hint in this direction can be found also with the Ni – Mo – Cd alloy [520].

The specific role and the fate of Mo in the alloy has been investigated [141]. It has been found that Mo is not at all stable but tends to be leached out, which would be the origin of the deactivation observed on cathodic load. The deactivation results in a progressive increase in the Tafel slope, which cannot be reactivated *in situ* by addition of molybdenum salts. On the other hand, that Mo is leachable can be inferred also from the observation that *in situ* deposited Co – Mo alloys are quickly dissolved as the current is interrupted [528, 529]. This seems to indicate a provisory activation of the cathode by Mo, which cannot be recovered in a simpley way once decayed [141]. However, this contrasts somewhat with the claim of long term stability and resistance to cell shut-downs for the thermally prepared Ni – Mo coating [5]. The structure of the layer may differ depending on the details of the preparation procedure.

The above coatings have been applied on various substrates including Ni, steel, Ti and Au. In some cases no effect of the support has been noticed [511, 517] (Fig. 27). In other cases, the effect is evident [79, 530]. Steel is worse than Ni for thermal coatings [5, 519]. Synergetic effects involving the support are claimed in the case of *in situ* activation with Co – Mo coatings [79, 528] (Fig. 28).

Despite the large amount of data collected in this field, options seem to be restricted to coatings containing Ni or Co, and Mo, with some additives apparently necessary to impart the wanted properties. It follows that the problem of cathode activation is only in part a question of synergism, while the microscopic structure of the catalyst appears to be of greater importance. Thus, Raney Ni still stands out in the group of possible catalysts [110, 531]. The role of Al (or Zn) does not seem to be simply that of sacrificial components. Residual Al present in the structure plays probably a role which can be similar to that of Cd in Ni – Mo. For this reason mixed Raney metals show great promise [415]. Raney Ni – Co (10%) exhibit a very extended

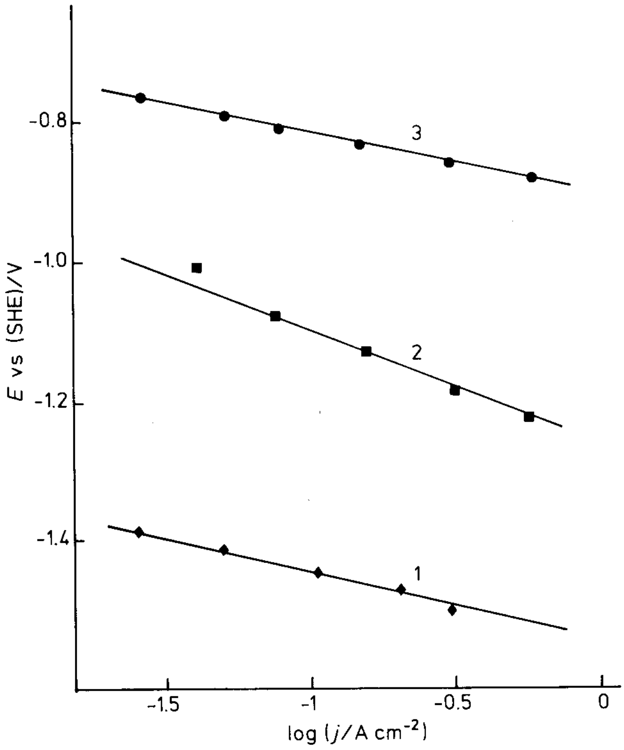

Fig. 27. Current-potential curves for hydrogen evolution in 5 M NaCl at 80 °C. (1) Ti; (2) Steel; (3) Ti and steel coated with electroplated Co-Mo alloy. After ref. 511, by permission of Chapman & Hall.

low Tafel slope section [532] while Raney Ni–Mo seems to be the most stable system [141]. It is necessary to stress again that for techological applications the electrocatalytic activity is not the only property that requires optimization. Stability can be by far more crucial. Raney metal structures need to be strengthened without losing their activity. The presence of foreign components besides Ni appears to improve this specific aspect both in the case of Co and Mo.

4.7 Intermetallic Compounds

This section differs from the previous one in that the materials considered here are obtained by combining two (or more) metals in well defined proportions corresponding to the appearance of a new phase. Since the electronic structure of the component metals is drastically changed in intermetallic compounds, it is expected that the mechanism of the hydrogen evolution reaction can change as well. The majority of

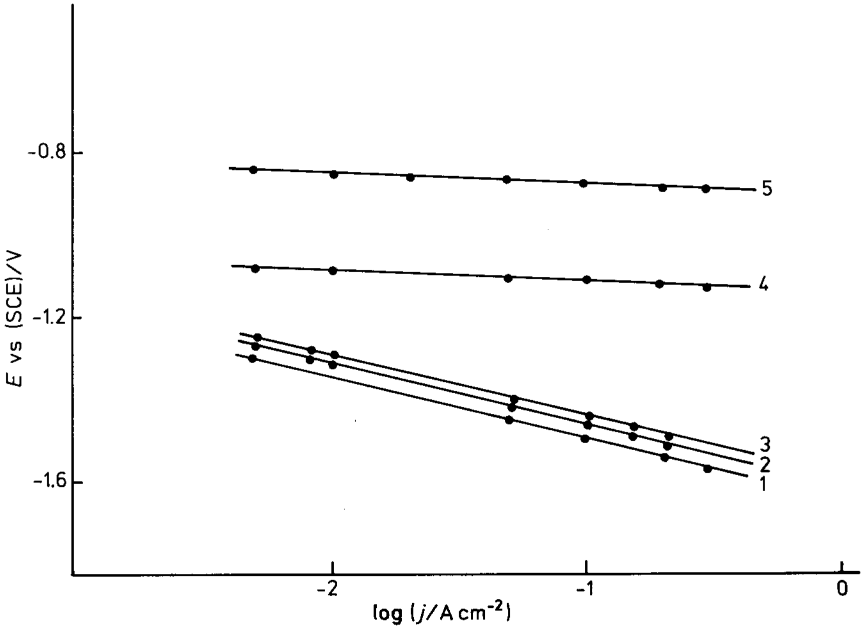

Fig. 28. Synergetic effects with *in situ* activated cathodes. Hydrogen evolution in 1 M NaOH on (1) mild steel, (2) mild steel in the presence of Co(III) in solution, (3) mild steel in the presence of Mo(VI) in solution, (4, 5) mild steel in the presence of Co(III)+Mo(VI) in solution at (4) 20 °C and (5) 80 °C. Adapted from ref. 528.

the materials thus far proposed are intermetallic compounds of Ni with valve metals, followed by a few intermetallics of Co and Fe. These phases can fall into the group of those expected to be active according to the approach proposed by Jakšić [77, 79, 83].

Justi et al. were among the first (but see ref. 74) to report investigations of intermetallic compounds, such as Ti_2Ni and TiNi, for hydrogen generation in strongly alkaline solutions [533, 534]. Later, Miles [72] tested a number of intermetallic compounds using cyclic voltammetry.

Metallurgical methods are usually needed to prepare intermetallics [535]. Therefore, an extension of the surface area cannot be expected. If there is an increase in activity this can realistically be attributed to electrocatalytic effects. Since in most cases the Tafel slope is not lower but actually higher than for Ni [53], the activity enhancement has to be related to a change in the adsorptive properties of the surface so that both the M–H surface bond strength and the degree of coverage with H are different. For instance, in the case of TiFe, a lower M–H bond strength and a lower θ_H shifts the catalyst to higher activities with respect to Ti since both lie on the descending branch of the "volcano" curve [536].

The modification of the properties of the surface of intermetallics is usually related to their capability of absorbing hydrogen with formation of hydride phases [537, 538]. However, the formation of a hydride is not necessarily a reason for better activity [127, 539]. In some cases, hydrides are responsible for a lower activity (cf. Ni, Co, $LaNi_5$, etc.). At the same time, the large amount of hydrogen dissolved in the bulk of intermetallics is often a reason for mechanical instability. A method to pulverize $LaNi_5$ consists precisely of charging and discharging the compound with hydrogen [127]. Hence, in most cases, massive electrodes cannot be fabricated.

Among the intermetallics of Ni, $LaNi_5$ is the most promising, hence the most investigated. Various methods of preparation have been proposed. In one case, using flash evaporation, thin films have been prepared with thicknesses ranging 100–200 nm. In the specific cases of NiTi and $LaNi_5$, surface analysis has revealed that La and Ti are present on the surface as inert oxides while the active component is Ni [103].

In other cases [127, 149, 539], powdered $LaNi_5$ has been Teflon-bonded, or compressed and sintered, or pressed as a coating on a support. The last procedure has been found to be the most efficient. The presence of small amounts of substitutes of Ni (Al, Co, Cu) improves the situation. These coated cathodes could be operated for 7000 h with a number of current interruptions lasting several hours. However, it has been reported that some erosion of the surface may occur with extensive roughening and scaling, probably related to hydride formation. Because of surface segregation of the active components, $LaNi_5$ cathodes have been defined as stabilized, high surface area Ni electrodes [539].

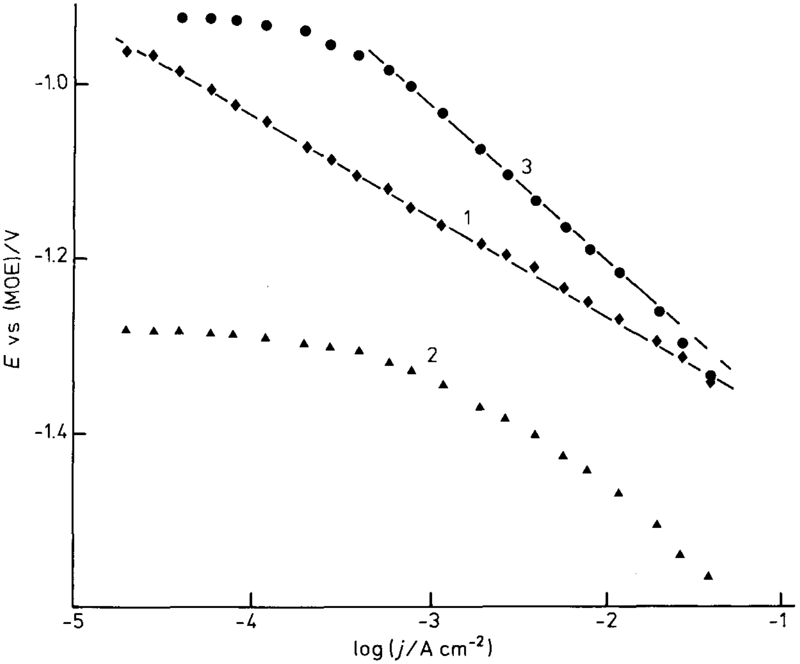

Fig. 29. Synergetic effects with intermetallic compounds. Hydrogen evolution in 1 M KOH at 30 °C on (1) Ni, (2) La, and (3) $LaNi_5$. (MOE = mercury oxide electrode). Adapted from ref. 226, by permission of Elsevier Sequoia.

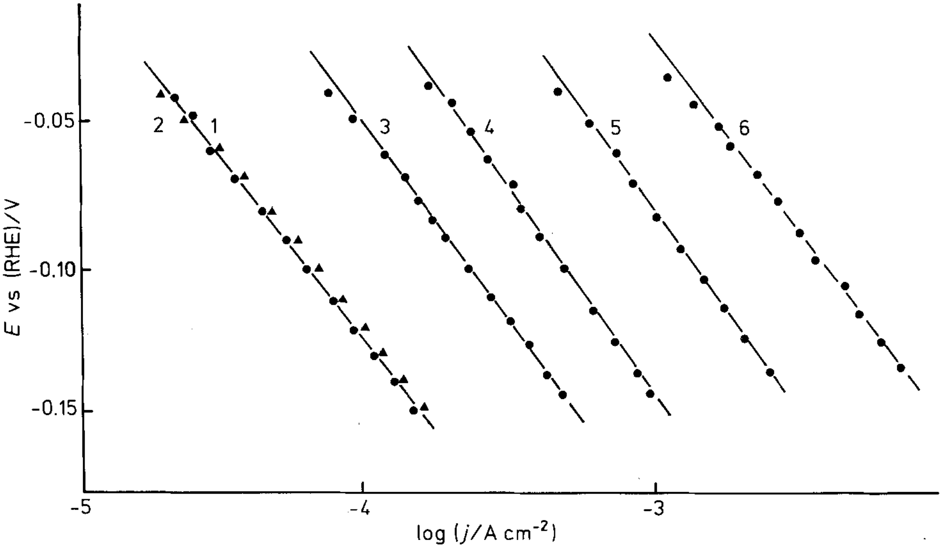

Fig. 30. Synergetic effects with intermetallic compounds. Hydrogen evolution in 1 M KOH at 25 °C on (1) Raney Ni, (2) $LaNi_5$, (3) $CeCo_3$, (4) $CeCo_2Ni$, (5) $CeCoNi_2$, and (6) $CeNi_3$. After ref. 541, by permission of Elsevier Sequoia.

Despite definite evidence pointing to that high surface area may play a major role [103], some synergetic effects are undisputable [540] (Fig. 29). Comparison of high temperature prepared and Teflon-bonded $LaNi_5$ with a series of intermetallics of Ni and Co with Ce, has shown [541] the same activity for $LaNi_5$ as that of Raney Ni (however, the low activity of the Raney Ni reported in this paper is surprising), while the activity of $CeNi_3$ is two orders of magnitude higher. Nevertheless, the Tafel slope is not lower than 120 mV (Fig. 30). Since only one paper has reported data for Ce intermetallics, further studies would be welcome in view of these interesting features.

In NiV intermetallics, Ni has been identified as providing the active sites, and it has been found that the as-prepared materials are less active because they are partially passivated by surface oxides. A treatment with HF greatly improves the activity, which is mainly related to the formation of a surface porous layer enriched with Ni as proven by AES analysis (Fig. 31). However, when NiV and Raney Ni are compared, for both the activity has been found to vary proportionally to the surface roughness factor, but the specific activity is much higher for NiV [542]. This indicates that synergetic effects are real in this case; this recalls the observations made in the cases of Ni–Mo and Ni–Mo–Cd solid solutions [141, 518].

Real electrocatalytic effects are suggested by the "volcano" curve resulting as the activity of various Ni intermetallics is plotted against the ΔH_f of the related hydrides [53] (Fig. 7), and by the linear correlation between $\Delta H^{\ddagger}$ and ΔH_f for another group of intermetallics [226] (Fig. 8). It has been suggested [226] that the origin of the synergetic effect is to be sought in the heat of formation of the inter-

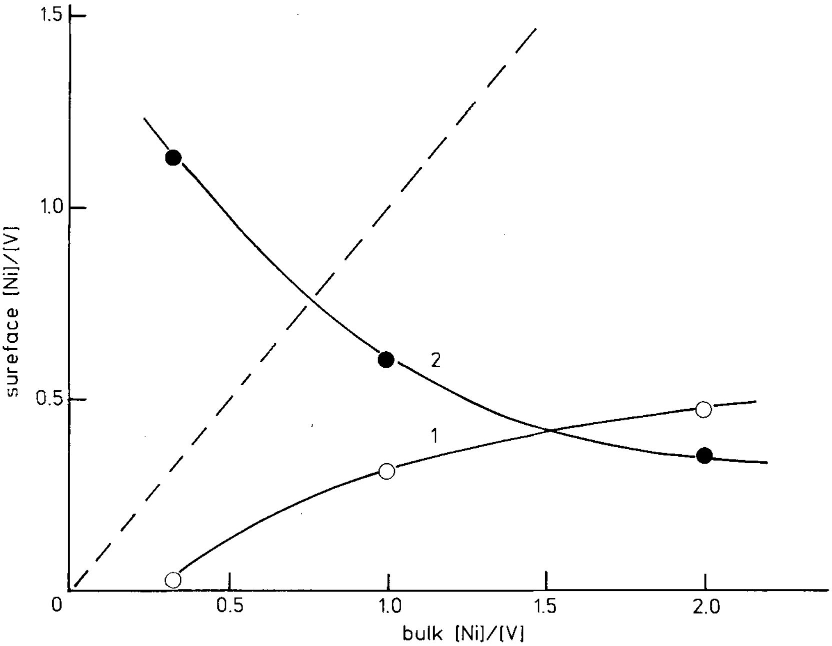

Fig. 31. Surface atomic ratio *vs* bulk atomic ratio for a series of NiV intermetallic alloys. (1) Untreated surfaces; (2) HF-treated surfaces. (– – – –) Straight line of unit slope. After ref. 542, by permission of the Chemical Society of Japan.

metallic phase since the heat of formation of the intermetallic hydrides follows the Miedema rule of reversed stability [544], which is formulated as follows:

$$\Delta H_f(AB_nH_{2m}) = \Delta H_f(AH_m) + \Delta H_f(B_nH_m) - \Delta H_f(AB_n) \ . \qquad (12)$$

If $\Delta H_f(AB_n)$ were equal to zero, a mere linear dependence between activity and composition should be obtained. A corollary of this is that the higher $\Delta H_f(AB_n)$, the more marked the synergetic effect, a "rule" which has been enunciated also by Jakšić [73] with reference to the Brewer-Engel stability theory of intermetallics. Therefore, some predictive basis for designing new materials can indeed be recognized in the specific field of intermetallics.

Intermetallics of Ni with Sn have been also studied [545, 546]. No synergetic effects have been recognized in this case. Sn is not a metal falling in the group of those expected to activate Ni. However, although this is also the case for Zn, it has been mentioned above that the latter is very likely to play a role in activating Raney Ni.

Since intermetallics show a great capacity of hydrogen dissolution, they are also used as hydrogen storing materials [547, 548]. Thus, several investigations report the isotherms of absorption and the phase diagrams of hydrides [128, 537, 541, 549]. The effect of different methods of preparations on the property of absorbing hydrogen has been explored [550]. The ability to release the absorbed hydrogen has been studied by voltammetric curves using Pd plated intermetallics to enhance the hydrogen ionization current [551]. In view of the fragility of these materials, intermetallics microcapsulated into IB metal deposits have been studied as hydrogen storing devices [552].

FeTi with the addition of 6% Nb, or 10% Mn or Ni, has been studied with respect to hydrogen absorption [553]. The presence of Nb enhances hydrogen absorption but the catalytic activity appears to be lower than that of NiTi. Impedance and voltammetric measurements have been used. The presence of 10% Mn in FeTi increases its hydrogen storage capacity slightly, whereas 20% Ni decreases it by ca. 20–30%. The enthalpies of hydride formation have been determined [537].

In the case of ZrNi and ZrCo intermetallics, the preformed hydrides are seen to loose hydrogen at open circuit in acid solutions, after which the intermetallic matrix dissolves [554]. A relatively higher stability of the hydride of ZrCo has been attributed to the presence of higher Co oxides which are more resistant to acids. Studies of this kind have relevance to the possible open circuit behaviour of cathodes based on intermetallic compounds.

Some ancillary investigations should also be mentioned. An interesting approach is the deposition of La on Ni from melts at 953 °C [555]. Several different phases have been identified, including $LaNi_5$. ΔG_f^0 has been determined from these experiments. Fe and Co silicides have been studied as cathodes for H_2 evolution. These materials show high resistance to corrosion due to the presence of Si. On the other hand, the active sites for hydrogen evolution are the metal atoms. No particularly interesting behavior can be recognized with $FeSi_2$ [556]. In the case of CoSi single crystal faces have also been investigated [557]. The Tafel slope is invariably close to 120 mV and no sizable influence of the crystal orientation can be recognized, in agreement with the findings with pure metals. Organic substances (diols) and chlorides do not deactivate these electrodes, while iodide ions and TEAI greatly inhibit the hydrogen evolution reaction. These materials may have some interest as cathodes for acid solutions (cf. carbides, borides).

4.8 Amorphous Materials

Since the electronic properties of solids depend on the crystal structure, the transition from the crystalline to the amorphous state is expected to result in some modification of electronic (and surface) properties. Amorphous materials have first been used in catalysis [558–560] where some evidence for higher activity has been obtained [561]. In particular, hydrogenation reactions are catalyzed by this class of materials [562]. Studies on the H recombination reaction are also available [563]. However, the evidence that the amorphous state is really the origin of enhanced catalytic activity is not completely clear [562, 564]. These materials have the peculiarity that their surface is relatively homogeneous for a solid and in particular it is free from grain boundaries [565, 566]. Therefore, they have been suggested [562] as ideal model surfaces for studying elementary catalytic reactions, since they can be prepared with controlled electronic properties and controlled dispersion. Nevertheless, many problems have to be faced in the application of amorphous materials, such as (i) their low surface area, (ii) high price, (iii) the presence of surface inactive oxides, and (iv) the trend to crystallize at higher temperature or under severe conditions.

Amorphous materials are usually highly corrosion resistant; this quality has first attracted the attention of electrochemists [567, 568]. Recent reviews are available in the literature [569, 570]. The idea of applying amorphous materials to hydrogen cathodes is very recent [571]: most of the papers on this subject have appeared during the past few years. The hope for good electrocatalytic properties is based on the good performances observed in specific catalytic processes.

Several materials have been investigated as cathode activators. Among the most studied systems we find CuTi, CuZr, NiTi, NiZr, FeCo, NiCo. A variety of methods are available to prepare amorphous alloys [562] and, as expected, the resulting activity is largely dependent on them. Normally, amorphous phases are obtained by rapidly quenching a melt. The material can thus be obtained in the form of ribbons, but mechanical alloying by compaction is also possible [572]. The metallic components are usually alloyed with non-metallic components such as B, Si and P which stabilize the metastable non-crystalline structures. Electrodeposition is thus also a viable preparation route [573, 574].

A common observation in most cases is that the surface of amorphous alloys, especially those containing Ti, Zr and Mo, is largely covered with inactive oxides which impart low electrocatalytic properties to the material as prepared [562, 569, 575]. Activation is achieved by removing these oxides either by prepolarization or, more commonly and most efficiently, by leaching in HF [89, 152, 576]. Removal of the passive layer results in a striking enhancement of the electrocatalytic activity [89], but surface analysis has shown [89, 577] that this is due to the formation of a very porous layer of fine particles on the surface (Fig. 32). A Raney type electrode is thus obtained which explains the high electrocatalytic activity. Therefore, it has been suggested [562, 578] that some amorphous alloys are better as catalyst precursors than as catalysts themselves. However, it has been pointed out that the amorphous state appears to favor the formation of such a porous layer which is not effectively formed if the alloy is in the crystalline state [575].

A second general observation is that amorphous materials usually absorb hydrogen and this must be taken into account in evaluating the electrocatalytic activity [579, 580]. In some instances no pulverization of the cathode is observed, but fragile materials can result [572, 574, 581]. Usually, hydrogen absorption causes electrocatalytic deactivation [582, 583]. Hydrogen is more absorbed by Ti and Zr containing alloys than by amorphous metals or by Ni and Co containing alloys. Impedance, voltammetric and potential decay measurements have been used to elucidate the mechanism of hydrogen penetration [579, 580, 583–585]. Comparison of hydrogen diffusivity into amorphous and crystalline PdGe and PdSi alloys has revealed that the two amorphous phases do not differ in their behavior but both differ with respect to the crystalline modifications. This is not surprising considering that hydrogen migrates through the interstices [124, 586]. In the case of PdSiCu alloys, the presence of Si and Cu decreases the amount of H absorbed by Pd, which also decreases upon going from the amorphous to the crystalline state [587].

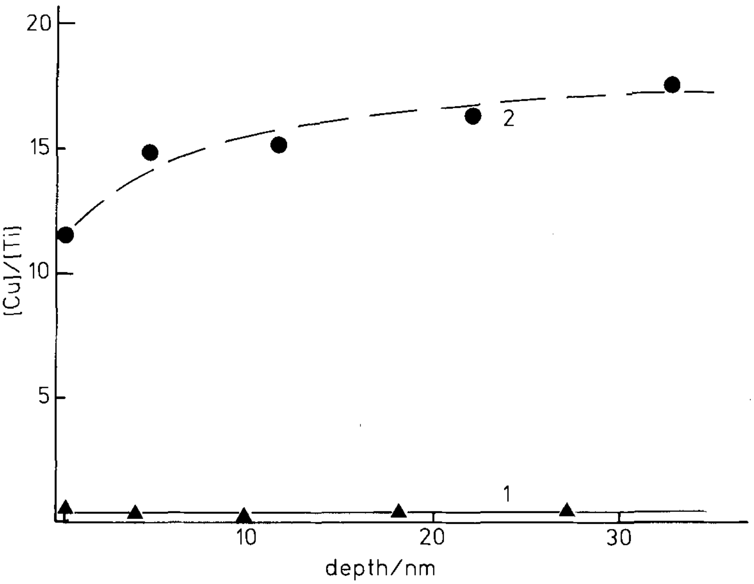

Fig. 32. Depth profiles of the atomic ratio in the amorphous $Cu_{35}Ti_{65}$ alloy before (1) and after (2) treatment with aq. HF. After ref. 89, by permission of Elsevier Sequoia.

Numerous physical techniques have been used to characterize the bulk and the surface of amorphous phases, including X-ray, AES, SEM, XPS, Mossbauer spectroscopy (MOS) and STM. MOS has been able to highlight the state of Fe in a electrodeposited FeP alloy [573]. Three different non-equivalent positions of Fe with different Fe-P distances have been identified. In $Fe_{93}P_7$, 16% of Fe is in the amorphous state. This indicates the extent by which the properties of these phases can be controlled. STM of FeCo alloys has shown that the surface may possess properties depending on the size of the homogeneous zones (cf. particle size effect) [588].

Results with Ni have shown [589, 590] that the amorphous metal can be more active than the crystalline material, but the small decrease in Tafel slope for the amorphous electrode is outweighed by the higher overpotential at low current densities (Fig. 33). An increase in temperature raises the Tafel slope substantially, presumably on account of the incipient crystallization of Ni. Higher adsorption strength on amorphous Ni is pointed out, while surface diffusion of H_{ad} is suggested as the possible r. d. s.

Other results point to no electrocatalytic increment with amorphous metals. Heusler and Huerta [591] have investigated amorphous $Co_{75}B_{25}$ and $Ni_{67}B_{33}$ with respect to corrosion. For the reaction of hydrogen evolution, in the case of the Co alloy, Tafel slopes of 120 mV, along with lower exchange currents for the amorphous material have been reported. Thus, the mechanism is the same as for the crystalline metal. In the case of the Ni alloy, some decrease in the Tafel slope has been observed with heat treatment (which promotes crystallization). Similarly, the same Tafel slope of 120 mV and the same exchange current as for pure Fe have been measured with

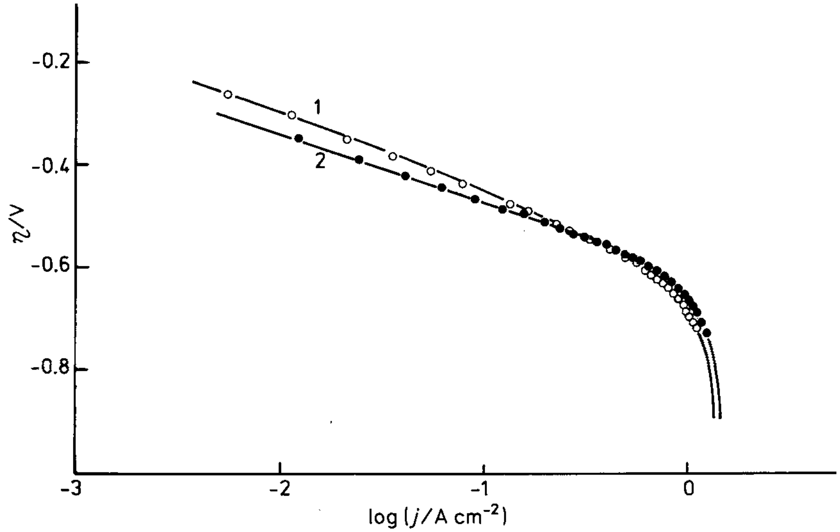

Fig. 33. Current-potential curves for hydrogen evolution in 1 M KOH at 50 °C on (1) polycrystalline and (2) amorphous Ni ($Ni_{78}Si_8B_{14}$, Vitrovac 0080). Adapted from ref. 589, by permission of Pergamon Press.

amorphous $Fe_{80}B_{20}$ [592]. Therefore, the results obtained with amorphous metals do not appear to offer any decisive improvements. This should not be surprising in view of the insensitivity usually manifested by the hydrogen evolution reaction to the surface structure of metals (cf. Sections 3.1, 3.2, 3.4).

In the case of alloys [593, 594], the amorphous alloy of $Fe_{60}Co_{20}B_{10}Si_{10}$ has been identified as among the most active electrocatalysts, with an activity comparable to polycrystalline Pt. However, the Tafel slope is always close to or higher than 120 mV, and it normally increases with temperature [593] so that the latter has no activating effect on the state of the surface. It has been proposed [594] that the application of amorphous alloys to both electrodes in a water electrolyzer can reduce the expenditure of electrical energy by about 6%. However, the polycrystalline Pt taken as a reference for these studies showed [593] $b = 140\,\text{mV}$ and $j_0 \simeq 10^{-4}\,\text{A cm}^{-2}$. At $1\,\text{A cm}^{-2}$ this polycristalline Pt exhibits an overpotential of 560 mV. If we compare this activity with that claimed [5, 519], for instance, for thermal Ni–Mo alloys, the expectations for amorphous phases cannot be great.

Similarly, a number of amorphous alloys based on Fe–Zr, Ni–Zr, Co–Zr, Ni–Nb, have not shown any increase in activity over that expected for the mechanical mixture of the crystalline components [571]. For Ni–Nb the overpotential has even increased. Only Cu–Ti alloys have shown apparent synergetic effects, but the results of Machida et al. [89] (cf. Fig. 32) should also be taken into account. Jorge et al. [152] have observed higher activity for the amorphous form of Cu–Ti alloys, but they have attributed it to the preferential dissolution of Ti in the amorphous sample under cathodic load, with formation of a relatively porous Cu layer. The same effect was obtained more rapidly by means of HF etching [89, 152].

In the case of PdZr, the behavior of the amorphous state was found to be similar to that of the crystalline state [576]. Before HF etching, the activity was two orders of magnitude lower than for Pd. Amorphous FeZr and FeHf were found to absorb hydrogen with deactivation [584]. The cathodic discharge created surface defects. $Fe_{60}Co_{20}B_{10}Si_{10}$ has been observed to be activated by anodic pulsing [578]. Fe_3O_4 is produced on the surface, and its cathodic reduction, coupled with a mechanism of dissolution-reprecipitation, gives rise to a porous Fe layer exhibiting a Tafel slope of 77 mV, which is similar to a Raney metal activation type. Hydrogen absorption in ZrCoNi phases may have an effect on the phase structure which may undergo recrystallization phenomena [580]. Amorphous NiNb, NiAl and NiMo have been found to be less active than NiZr and NiCoZr. After HF treatment, the Tafel slope is higher than 120 mV. However, the less active phases remain ductile after hydrogenation, while the others are more sensitive to embrittlement [583].

A series of Pt-Si amorphous alloys has been compared with polycrystalline Pt. The activity has been found to be always less than the crystalline metal. Although no grains are present on the amorphous alloy surface, the presence of Si reduces the M−H adsorption strength which is the reason for the lower activity. Oxidation of the surface produces SiO_2. On oxidized surfaces spillover of hydrogen from Pt to SiO_2 has been observed [565].

Conclusions

This chapter has been devised to provide a broad survey of the state of the art of research and applications in the field of hydrogen cathodes. Analysis of problems was preferred to mere recipes of preparation and sterile quotations of experimental parameters. Although the main target has been to illustrate the special demands for application, the chapter provides in fact an interplay between theory and practice, emphasizing on one hand the importance of theory in guiding research and development, and on the other hand the irreplaceable role of the feedback from experiments to orient theory.

The range of materials thus far investigated is strikingly broad and the number of electrocatalysts is astonishingly large. Therefore, only very specific and significant examples could be discussed in some detail in this chapter. For these reasons, a "Materials Index" is provided in Table 1, where all composite electrodes mentioned in the literature have been included. Purposely, in line with the spirit of the chapter, no experimental parameters are quoted; the reader is simply referred to the original papers. Considering the outstanding importance of the preparation of the electrode surface and of the operating conditions on the electrode performances, any quotation of "exchange current" or of "overpotential" would be substantially meaningless if a number of other conditions are not mentioned.

As already anticipated at the beginning of Section 4, the separation of materials into various classes is believed to be fairly accurate, maybe with the sole exception of very few cases involving alloys vs intermetallics (or vice versa). In view of the prac-

Table 1. References for specific materials, temperature effects and electrode stability.

Interstitial compounds	
WC	72, 92, 418, 419, 423, 424, 425, 426, 427, 428, 429, 432, 433
$WC_{0.9}$	92, 419, 428
WTiC	419
TiC	421
Cr_3C_2	420, 427, 428
Cr_7C_3	420, 427, 428
Ni_2B	10, 32, 400, 437
TiN_x	434
Sulfides	
NiS_x	20, 25, 93, 151, 400, 411, 416, 438, 439, 442, 443, 446, 447, 449, 451
CoS_x	25, 151, 449, 451
FeS_x	25, 151, 441, 445, 448, 508
MoS_2	25, 151
Ni_3S_2	139, 439
$NiCo_2S_4$	20, 444, 452
Oxides	
$Sr_xNbO_{3-\delta}$	461
RuO_2	168, 227, 253, 470, 475, 481, 487, 489, 490, 495, 496, 497
IrO_2	227, 480
TiO_x (or doped TiO_2)	464, 467
NiO_x	140
$LaMoO_x$	143
Co_3O_4	8, 482
Composite coatings	
NiMo	17, 73, 83, 108, 120, 141, 142, 145, 153, 505, 507, 508, 509, 515, 518, 519, 522, 523, 527, 531
NiMoV	141, 525
NiMoCd	104, 120, 141, 518, 520, 521, 522
NiMoFe	506, 509, 523, 524
MoFe	83, 108, 142, 515, 516, 517, 519
CoMo	78, 79, 83, 147, 511, 519, 526
NiCo	93, 148, 407, 415, 433, 507, 532
MoCo	512, 528, 529, 530
NiFe	93, 249, 507, 510, 514
NiSn	546
NiMoCu	509
NiMoCo	509
NiMoCr	509
NiMn	506
NiFeMoAlTi	141
NiZnFe	506
NiMoFeZn	506
FeMoW	73, 83
LaMo	143
NiW	73, 83, 507, 519
NiCr	507

Table 1 (continued)

NiRe	508
$Ni + PW_{12}(PW_{12}O_{40}^{3-})$	351
PW_{12}	341, 355
SiW_{12}	341, 342, 348, 353, 354, 355, 356, 362, 363
PMo_{12}	341, 348
P_2W_{18}	341, 355
$SiMo_{12}$	341, 349
$P_2W_{17}Mo$	341, 347, 357
CoW_{12}	341
H_2W_{12}	341, 346
Co porphyrin	339, 340
NiPt	99
NiRu	99
RuRe	145
CoV	39
Intermetallic compounds	
$NiTi_3$	537
NiTi	53, 72, 103, 537, 553
$NiTi_2$	72
Ni_3Ti	53, 103, 553
$NiTi_9$	103
Ni_2Ti	553
$LaNi_5$	72, 103, 127, 128, 226, 538, 539, 540, 541, 543, 549, 550, 551, 552
$FeSi, FeSi_2$	556
$CeNi_3$	541, 549
$CeNi_2Co$	541, 549
$CeCo_3$	541, 549
$CeNiCo_2$	541, 549
$LaCo_5$	226, 543
$LaFe_5$	226, 543
NiV	519, 542
NiV_2, NiV_3	542
$LaNi_3Co_2$	127
$LaNi_{4.7}Al_{0.3}$	127, 149, 539
$LaNi_4Cu$	127, 549
$LaNi_4Al$	549
$LaMm_5$	540, 551
TiFe	72, 536, 553
TiFeNb	553
TiCo	72, 553
$TiCo_2, TiCo_3$	553
CoSi	557
$TiZr_2$	572
CoZr	554
NiZr	53, 72, 83, 537, 554
$ZrNi_5$	83, 537
$NiZr_2$	53, 83, 537
Ni_3Zr	53, 83, 537
Ni_7Zr_2	53, 83, 537
NiHf	53

Table 1 (continued)

Ni_3Ta	53
Ni_7Hf_2	53
Ni_2Ta	53
Ni_3Nb	53
NiSn	546
TiCu	72
CrFe	72
Mg_2Cu	72
TiAg	72
Amorphous materials	
NiZr	569, 570, 571, 572, 575, 577, 581, 582
NiNb	569, 570, 571, 583
NiB	570, 591
NiP	570, 574
NiTi	575, 577, 585
NiSiB	589, 590, 594
NiAlB	583
NiCoZr	580; 582
NiCoSiB	588, 593, 594
NiCoFeSiB	588, 593, 594
NiFeB	594
NiFeMoSiB	594
NiMoSiB	583, 590
NiMoCrB	585
NiMoFeB	585
NiMoCrSiB	579
CoZr	569, 570, 571
CoNb	569, 570, 571
CoB	570, 591
CoSiB	590
CoWP	8
CoFeMoSiB	594
FeZr	569, 570, 571, 584
FeB	570, 579, 592
FeHf	584
FeP	573
FeSiB	578, 590, 593, 594
FeCoSiB	578, 588, 593, 594
TiCu	89, 152, 569, 570, 571, 590
TiNiV	585
PdZr	576
PdGe	486
PdSi	486
PdNiP	590
PdSiCu	587
ZrCu	89, 152, 568
PtSi	565
Effect of temperature	146, 230, 246, 247, 248, 249, 273, 366, 380, 384, 391, 407, 415, 431, 433, 442, 443, 447, 449, 461, 507, 510, 514, 518, 521, 523, 528, 546, 589, 593, 594

Table 1 (contined)

Electrode stability	17, 25, 99, 107, 109, 111, 122, 137, 140, 151, 156, 158, 159, 162, 163, 167, 168, 171, 172, 253, 380, 381, 406, 409, 411, 424, 438, 445, 446, 448, 489, 497, 507, 519, 523, 524

tical impact of temperature effects and of long-term stability, these two specific items have been added by simply quoting the papers in which mention of these factors is made.

The first firm conclusion resulting from the analysis of the situation is that a thorough physicochemical characterization of the electrode surface is strictly needed to be able to assess if and when *real* progress is being made. This is also necessary to be able to appreciate which classes of materials are really worth investigating in depth for applications. Although both geometric (surface area) and electronic (catalytic) effects result indeed in better performances, it is convenient to identify at an early stage those options for which electrocatalytic and stability factors combine with economically practicable solutions. In several cases, the very analysis of the electrode surface could disclose the geometric effects behind some *apparent* catalytic enhancement. Knowledge of the real situation does help to optimize electrodes much more efficiently.

Although "synergetic" effects in composite materials have been often claimed, it appears that most of the progresses have issued from the outstanding role of the morphological texture and physical structure of active coatings. A typical example is the case of Raney Ni which (without further activation) is able to reduce the overpotential by more than 70% at high current densities. In several cases Ni-based composite materials undergo modifications under cathodic load, and what comes up in the end is nothing but a different (even more active) form of Raney Ni. Most of the more active cathodes are in fact based on activated, stabilized Raney Ni electrodes, which combine activating procedures with large surface area substrates.

Some apparently *true* synergetic effects have indeed been reported. However, while any activity enhancement is welcome for practical applications, synergetic effects have to be carefully confirmed before proceeding along a specific research line. One undisputable proof of electronic effects is believed to be any modification in the Tafel slope, although low Tafel slopes can result from solution supersaturation effects and porous electrode structures as well. The target of "applied" research is indeed to find a material, or a modification of a given material, exhibiting the lowest Tafel slope over the widest range of current. However, it is a fact that in most of the cases the appearance of low Tafel slopes is strongly favored by a high surface area. In other words, the "less active" material would certainly show the same low Tafel slope as the "more active" form if it were possible to explore experimentally a wider range of low current densities. While some hints in this direction can be found in available data, this concept clearly explains why extrapolated exchange currents may not possess any definite kinetic meaning. Sometimes theory predicts a lower Tafel slope at small overpotentials which cannot be observed owing to the undetectable value of the actual exchange current. It is, however, important to realize that, if surface area is so much increased that the low Tafel slope reaches practical current densities, the overpotential decrease will anyway benefit from both effects. In this respect, it is expedient to recall that oxide anodes have been principally successful for their extended surface area and for their stability. The catalytic activity normalized to the unit real surface area is not higher than for precious metals. Thus, recognition of *true* electrocatalytic effects is not a problem directly relevant to applications, but it is essential to bringing theory ahead to be able to efficiently design composite catalysts without wasting time (and money) in the old-fashioned approach of "try and see".

Among the various classes of materials, some have not yet kept their early promise. This is the case of amorphous compounds, whose use is also hampered by the severe conditions often employed in electrolysis cells. In the case of sulphides it is not yet clear how much of their activity is due to the chemical composition of the surface and how much to the structure resulting from the modification of the surface under cathodic load. In the case of composite materials, it is necessary to take into account that the surface area is normally higher for multicomponent phases, depending in particular on the method of preparation.

The above considerations should not sound as pessimistic, but rather as realistic. They are strictly necessary as conslusions of fundamental value are to be drawn from results of experiments aimed at practical applications. Well documented great advances have indeed been made. In some cases a reduction in overpotential close to 90% has been claimed. Whatever the origin, the achievement is undisputable. It is to be noted that a comparable lowering of overpotential is documented also for oxides.

Some predictions beyond the theory of electrocatalysis for pure metals seem indeed possible. It is, however, necessary to stress again that the applicability of a cathode depends on the impact of many factors, the most outstanding ones being the intrinsic stability and the resistance to poisoning. This is probably still the weak point of cathodes. Their life-time appears to be lower than for anodes, although the deactivation process for cathodes is slower and less abrupt than for anodes.

The field of stability still lacks definite concepts for guiding the search for stabilizers. Nevertheless, efforts in this direction are many and positive improvements have been documented. This is the field of "additives" and "dopants", and therefore of electronic interactions and chemical shifts. Most of the remedies thus far proposed are not known with certainty because applied to proprietary electrocatalysts. A careful investigation of their actions would be necessary. In fact, fundamental research is still mostly aimed at investigating electrocatalytic and mechanistic aspects.

The field of electrocatalyst poisoning seems less obscure, also because the physical parameters are probably simpler. Again, a large surface area reduces deactivation primarily because of the large dilution of the impurities on the electrode surface so that a much lower fraction of the active surface is covered by the same amount of impurities. However, concepts of surface chemistry are also important, in that the adsorption of impurities may be different on different surfaces. Some composite materials of large surface area (e.g., oxides) are especially efficient in this particular respect. Surface science concepts can be of great help in the development of a strategy of protection from poisoning.

Finally, it is to be mentioned that research activities in electrochemistry are becoming more and more interdisciplinary. This should lead in the near future to the identification of a number of still undefined factors, and to the clarification of aspects which are still obscure. However, for reasons already discussed in the introduction, and because of the delay in the development of a hydrogen economy (despite the urgency of replacing fossile fuels as stressed by everyday events), the possible options offered by research are at present far more numerous than the solutions which have already found technological application.

Acknowledgements. Financial support from the National Research Council (C.N.R., Rome) is gratefully acknowledged.

6 References

1. R.L. LeRoy, Int. J. Hydrogen Energy 8, 401 (1983).
2. H. Wendt, Chem.-Ing.-Tech. 56, 265 (1984).
3. J.O'M. Bockris, O.J. Murphy, F. Gutmann, in: Nuclear Hydrogen Biogas. Alternative Energy Sources IV: T.N. Vezirŏglu (ed.). Ann Arbor: Ann Arbor Science (1982) Vol. 5, p. 169.
4. F. Gutmann, O.J. Murphy, in: Modern Aspects of Electrochemistry: R.E. White, J.O'M. Bockris, B.E. Conway (eds.). New York: Plenum Press (1983) Vol. 15, p. 1.
5. M.N. Mahmmood, A.K. Turner, M.C.M. Man, P.O. Fogarty, Chem. Ind. 50 (1984).
6. K. Tennakone, Int. J. Hydrogen Energy 14, 681 (1989).
7. K. Viswanathan, B.V. Tilak, J. Electrochem. Soc. 131, 1551 (1984).
8. W.B. Darlington, Proceedings of the O. De Nora Symposium on Chlorine Technology. Milan: O. De Nora (1979), p. 30.
9. S. Srinivasan, F.J. Salzano, Int. J. Hydrogen Energy 2, 53 (1977).
10 P.W.T. Lu, S. Srinivasan, J. Appl. Electrochem. 9, 269 (1979).
11. P.M. Spaziante, Ing. Chim. Ital. 11, 155 (1975).
12. Industrial Water Electrolysis: S. Srinivasan, F.J. Salzano, A.R. Landgrebe (eds.) Princeton, NJ: The Electrochemical Soc (1977).
13. G. Imarisio, Int. J. Hydrogen Energy 6, 153 (1981).
14. O. De Nora, Chem.-Eng.-Tech. 42, 222 (1970).
15. J. Horacek, S. Puschaver, Chem. Eng. Progr. 67, 71 (1971).
16. S. Trasatti, in: Electrochemical Hydrogen Technologies: H. Wendt (ed.) Amsterdam: Elsevier (1990), p. 1.
17. M. Nagamura, H. Ukihashi, O. Shiragami, in: Modern Chlor-Alkali Technology: C. Jackson (ed.). Chichester: Ellis Horwood (1983), Vol. 2, p. 61.
18. D.E. Grove, in: Modern Chlor-Alkali Technology: K. Wall (ed.). Chichester: Ellis Horwood (1986), Vol. 3, p. 250.
19. W. Dönitz, Int. J. Hydrogen Energy 9, 817 (1984).
20. H. Wendt, G. Imarisio, J. Appl. Electrochem. 18, 1 (1988).
21. L.I. Krishtalik, A.F. Mazanko, Elektrokhimiya 21, 584 (1985).
22. A.T. Kuhn, P.M. Wright, in: Industrial Electrochemical Processes: A.T. Kuhn (ed.). Amsterdam: Elsevier (1971), p. 560.
23. M. Yasuda, K. Fukumoto, Y. Ogata, F. Hine, in: Electrochemical Engineering in the Chlor-Alkali and Chlorate Industries: F. Hine, R.E. White, W.B. Darlington, R.D. Varjian (eds.). Pennington: The Electrochemical Society (1988), p. 219.

24. B. Combrade, in: Hydrogen as an Energy Carrier: G. Imarisio, A.S. Strub (eds.). Dordrecht: D. Reidel (1983), p. 183.
25. A. Nidola, R. Schira, Int. J. Hydrogen Energy 11, 449 61986).
26. V. Yegnaraman, S. Vasudevan, Trans. SAEST 24, 223 (1989).
27. T.N. Veziroğlu, Int. J. Hydrogen Energy 12, 99 (1987).
28. K. Yamaguchi, in: Electrochemical Engineering in the Chlor-Alkali and Chlorate Industries: F. Hine, R.E. White, W.B. Darlington, R.D. Varjian (eds.). Pennington, NJ: The Electrochemical Society (1988), p. 25.
29. T.N. Veziroğlu, I. Gurkan, M.M. Padki, Int. J. Hydrogen Energy 14, 257 (1989).
30. T.N. Veziroğlu, Int. J. Hydrogen Energy 14, 491 (1989).
31. Y. Ogata, H. Koide, M. Yasuda, F. Hine, in: Performance of Electrodes for Industrial Electrochemical Processes: F. Hine, B.V. Tilak, J.M. Fenton, J.D. Lisius (eds.). Pennington, NJ: The Electrochemical Society (1989), p. 185.
32. H. Gerischer, Z. Phys. Chem. N.J. 8, 137 (1956).
33. R. Parsons, Trans. Faraday Soc. 54, 1053 (1958).
34. C. Bailleux, A. Damien, A. Montet, Int. J. Hydrogen Energy 8, 529 (1983).
35. Electrodes of Conductive Metallic Oxides: S. Trasatti (ed.). Amsterdam: Elsevier (1980/81), Part A and B.
36. E. Yeager, P. Bindra, Chem.-Ing.-Tech. 52, 384 (1980).
37. K.H. Simmrock, J. Poblotzki, in: Electrochemical Engineering in the Chlor-Alkali and Chlorate Industries: F. Hine, R.E. White, B. Darlington, R.D. Varjian (eds.). Pennington, NJ: The Electrochemical Society (1988), p. 369.
38. A.J. Appleby, H. Kita, M. Chemla, G. Bronoël, in: Encyclopedia of Electrochemistry of the Elements: A.J. Bard (ed.). New York: Marcel Dekker (1982), Vol. IX, Part A, p. 383.
39. M. Enyo, in: Comprehensive Treatise of Electrochemistry: B.E. Conway, J.O'M. Bockris, E.B. Yeager, S.U.M. Kahn, R.E. White (eds.). New York: Plenum Press (1983), Vol. 7, p. 241.
40. The book quoted in ref. 16 was published as the manuscript of this chapter had already been completed. The discussion of cathode activation is however restricted to one chapter.
41. A.J. Appleby, in: Comprehensive Treatise of Electrochemistry: B.E. Conway, J.O'M. Bockris, E. Yeager, S.U.M. Kahn, R.E. White (eds.). New York: Plenum Press (1983), Vol. 7, p. 173.
42. B.V. Tilak, S. Sarangapani, N.L. Weinberg, in: Techniques in Chemistry: N.L. Weinberg, B.V. Tilak (eds.). New York: Wiley (1983), Vol. 5, Part 3, p. 195.
43. B.V. Tilak, P.W.T. Lu, J.E. Colman, S. Srinivasan, in: Comprehensive Treatise of Electrochemistry: J.O'M. Bockris, B.E. Conway, E. Yeager, R.E. White (eds.). New York: Plenum Press (1981), Vol. 2, p. 1.
44. D. Pletcher, J. Appl. Electrochem. 14, 403 (1984).
45. R.R. Adžić, in: Advances in Electrochemistry and Electrochemical Engineering: H. Gerischer, C.W. Tobias (eds.). New York: Wiley (1985), Vol. 13, p. 159.
46. P. Stonehart, P.N. Ross, Catal. Rev. – Sci. Eng. 12, 1 (1975).
47. S.U.M. Khan, Appl. Phys. Commun. 6, 1 (1986).
48. L.I. Krishtalik, in: Comprehensive Treatise of Electrochemistry: B.E. Conway, J.O'M. Bockris, E. Yeager, S.U.M. Khan, R.E. White (eds.). New York: Plenum Press (1983), Vol. 7, p. 87.
49. B.E. Conway, J. Electrochem. Soc. 124, 410C (1977).
50. A.D. Davydov, G.R. Engelgardt, Elektrokhimiya 24, 3 (1988).
51. D.E. Hall, J. Electrochem. Soc. 128, 740 (1981).
52. A. Reintjes-Saraby, Electrochim. Acta 31, 251 (1986).
53. E. Yeager, D. Tryk, in: Hydrogen Energy Progress V: T.N. Veziroğlu, J.B. Taylor (eds.). Oxford: Pergamon Press, Vol. 2, p. 827.
54. S. Trasatti, J. Electroanal. Chem. 39, 163 (1972).
55. E. Yeager, J. Electrochem. Soc. 128, 160C (1981).
56. Y. Takasu, Y. Matsuda, Electrochim. Acta 21, 133 (1976).
57. P.C. Searson, P.V. Nagarkar, R.M. Latanision, Int. J. Hydrogen Energy 14, 131 (1989).
58. B.Ya. Moizhes, Elektrokhimiya 22, 393 (1986).

59. A.T. Kuhn, C.J. Mortimer, G.C. Bond, J. Lindley, J. Electroanal. Chem. 34, 1 (1972).
60. D.G. Naryshkin, I.V. Kudryashov, Elektrokhimiya 18, 975 (1982).
61. B. Bélanger, A.K. Vijh, Elektrokhimiya 10, 1854 (1974).
62. H. Kita, T. Kurisu, J. Res. Inst. Catalysis, Hokkaido Univ. 21, 200 (1973).
63. B.E. Conway, J.O'M. Bockris, J. Chem. Phys. 26, 532 (1957).
64. P. Rüetschi, P. Delahay, J. Chem. Phys. 23, 195 (1955).
65. J.O'M. Bockris, M. Szklarczyk, A.Q. Contractor, S.U.M. Khan, Int. J. Hydrogen Energy 9, 741 (1984).
66. S. Trasatti, in: Advances in Electrochemistry and Electrochemical Engineering: H. Gerischer, C.W. Tobias (eds.). New York: Wiley-Interscience (1977), Vol. 10, p. 213.
67. L.Yu. Firsova, V.N. Gramm-Osipova, Zh. Fiz. Khim. 52, 3166 (1978).
68. N.V. Korovin, D.G. Naryshkin, N.V. Fadaeva, Zh. Fiz. Khim. 53, 1487 (1979).
69. D.G. Naryshkin, Zh. Fiz. Khim. 53, 2030 (1979).
70. H. Kita, J. Electrochem. Soc. 113, 1095 (1966).
71. M.H. Miles, M.A. Thomason, J. Electrochem. Soc. 123, 1459 (1976).
72. M.H. Miles, J. Electroanal. Chem. 60, 89 (1975).
73. M.M. Jakšić, Mat. Chem. Phys. 22, 1 (1989).
74. A.K.M.S. Huq, A.J. Rosenberg, J. Electrochem. Soc. 111, 260 (1964). It is interesting that this paper claims synergetic effects for some of such compounds as NiS, NiAs, NiSb, $NiTe_2$, NiSi, thus anticipating the rationale behind the present research on sulphides and intermetallic compounds.
75. G.C. Bond, P.A. Sermon, Gold. Bull. 6, 102 (1973).
76. R. Parsons, Surf. Sci. 18, 28 (1969).
77. M.M. Jakšić, Electrochim. Acta 29, 1539 (1984).
78. M.M. Jakšić, Č.M. Lačnjevac, R.T. Atanasoski, R. Adžić, in: Proceedings of the O. De Nora Symposium on Chlorine Technology. Milan: O. De Nora (1979), p. 57.
79. M.M. Jakšić, Int. J. Hydrogen Energy 11, 519 (1986).
80. L.I. Krishtalik, in: Advances in Electrochemistry and Electrochemical Engineering: P. Delahay, C.W. Tobias (eds.). New York: Wiley-Interscience (1970), Vol. 7, p. 283.
81. B.E. Conway, L. Bai, J. Electroanal. Chem. 198, 149 (1986).
82. L. Brewer, in: Electronic Structure and Alloy Chemistry of Transition Elements: P.A. Beck (ed.). New York: Interscience (1963), p. 221.
83. M.M. Jakšić, J. Mol. Catal. 38, 161 (1986).
84. J. Swarup, Indian J. Chem. 7, 896 (1969).
85. O. Johnson, J. Res. Inst. Catalysis, Hokkaido Univ. 19, 152 (1972).
86. N.E. Khomutov, Zh. Fiz. Khim. 37, 526 (1963).
87. H. Leidheiser, J. Am. Chem. Soc. 71, 3634 (1949).
88. N. Ohtani, Sci. Rep. Inst. Tokyo Univ. A8, 399 (1956).
89. K. Machida, M. Enyo, K. Suzuki, J. Less-Common Met. 100, 377 (1984).
90. J.D. Hansen, G.L. Cahen, G.E. Stoner, J. Electrochem. Soc. 132, 132 (1985).
91. Ya.M. Kolotyrkin, A.N. Frumkin, Zh. Fiz. Khim. 15, 346 (1941).
92. G.A. Tsirlina, O.A. Petrii, V.B. Kozhevnikov, Elektrokhimiya 20, 420 (1984).
93. A.G. Pshenichnikov, Mat. Chem. Phys. 22, 121 (1989).
94. I.M. Novoselskii, N.I. Konevskikh, L.Ya. Egorov, E.P. Sidorov, Elektrokhimiya 7, 893 (1971).
95. G. Valette, A. Hamelin, J. Electroanal. Chem. 45, 301 (1973).
96. D.V. Sokolskii, B.Yu. Nogerbekov, N.N. Gudeleva, R.G. Mustafina, Elektrokhimiya 22, 1185 (1986).
97. G.G. Barna, S.N. Frank, T.H. Teherani, J. Electrochem. Soc. 129, 746 (1982).
98. V.V. Chernyi, V.S. Zuikova, Yu.B. Vasiliev, V.M. Gryaznov, N.B. Gorina, V.S. Bagotskii, Elektrokhimiya 8, 1341 (1972).
99. A. Nidola, in: High Tech Ceramics: P. Vincenzini (ed.). Amsterdam: Elsevier (1987), p. 2191.
100. A. Frumkin, N. Polianovskaya, I. Bagotskaya, N. Grigoryev, J. Electroanal. Chem. 33, 319 (1971).

101. M. von Bradke, W. Schnurnberger, in: Hydrogen Energy Progress VI: T.N. Veziroğlu, N. Getoff, P. Weinzierl (eds.). Oxford: Pergamon Press (1986), Vol. 1, p. 438.
102. T. Kenjo, Electrochim. Acta 33, 41 (1988).
103. K. Machida, M. Enyo, G. Adachi, J. Shiokawa, J. Electroanal. Chem. 29, 807 (1984).
104. B.E. Conway, L. Bai, D.F. Tessier, J. Electroanal. Chem. 161, 39 (1984).
105. M. Elam, B.E. Conway, J. Appl. Electrochem. 17, 1002 (1987).
106. D.A. Harrington, B.E. Conway, J. Electroanal. Chem. 221, 1 (1987).
107. R.L. LeRoy, M.B. Janjua, R. Renaud, U. Leuenberger, J. Electrochem. Soc. 126, 1674 (1979).
108. M.B.I. Janjua, R.L. LeRoy, Int. J. Hydrogen Energy 10, 11 (1985).
109. E. Endoh, H. Otouma, T. Morimoto, Int. J. Hydrogen Energy 13, 207 (1988).
110. J. Divisek, J. Mergel, H. Schmitz, Int. J. Hydrogen Energy 15, 105 (1990).
111. Hydrogen in Intermetallic Compounds I (Topics in Applied Physics, Vol. 83): L. Schlapbach (ed.). Berlin: Springer-Verlag (1988).
112. M.E. Martins, J.J. Podestà, A.J. Arvia, Electrochim. Acta 32, 1013 (1987).
113. K. Machida, M. Enyo, Bull. Chem. Soc. Jpn. 59, 725 (1986).
114. A.M. Sukhotin, M.N. Shlepakov, P.Yu. Kostikov, V.S. Strykanov, Elektrokhimiya 17, 1361 (1981).
115. S. Hadži-Jordanov, H. Angerstein-Kozlowska, M. Vuković, B.E. Conway, J. Phys. Chem. 81, 2271 (1977).
116. M.W. Breiter, J. Electroanal. Chem. 178, 53 (1984).
117. H.M. Lee, J. Mater. Sci. Lett 14, 1002 (1979).
118. H.M. Lee, Met. Trans. 7A, 431 (1976).
119. S. Trasatti, J. Electroanal. Chem. 111, 125 (1980).
120. B.E. Conway, L. Bai, in: Hydrogen Energy Progress V: T.N. Veziroğlu, J.B. Taylor (eds.). Oxford: Pergamon Press (1984), Vol. 2, p. 879.
121. B.E. Conway, L. Bai, Electrochim. Acta 31, 1013 (1986).
122. H.E.G. Rommal, P.J. Morgan, J. Electrochem. Soc. 135, 343 (1988).
123. Ya.M. Kolotyrkin, V.V. Losev, A.N. Chemodanov, Mat. Chem. Phys. 19, 1 (1988).
124. H.J. Flit, J.O'M. Bockris, Int. J. Hydrogen Energy 6, 119 (1981).
125. R.N. Iyer, H.W. Pickering, M. Zamanzadeh, J. Electrochem. Soc. 136, 2463 (1989).
126. J.J. DeLuccia, in: Electrochemical Aspects of Hydrogen in Metals (ASTM STP 962): L. Raymong (ed.). Philadelphia: American Society for Testing and Materials (1988), p. 17.
127. D.E. Hall, V.R. Shepard, Int. J. Hydrogen Energy 9, 1005 (1984).
128. T. Kitamure, C. Iwakura, H. Tamura, Electrochim. Acta 27, 1723 (1982).
129. M.Y.C. Woo, in: Industrial Applications of Titanium and Zirconium: C.S. Young, J.C. Durham (eds.). Philadelphia: ASTM (1986), Vol. 4, p. 3.
130. D.J. Blackwood, L.M. Peter, H.E. Bishop, P.R. Chalker, D.E. Williams, Electrochim. Acta 34, 1401 (1989).
131. V.N. Modestova, N.D. Tomashov, A.R. Yakubenko, I.V. Kasatkina, V.I. Skryabina, S.N. Vashchenko, E.A. Borisova, Elektrokhimiya 20, 39 (1984).
132. V.I. Kichigin, N.I. Kavardakov, V.V. Kuznetsov, Elektrokhimiya 18, 1059 (1982).
133. T. Okada, Electrochim. Acta 27, 1273 (1982).
134. P.M. Spaziante, in: Proceedings of the O. De Nora Symposium on Chlorine Technology. Milano: O. De Nora (1979), p. 284.
135. H. Wendt, H. Hofmann, V. Plzak, Mat. Chem. Phys. 22, 27 (1989).
136. K. Mund, G. Richter, F. von Sturm, J. Electrochem. Soc. 124, 1 (1977).
137. E. Endoh, H. Otouma, T. Morimoto, Y. Oda, Int. J. Hydrogen Energy 12, 473 (1987).
138. Y. Choquette, H. Menard, L. Brossard, Int. J. Hydrogen Energy 14, 6371 (1989).
139. G.P. Power, Electrochim. Acta 27, 359 (1982).
140. M. Yoshida, Y. Noaki, in: Performance of Electrodes for Industrial Electrochemical Processes: F. Hine, B.V. Tilak, J.M. Fenton, J.D. Lisius (eds.). Pennington: The Electrochemical Society (1989), p. 15.
141. J. Divisek, H. Schmitz, J. Balej, J. Appl. Electrochem. 19, 519 (1989).

142. E. Bełtowska-Lehman, J. Appl. Electrochem. 20, 132 (1990).
143. N.V. Krstajić, M.D. Spasojević, R.T. Atanasoski, J. Appl. Electrochem. 14, 131 (1984).
144. C. Welch, G.N. Hughes, R.A. Crawford, D.W. Dubois, in: Advances in Chlor-Alkali and Chlorate Industry: M.M. Silver, E.M. Spore (eds.). Pennington: The Electrochemical Society (1984), p. 192.
145. P.M. Spaziante, in: Hydrogen as an Energy Vector: A.A. Strub, G. Imarisio (eds.). Dordrecht: D. Reidel (1980), p. 213.
146. W. Schnurnberger, R. Hennen, M. von Bradke, in: Hydrogen Energy Progress V: T.N. Veziroğlu, J.B. Taylor (eds.). Oxford: Pergamon Press (1984), Vol. 2, p. 933.
147. J.Y. Huot, L. Brossard, J. Appl. Electrochem. 18, 815 (1988).
148. H. Wendt, H. Hofmann, H. Berg, V. Plzak, J. Fischer, in: Hydrogen as an Energy Carrier: G. Imarisio, A.S. Strub (eds.). Dordrecht: D. Reidel (1983), p. 267.
149. D.E. Hall, J.M. Sarver, D.O. Gothard, in: Electrochemical Engineering in the Chlor-Alkali and Chlorate Industries: F. Hine, R.E. White, W.B. Darlington, R.D. Varjian (eds.). Pennington: The Electrochemical Society (1988), p. 184.
150. D. Ravier, J. Grosbois, Fr. Appl. 7521364 (1975).
151. A. Nidola, R. Schira, in: Hydrogen Energy Progress V: T.N. Veziroğlu, J.B. Taylor (eds.). Oxford: Pergamon Press (1984), Vol. 2, p. 909.
152. G. Jorge, R. Faure, R. Durand, A.R. Yavari, Mat. Sci. Eng. 99, 517 (1988).
153. D.E. Brown, S.M. Hall, M.N. Mahmood, M.C.M. Man, A.K. Turner, D. Wood, S. Anderson, in: Electrocatalysis: W.E. O'Grady, P.N. Ross, F.G. Will (eds.). Pennington: The Electrochemical Society (1982), p. 145.
154. A.A. Kuznetsov, Yu.V. Fedorov, Elektrokhimiya 18, 828 (1982).
155. C. Bailleaux, Int. J. Hydrogen Energy 6, 469 (1981).
156. A. Nidola, R. Schira, J. Electrochem. Soc. 133, 1653 (1986).
157. A.A. Sutyagina, J.M. Matveeva, T.E. Umantseva, A.D. Aliev, Zh. Fiz. Khim. 55, 700 (1981).
158. E. Protopopoff, P. Marcus, J. Electrochem. Soc. 135, 3073 (1988).
159. E. Lamy-Pitara, L. Lghouzouani, Y. Tainon, J. Barbier, J. Electroanal. Chem. 260, 157 (1989).
160. P. Marcus, E. Protopopoff, Surf. Sci. 17, 533 (1985).
161. E.P.M. Leiva, E. Santos, T. Iwasita, J. Electroanal. Chem. 215, 357 (1986).
162. A. Nidola, R. Schira, in: Advances in the Chlor-Alkali and Chlorate Industry: M.M. Silver, E.M. Spore (eds.). Pennington: The Electrochemical Society (1984), p. 206.
163. M.A. Riley, P.J. Moran, J. Electrochem. Soc. 133, 760 (1986).
164. M.L. Kronenberg, J. Electroanal. Chem. 12, 122 (1966).
165. J.E. Bennett, Int. J. Hydrogen Energy 5, 401 (1980).
166. H. Vogt, J. Electrochem. Soc. 128, 29C (1981).
167. L. Brossard, J.-Y. Huot, J. Appl. Electrochem. 19, 882 (1989).
168. E.R. Kötz, S. Stucki, J. Appl. Electrochem. 17, 1190 (1987).
169. S. Ardizzone, A. Carugati, G. Lodi, S. Trasatti, J. Electrochem. Soc. 129, 1689 (1982).
170. S. Ardizzone, G. Fregonara, S. Trasatti, Electrochim. Acta 35, 263 (1990).
171. J.Y. Huot, L. Brossard, Int. J. Hydrogen Energy 12, 821 (1987).
172. A.E. Avrushchenko, B.N. Yanchuk, N.V. Korovin, L.G. Ganichenko, Elektrokhimiya 22, 1258 (1986).
173. J.A. Harrison, A.T. Kuhn, Surf. Technol. 19, 249 (1983).
174. J.A. Harrison, A.T. Kuhn, J. Electroanal. Chem. 184, 347 (1985).
175. V.G. Nefedov, V.M. Serebritskii, O.S. Ksenzhek, Elektrokhimiya 10, 1382 (1987).
176. S.F. Chen, T.J. O'Keefe, Electrochim. Acta 33, 789 (1988).
177. L.J.J. Janssen, E. Barendrecht, Electrochim. Acta 30, 683 (1985).
178. Y. Fukunaka, K. Suzuki, A. Ueda, Y. Kondo, J. Electrochem. Soc. 136, 1002 (1989).
179. A.T. Kuhn, M. Stevenson, Electrochim. Acta 27, 329 (1982).
180. P. Gallone, G. Modica, S. Maffi, J. Electroanal. Chem. 180, 421 (1984).
181. B.E. Bongenaar-Schlenter, L.J.J. Janssen, S.J.D. van Stralen, E. Barendrecht, J. Appl. Electrochem. 15, 537 (1985).

182. J. Dukovic, C.W. Tobias, J. Electrochem. Soc. 134, 331 (1987).
183. J.-Y. Huot, J. Appl. Electrochem. 19, 453 (1989).
184. J.O'M. Bockris, in: Modern Aspects of Electrochemistry: J.O'M. Bockris, B.E. Conway (eds.). London: Butterworths (1954), p. 180.
185. J.G.N. Thomas, Trans. Faraday Soc. 57, 1603 (1961).
186. B.E. Conway, M. Salomon, Electrochim. Acta 9, 1599 (1964).
187. E.E. Kuzminskii, A.V. Gorodyskii, I.L. Kasatkina, Elektrokhimiya 19, 962 (1983).
188. J. Horiuti, T. Keii, K. Hirota, J. Res. Inst. Catalysis, Hokkaido Univ. 2, 1 (1951).
189. T. Matsushima, M. Enyo, Electrochim. Acta 19, 117 (1974).
190. T. Ohmori, A. Matsuda, J. Res. Inst. Catalysis, Hokkaido Univ. 26, 53 (1978).
191. A. Matsuda, R. Notoya, J. Res. Inst. Catalysis, Hokkaido Univ. 14, 165 (1966).
192. T. Sasaki, A. Matsuda, J. Res. Inst. Catalysis, Hokkaido Univ. 21, 157 (1973).
193. H. Gerischer, D.M. Kolb, M. Przasnyski, Surf. Sci. 43, 662 (1974).
194. S. Trasatti, Z. Phys. Chem. N.F. 98, 75 (1975).
195. T. Yamazaki, M. Enyo, Electrochim. Acta 35, 523 (1990).
196. F. Dalard, M.A. Ulmann, J. Augustynski, P. Selvam, J. Electroanal. Chem. 270, 445 (1989).
197. A. Saraby-Reintjes, J. Chem. Soc. Faraday Trans. 1, 82, 3343 (1986).
198. J. Divisek, J. Electroanal. Chem. 214, 615 (1986).
199. G.J. Brug, M. Sluyters-Rehbach, J.H. Sluyters, A. Hamelin, J. Electroanal. Chem. 181, 245 (1984).
200. R.J. Nichols, A. Bewick, J. Electroanal. Chem. 243, 445 (1988).
201. L.I. Krishtalik, Elektrokhimiya 13, 1889 (1977).
202. L.I. Krishtalik, Zh. Fiz. Khim. 39, 1087 (1965).
203. L.B. Kriksunov, L.I. Krishtalik, V.M. Tsionskii, Elektrokhimiya 25, 692 (1989).
204. U.V. Palm, M.A. Salve, Yu. É. Khaller, Elektrokhimiya 14, 794 (1978).
205. V.I. Bystrov, L.I. Krishtalik, Elektrokhimiya 5, 392 (1969).
206. R. Parsons, G. Picq, P. Vennereau, J. Electroanal. Chem. 181, 281 (1984).
207. Yu.I. Kharkats, J. Ulstrup, J. Electroanal. Chem. 65, 555 (1975).
208. A.A. Ovchinnikov, V.A. Benderskii, J. Electroanal. Chem. 100, 563 (1979).
209. V.A. Benderskii, Yu.I. Dachnovskii, A.A. Ovchinnikov, J. Electroanal. Chem. 148, 161 (1983).
210. L.I. Krishtalik, J. Electroanal. Chem. 130, 9 (1981).
211. L.I. Krishtalik, Elektrokhimiya 18, 781 (1982).
212. S. Holloway, J.W. Gadzuk, Phys. Scr. T4, 86 (1983).
213. T.R. Knowles, J. Electroanal. Chem. 150, 365 (1983).
214. W. Lorenz, J. Electroanal. Chem. 265, 159 (1989).
215. B.E. Conway, D.F. Tessier, D.P. Wilkinson, J. Electroanal. Chem. 204, 111 (1986).
216. B.E. Conway, D.P. Wilkinson, J. Chem. Soc. Faraday Trans. 1, 84, 3389 (1988).
217. B.E. Conway, D.F. Tessier, Int. J. Chem. Kin. 13, 925 (1981).
218. L.I. Krishtalik, J. Electroanal. Chem. 100, 547 (1979).
219. R. Parsons, G. Picq, P. Vennereau, J. Electroanal. Chem. 181, 267 (1984).
220. V.L. Krasikov, Elektrokhimiya 17, 1518 (1981); 19, 209 (1983).
221. R. Notoya, A. Matsuda, J. Phys. Chem. 93, 5521 (1989).
222. S. Trasatti, G. Lodi, in: Electrodes of Conductive Metallic Oxides: S. Trasatti (ed.). Amsterdam: Elsevier (1981); Part B, p. 521.
223. S. Trasatti, Electrochim. Acta 28, 1083 (1983).
224. D.J. Barclay, J. Electroanal. Chem. 44, 47 (1973).
225. S. Trasatti, in: Electrocatalysis: W.E. O'Grady, P.N. Ross, F.G. Will (eds.). Pennington: The Electrochemical Society (1982), p. 73.
226. H. Tamura, C. Iwakura, T. Kitamura, J. Less-Common Met. 89, 567 (1983).
227. J.C.F. Boodts, G. Fregonara, S. Trasatti, in: Performance of Electrodes for Industrial Electrochemical Processes: F. Hine, B.V. Tilak, J.M. Fenton, J.D. Lisius (eds.). Pennington: The Electrochemical Society (1989), p. 135.

228. O.A. Petrii, I.V. Kovrigina, S.Ya. Vasina, Mat. Chem. Phys. 22, 51 (1989).
229. B.E. Conway, D.F. Tessier, D.P. Wilkinson, J. Electroanal. Chem. 199, 249 (1986).
230. Lj.M. Vračar, D.M. Dražić, J. Electroanal. Chem. 265, 171 (1989).
231. K. Szabó, J. Mika, Acta Chim. Hung. 126, 99 (1989).
232. U. Freese, U. Stimming, J. Electroanal. Chem. 198, 409 (1986).
233. B.E. Conway, D.J. MacKinnon, J. Electrochem. Soc. 116, 1665 (1969).
234. B.E. Conway, D.P. Wilkinson, J. Electroanal. Chem. 214, 633 (1986).
235. B.E. Conway, D.P. Wilkinson, J. Electroanal. Chem. 210, 167 (1986).
236. J.O'M. Bockris, A. Gochev, J. Electroanal. Chem. 214, 655 (1986).
237. B.E. Conway, D.P. Wilkinson, D.F. Tessier, Ber. Bunsenges. Phys. Chem. 91, 484 (1987).
238. J.O'M. Bockris, A. Gochev, J. Phys. Chem. 90, 5232 (1986).
239. E. Gileadi, J. Electroanal. Chem. 134, 117 (1987).
240. B.E. Conway, D.F. Tessier, D.P. Wilkinson, J. Electroanal. Chem. 1989, 2486 (1989).
241. M.J. Weaver, J. Phys. Chem. 80, 2645 (1976).
242. W. Schmickler, J. Electroanal. Chem. 284, 269 (1990).
243. E. Kirowa-Eisner, M. Schwarz, E. Gileadi, Electrochim. Acta 34, 1103 (1989).
244. L.B. Kriksunov, V.M. Tsionskii, Elektrokhimiya 21, 1582 (1985).
245. E.N. Potapova, L.I. Krishtalik, I.A. Bagotskaya, Elektrokhimiya 10, 53 (1974).
246. A.C. Ferreira, E.R. González, E.A. Ticianelli, L.A. Avaca, B. Matvienko, J. Appl. Electrochem. 18, 894 (1988).
247. I.P. Ivanov, M.P. Vasileva-Dimova, Kh.I. Noninski, Elektrokhimiya 20, 1522 (1984).
248. K. Lohrberg, P. Kohl, Electrochim. Acta 29, 1557 (1984).
249. J. De Carvalho, G. Tremiliosi-Filho, L.A. Avaca, E.R. González, in: Electrode Materials and Processes for Energy Conversion and Storage: S. Srinivasan, S. Wagner, H. Wroblowa (eds.). Pennington: The Electrochemical Society (1987), p. 356.
250. Y.S. Terminasow, M.S. Beletzki, Dokl. Akad. Nauk. SSSR 63, 411 (1948).
251. V.M. Tsionskii, L.I. Krishtalik, L.B. Kriksunov, Electrochim. Acta 33, 623 (1988).
252. V.M. Tsionskii, L.B. Kriksunov, Elektrokhimiya 24, 311 (1988).
253. A. Nidola, R. Schira, 151st Meeting of the Electrochemical Society. Extended Abstracts. Pennington: The Electrochemical Society (1987), Vol. 87-1, p. 552.
254. J.A. Leistra, P.J. Sides, J. Electrochem. Soc. 134, 2442 (1987).
255. H.-J. Heidrich, L. Müller, Electrochim. Acta 35, 1089 (1990).
256. S. Trasatti, Electrochim. Acta 32, 369 (1987).
257. L. Müller, H.-J. Heidrich, Elektrokhimiya 25, 1145 (1989).
258. Ya.M. Kolotyrkin, A.N. Chemodanov, Dokl. Akad. Nauk. SSSR 134, 128 (1960).
259. H. Wendt, H. Hofmann, V. Plzak, Int. J. Hydrogen Energy 9, 297 (1984).
260. V.N. Dakhov, T.E. Tsupak, L.S. Chernyshova, Zh. Prikl. Khim. 62, 1715 (1989).
261. B.N. Kabanov, S.A. Rozentsveie, J. Phys. Chem. USSR 22, 513 (1948).
262. L. Angely, G. Bronoël, G. Peslerbe, J. Electroanal. Chem. 96, 183, 191, 203 (1979).
263. Kh.I. Noninski, I.P. Ivanov, M.P. Vasileva-Dimova, Elektrokhimiya 19, 698 (1983).
264. G.T. Burshtein, M.A. Kearns, J. Electroanal. Chem. 131, 991 (1984).
265. G.I. Lacconi, A.S. Gioda, V.A. Macagno, Electrochim. Acta 30, 211 (1985).
266. H.M. Villullas, G.I. Lacconi, A.S. Gioda, V.A. Macagno, Electrochim. Acta 32, 1657 (1987).
267. K.I. Popov, R.R. Adžić, M.D. Maksimović, G.R. Ostojić, Bull. Soc. Chim. Beog. 42, 731 (1977).
268. T. Ohmori, J. Electroanal. Chem. 172, 123 (1984).
269. H.-J. Heidrich, B.I. Podlovchenko, L. Müller, Elektrokhimiya 24, 1119 (1988).
270. J.-P. Candy, P. Fouilloux, M. Keddam, H. Takenouti, Electrochim. Acta 27, 1585 (1982).
271. J.-P. Candy, P. Fouilloux, Electrochim. Acta 26, 1029 (1981).
272. A.P. Brown, M. Krumpelt, R.O. Loutfy, N.P. Yao, Electrochim. Acta 27, 557 (1982).
273. A.P. Brown, M. Krumpelt, R.O. Loutfy, N.P. Yao, J. Electrochem. Soc. 129, 2481 (1982).
274. G.D. Scott, G.E. Stoner, G.L. Cahen, J. Electrochem. Soc. 134, 2739 (1987).
275. O. Radovici, M. Macovschi, Rev. Roum. Chim. 14, 159 (1969).

276. D. V. Sokolskii, P. I. Zabotin, S. V. Druz, A. M. Zagorev, O. P. Polovyanova, Zh. Fiz. Kim. 59, 2978 (1985).
277. T. A. Liederbach, A. M. Greenberg, V. H. Thomas, in: Modern Chlor-Alkali Technology: M. O. Coulter (ed.). Chichester: Ellis Horwood (1980), p. 145.
278. N. Tchernikovsky, P. J. Moran, E. Gileadi, J. Electroanal. Chem. 136, 1089 (1989).
279. B. V. Tilak. Mat. Chem. Phys. 22, 149 (1989).
280. I. I. Pyshnograeva, Yu. B. Vasiliev, I. E. Zimakov, V. S. Bagotskii, V. I. Spitsyn, Dokl. Akad. Nauk. SSSR 189, 1048 (1969).
281. V. V. Poplavskii, G. I. Novikov, É. V. Ratnikov, Zh. Prikl. Khim. 59, 995 (1986).
282. H. Kasten, G. K. Wolf, Electrochim. Acta 25, 1581 (1980).
283. B. Love, K. Seto, J. Lipkowski, Revs. Chem. Interm. 8, 87 (1987).
284. P. N. Ross, Surf. Sci. 102, 463 (1981).
285. P. N. Ross, J. Electrochem. Soc. 126, 67 (1979).
286. D. Armand, J. Clavilier, J. Electroanal. Chem. 225, 205 (1987); 233, 251 (1987).
287. A. Rodes, K. El Achi, M. A. Zamakhchari, J. Clavilier, J. Electroanal. Chem. 284, 245 (1990).
288. A. M. Meretskii, I. V. Kudryashov, Yu. B. Vasiliev, Elektrokhimiya 13, 447 (1977).
289. I. M. Novoselskii, Elektrokhimiya 15, 1285 (1979).
290. N. Markovic, M. Hanson, G. McDougall, E. Yeager, J. Electroanal. Chem. 214, 555 (1986).
291. S. Motoo, N. Furuya, J. Electroanal. Chem. 181, 301 (1984).
292. S. Trasatti, Mat. Chem. Phys. 12, 507 (1985).
293. V. L. Kheifets, B. S. Krastskov, A. L. Rotinyan, Elektrokhimiya 6, 916 (1970).
294. K. Seto, A. Iannelli, B. Love, J. Lipkowski, J. Electroanal. Chem. 226, 351 (1987).
295. J. Arold, J. Tamm, Elektrokhimiya 25, 418 (1989).
296. A. Hamelin, M. J. Weaver, J. Electroanal. Chem. 223, 171 (1987).
297. J. A. Garrido, F. Illas, J. M. Ricart, J. Rubio, J. Electroanal. Chem. 196, 387 (1985).
298. D. M. Kolb, in: Advances in Electrochemistry and Electrochemical Engineering: H. Gerischer, C. W. Tobias (eds.). New York: Wiley-Interscience (1978), Vol. 11, p. 125.
299. K. Jüttner, Electrochim. Acta 31, 917 (1986).
300. A. M. Abd El-Halim, K. Jüttner, W. J. Lorenz, J. Electroanal. Chem. 106, 193 (1980).
301. R. R. Adžić, M. D. Spasojević, A. R. Despić, Electrochim. Acta 24, 577 (1979).
302. N. Furuya, S. Motoo, J. Electroanal. Chem. 102, 155 (1979).
303. R. R. Adžić, M. D. Spasojević, A. R. Despić, Electrochim. Acta 24, 569 (1979).
304. S. Motoo, N. Furuya, Mat. Chem. Phys. 22, 309 (1989).
305. N. Furuya, S. Motoo, J. Electroanal. Chem. 72, 165 (1976).
306. N. Furuya, S. Motoo, J. Electroanal. Chem. 88, 151 (1978).
307. N. V. Korovin, N. I. Kozlova, O. N. Saveleva, T. V. Lapshina, M. V. Kumenko, J. Res. Inst. Catalysis, Hokkaido Univ. 29, 17 (1981).
308. N. V. Korovin, N. I. Kozlova, O. N. Saveleva, Elektrokhimiya 16, 583 (1980).
309. N. V. Korovin, E. Ya. Udris, O. N. Saveleva, Elektrokhimiya 22, 360 (1986).
310. N. V. Korovin, O. N. Saveleva, N. I. Kozlova, Elektrokhimiya 16, 585 (1980).
311. N. V. Korovin, N. I. Kozlova, O. N. Saveleva, Elektrokhimiya 10, 1575 (1978).
312. N. V. Korovin, O. N. Saveleva, N. I. Kozlova, T. V. Lapshina, M. V. Kumenko, Dokl. Akad. Nauk. SSSR 257, 149 (1981).
313. R. Ya. Shaidullin, A. D. Semenova, G. D. Vovchenko, Yu. B. Vasiliev, Elektrokhimiya 19, 747 (1983).
314. R. Ya. Shaidullin, A. D. Semenova, G. D. Vovchenko, Yu. B. Vasiliev, Elektrokhimiya 18, 75 (1982).
315. Yu. B. Vassiliev, J. Res. Inst. Catalysis, Hokkaido Univ. 30, 89 (1982).
316. A. S. Lapa, O. A. Petrii, Elektrokhimiya 22, 1637 (1986).
317. X.-K. Xing, D. A. Scherson, J. Electroanal. Chem. 196, 439 (1985).
318. S. W. Bushnell, P. M. Purkis, Chem. Ind. 61 (1984).
319. G. G. Scherer, H. Devantay, R. Oberlin, S. Stucki, Dechema Monograph 98, 407 (1985).
320. A. Katayama-Aramata, H. Nakajima, K. Fujikawa, H. Kita, Electrochim. Acta 28, 777 (1983).

321. K. Kinoshita, in: Modern Aspects of Electrochemistry: J. O'M Bockris, B. E. Conway, R. E. White (eds.). New York: Plenum Press (1982), Vol. 14, p. 557.
322. K. Kinoshita, P. Stonehart, in: Modern Aspects of Electrochemistry: J. O'M. Bockris, B. E. Conway (eds.). New York: Plenum Press (1977), Vol. 12, p. 183.
323. K. Kinoshita, J. Lundquist, P. Stonehart, J. Catal. 31, 325 (1973).
324. P. Stonehart, J. Lundquist, Electrochim. Acta 18, 907 (1973).
325. K. Kinoshita, P. Stonehart, Electrochim. Acta 20, 101 (1975).
326. V. S. Bagotzky, A. M. Skundin, Electrochim. Acta 29, 757 (1984).
327. N. N. Kim, Yu. B. Vasiliev, I. V. Kudryashov, A. M. Skundin, Zh. Fiz. Khim. 58, 229 (1984).
328. V. S. Bagotzky, A. M. Skundin, Electrochim. Acta 29, 951 (1984).
329. V. S. Bagotzky, Yu. B. Vassiliev, V. E. Kazarinov, A. M. Skundin, Mat. Chem. Phys. 22, 325 (1989).
330. V. S. Bagotzy, A. M. Skundin, Electrochim. Acta 30, 485 (1985).
331. Y. Takasu, Y. Fujii, K. Yasuda, Y. Iwanaga, Y. Matsuda, Electrochim. Acta 34, 453 (1989).
332. N. N. Kim, Yu. B. Vasiliev, I. V. Kudryashov, A. M. Skundin, V. V. Belik, Elektrokhimiya 20, 673 (1984).
333. N. A. Zakarina, G. D. Zakumbaeva, N. F. Toktabaeva, Elektrokhimiya 19, 938 (1983).
334. R. W. Joyner, J. B. Pendry, D. K. Saldin, S. R. Tennison, Surf. Sci. 138, 84 (1984).
335. T. V. Balashova, V. S. Bagotskii, A. M. Skundin, L. G. Gindin, Elektrokhimiya 8, 1600 (1972).
336. G. D. Zakumbaeva, L. A. Beketaeva, Z. I. Azebaeva, A. Sh. Kuanyshev, L. I. Fridman, Elektrokhimiya 20, 1364 (1984).
337. V. N. Fateev, L. L. Antonova, G. V. Balakirev, V. A. Kondratiev, M. A. Sevastyanov, Elektrokhimiya 23, 548 (1987).
338. R. W. Murray, Acc. Chem. Res. 13, 135 (1980).
339. R. M. Kellett, T. G. Spiro, Inorg. Chem. 24, 2373 (1985).
340. R. M. Kellett, T. G. Spiro, Inorg. Chem. 24, 2378 (1985).
341. B. Keita, L. Nadjo, Mat. Chem. Phys. 22, 2378 (1989).
342. B. Keita, L. Nadjo, J. Electroanal. Chem. 191, 441 (1985).
343. B. Keita, L. Nadjo, J. Electroanal. Chem. 199, 229 (1986).
344. B. Keita, L. Nadjo, J. Electroanal. Chem. 243, 87 (1988).
345. B. Keita, L. Nadjo, J. M. Savéant, J. Electroanal. Chem. 243, 105 (1988).
346. B. Keita, L. Nadjo, G. Krier, J. F. Muller, J. Electroanal. Chem. 223, 287 (1987).
347. B. Keita, L. Nadjo, J. Electroanal. Chem. 240, 325 (1988).
348. B. Keita, L. Nadjo, J. P. Haeussler, J. Electroanal. Chem. 243, 481 (1988).
349. B. Keita, D. Bonaziz, L. Nadjo, J. Electroanal. Chem. 255, 303 (1988).
350. B. Keita, D. Bonaziz, L. Nadjo, J. Electroanal. Chem. 284, 431 (1990).
351. O. Savadogo, S. Thibault, Int. J. Hydrogen Energy 14, 865 (1989).
352. B. Keita, T. Lucas, L. Nadjo, J. Electroanal. Chem. 208, 343 (1986).
353. B. Keita, L. Nadjo, J. Electroanal. Chem. 217, 287 (1987).
354. B. Keita, L. Nadjo, J. Electroanal. Chem. 230, 267 (1987).
355. B. Keita, L. Nadjo, J. Electroanal. Chem. 227, 77 (1987).
356. B. Keita, L. Nadjo, J. P. Haeusler, J. Electroanal. Chem. 230, 85 (1987).
357. B. Keita, L. Nadjo, R. Parsons, J. Electroanal. Chem. 258, 207 (1989).
358. B. Keita, L. Nadjo, J. Electroanal. Chem. 287, 149 (1990).
359. B. Keita, L. Nadjo, J. Electroanal. Chem. 269, 447 (1989).
360. M. Ai, J. Catal. 71, 88 (1981).
361. M. Mizuno, T. Watanabe, M. Misono, J. Phys. Chem. 89, 80 (1985).
362. A. J. McEvoy, M. Grätzel, J. Electroanal. Chem. 209, 391 (1986).
363. W.-T. Wu, A. J. McEvoy, J. Electroanal. Chem. 270, 395 (1989).
364. D. M. Dražić, in: Modern Aspects of Electrochemistry: B. E. Conway, J. O'M. Bockris, R. E. White (eds.). New York: Plenum Press (1989), Vol. 19, p. 69.
365. L. Peraldo Bicelli, C. Romagnani, J. chim. Phys. 72, 975 (1975).
366. S. P. Shavkunov, I. N. Sherstobitova, V. V. Kuznetsov, Elektrokhimiya 19, 549 (1983).

367. L. Peraldo Bicelli, C. Romagnani, M.T. Rosania, J. chim. Phys. 74, 529 (1977).
368. J. Tamm, P. Vares, Elektrokhimiya 23, 1269 (1987).
369. J.O'M. Bockris, J.L. Carbajal, B.R. Scharifker, K. Chandrasekaran, J. Electrochem. Soc. 134, 1957 (1987).
370. V.I. Kichigin, Elektrokhimiya 23, 1689 (1987).
371. S.P. Shavkunov, I.N. Sherstobitova, V.V. Kuznetsov, Elektrokhimiya 19, 706 (1983).
372. V.I. Kichigin, Elektrokhimiya 25, 260 (1989).
373. J. Tamm, P. Vares, V. Past, Elektrokhimiya 24, 402 (1988).
374. T. Hurlen, S. Gunvaldsen, F. Blaker, Electrochim. Acta 29, 1163 (1984).
375. V.M. Tsionskii, T.Sh. Korkashvili, Elektrokhimiya 16, 451 (1980).
376. P.M. Vares, Yu.K. Tamm, V.É. Past, Elektrokhimiya 17, 327 (1981).
377. S.P. Shavkunov, I.N. Sherstobitova, V.V. Kuznetsov, Elektrokhimiya 19, 816 (1983).
378. J.O'M. Bockris, E.C. Potter, J. Chem. Phys. 20, 614 (1952).
379. T. Ohmori, A. Matsuda, J. Res. Inst. Catalysis, Hokkaido Univ. 15, 201 (1967).
380. J.-T. Huot, J. Electrochem. Soc. 136, 1933 (1989).
381. H.E.G. Rommal, P.J. Moran, J. Electrochem. Soc. 132, 325 (1985).
382. L.A. Burkaltseva, A.G. Pshenichnikov, Elektrokhimiya 12, 42 (1976).
383. J.-F. Marêche, J.-C. Rat, A. Herold, J. chim. Phys. 75, 735 (1978).
384. M.H. Miles, G. Kissel, P.W.T. Lu, S. Srinivasan, J. Electrochem. Soc. 123, 332 (1976).
385. S. Maximovitch, R. Dúrand, J. Electroanal. Chem. 149, 273 (1983).
386. D.E. Hall, J. Appl. Electrochem. 14, 107 (1984).
387. C.K. Dyer, Int. J. Hydrogen Energy 9, 993 (1984).
388. J.-P. Diard, B. Legorrec, S. Maximovitch, Electrochim. Acta 35, 1099 (1990).
389. N. Yoshida, M. Yoshitake, E. Endoh, T. Morimoto, in: Performance of Electrodes for Industrial Electrochemical Processes: F. Hine, B.V. Tilak, J.M. Fenton, J.D. Lisius (eds.). Pennington: The Electrochemical Society (1989), p. 123.
390. N. Yoshida, M. Yoshitake, E. Endoh, T. Morimoto, Int. J. Hydrogen Energy 14, 137 (1989).
391. L. Brossard, Int. J. Hydrogen Energy 13, 315 (1988).
392. A.G. Pshenichnikov, R.Kh. Burshtein, V.D. Kovalevskaya, Elektrokhimiya 11, 1465 (1975).
393. G.L. Padyukova, G.A. Pushkareva, A.B. Fasman, Elektrokhimiya 20, 963 (1984).
394. G.N. Trusov, M.F. Fandeeva, Elektrokhimiya 12, 1832 (1976).
395. L.V. Tamm, Yu.K. Tamm, V.É. Past, Elektrokhimiya 9, 1382 (1973).
396. L.V. Tamm, Yu.K. Tamm, V.É. Past, Elektrokhimiya 11, 1581 (1975).
397. L.V. Tamm, Yu.K. Tamm, V.É. Past, Elektrokhimiya 10, 83 (1974).
398. B.N. Afanasiev, Elektrokhimiya 22, 32 (1986).
399. E. Potvin, H. Menard, J.M. Lalancette, L. Brossard, J. Appl. Electrochem. 20, 252 (1990).
400. J. Balajka, Int. J. Hydrogen Energy 8, 755 (1983).
401. G.L. Cahen, P.J. Moran, L.L. Scribner, G.E. Stoner, J. Electrochem. Soc. 128, 1877 (1981).
402. M. Bonner, T. Botts, J. McBreen, A. Mezzina, F. Salzano, C. Yang, Int. J. Hydrogen Energy 9, 269 (1984).
403. A.G. Pshenichnikov, S.F. Chernyshov, Yu.I. Kryukov, L.I. Altentaller, E.I. Tumasova, V.N. Dudin, Elektrokhimiya 18, 1011 (1982).
404. E. Justi, W. Scheibe, A. Winsel, German Patent DPB 1 101 361 (1954).
405. N.V. Korovin, M.V. Kumenko, N.I. Kozlova, Elektrokhimiya 23, 408 (1987).
406. J. Divisek, J. Mergel, H. Schmitz, Int. J. Hydrogen Energy 7, 695 (1982).
407. Y. Coquette, H. Ménard, L. Brossard, Int. J. Hydrogen Energy 15, 21 (1990).
408. A.G. Pshenichnikov, Int. J. Hydrogen Engergy 7, 51 (1982).
409. G.L. Padyukova, G.A. Pushkareva, A.B. Fasman, B.K. Almashev, Elektrokhimiya 22, 747 (1986).
410. V.G. Shalyukhin, G.L. Padyukova, A.Sh. Kuanyshev, A.B. Fasman, Elektrokhimiya 25, 134 (1989).
411. M. Prigent, T. Nenner, L. Martin, M. Roux, in: Hydrogen as an Energy Carrier: G. Imarisio, A.S. Strub (eds.) Dordrecht: D. Reidel (1983), p. 256.

412. M. Bernard, L. Mas, M. Prigent, J. C. Sohm, in: Hydrogen as an Energy Vector: A. A. Strub, G. Imarisio (eds.). Dordrecht: D. Reidel (1980), p. 283.
413. T. M. Grishina, V. V. Selyukova, Zh. Fiz. Khim. 53, 1582 (1979).
414. T. M. Grishina, L. I. Lazareva, Zh. Fiz. Khim. 57, 228 (1983).
415. H. Wendt, V. Plzak, Electrochim. Acta 28, 27 (1983).
416. A. Senda, A. Sakata, K. Yamaguchi, in: Performance of Electrodes for Industrial Electrochemical Processes: F. Hine, B. V. Tilak, J. M. Fenton, J. D. Lisius (eds.). Pennington: The Electrochemical Society (1989), p. 111.
417. T. Ohta, J. E. Funk, J. D. Porter, B. V. Tilak, Int. J. Hydrogen Energy 227, 483 (1970).
418. G. V. Boikova, G. V. Zhutaeva, M. R. Tarasevich, V. S. Bagotskii, N. A. Shumilova, Elektrokhimiya 16, 847 (1980).
419. R. D. Armstrong, M. F. Bell, Electrochim. Acta 23, 1111 (1978).
420. G. A. Tsirlina, O. A. Petrii, N. S. Kandakova, Elektrokhimiya 22, 933 (1986).
421. I. Paseka, J. Balej, Coll. Czech. Chem. Commun. 38, 3600 (1973).
422. H. Bohm, Nature 227, 483 (1970).
423. G. Bianchi, F. Mazza, S. Trasatti, Z. Phys. Chem. 226, 40 (1964).
424. I. Nikolov, K. Petroov, T. Vitanov, A. Gushev, Int. J. Hydrogen Energy 8, 437 (1983).
425. M. Neumann-Spallart, in: Hydrogen Energy Progress VI: T. N. Veziroğlu, N. Getoff, P. Weinzierl (eds.). Oxford: Pergamon Press (1986), Vol. 2, p. 577.
426. K. Wiesener, E. Winkler, W. Schneider, Z. Phys. Chem. 266, 579 (1985).
427. G. A. Tsirlina, O. A. Petrii, Electrochim. Acta 32, 649 (1987).
428. G. A. Tsirlina, O. A. Petrii, Electrochim. Acta 32, 637 (1987).
429. G. V. Boikova, W. Schneider, K. Wiesener, G. V. Zhutaeva, M. R. Tarasevich, Elektrokhimiya 22, 1135 (1986).
430. E. Winkler, W. Schneider, K. Wiesener, Z. Phys. Chem. 266, 589 (1985).
431. A. A. Tanaka, E. R. González, L. A. Avaca, Int. J. Hydrogen Energy 11, 455 (1986).
432. B. D. Struck, H. Neumeister, A. Naoumidis, Int. J. Hydrogen Energy 11, 541 (1986).
433. B. D. Struck, H. Neumeister, H. Schirbach, D. Triefenbach, A. Naoumidis, in: Hydrogen Energy Progress V: T. N. Veziroğlu, J. B. Taylor (eds.). Oxford: Pergamon Press (1984), Vol. 2, p. 943.
434. I. I. Vasilenko, N. N. Nechiporenko, P. M. Bugai, Elektrokhimiya 7, 1621 (1971).
435. G. Benczur-Urmassy, German Offen. 2 307 852 (1974).
436. V. A. Lavrenko, L. N. Yagupolskaya, L. I. Kuznetsova, Elektrokhimiya 10, 1078 (1974).
437. H. Vanderborre, R. Leysen, H. Nackaerts, Int. J. Hydrogen Energy 8, 81 (1983).
438. H. Vanderborre, R. Leysen, H. Nackaerts, Ph. van Asbroeck, Int. J. Hydrogen Energy 9, 277 (1984).
439. K. Yamakawa, H. Tubakino, K. Akiyoshi, H. Inoue, K. Yoshimoto, in: Electrochemical Engineering in the Chlor-Alkali Industries: F. Hine, R. E. White, W. B. Darlington, R. D. Varjian (eds.). Pennington: The Electrochemical Society (1988), p. 174.
440. E. Dayalan, R. Narayan, J. Electroanal. Chem. 179, 167 (1984).
441. K. Winkler, T. Krogulec, Pol. J. Chem. 60, 239 (1986).
442. H. Vanderborre, Ph. Vermeiren, R. Laysen, Electrochim. Acta 29, 297 (1984).
443. R. Kh. Burshtein, V. E. Kazarinov, O. A. Gafarova, I. E. Barbasheva, Ya. S. Lapin, N. P. Kuznetsova, Elektrokhimiya 24, 1450 (1984).
444. A. C. C. Tseung, J. A. Antonian, D. B. Hibbert, Chem. Ind. 54 (1984).
445. A. I. Onuchukwu, Electrochim. Acta 27, 529 (1982).
446. R. Sabela, I. Paseka, J. Appl. Electrochem. 20, 500 (1990).
447. R. Kh. Burshtein, V. E. Kazarinov, A. G. Pshenichnikov, I. E. Barbasheva, O. A. Gafarova, I. V. Obrushnikova, Elektrokhimiya 23, 711 (1987).
448. G. K. Sisenov, N. K. Abasova, V. A. Bogdanovskaya, M. R. Tarasevich, Elektrokhimiya 25, 726 (1989).
449. N. V. Korovin, O. N. Saveleva, T. L. Dogonova, E. Ya. Udris, Elektrokhimiya 23, 707 (1987).
450. R. Prins, V. H. J. De Beer, G. A. Somorjai, Catal. Rev. 31, 1 (1989).

451. Ph. Vermeiren, R. Laysen, H. Vanderborre, Electrochim. Acta 30, 1253 (1985).
452. A.C.C. Tseung, P. Rasiyah, M.C.M. Man, K.L.K. Yeung, in: Hydrogen as an Energy Vector: A.A. Strub, G. Imarisio (eds.). Dordrecht: D. Reidel (1980), p. 240.
453. J.F. Cairns, D.A. Denton, P.A. Izard, Eur. Pat. Appl. EP 129 374 (1984); Chem. Abstr. 102, 102 442 (1985).
454. A. Nidola, PCT Int. Appl. WO86 03 790 (1986); Chem. Abstr. 105, 122 974 (1986).
455. H. Debrodt, Eur. Pat. Appl. EP 120 088 (1984); Chem. Abstr. 102, 122 040 (1984).
456. E. Palibroad, J. Electroanal. Chem. 21, 410 (1969).
457. N. Azzerri, J. Electroanal. Chem. 66, 99 (1975).
458. R.M. Torresi, C.P. De Pauli, Thin Solid Films 162, 353 (1988).
459. M. Shinagawa, H. Nezu, A. Muromatsu, N. Yano, Rev. Polarogr. Kyoto 15, 108 (1968).
460. W.A. Badawy, J. Appl. Electrochem. 20, 139 (1990).
461. R. Manoharan, J.B. Goodenough, J. Electrochem. Soc. 137, 910 (1990).
462. D.B. Sepa, D.S. Ovcin, M.V. Vojnović, J. Electrochem. Soc. 119, 1285 (1972).
463. J.O'M. Bockris, J. McHardy, J. Electrochem. Soc. 120, 53 (1973).
464. A.P. Brynza, L.M. Danilova, Elektrokhimiya 9, 352 (1973).
465. R.M. Torresi, O.R. Cámara, C.P. De Pauli, M.C. Giordano, Electrochim. Acta 32, 1291 (1987).
466. V.V. Egorov, P.D. Lukotsev, Elektrokhimiya 5, 387 (1969).
467. Kh.Z. Brainina, M.Ya. Khodos, G.M. Belysheva, M.V. Krivosheev, Elektrokhimiya 20, 1380 (1984).
468. R.M. Torresi, O.R. Cámara, C.P. De Pauli, Electrochim. Acta 32, 1357 (1987).
469. B.I. Bairachnyi, V.P. Gomozov, L.V. Lyashok, L.I. Skatkov, Elektrokhimiya 25, 994 (1989).
470. G. Barral, J.-P. Diard, C. Montella, Electrochim. Acta 31, 277 (1986).
471. G. Lodi, C. De Asmundis, S. Ardizzone, E. Sivieri, S. Trasatti, Surf. Technol. 14, 335 (1981).
472. Y.-C. Long, Z.-D. Zhang, K. Dwight, A. Wold, Mat. Res. Bull. 23, 631 (1988).
473. D. Klisurski, R. Dimitrova, Bull. Chem. Soc. Jpn. 63, 590 (1990).
474. D. Galizzioli, F. Tantardini, S. Trasatti, J. Appl. Electrochem. 5, 203 (1975).
475. J.C.F. Boodts, S. Trasatti, J. Appl. Electrochem. 19, 255 (1989).
476. H. Chen, S. Trasatti, unpublished results.
477. S. Ardizzone, G. Fregonara, S. Trasatti, J. Electroanal. Chem. 205, 347 (1986).
478. C. Angelinetta, M. Falciola, S. Trasatti, J. Electroanal. Chem. 205, 347 (1986).
479. A. Daghetti, G. Lodi, S. Trasatti, Mat. Chem. Phys. 8, 1 (1983).
480. T. Hepel, F.H. Pollak, W.E. O'Grady, J. Electrochem. Soc. 132, 2385 (1985).
481. T. Hepel, F.H. Pollak, W.E. O'Grady, J. Electrochem. Soc. 131, 2094 (1984).
482. E. Nicolas, Fr. Appl. 79 17 441 (1979).
483. E. Veggetti, S. Trasatti, unpublished results.
484. A.S. Ivanova, V.A. Dzisko, É.M. Moroz, S.P. Noskova, Kinet. Katal. 26, 1193 (1985).
485. A.S. Ivanova, V.A. Dzisko, É.M. Moroz, S.P. Noskova, Kinet. Katal. 27, 428 (1986).
486. S. Trasatti, G. Lodi, in: Electrodes of Conductive Metallix Oxides: S. Trassati (ed.). Amsterdam: Elsevier (1980), Part A, p. 301.
487. M. Kleijn, H.P. Van Leeuwen, J. Electroanal. Chem. 247, 253 (1988).
488. S. Trasatti, Mat. Chem. Phys. 16, 157 (1987).
489. M. Jaccaud, F. Leroux, J.C. Millet, Mat. Chem. Phys. 22, 105 (1989).
490. S. Ho, D.P. Whelan, K. Rajeshwar, A. Weiss, M. Murley, R. Reid, J. Electrochem. Soc. 135, 1452 (1988).
491. T. Sakata, T. Kawai, K. Hashimoto, Denki Kagaku 51, 79 (1983).
492. E. Amouyal, P. Keller, A. Moradpour, J. Chem. Soc. Faraday Trans. 1, 78, 3331 (1982).
493. J.M. Kleijn, E. Rouwendal, H.P. Van Leeuwen, J. Lyklema, J. Photochem. Photobiol. A: Chem. 44, 29 (1988).
494. S. Matsura, M. Kurumatani, Y. Ozaki, Jpn. Kokai Tokyo Koho JP 54/90 080 (1979); Chem. Abstr. 91, 165 637 (1979).
495. P. Keller, A. Moradpour, E. Amouyal, J. Chem. Soc. Faraday Trans. 1, 78, 3331 (1982).

496. A. Mills, G. Williams, J. Chem. Soc., Chem. Commun. 321 (1984).
497. A. Nidola, R. Schira, 171st Meeting of the Electrochemical Society. Extended Abstracts. Pennington: The Electrochemical Society (1987), Vol. 87-1, p. 554.
498. J.O'M. Bockris, A. Damjanovic, R.J. Mannan, J. Electroanal. Chem. 18, 349 (1986).
499. E.W. Brooman, A.T. Kuhn, J. Electroanal. Chem. 49, 325 (1974).
500. A. Bélanger, A.K. Vijh, Surf. Technol. 15, 59 (1982).
501. A.K. Vijh, A. Bélanger, Int. J. Hydrogen Energy 11, 147 (1986).
502. Zh.L. Vert, V.F. Pavlova, I.P. Tverdovskii, Elektrokhimiya 18, 1055 (1982).
503. M. Enyo, K. Machida, J. Res. Inst. Catalysis, Hokkaido Univ. 31, 67 (1983).
504. M.M. Jakšić, I.M. Csonka, Electrochem. Technol. 4, 49 (1966).
505. D.E. Brown, M.N. Mahmood, A.K. Turner, S.M. Hall, P.O. Fogarty, Int. J. Hydrogen Energy 7, 405 (1982).
506. M.V. Ananth, N.V. Parthasaradhy, Int. J. Hydrogen Energy 15, 193 (1990).
507. I.A. Raj, K.I. Vasu, J. Appl. Electrochem. 20, 32 (1990).
508. A. Nidola, Int. J. Hydrogen Energy 9, 367 (1984).
509. I.A. Raj, R. Pattabiraman, S. Dheenadayalan, R. Chandrasakaran, V.K. Venkatesan, Bull. Electrochem. 2, 477 (1986).
510. E.R. González, L.A. Avaca, A. Carubelli, A.A. Tanaka, G. Tremiliosi-Filho, Int. J. Hydrogen Energy 9, 689 (1984).
511. M. Spasojević, N. Krstajić, P. Despotov, R. Atanasoski, K. Popov, J. Appl. Electrochem. 14, 265 (1984).
512. M.M. Jakšić, V. Komnenić, R. Atanasoski, R.R. Adžić, Elektrokhimiya 3, 21 (1978).
513. A.J. Appleby, G. Crépy, J. Jacquelin, Int. J. Hydrogen Energy 3, 21 (1978).
514. J. De Carvalho, G. Tremiliosi-Filho, L.A. Avaca, E.R. González, Int. J. Hydrogen Energy 14, 161 (1989).
515. J.-Y. Huot, L. Brossard, J. Appl. Electrochem. 20, 281 (1990).
516. J.-Y. Huot, L. Brossard, Surf. Coat. Technol. 34, 373 (1988).
517. J.-Y. Huot, L. Brossard, Int. J. Hydrogen Energy 14, 229 (1989).
518. B.E. Conway, L. Bai, J. Chem. Soc., Faraday Trans. 1, 81, 1841 (1985).
519. D.E. Brown, M.N. Mahmood, M.C.M. Man, A.K. Turner, Electrochim. Acta 29, 1551 (1984).
520. B.E. Conway, L. Bai, Int. J. Hydrogen Energy 11, 533 (1986).
521. B.E. Conway, L. Bai, M.A. Sattar, Int. J. Hydrogen Energy 12, 607 (1987).
522. B.E. Conway, H. Angerstein-Kozlowska, M.A. Sattar, B.V. Tilak, J. Electrochem. Soc. 130, 1825 (1983).
523. I.A. Raj, V.K. Venkatesan, Int. J. Hydrogen Energy 13, 215 (1988).
524. I.A. Raj, V.K. Venkatesan, Trans. SAEST 22, 189 (1987).
525. J. Gala, A. Małachowski, G. Nawrat, J. Appl. Electrochem. 14, 221 (1984).
526. N. Krstajić, K. Popov, M. Spasojević, R. Atanasoski, J. Appl. Electrochem. 12, 435 (1982).
527. E. Chassaing, K. Vu Quang, R. Wiart, J. Appl. Electrochem. 19, 839 (1989).
528. Č.M. Lačnjevac, M.M. Jakšić, J. Res. Inst. Catalysis, Hokkaido Univ. 31, 7 (1982).
529. M.M. Jakšić, Č.M. Lačnjevac, Chem. Techn. 37, 330 (1985).
530. Č.M. Lačnjevac, N.M. Marković, M.M. Jakšić, Surf. Technol. 22, 51 (1984).
531. J. Divisek, P. Malinowski, J. Mergel, H. Schmitz, Int. J. Hydrogen Energy 13, 141 (1988).
532. R.Kh. Burshtein, I.E. Barbashova, S.F. Cernyshov, A.G. Pshenichnikov, L.I. Altenteller, Elektrokhimiya 19, 1328 (1983).
533. E.W. Justi, H.H. Ewe, A.W. Kalberlah, N.M. Sadridakis, M.H. Schäfer, Energy Conversion 10, 183 (1970).
534. H. Ewe, E.W. Justi, K. Stephan, Energy Conversion 13, 109 (1973).
535. Z.Y. Jiang, D. Tryk, E. Yeager, 161st Meeting of the Electrochemical Society. Extended Abstracts. Pennington: The Electrochemical Society (1982), Vol. 82-1, p. 600.
536. N.I. Kavardakov, V.I. Kichigin, V.V. Kuznetsov, S.B. Prima, L.A. Tretyachenko, Elektrokhimiya 22, 1084 (1986).

537. J. Kumar, S. Saxena, Int. J. Hydrogen Energy 14, 331 (1989).
538. T. Matsumoto, A. Matsushita, J. Less-Common Met. 123, 135 (1986).
539. D.E. Hall, J.M. Sarver, D.O. Gothard, Int. J. Hydrogen Energy 13, 547 (1988).
540. T. Kitamura, C. Iwakura, H. Tamura, Chem. Lett. 965 (1981).
541. O.A. Petrii, K.N. Semenenko, I.I. Korobov, S.Ya. Vasina, I.V. Kovrigina, V.V. Burnasheva, J. Less-Common Met. 136, 121 (1987).
542. K. Machida, M. Enyo, K. Oguro, M. Nakane, Bull. Chem. Soc. Jpn. 57, 2809 (1984).
543. T. Kitamura, C. Iwakura, H. Tamura, Chem. Lett. 1755 (1981).
544. H.H. Van Mal, K.H.J. Buschow, A.R. Miedema, J. Less-Common Met. 35, 65 (1974).
545. A. Bélanger, A.K. Vijh, Surf. Coat. Technol. 28, 93 (1986).
546. A. Bélanger, A.K. Vijh, Int. J. Hydrogen Energy 12, 227 (1987).
547. H.F. Bittner, C.C. Badcock, J. Electrochem. Soc. 130, 193C (1983).
548. C.M. Luedecke, G. Deublein, R.A. Huggins, J. Electrochem. Soc. 132, 52 (1985).
549. O.A. Petrii, I.V. Kovrigina, S.Ya. Vasina, Mat. Chem. Phys. 22, 51 (1989).
550. Y. Xin-nan, L. Schlapbach, Int. J. Hydrogen Energy 13, 429 (1988).
551. T. Kitamura, C. Iwakura, H. Tamura, Electrochim. Acta 27, 1729 (1982).
552. K. Machida, M. Enyo, G. Adachi, H. Sakaguchi, J. Shiokawa, Bull. Chem. Soc. Jpn. 59, 925 (1986).
553. S. Fukushima, H. Tanabe, Int. J. Hydrogen Energy 8, 33 (1983).
554. E.N. Anisochkina, V.V. Lunin, Elektrokhimiya 23, 1131 (1987).
555. A.G. Morachevskii, E.B. Klebanov, D. Yan, Elektrokhimiya 23, 1133 (1987).
556. A.K. Vijh, G. Bélanger, R. Jacques, Mat. Chem. phys. 21, 529 (1989).
557. A.B. Shein, Elektrokhimiya 24, 1335 (1988).
558. A. Baiker, Faraday Disc. Chem. Soc. 87, 239 (1989).
559. D.L. Cocke, J. Metals 38, 70 (1986).
560. C. Yoon, D.L. Cocke, J. Non-Cryst. Solids 79, 217 (1986).
561. A. Yokoyama, K. Komiyama, H. Inoue, T. Masumoto, H.M. Kimura, J. Catal. 68, 355 (1981).
562. M. Shibata, T. Masumoto, in: Preparation of Catalysts IV: B. Delmon. P. Grange, P.A. Jacobs, G. Poncelet (eds.). Amsterdam: Elsevier (1987), p. 353.
563. W. Brower, M. Matyjaszczyk, T. Pettit, G. Smith, Nature 301, 497 (1983).
564. R. Schoegl, in: Rapidly Quenched Metals: S. Steeb, H. Warlimont (eds.). Amsterdam: North Holland (1985), p. 1723.
565. K. Seto, J. Noël, J. Lipkowski, Z. Altounian, R. Reeves, J. Electrochem. Soc. 136, 1910 (1989).
566. S.G. Sun, J. Noël, J. Lipkowski, Z. Altounian, J. Electroanal. Chem. 278, 205 (1990).
567. K. Hashimoto, M. Naka, J. Noguchi, K. Asami, T. Masumoto, in: Passivity of Metals: R.P. Frankenthal, J. Kruger (eds.). Princeton: The Electrochemical Society (1978), p. 156.
568. J.C. Turn, R.M. Latanision, Corrosion 39, 271 (1983).
569. M.D. Archer, C.C. Corke, B.H. Harji, Electrochim. Acta 32, 13 (1987).
570. P.C. Searson, P.V. Nagarkar, R.M. Latanision, in: Modern Aspects of Electrochemistry: R.E. White, J.O'M. Bockris, B.E. Conway (eds.). New York: Plenum Press (1990), Vol. 21, p. 121.
571. M. Naka, K. Hashimoto, T. Masumoto, I. Okamoto, in: 4th International Conference on Rapidly Quenched Metals: T. Masumoto, K. Suzuki (eds.). Sendai: Japan Institute of Metals (1982), p. 1431.
572. J.-Y. Huot, M. Trudeau, R. Schulz, A. Van Neste, Int. J. Hydrogen Energy 15, 287 (1990).
573. E. Kuzmann, A. Vértes, L. Kiss, G. Raichewski, S. Vitkova, Electrochim. Acta 33, 1455 (1988).
574. R.L. Zeller III, U. Landau, J. Electrochem. Soc. 137, 1107 (1990).
575. K. Machida, M. Enyo, I. Toyoshima, K. Miyahara, K. Kai, K. Suzuki, Bull. Chem. Soc. Jpn. 56, 3393 (1983).
576. M. Enyo, T. Yamazaki, K. Kai, K. Suzuki, Electrochim. Acta 28, 1573 (1983).
577. K. Machida, M. Enyo, I. Toyoshima, K. Kai, K. Suzuki, J. Less-Common Met. 96, 305 (1984).
578. J.-Y. Huot, M. Trudeau, L. Brossard, R. Schulz, J. Electrochem. Soc. 136, 2224 (1989).
579. V.Yu. Vasiliev, A.Yu. Chechetkin, Zash. Metall. 25, 590 (1989).
580. R. Schulz, A. Van Neste, L. Brossard, J.-Y. Huot, Mat. Sci. Eng. 99, 469 (1988).

581. J.-Y. Huot, L. Brossard, Int. J. Hydrogen Energy 12, 599 (1987).
582. J.-Y. Huot, A. Van Neste, L. Brossard, R. Schulz, Surf. Coat. Technol. 35, 241 (1988).
583. J. Y. Huot, M. Trudeau, L. Brossard, R. Schulz, Int. J. Hydrogen Energy 14, 319 (1989).
584. P. Kovács, T. Ando, M. Ishiwatari, Y. Ujihira, E. Kuzmann, A. Vértes, J. Electrochem. Soc. 136, 1958 (1989).
585. L. Vračar, B. E. Conway, J. Electroanal. Chem. 277, 253 (1990).
586. G. Jorge, R. Duránd, R. Faure, R. Yavari, J. Less-Common Met. 145, 383 (1988).
587. N. S. Kopylova, O. A. Petrii, Yu. V. Efimov, L. I. Voronova, Elektrokhimiya 24, 1100 (1988).
588. G. Kreysa, J. Gomez, A. Baró, A. J. Arvia, J. Electroanal. Chem. 265, 67 (1989).
589. G. Kreysa, B. Håkansson, P. Ekdunge, Electrochim. Acta 33, 1351 (1988).
590. P. Ekdunge, H. Thulin, G. Kreysa, Chem.-Ing.-Tech. 61, 638 (1989).
591. K. E. Heusler, D. Huerta, in: Corrosion, Electrochemistry, and Catalysis of Metallic Glasses: R. B. Diegle, K. Hashimoto (eds.). Pennington: The Electrochemical Society (1988), p. 1.
592. T. P. Moffat, W. F. Flanagan, B. D. Lichter, J. Electrochem. Soc. 133, 2712 (1988).
593. H. Alemu, K. Jüttner, Electrochim. Acta 33, 1101 (1988).
594. G. Kreysa, B. Håkansson, J. Electroanal. Chem. 201, 61 (1986).

Advances in Electrochemical Science and Engineering
Edited by Heinz Gerischer and Charles W. Tobias

Solid Oxide Fuel Cells

A. Hammou

Laboratoire d'Ionique et d'Electrochimie du Solide de Grenoble,
ENSEEG-INPG, Domaine Universitaire-BP 75, F-38402 Saint Martin d'Hères,
France

Contents

1 Introduction

Suggested by Nernst in 1900, the first working fuel cell involving a solid electrolyte was developed only in 1937 by Baur and Preis [1]. These authors demonstrated the particular interest of ZrO_2 based solid solutions, especially in the ZrO_2-Y_2O_3 system. Their results were further explained by Wagner [2] who considered the type of conduction in the electrolytes employed and defined one of the required properties for their use in fuel cells, i.e. exclusively ionic conduction. In the early 1960's, extensive research programs were undertaken on Solid Oxide Fuel Cells (SOFC) using solid oxide electrolytes and working between 800 and 1000 °C. The reason was new energy needs, mainly in space, submarine and military uses. Many companies and institutes all over the world devoted a great deal of their research and development efforts to SOFCs. Among them were Westinghouse, Argonne National Laboratory and the Batelle Institute in the USA, Brown Boveri and Dornier in West Germany, the Electroanalytical Laboratory in Japan, and the Sverdlovsk Institute in USSR.

The main characteristics of SOFCs compared to other electrochemical cells are the high temperature and the thick film technology required. This offers non negligible advantages in terms of both electrode polarization and ohmic losses mainly in the electrolyte. Furthermore, catalysts are not always necessary. However, the solid state components and elevated temperatures impose severe technological constraints which are to a large extent responsible for the relatively slow development of this type of fuel cells. Another characteristic of SOFCs is the possibility of using them as high temperature water electrolysers or as fuel cells without modifying the design. Phosphoric acid fuel cells and alkaline water electrolysers can be operated in only one mode because of the special method required for adding or removing the reactants and products when liquid electrolytes are used. As mentioned by Isaacs [3], in an analysis of four potential fuel cell power plant systems [4, 5] phosphoric acid, alkaline, molten carbonate and zirconia), SOFCs based on zirconia offer the greatest advantages in terms of capital investment, electricity costs, and overall system efficiency.

2 Thermodynamic Considerations

2.1 Cell Potential

Schematically speaking an elementary SOFC is composed of a solid oxide electrolyte, an oxygen electrode (cathode) and a fuel electrode (anode), as shown in Fig. 1. To form a battery, several elementary cells must be connected using an appropriate material. A SOFC may be considered as an oxygen concentration cell [6] of the following type

$$O_2(P_c)/\text{Oxide Solid Electrolyte}/O_2(P_a)$$

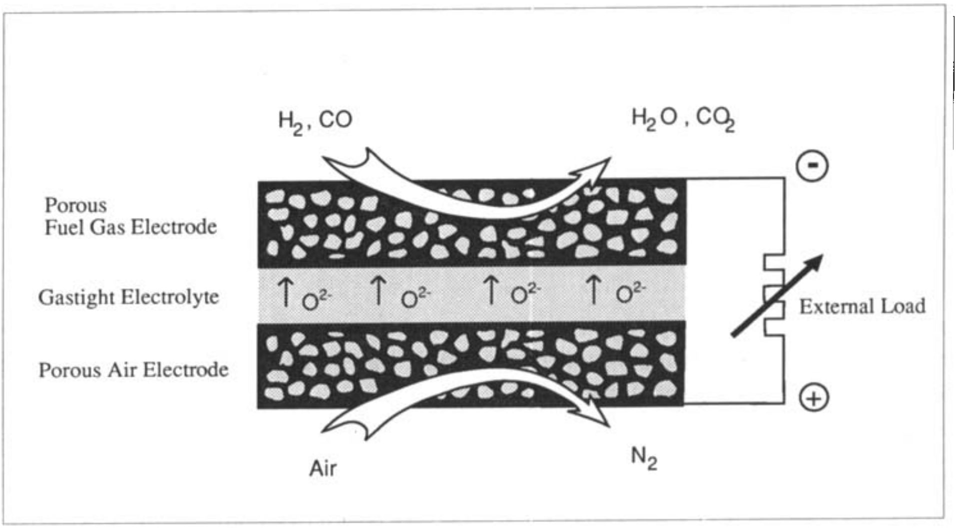

Fig. 1. Schematic representation of an SOFC. From ref. [132].

where P_c and P_a are the oxygen partial pressures at the cathode and the anode respectively. The thermodynamic voltage E_{th} of this cell is given by the Nernst law

$$E_{th} = \frac{RT}{4F} \ln \frac{P_c}{P_a}$$

where R, T and F have their usual meanings. The open cell voltage $E_{i=0}$ is related to the thermodynamic voltage by the expression

$$E_{i=0} = (1 - \overline{t_e}) E_{th}$$

where $\overline{t_e}$ is the average electronic transference number of the solid electrolyte. The open cell voltage is rigorously calculated as:

$$E_{i=0} = \frac{1}{4F} \int_{\mu_a}^{\mu_c} (1 - t_e) \, \mathrm{d}\mu_{O_2}$$

where μ_a and μ_c are the oxygen chemical potentials at the anode and the cathode, respectively.

The existence of electronic conductivity in oxide solid electrolytes gives rise to an exchange current i_0 and to fuel consumption, even at open circuit. Wagner [7] established the expression for i_0:

$$i_0 = \frac{1}{4F} \sigma_e (1 - t_e) \frac{\partial \mu_{O_2}}{\partial x}$$

where σ_e is the electronic conductivity of the solid electrolyte, μ_{O_2} varying continuously between the cathode/electrolyte interface ($x = 0$) and the anode/electrolyte interface ($x = L$), these interfaces being parallel. In solving the previous equation between the limit values of μ_{O_2} at $x = 0$ and $x = l$, one obtains

$$i_0 l = (\overline{\sigma_e} - \overline{\sigma_e t_e}) \frac{\mu_{O_2}^{(c)} - \mu_{O_2}^{(a)}}{4F}$$

$$i_0 l = (\overline{\sigma_e} - \overline{\sigma_e t_e}) E_{th}$$

where $\overline{\sigma_e}$ and $\overline{t_e}$ are the average values of σ_e and t_e respectively. This expression can be simplified if one considers that the electronic transference number t_e is negligible in practical working conditions

$$i_0 = \frac{\sigma_e E_{th}}{l} \ .$$

Then, the oxygen flux J_{O_2} through the electrolyte is:

$$\xi_{O_2} = \frac{i_0}{4F} = \frac{\overline{\sigma_e} E_{th}}{4Fl} \ .$$

Due to the very low dependence of the total conductivity σ on the oxygen chemical potential, one may write

$$\overline{\sigma_e} = \overline{t_e} \sigma \ .$$

The amount of oxygen consumed per second within the cell is given by the equation

$$\frac{dn_{O_2}}{dt} = t_e \frac{E_{th}}{4FR}$$

where R is the internal resistance of the electrolyte. This oxygen transfer phenomenon at open circuit is called "electrochemical semi-permeability" [8]. It can be seen from the previous equations that an increase in the electrolyte conductivity leads to an increase in fuel losses.

When an electric current I is delivered by an SOFC, the actual operating voltage V effectively delivered is lower than $E_{i=0}$ and equal to

$$V(I) = E_{i=0} - (R_e + R_c + R_a) I - \eta_a - \eta_c$$

where R_e, R_c and R_a indicate electrolyte, cathode and anode ohmic resistances respectively and η_a and η_c the anodic and cathodic polarizations. The latter may depend on several parameters such as gas phase composition, nature, microstructure and conduction type of the electrode material, conductivity of the solid electrolyte, contact area between reduction and fuel oxidation is rather complicated because of the many steps to be considered and the non-reproducibility of experimental results due to the variation of the electrical and geometrical characteristics of the cell as a function of current density, temperature and time. Most results concern platinum electrodes. Prohibitive cost and insufficient long-term stability exclude its use in commercial SOFCs. Some results available for oxide solid solution electrodes will be discussed later.

2.2 Efficiency Parameters

Let us consider the combustion reaction of one mole of oxygen at the cell working temperature T. We can define:

- the thermodynamic efficiency factor

$$\varepsilon_{\mathrm{th}} = \frac{\Delta G}{\Delta H} = \frac{4FE_{\mathrm{th}}}{\Delta H}$$

where ΔG and ΔH are the free enthalpy and the enthalpy of the combustion reaction respectively,

- the voltage efficiency factor

$\varepsilon_{\mathrm{V}} = V/E_{\mathrm{th}}$ = actual cell voltage/thermodynamic cell voltage

- the current efficiency factor

ε_{I} = actual current/current equivalent of reactant molar flow rate

- the electrochemical efficiency factor

$\varepsilon_{\mathrm{E}} = \varepsilon_{\mathrm{th}}\varepsilon_{\mathrm{V}}\varepsilon_{\mathrm{I}}$ = dc energy produced by the consumption of one mole of oxygen/enthalpy chang.

The oxygen consumption corresponds not only to the fuel participating in the electrochemical reaction but also to cell imperfections, particularly the physical permeability and the electrochemical semi-permeability of the electrolyte. This efficiency factor can be expressed by the following equation:

$$\varepsilon_{\mathrm{E}} = VI/\Delta H(I_{\mathrm{ion}}/4F + v)$$

where I_{ion} is the ionic current passing through the electrolyte and v is the velocity of the chemical combustion expressed in moles of oxygen per second.

2.3 Fuel and Oxidant Components

Pure oxygen or air are generally used as the oxidant in SOFCs. The most frequently considered fuels are H_2, CO, coal and light alkanes C_nH_{2n+2}, mainly methane. The moderate oxidation of alkanes or coal by water vapor or carbon dioxide provides $H_2-CO-CO_2-H_2O$ mixtures with various compositions. Then the thermodynamic cell EMF is a function of fuel gas composition in the close vicinity of the anode and can be calculated considering the following equilibria:

$$H_2 + 1/2\ O_2 \rightleftharpoons H_2O$$

$$CO + 1/2\ O_2 \rightleftharpoons CO_2$$

$$CH_4 + 3/2\ O_2 \rightleftharpoons CO + 2H_2O\ .$$

The variation of the standard EMF of these systems versus temperature is plotted in Fig. 2, showing that high EMF values are reached at low temperature.

EMF calculations were made by Archer and Sverdrup [9] for an O_2-H_2 cell as a function of anodic gas composition (H_2-H_2O) expressed by the n_O/n_H ratio where n_O and n_H are the number of oxygen and hydrogen gram-atoms in the gas phase respectively, i.e.

$$n_O = 2n_{O_2} + n_{H_2O}$$

$$n_H = 2n_{H_2} + 2n_{H_2O}\ .$$

The results are plotted in Fig. 3 showing a buffer effect around $n_O/n_H = 0.25$. Binder et al. [10] have considered the in situ reforming of alkanes, i.e. the direct

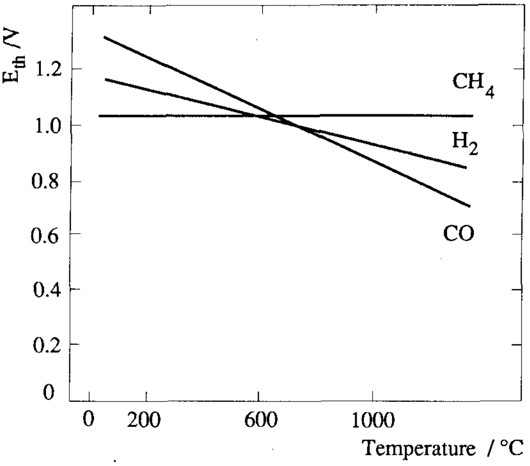

Fig. 2. Standard EMF for H_2, CO and CH_4.

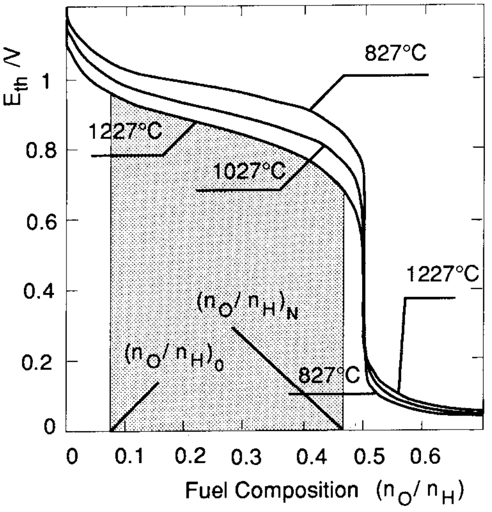

Fig. 3. Thermodynamic EMF dependence on fuel composition. From ref. [8].

utilization of gas mixtures like $C_nH_{2n+2}-H_2O-CO_2$ at the anode. These authors characterised the fuel gas by the ratio

$$b = \frac{\nu_{C_nH_{2n+2}}}{\nu^{max}_{C_nH_{2n+2}}}$$

where $\nu_{C_nH_{2n+2}}$ is the alkane mole number in the mixture and $\nu^{max}_{C_nH_{2n+2}}$ the maximum alkane role number which corresponds to the total conversion of the fuel. Results corresponding to $C_3H_8-H_2O$, $C_3H_8-CO_2$ at 1000 °C and $C_3H_8-H_2O-CO_2$ at 811 °C are shown in Fig. 4.

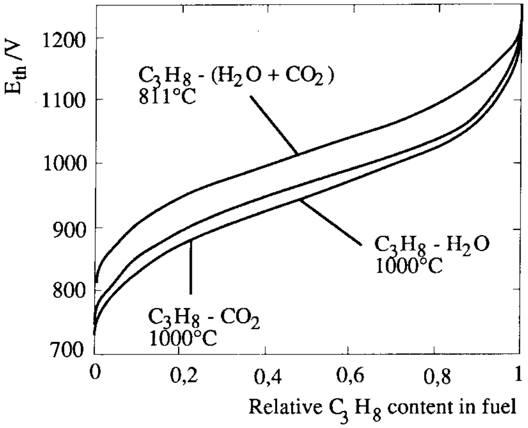

Fig. 4. Thermodynamic EMF of an O_2/H_2-CO mixture obtained by in situ reformed propane versus the initial composition of the fuel (see text). From ref. [8].

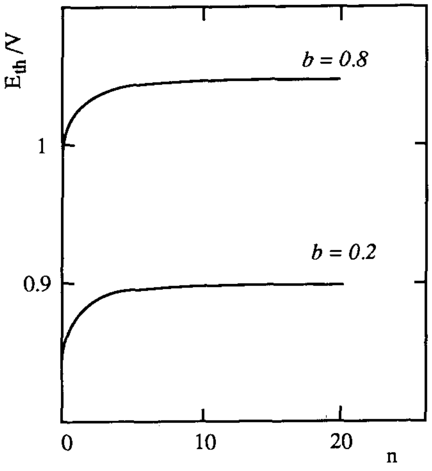

Fig. 5. Thermodynamic EMF of an in situ reformed alkane cell versus carbon atom number in the alkane molecule. From ref. [10].

Binder et al. [10] have also calculated the thermodynamic EMFs corresponding to various mixtures of alkanes and water vapor as a function of the atom number n of carbon in the alkane, for a given value of the b parameter. The results corresponding to these calculations are plotted in Fig. 5. It can be seen that at 1000 °C E_{th} increases progressively up to propane ($n = 3$) and then remains practically constant for the higher values of n.

In actual operation, a progressive fuel exhaust appears in the anodic gaseous mixture running through a series of connected cells, leading to the decrease of the EMF. Archer et al. [11, 12] have used the $E_{th} = f(n_O/n_H)$ diagrams, shown in Fig. 3, to determine the energy W theoretically recovered within a battery of N elements connected together in series. When this energy is related to one mole of hydrogen, its value is given by the equation

$$W = 4F \sum (E_{th})_i \frac{(n_O/n_H)_N - (n_O/n_H)_0}{N}$$

where $(E_{th})_i$ is the thermodynamic EMF of the element i and $(n_O/n_H)_N$ and $(n_O/n_H)_0$ are the values of the ratio n_O/n_H at the entance of the first element and the exit from the last element. If the number N of elements is large, the previous equation can be changed as follows

$$W = 4F \int_{(n_O/n_H)_0}^{(n_O/n_H)_N} E_{th} \, d(n_O/n_H) = 4Fa$$

where a is the area of the dashed surface in Fig. 3.

3 Cell Components and Kinetic Considerations

The constituent materials of an SOFC can be divided into three families:

- electrolytes
- electrode materials
- interconnection materials (ICM).

3.1 Electrolytes

The electrical conductivity of the involved solid electrolytes must be exclusively ionic, the charge carrier being an ion associated with the oxidant (O_2) or the fuel (H_2, hydrocarbons, etc.). Then the choice is reduced to solid electrolytes conducting by O^{2-} or H^+. The required properties for these materials, fixed by both electrochemical constraints and the high operating temperature, are the following:

- high ionic conductivity (≥ 0.1 S cm^{-1} at 900 °C),
- low electronic transference number ($< 10^{-3}$ at 900 °C),
- phase stability from room temperature to 1100 °C approximately,
- thermal expansion characteristics compatible with other cell components,
- chemical compatibility with electrode and interconnection materials and with oxygen and fuel gas as well,
- gas tightness,
- fracture toughness ($>$400 MPa at room temperature).

To these technological constraints must be added an economic constraint, the moderate cost of raw materials and fabrication. All these constraints have oriented most research and development toward oxide-based ceramics.

3.1.1 Oxide Conducting Solid Electrolytes

Solid solutions of this type that have been investigated belong to one of the following three families:

1. The first category includes fluorite-type solid solutions with the formula $MO_2-M'O$ or $MO_2-M''_2O_3$ where MO_2 is the basic oxide and $M'O$ and M''_2O_3 the dopant oxide, with

M = Zr, Ce

M′ = Ca, Mg

M″ = Sc, Y, Rare Earth

The addition of a dopant oxide gives rise to the creation of oxygen vacancies which are responsible for the ionic conductivity in these materials. Most work devoted to SOFCs has used doped zirconias as electrolytes. The salient features of electrical conductivity of doped zirconia are:

- The conductivity variation curve shows a maximum, the position of which depends on the type of dopant. This maximum is located at 15 and 9 mol% of dopant for ZrO_2-CaO and $ZrO_2-Y_2O_3$ systems, respectively (see Fig. 6) [13].
- The activation energy which corresponds to the maximum compositions is in the range 0.8 – 1.0 eV, as shown in Fig. 7 [14].
- For a given composition and a given charge cation, the conductivity increases as the radius of the dopant cation approaches that of zirconium. Thus, scandia-doped zirconia shows the best conductivity ($r_{Sc^{3+}} = 0.81$ Å and $z_{Zr^{4+}} = 0.8$ Å) in this family.
- The electrolytic domain extends over several orders of magnitude of oxygen partial pressure, n-type semi-conduction occurring in highly reducing media.
- An aging effect appears in the working temperature range of SOFCs giving rise to resistivity increase [15]. For example, an increase of 7% is observed for $(ZrO_2)_{0.91}-(Y_2O_3)_{0.09}$ after annealing for 90 h at 800 °C. This phenomenon is generally attributed to a cation ordering within the zirconia matrix. An exponential variation of bulk resistivity versus time has been observed for single crystals and for highly pure polycrystalline specimens [16, 17]. For common polycrystalline zirconias, a $\sqrt{t}$ law describes the aging effect which involves the microstructure of the sample and the impurity content [16, 18]. For technical and economic reasons, solid solutions $(ZrO_2)_{1-x}(Y_2O_3)_x$ with $x = 0.08$ to 0.1 have been preferred as solid electrolytes for SOFCs. In this range of composition, as shown in the phase diagram of the system (see Fig. 8) [19], zirconia crystallizes within the fluorite structure and is called yttria-stabilized zirconia (YSZ). For lower yttrium contents ($x \leq 0.05$) one obtains the so-called tetragonal polycrystalline zirconia (TPZ) which is characterized by better mechanical properties [20, 21]. It has been demonstrated that TPZ is a pure ionic conductor over a large range of oxygen partial pressure. No significant influence of the dopant concentration has been established [22, 23]. Its bulk conductivity is close to that observed for YSZ with a rather large grain boundary resistance [23]. This effect is likely to be due to the very fine microstructure of TPZ, which leads to large contact areas between the grains. This point may be rather detrimental to possible electrolytic applications of this material, especially at low temperatures. Ishizaki et al. [24] have studied the effect of Al_2O_3 additions to YSZ on the microstructure electrical resistivity, mechanical strength and SOFC performance. Alumina added to YSZ is just a physical mixture as shown in Fig. 9. Both electrical resistivity and mechanical strength increase with increasing alumina content, as shown in Fig. 10. In view of SOFC performances using this type of electrolyte, the authors conclude that alumina addition to YSZ could provide a self-supported SOFC electrolyte.

Another oxide family involving zirconium oxide has been examined as a possible alternative to YSZ as electrolytes in SOFCs. They are the pyrochlore solid solutions of the general formula $M_2Zr_2O_7$, where M is a rare-earth metal [25 – 29]. Zirconium can be substituted by a transition metal such as titanium. Moon et al. [29] have in-

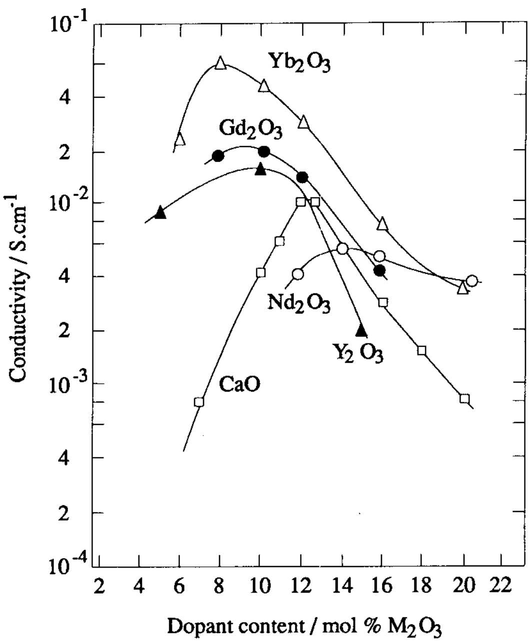

Fig. 6. Electrical conductivity versus composition for ZrO_2 based solid solutions at 800 °C. From ref. [13].

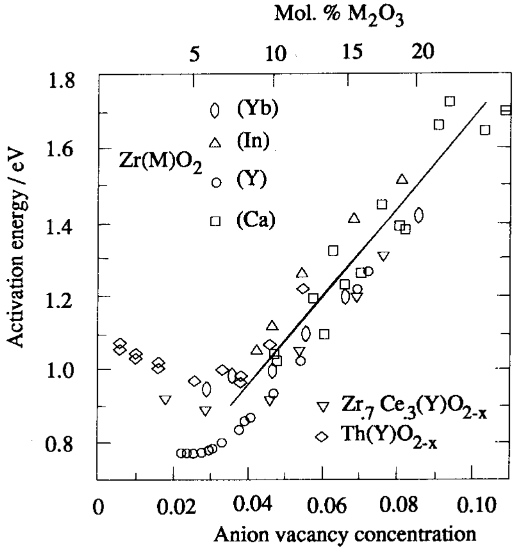

Fig. 7. Activation energy dependence of the anion vacancy concentration in various fluorite type oxide solid solutions. From ref. [14].

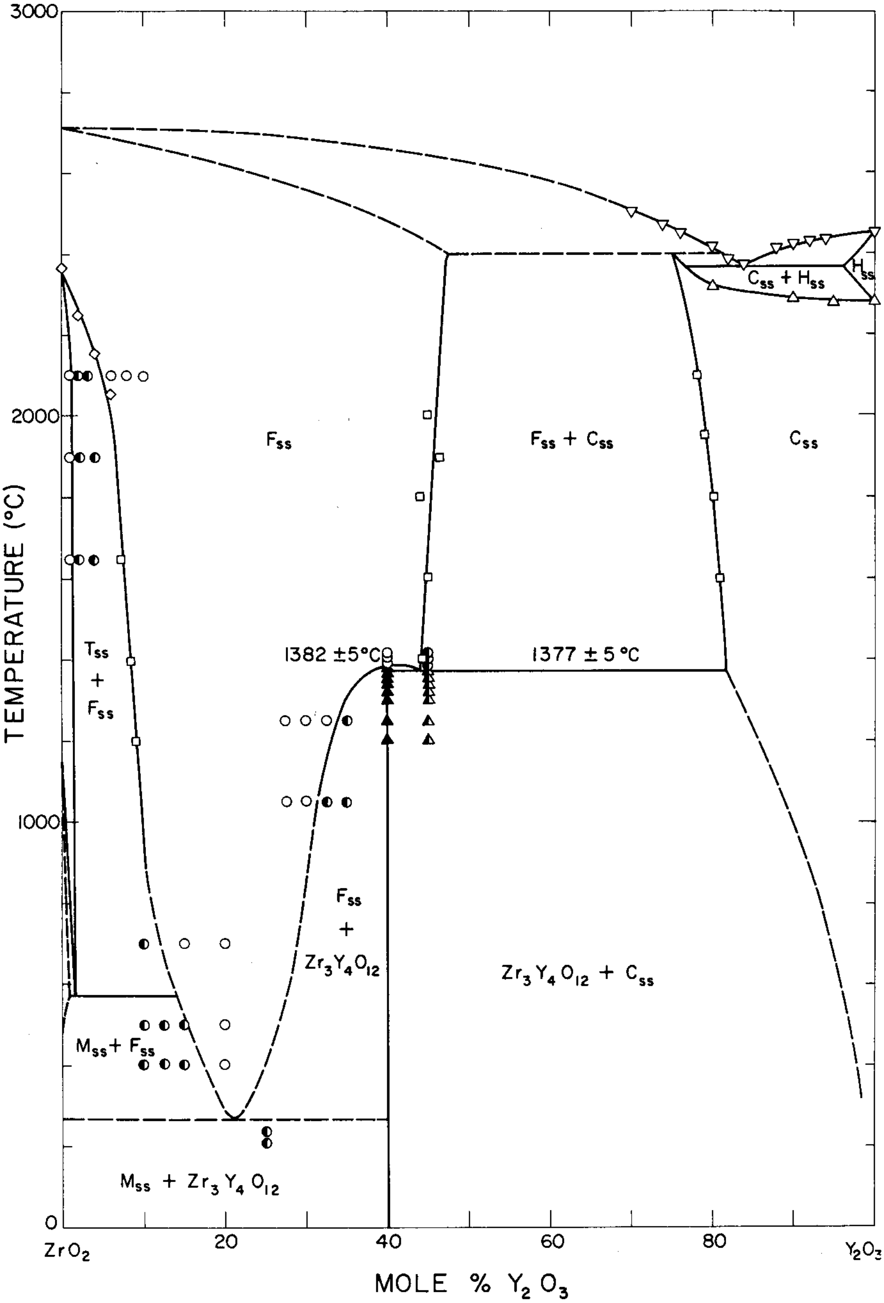

Fig. 8. Phase diagram for the ZrO_2–Y_2O_3 system. From ref. [19]. Reprinted by permission of the American Ceramic Society.

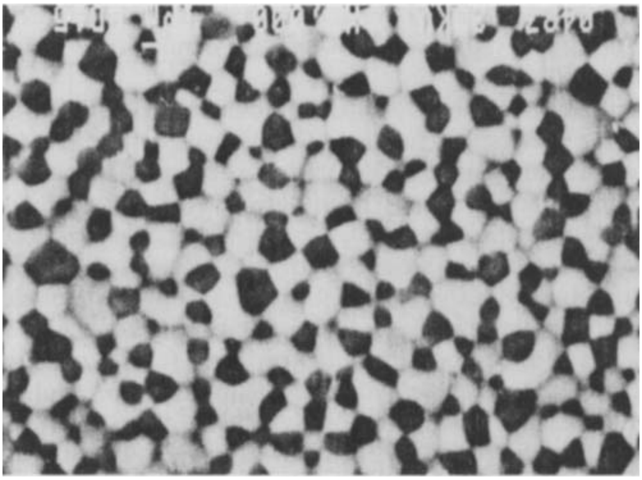

Fig. 9. Scanning Electron Micrographs of alumina-added yttria stabilized zirconia. Black grains have been identified as pure alumina. From ref. [24]. This paper was originally presented at the Fall 1989 Meeting of the Electrochemical Society held in Hollywood, Florida.

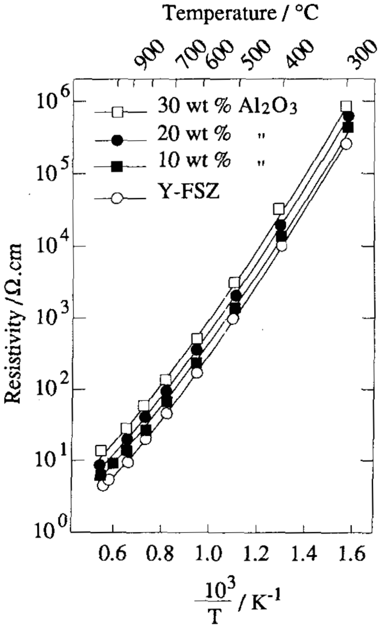

Fig. 10. Effect of alumina content on the electrical resistivity of alumina-added yttria stabilized zirconia. From ref. [24]. This paper was originally presented at the Fall 1989 Meeting of the Electrochemical Society held in Hollywood, Florida.

vestigated the $Gd_2(Zr_xTi_{1-x})_2O_7$ system and have shown that an intrinsic anion conductor can be obtained for large x values with however low conductivity which is approximately 1/5 of YSZ at 1000 °C.

CeO_2-based solid solutions exhibit higher ionic conductivity than in YSZ but they are partially reduced in the presence of fuel gas. The oxygen partial pressure domain where the conductivity is purely ionic is very narrow because of the reduction of cerium cations. For example, it extends from 1 to 10^{-2} at 1000 °C for $(CeO_2)_{0.95}-(Y_2O_3)_{0.05}$, thus excluding their use as electrolyte [30, 31].

The second family of oxide conducting solid electrolytes involves oxide solid solutions with a perovskite structure with the general formula ABO_3. A is a di- or trivalent cation with a large ionic radius and B is a tri- or tetravalent cation with a small ionic radius [32–36]. A and B can be substituted by lower valence cations, leading to the formation of oxygen vacancies. Electrolytes of this type studied within the framework SOFCs include the following systems: $CaTi_{1-x}Al_xO_{3-\delta}$, $CaTi_{1-x}Mg_xO_{3-\delta}$, $La_{1-x}Ca_xAlO_{3-\delta}$, where δ is the number of oxide ion vacancies. According to Takahashi [36], it can be said that $CaTi_{0.7}Al_{0.3}O_{3-\delta}$ may be a hopeful material as a new electrolyte for SOFCs.

The third oxide conductor family is composed of a trivalent basic metal oxide (La_2O_3, Y_2O_3, Sc_2O_3,...) doped by a divalent metal oxide (CaO, SrO) [37, 38]. The ionic conductivity of these oxides, measured at 1000 °C, are two or three orders of magnitude lower than for YSZ, except for La_2O_3-SrO solid solutions. At 900 °C, the $(La_2O_3)_{0.945}(SrO)_{0.055}$ has slightly lower conductivity than YSZ and a higher conductivity at low temperature with a relatively low activation energy ($E_a = 0.55$ eV). Unfortunately, this material cannot be used as electrolyte in SOFCs since is decomposes in the presence of water vapor or carbon dioxide. To expand the base of materials exhibiting oxide ion conductivity, Bi_2O_3-based oxides have been investigated [39, 49]. The reported conductivities are often several orders of magnitude higher than in YSZ, at the same temperature. Enhancement of conductivity is generally attributed to the high polarisability of bismuth ion. One of the best oxide conductors belongs to this family: the β cubic phase in the system Bi_2O_3-PbO, whose conductivity is higher than 1 S cm^{-1} at 600 °C with a relatively low activation energy (0.4–0.5 eV). Here again, these excellent oxide conductors are characterized by a very narrow electrolytic domain because of the partial reduction of Bi^{3+} at intermediate oxygen partial pressures and moderate temperatures, excluding their use as electrolytes in SOFCs. Figure 11 gives a compilation of oxide conductivity versus temperature for selected ceramic electrolytes [50].

3.1.2 Proton Conductor Solid Electrolytes

Forrat et al. [51] suggested the likely existence of protonic conduction in oxide solid solutions with a perovskite structure in hydrogen atmosphere at high temperature. This conduction type has been reported in some oxides such as Cu_2O [52], ThO_2 [53] and $LaYO_3$ and $SrZrO_3$ based ceramics [54] with some electronic conductivity. It has to be pointed out that all these oxides exhibit p-type semiconduction at high oxygen partial pressure, i.e. in air. It seems that protonic conduction in a hydrogen

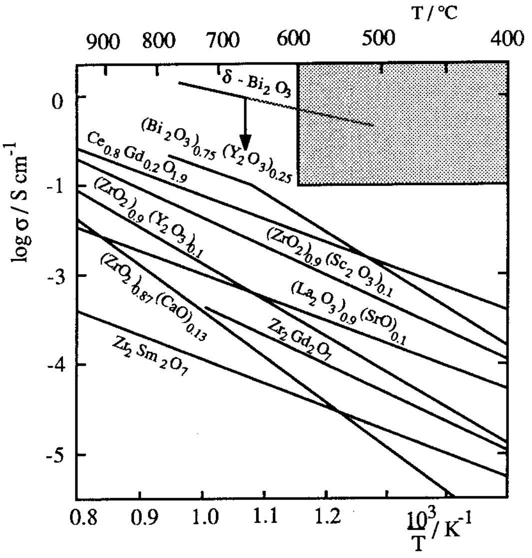

Fig. 11. Oxygen ion conductivity versus temperature for selected electrolytes. From ref. [50].

atmosphere appears in the oxides at the expense of electron holes initially present in the crystals, the possible rection equilibrium being

$$H_2(g) + 2h^{\bullet} \rightleftharpoons 2H^{\bullet} \ .$$

Oxygen vacancies could play the same role in a water vapor atmosphere giving rise to the following equilibrium:

$$H_2O(g) + V_O^{\bullet\bullet} \rightleftharpoons O_O^x + 2H^{\bullet} \ .$$

Recently, Invahara et al. [55–59] found that $SrCeO_3$- and $BaCeO_3$-based ceramics had appreciable protonic conduction in an atmosphere containing hydrogen at high temperature. The materials investigated where trivalent cations such as Y^{3+}, Sc^{3+}, Yb^{3+} are partially substituted for cerium, have a perovskite-type structure. They exhibit p-type electronic conduction in an atmosphere free from hydrogen or water vapor. When the ceramics are exposed to hydrogen or water vapor at several hundreds degrees Celsius, electronic conductivity decreases and simultaneously protonic conduction appears. Figures 12 and 13 show the Arrhenius plots of the total conductivity of some proton conductors in hydrogen. On the basis of the results obtained with $SrCe_{0.95}Yb_{0.05}O_{2.975}$, Bonanos et al. [60] do not completely agree with the conclusions of Iwahara et al. These authors claim that $SrCe_{0.95}Y_{0.05}O_{2.975}$ appears to be predominantly a mixed oxide ion/p-type conductor in air at high temperature. In hydrogen, it retains its oxide ion conductivity; below 600 °C an additional component, believed to be protonic, is acquired, which is coupled to oxide ion trans-

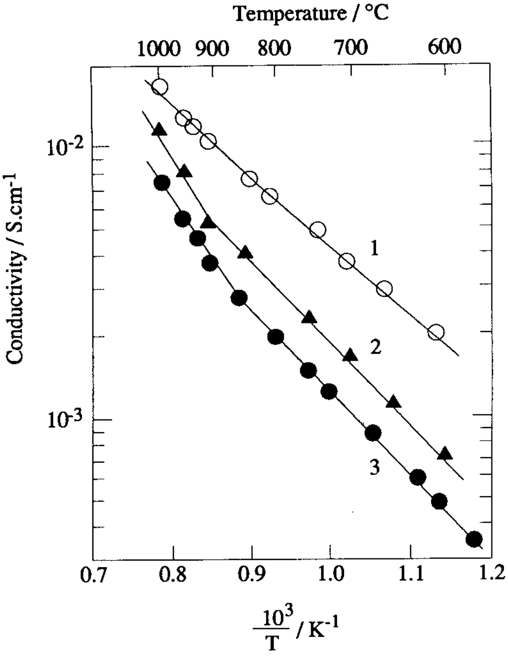

Fig. 12. Temperature dependence of the electrical conductivity for perovskite-type solid solutions in hydrogen. 1. $SrCe_{0.95}Yb_{0.05}O_{3-\delta}$. 2. $SrCe_{0.9}Y_{0.1}O_{3-\delta}$. 3. $SrCe_{0.95}Sc_{0.05}O_{3-\delta}$. From ref. [55].

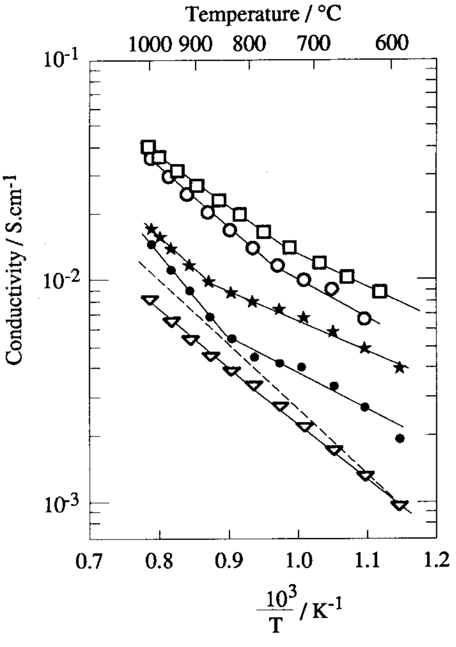

Fig. 13. Conductivity of $BaCe_{1-x}M_xO_{3-\delta}$ in hydrogen M (x value). □ Y (0.10), ○ Nd (0.10), * La (0.10), ● Nd (0.05), ▽ Ca (0.05), – – – $SrCe_{0.95}Yb_{0.05}O_{3-\delta}$.
From ref. [59]. Reprinted by permission of the publisher, the Electrochemical Society, Inc.

port. This question has to be investigated to make clear the nature of the site occupied by the proton and the protonic conduction mechanism.

3.2 Electrode Materials

SOFC performance largely depends on the choice of the electrode material. Selection criteria of specific electrode materials are related to both intrinsic physical properties and to microstructures. These criteria can be summarized as follows:

- high electronic conductivity,
- high ionic (oxide) conductivity,
- high catalytic activity for oxygen reduction at the cathode and for fuel oxidation at the anode,
- chemical compatibility with electrolyte and interconnection materials and with the working atmosphere,
- no destructive phase transition within the operating temperature range,
- thermal expansion coefficient compatible with other cell components,
- low volatility at the operating temperature,
- ability to be formed into films having sufficient porosity and a good adherence to the electrolyte.

3.2.1 Cathode Materials

Taking into account the oxidizing character of the cathodic atmosphere, only noble metals (Pt, Au, Ag) and electronically conducting metal oxides can be considered. The former may be disregarded because of their prohibitive cost and insufficient long-term stability due to their volatility at high temperature. Some tests have been conducted using SnO_2 doped In_2O_3 which appeared to be a good candidate as a cathode material [61, 62]. No information however is available regarding long term electrode performance. Among the most promising metal oxides are the ABO_3 oxides with a perovskite-type structure, where A and B are rare earth (La, Pr) and transition (Fe, Ni, Co, Mn, Cr, Cu) metals, respectively [63–69]. When alkaline earth cations (mainly Sr^{2+}) are partially substituted for rare earth cations, the subsequent deficit charge is compensated by a valence change of transition metal ions, and under certain operating conditions, by the creation of oxygen vacancies [70–72]. Yamamoto et al. [73, 74] have published electrode polarization and electrical conductivity results obtained at 800 °C in open air using the perovskite-type oxides $La_{1-x}Sr_xMO_3$ (M = Cr, Mn, Fe, Co) sputtered on YSZ electrolyte. The lowest cathodic overpotential and the highest conductivity were obtained for the undoped $LaCoO_{3-\delta}$ electrode (see Figs. 14 and 15). However, the cathodic overpotential of all these perovskite-type oxides, though extremely low at 800 °C in air, increases with increasing annealing time of the cell at 1000 °C or higher. This decline in electrode performance is explained by the chemical reaction of YSZ and electrode materials

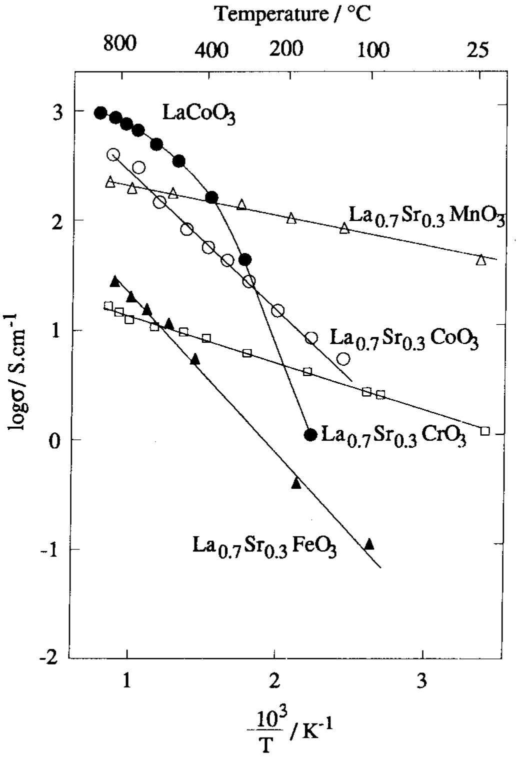

Fig. 14. Temperature dependence of electrical conductivity for sputtered films of perovskite-type solid solutions. From ref. [73].

at high temperature. X-ray diffraction revealed the formation of $La_2Zr_2O_7$ and/or Sr_2ZrO_4. This causes a serious problem for long-term performance of high temperature SOFCs. To avoid the reaction, it has been suggested that a film of stable oxide can be inserted between the YSZ and the perovskite electrode material [75]. The protective film has to be an oxide ion conductor and non-reactive with both YSZ and the cathode material. It was selected from among the perovskite-type oxide ion conductors to make a good match for the electrodes. The best results in terms of cathodic overpotential are obtained when a $La_{0.9}Ba_{0.1}AlO_{2.95}$ or $Nd_{0.9}Sr_{0.1}AlO_{2.95}$ film is inserted between YSZ and $LaCoO_3$, as shown in Fig. 16. The variation of the overpotential at 100 mA/cm^2 with the annealing period for the half cell $LaCoO_3/La_{0.9}Ba_{0.1}AlO_{2.95}/YSZ$ in air at 800 °C is shown in Fig. 17. The overpotential increases slightly with the annealing time and tends to a constant value. According to the authors, this behaviour may be attributed to the morphological change of the lanthanum cobaltite electrode.

Based on the selection criteria described above, the $La_{1-x}Sr_xMnO_3$ based cathodes seem up to now to be the best materials available. As a consequence, major research efforts have been devoted to this system. Thermal expansion studies have

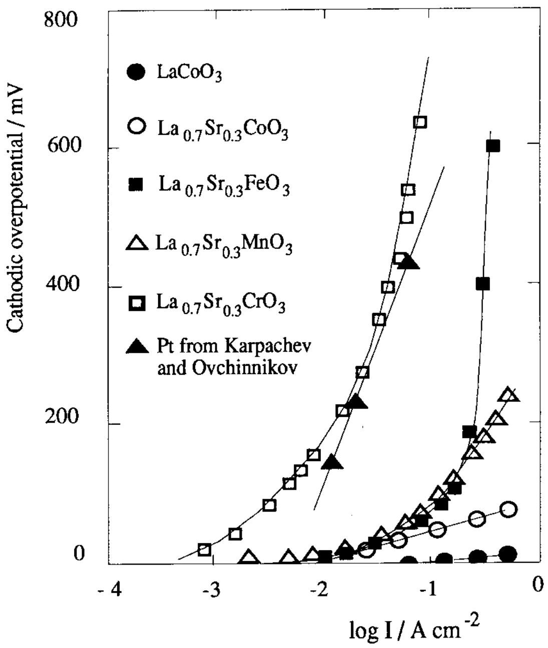

Fig. 15. Cathodic polarization for sputtered $La_{1-x}Sr_xMO_3$ films at 800 °C. From ref. [75]. Reprinted by permission of the American Ceramic Society.

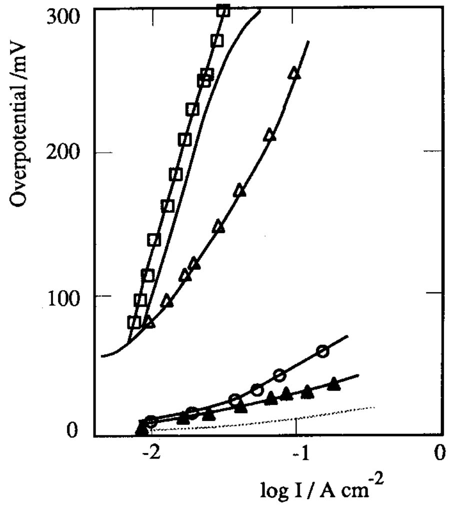

Fig. 16. Cathodic overpotential versus current density for the cells $LaCoO_3$/protector/YSZ and $LaCoO_3$/YSZ in air at 800 °C.
– – – $LaCoO_3$ annealed at 800 °C for 12 h, ——— $LaCoO_3$ annealed at 1000 °C for 12 h,
□ $LaCoO_3/CaTi_{0.7}Al_{0.3}O_{2.85}$/YSZ annealed at 1000 °C for 12 h, △ $LaCoO_3/La_{0.9}Sr_{0.1}InO_{2.95}$/YSZ annealed at 1000 °C for 12 h, ○ $LaCoO_3/Nd_{0.9}Sr_{0.1}AlO_{2.95}$/YSZ annealed at 1000 °C for 12 h,
▲ $LaCoO_3/La_{0.9}Ba_{0.1}AlO_{2.95}$/YSZ annealed at 1000 °C for 12 h.
From ref. [75]. Reprinted by permission of the American Ceramic Society.

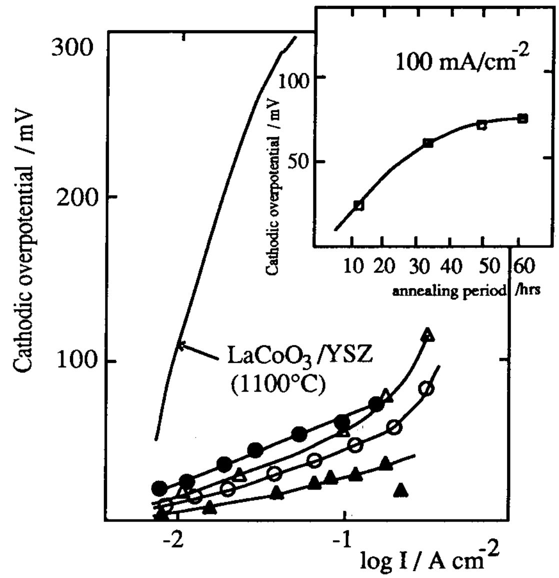

Fig. 17. Cathodic overpotential versus current density for different annealing periods at 1000 °C for the cell $LaCoO_3/La_{0.9}Ba_{0.1}AlO_{2.95}$/YSZ in air at 800 °C. The variation of overpotential at the current density of 100 mA/cm^2 with the preannealing period is also shown. ▲ 12 h, ○ 36 h, △ 48 h, ● 60 h. From ref. [75]. Reprinted by permission of the American Ceramic Society.

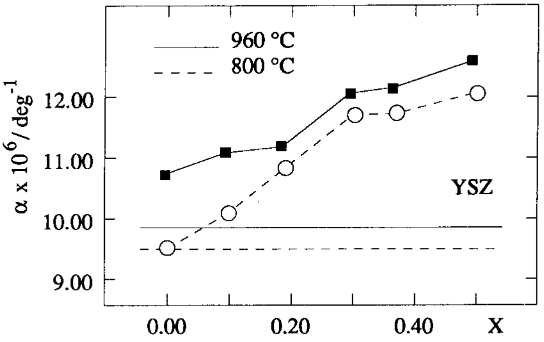

Fig. 18. Dopant content x dependence of thermal expansion coefficient of $La_{1-x}Sr_xMnO_3$ at 800 and 960 °C. From ref. [76].

shown a regular increase of the expansion coefficient as a function of strontium content for $x \leq 0.5$. This behaviour is illustrated in Fig. 18. Electrical studies carried out within the same composition range indicate also a regular increase of conductivity versus x. p-type semiconduction is observed for the low strontium content, up to x = 0.4 and a metallic-type conductivity is observed for x = 0.5. This composition exhibits the highest conductivity obtained for massive specimens prepared by co-sintering oxides and carbonates of the constitutive elements.

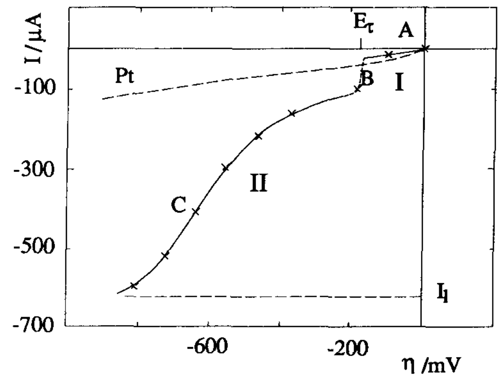

Fig. 19. Steady-state current-voltage characteristics of Pt and $La_{0.7}Sr_{0.3}MnO_3$ cathode in air at 960 °C. From ref. [76].

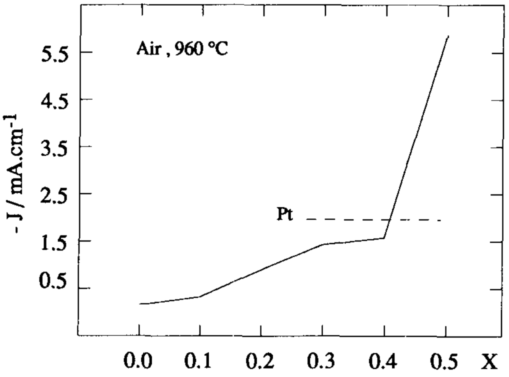

Fig. 20. Dependence of current density on $La_{1-x}Sr_xMnO_3$ cathode composition at −100 mV overpotential. From ref. [76].

The electrolytic activity of Sr-doped lanthanum manganites has been evaluated by Hammouche et al. [71, 76], using pinshaped electrodes. This kind of electrode was used to overcome difficulties in separating morphology effects from the effects of the electrode composition itself [77]. Previous studies on platinum electrodes [78] have shown that under high cathodic polarization the current reaches a limiting value which is commonly attributed to a limitation of the oxygen supply process to the electrode reaction zone. A typical example of a steady state current-potential curve obtained with $La_{1-x}Sr_xMnO_3$ under 10^{-3} atm is shown in Fig. 19. For comparison, the curve obtained with a Pt electrode of similar contact area, under the same experimental conditions, is also plotted in Fig. 19. The essential difference resides in the existence of two potential regions, noted I and II, for the manganite electrode. At a low cathodic potential (region I), the current-potential curve is similar to that of the platinum electrode. The catalytic activity for oxygen reduction is of the same

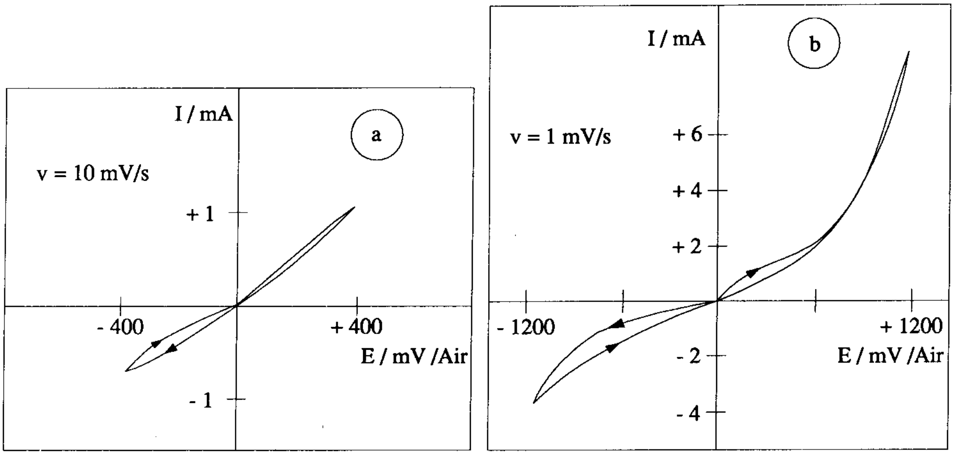

Fig. 21. Voltammograms obtained for two limited sweeping voltages for the $La_{0.6}Sr_{0.4}MnO_3$ electrode in air at 960 °C. (a) ±400 mV, (b) ±1200 mV. From ref. [76].

order of magnitude. In this potential range the electrode activity increases with the increase of the strontium content, as shown in Fig. 20. The best performance is obtained for x = 0.5 for which the manganite appears to be better than Pt.

At a high cathodic potential (region II), a sharp transition is observed at the potential referred to as E_T. The authors demonstrate that the sudden increase of the electrode kinetics could not be attributed to the sole electrochemical reduction of the electrode material, nor to the electrolyte reduction. They conclude that after the transition, the main electrode process is still an oxygen electrode reaction with a major change of mechanism, leading to the onset of an important electrocatalytic effect. This assertion is sustained by the analysis of:

- the voltammograms
- the transient responses of the electrode to a current or a potential step
- the reoxidation curve after a cathodic polarization
- the isothermal thermogravimetric curve
- the impedance diagrams.

a) Analysis of Voltammograms

Figure 21 shows the voltammogram obtained for the $La_{0.63}Sr_{0.37}MnO_3$ electrode in open air in the potential range ±400 mV with a scan rate of 10 mV/s and a starting potential equal to zero. As usually observed, a hysteresis loop is present and one observes the classical behavior of electrochemical systems. On the contrary, when the potential range is ± 1200 mV, the current is larger during the backwards scan and the hysteresis becomes increasingly important as the scan rate decreases. This is consistent with the fact that the current measured in steady-state conditions is systematically much higher than that observed on the voltammogram plotted under the same ex-

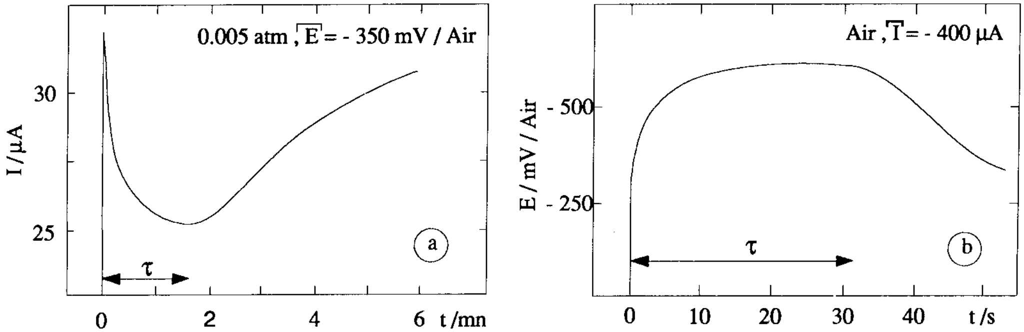

Fig. 22. Typical transient response of a $La_{0.9}Sr_{0.1}MnO_3$ electrode to: (a) a current step of 400 µA, (b) a potential step of 350 mV, located in region II. From ref. [76].

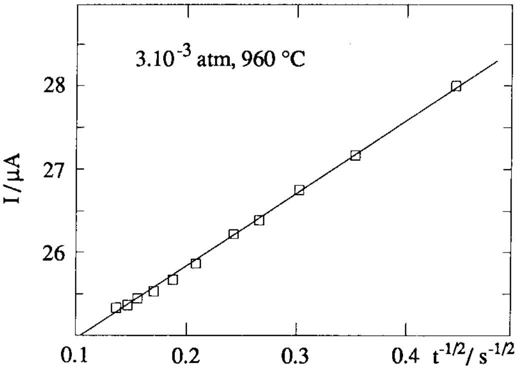

Fig. 23. Transient current versus $t^{-1/2}$ related to the data shown in Fig. 22a. From ref. [76].

perimental conditions. This behaviour indicates qualitatively that a slow modification of the electrode material is responsible for the enhancement of the reduction kinetics of oxygen. Such a behaviour has been observed within the whole investigated composition range, with a marked effect for $x = 0.5$.

b) Analysis of the Response of the Electrode to a Potential or a Current Step Corresponding to Region II

Typical curves are shown in Fig. 22a and b for current and potential steps respectively. For the short times ($t < \tau$) the electrode behaviour corresponds to the usual response observed when the rate determining step is due to a concentration polarization [78]. The variation of the transient current versus $\sqrt{t}$ is linear, described satisfactorily by the classical Cottrel-type relation (see Fig. 23). After a certain time which depends on the experimental conditions, mainly the oxygen partial pressure in the surrounding atmosphere, a "depolarization" effect is observed: the V(t) curve shows an overshoot while the I(t) curve shows a net enhancement of current.

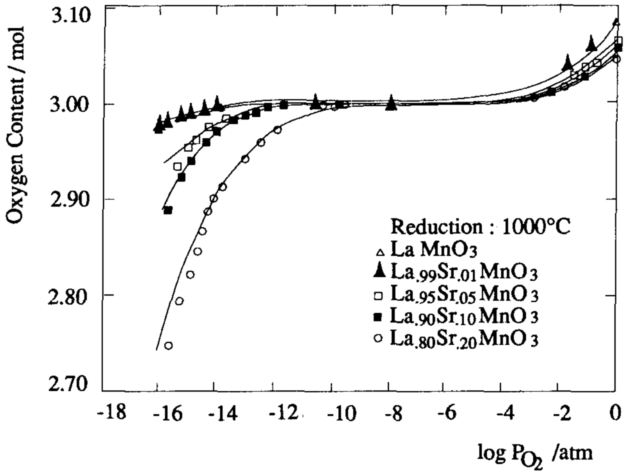

Fig. 24. Oxygen content in $La_{1-x}Sr_xMnO_3$ versus oxygen partial pressure at 1000 °C. From ref. [76, 79].

c) Analysis of the Thermogravimetric Results

Figure 24 shows the variation of the oxygen weight loss as a function of log P_{O_2} for various Sr dopant levels at 960 °C [79]. It mainly indicates that:

- little P_{O_2} dependence is observed at high oxygen partial pressure;
- the oxygen weight loss increases with the increase of the Sr dopant level. A similar behaviour has been observed by Caneiro [80]. The oxygen loss may be explained by the creation of oxygen vacancies leading to the enhancement of ionic conductivity in the perovskite material.

d) Analysis of Impedance Diagrams

This investigation has been made for the x = 0.3 composition at 960 °C. The steady state conditions (points A, B and C), where AC impedance measurements were performed are reported in Fig. 19. Impedance diagrams are plotted in Fig. 25. For small applied voltages, corresponding to region I, the impedance diagram is a capacitive semi-circle which increases as the cathodic polarization increases. Diagram A, obtained under equilibrium conditions, is characterized by a large capacitive effect and a resistive component varying with the oxygen partial pressure as $P_{O_2}^{1/2}$. This behaviour can be attributed to the dissociative adsorption process of oxygen at the triple contact point gas-electrode-electrolyte. Diagram B is plotted in the polarization region II when the current starts to increase significantly. It is particularly characterized by a large capacitive loop at low frequencies leading to a negative polarization

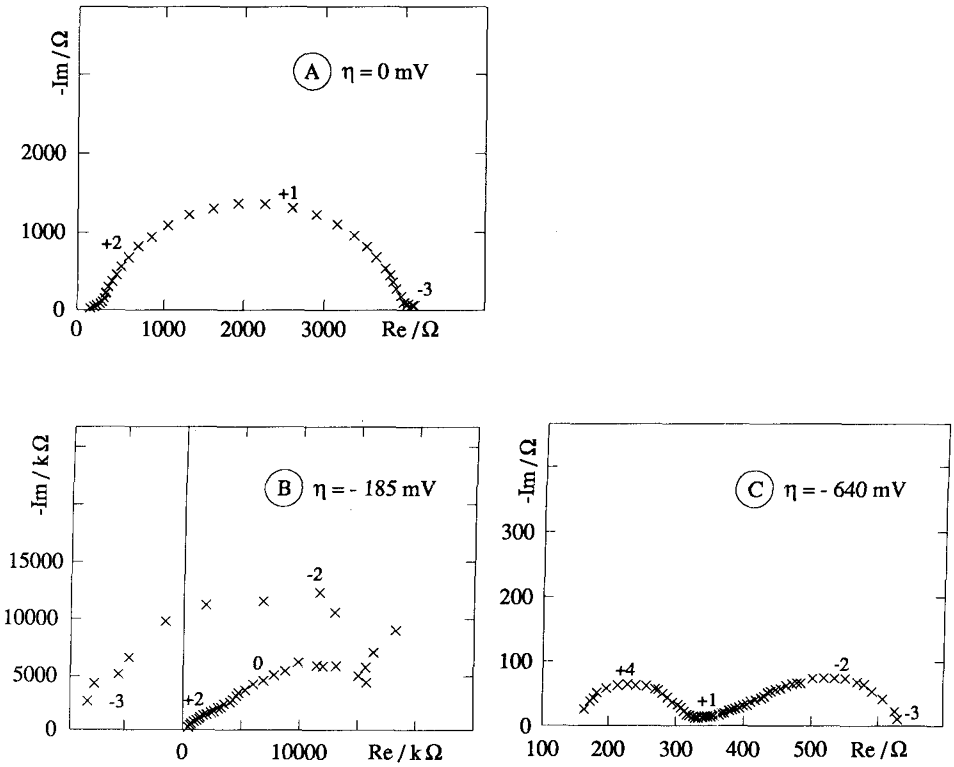

Fig. 25. Impedance diagrams of the electrode O_2, $La_{0.7}Sr_{0.3}MnO_3$/YSZ at 960 °C and $1.4 \cdot 10^{-3}$ atm. η indicates the cathodic polarization. From ref. [76].

resistance. According to this result, the slope of the polarization curve plotted in Fig. 19 should be negative at point B. The active-passive transition encountered in metals dissolution gives rise to similar impedance diagrams [81]. For the solid state cell studied here, this behaviour has been explained by the simultaneous increase of oxygen vacancy content in the manganite and a rapid decrease of its electrical conductivity [76]. Diagram C showing two capacitive loops describes the electrode behaviour at more cathodic overpotentials. The low frequency loop is very similar to that obtained when a diffusion process is involved. Its magnitude decreases as the electrode polarization increases but the top frequency remains constant. It was suggested that this loop could be attributed to the diffusion of oxygen vacancies through the electrode material which became a mixed anionic and electronic conductor at these overvoltages. Diffusion coefficients of oxygen were then estimated and compared in Table 1 to those of YSZ and pure $LaCoO_{3-\delta}$. The fact that the diffusion coefficient is slightly higher for YSZ is advantageous so that no oxide blocking effect can occur at the electrode-electrolyte interface. At high cathodic polarizations, one can observe a limiting value of the current density, proportional to $P_{O_2}^{1/2}$. This indicates that atomic oxygen species are involved in the rate-determining step of oxygen reduction.

Table 1. Oxygen coefficient diffusion in doped lanthanum manganite ($x = 0.3$) and yttria stabilized zirconia.

Oxide	$D_{800\,°C}$ ($cm^2\,s^{-1}$)	$D_{960\,°C}$ ($cm^2\,s^{-1}$)	Reference
$La_{0.7}Sr_{0.3}Mn_{3-\delta}$	–	$3.8\ 10^{-6}$	76
$La_{0.7}Sr_{0.3}MnO_{3-\delta}$	$1.04\ 10^{-6}$	–	36
$[ZrO_2]_{0.91}[Y_2O_3]_{0.09}$	–	$1.7\ 10^{-5}$	calculated[a]

[a] Using Nernst-Einstein relation.

According to all these considerations, the oxygen vacancy creation within the perovskite material at high cathodic polarization can be described by the following reaction

$$O^{x}_{O\,(ed)} + V^{\bullet\bullet}_{O\,(et)} + 2\,Mn^{\bullet}_{Mn\,(ed)} \rightleftharpoons V^{\bullet\bullet}_{O\,(ed)} + O^{x}_{O\,(ed)} + 2\,Mn^{x}_{Mn\,(et)} + 2\,h^{\bullet}$$

where "ed" and "et" refer to electrode and electrolyte respectively. One can simultaneously observe an oxide ion transfer from the electrode to the electrolyte and a reduction of an equivalent amount of manganese (IV) to manganese (III).

In conclusion, according to the experimental results provided by the different electrochemical methods and by thermogravimetry, Hammouche et al. [82] suggest the following mechanism for oxygen reduction on $La_{1-x}Sr_xMnO_{3-\delta}$ cathode:

- At low cathodic polarization ($E > E_\tau$), the reactions involved are:

$$\frac{1}{2}\,O_{2\,(g)} + s_{(ed)} \rightleftharpoons O_{ads\,(ed)}$$

$$O_{ads\,(ed)} + V^{\bullet\bullet}_{O\;(et)} \rightleftharpoons 2\,h^{\bullet}_{ed} + O^{x}_{O\,(et)} + s_{(ed)}$$

where s is referred to an active site on the electrode surface. The first step corresponds in fact to a rapid dissociation of oxygen molecule followed by a slow adsorption of atomic oxygen. The second step which characterizes electron transfer is assumed to be rapid [83]. The reduction takes place at the triple point contact.

- At high cathodic polarization ($E < E_\tau$), the electrochemical reaction can be described by the following sequence:

$$\frac{1}{2}\,O_{2\,(g)} + s_{(ed)} \rightleftharpoons O_{ads\,(ed)} \tag{1}$$

$$O_{ads\,(ed)} + V^{\bullet\bullet}_{O\;(ed)} \rightleftharpoons 2\,h^{\bullet}_{ed} + O^{x}_{O\,(ed)} + s_{(ed)} \tag{2}$$

$$O^{x}_{(ed)} \rightleftharpoons O^{x}_{int} \tag{3}$$

$$O^{x}_{int} + V^{\bullet\bullet}_{O\;(et)} \rightleftharpoons O^{x}_{O\,(et)} + V^{\bullet\bullet}_{O\;(ed)} \tag{4}$$

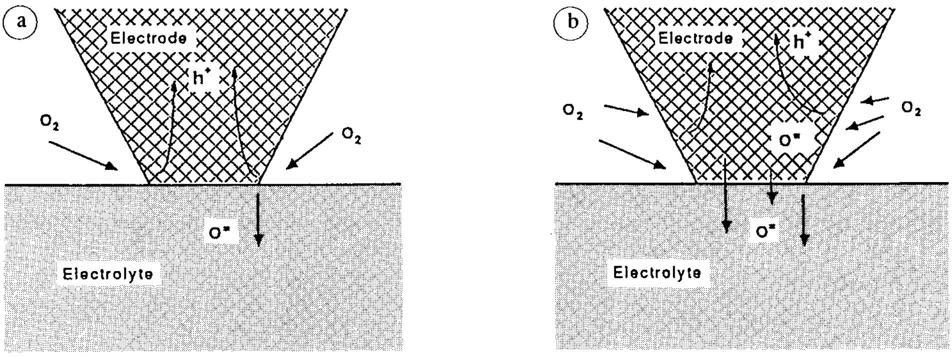

Fig. 26. Diagram of oxygen reduction in solid oxide electrolyte cell with: (a) a pure electronic conductor, (b) a mixed (electronic and ionic) conductor. From ref. [76].

where int refers to the interface manganite-zirconia. Reaction 3, corresponding to a diffusion process, is the limiting step at the vicinity of the transition potential E_τ. For the highest cathodic overpotentials, the limiting step reaction to be considered is the oxygen adsorption on the manganite. The complete results describing the electrochemical behaviour of $La_{1-x}Sr_xMnO_3$ are schematically drawn in Fig. 26.

3.2.2 Anode Materials

Anode materials must be essentially characterized by chemical stability for the reducing conditions imposed by the fuel containing atmosphere. Common metals can be used. Taking into consideration properties such as low volatility, thick porous layer feasibility and moderate cost, it appears that nickel and cobalt are the best candidates. Porous electrode layers, 30 to 100 μm thick, have been prepared by plasma spraying of fine metallic powder [84–86]. However, there is one obvious disadvantage in such a procedure in that both Ni and Co have thermal expansion coefficients substantially higher than that of yttria stabilized zirconia. Thus, they tend to detach from the electrolyte during thermal cycling and modify considerably the anodic polarization of the electrode. This can be partially overcome by sintering fine grained cobalt or nickel-yttria stabilised zirconia cermets on the electrolyte surface [87–89]. Adherence can be improved by roughening the electrolyte surface [84]. Dees et al. [89] have prepared several Ni/YSZ cermets starting from different ratios of NiO to zirconia to produce cermet samples ranging from 15 to 50% of Ni volume in the total solid. The NiO in the initial mixture is reduced to metallic Ni by heating the samples in a reducing atmosphere of H_2, H_2O and He at 1000 °C. A large increase in porosity is observed after reduction. Figure 27 shows the change in conductivity at 1000 °C with Ni volume percent for two zirconias which differ in origin and composition. Analysis of conductivity results reveals that Ni/YSZ cermets behave as electronic conductors at Ni contents higher than 30% in volume. Below this level, the conductivity falls to that of the oxide ion conducting zirconia. A jump in conductivity

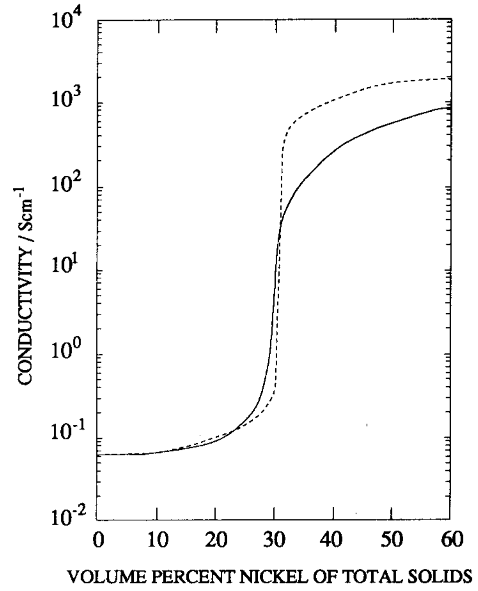

Fig. 27

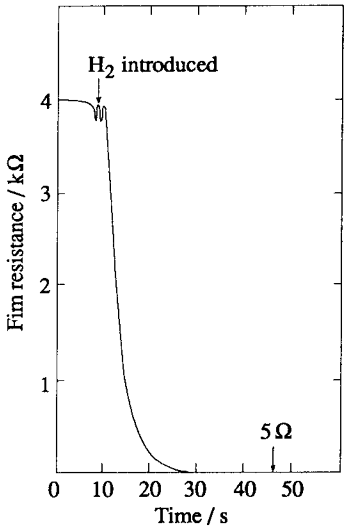

Fig. 28

Fig. 27. Conductivity of Ni-YSZ cermets versus Ni volume % at 1000 °C. From ref. [89]. Reprinted by permission of the publisher, The Electrochemical Society, Inc.

Fig. 28. Ni-YSZ cermet resistance versus time during hydrogen reduction at 850 °C. From ref. [90].

higher than three orders in magnitude is observed around this nickel to zirconia ratio. The fact that the conductivity cermet decreases with increasing temperature between 700 °C and 1000 °C clearly indicates that charge transport appears within the Ni metallic phase. Furthermore, an increase in conductivity by more than a factor of four with particle size of zirconia is observed. It is attributed to the improvement of Ni particle to particle contact. In a recent paper, Middelton et al. [90] have shown that the performance of the nickel-zirconia cermet anode is very much dependent on the microstructure. The investigated samples were prepared by casting a film of Ni/YSZ mixture on zirconia substrates. After sintering at 1150 °C for 2 hours, NiO was reduced in 10% H_2 in N_2, in the temperature range of 850–1000 °C. Metallographic observations revealed that the reduction of nickel oxide under the conditions previously described is not complete. Particles larger than 3 μm were found to retain NiO core. Despite this, the cermet is electronically conducting. Figure 28 shows the conductivity response of a sample initially maintained in an argon atmosphere. The conductivity increases from $8.3 \cdot 10^{-2}$ to $67\ \mathrm{S\,cm^{-1}}$ when hydrogen is introduced within the cell; this behaviour is reversible. Cyclic voltammetry measurements revealed that the cermet anode is oxidized at potentials more positive than −0.3 V at 850 °C, resulting in an increase of the cermet resistance. There is very little in the published literature about the current-voltage characteristics of H_2 oxidation on nickel electrodes, especially with cermets at high temperature.

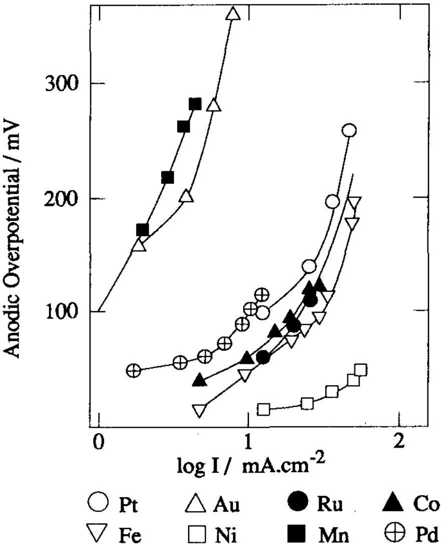

Fig. 29. Anodic polarization versus current density in metal-YSZ cell at 800 °C. Pt, Au, Ru, Co, Fe, Ni, Mn, Pd. From ref. [91].

Eguchi et al. [91] have investigated the behaviour of several metals (Ni, Fe, Co, Pt, etc.) as anodes when using yttria stabilized zirconia as the electrolyte and pure hydrogen at 1 atm. Anodic polarization curves and electrode resistances were measured by impedance spectroscopy. As shown in Fig. 29, Ni electrode exhibits the smallest anodic overpotential. One of the arguments which can explain the relatively good catalytic activity of nickel anode is the strong adsorption of hydrogen on nickel [92].

Another way to decrease the anodic overpotential is to intercalate a mixed conductor between the yttria stabilized zirconia electrolyte and the metallic anode. Such a combination enlarges the reaction area which theoretically lowers the anodic overpotential. Tedmon et al. [93] pointed out a significant decrease of polarization when ceria-based solid solutions like $(CeO_2)_{0.6}$ $(LaO_{1.5})_{0.4}$ are used as anode materials for SOFCs. This effect is generally attributed to the mixed conductivity resulting from the partial reduction of Ce^{4+} to Ce^{3+} in the reducing fuel atmosphere. A similar behaviour was observed in water vapor electrolysis at high temperature when the surface zirconia electrolyte is doped with ceria [94, 95].

One of the main objective of SOFCs in the future is the use of gaseous mixtures of $CO-H_2-H_2O$ produced by coal gasification plants or by steam reforming a hydrocarbon fuel, especially methane. Very little data is available about the direct oxidation of methane in SOFCs [96, 97]. Steele et al. [97] have recently confirmed the poor electrocatalytic activity of Pt electrodes for the anodic oxidation of methane at 800 °C. Although nickel fulfills major requirements for anode materials when H_2 and CO are employed as fuels, its use for the direct oxidation of methane encourages carbon deposition. To overcome this problem, alternative anode materials must be

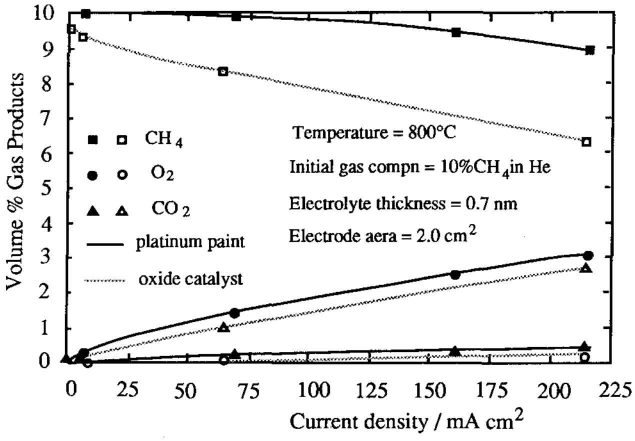

Fig. 30. Concentration (volume %) of CH_4, CO_2 and O_2 in exit gas as a function of current density for Pt and oxide anodes at 800 °C. From ref. [97].

found. It has been shown that oxides, initially used as automobile exhaust catalysts, were effective catalysts for the oxidation of methane. The results corresponding to one of these oxides used as anode are shown in Fig. 30. They clearly indicate more effective electrocatalysis than platinum. Furthermore, no carbon deposition has been detected even when the cell had been operated with 100% CH_4.

The operating conditions of SOFCs are quite appropriate for the in situ reforming of methane. The water produced at the anode gives rise to the reforming reaction:

$$CH_4 + H_2O \rightleftharpoons CO + 3H_2 \ .$$

This reaction is endothermic and therefore could introduce local thermal disturbances which can affect the operating conditions of the cell.

Finally, it is well known that sulfur and some sulfur containing compounds act as poisoning agents for electrode catalysts. The effect of sulfur on the Ni/YSZ anode resistance was examined by Dees et al. [98] by adding H_2S to an H_2-H_2O fuel mixture. Some increase of the interfacial resistance has been observed but, for concentrations as high as 100 ppm, the loss in the fuel cell performance was not devastating. However, this behaviour has to be confirmed by long term tests. In any case SOFCs exhibit a greater tolerance to sulfur than the other types of fuel cells. Desulfurization of fuel gas to less than 10 ppm is likely to be a requirement for operations at 1000 °C [99, 100].

3.3 Interconnection Materials

Interconnection materials are necessary to combine single cells to form multicell modules by connecting the anode material of one cell to the cathode material of the adjacent cell. They have to meet the following requirements at the operating conditions of SOFCs:

- high electronic conductivity ($>2\,\mathrm{S\,cm^{-1}}$) with small variation between 1 to 10^{-18} atm of oxygen partial pressure at 1000 °C,
- negligible ionic conductivity,
- chemical and phase stability in both air and fuel atmospheres up to 1000 °C,
- equivalent thermal expansion coefficient similar to that of the cathode and the anode materials,
- low volatility,
- mechanical strength,
- physical and electrochemical gas tightness,
- good adherence to the electrode materials,
- layer feasibility,
- moderate cost.

Considering all these stringent criteria, the most suitable materials are perovskite-type ceramics based on $LaCrO_3$. Pure $LaCrO_3$ is excluded for the following reasons:

- its conductivity is rather low, $1\,\mathrm{S\,cm^{-1}}$ at 1000 °C and 10^{-16} atm oxygen partial pressure,
- it exhibits a phase transition (orthorombic to rhombohedral) at about 240 °C,
- its thermal expansion coefficient is lower than that of yttria stabilized zirconia which is frequently considered as a reference.

A modification of the chemical composition by introducing adequate dopants provided some improvements. The most used dopants are alkaline earth cations (Mg^{2+}, Sr^{2+}) and isovalent cations as Al^{3+} and Mn^{3+}.

Anderson et al. [101, 102] have investigated $La_{0.95}Mg_{0.05}Cr_{1-x}Al_xO_3$. Their results can be summarized as follows:

- the electrical conductivity decreases substantially when Al is substituted for Cr, as shown in Fig. 31,
- the thermal expansion coefficient increases with Al content,
- the orthorhombic to rhombohedral transition is lowered to below room temperature when the Al content exceeds 20%.

More recently, Srilomsak et al. [103] have shown that the addition of 10% of SrO to $LaCrO_3$ is sufficient to shift the phase transition to below room temperature. Furthermore, their study indicates that the thermal expansion coefficient within Sr doped $LaCrO_3$ matches that of the electrolyte best for a composition close to 5% SrO. The most developed interconnection materials belong to the $LaCr_{1-x}Mg_xO_3$ system [104]. Exposed to a reducing atmosphere, one observes a decrease of conductivity probably because of the release of oxygen from the material and the variation of the Cr(IV)/Cr(III) ratio. Electrical conductivity values range between 2 and $0.7\,\mathrm{S\,cm^{-1}}$ in air and 10^{-18} atm oxygen partial pressure respectively. The thermal expansion of Mg-doped $LaCrO_3$ is about 13% lower than that of the electrolyte. Partial substitution of Sr or Ca can provide a better match.

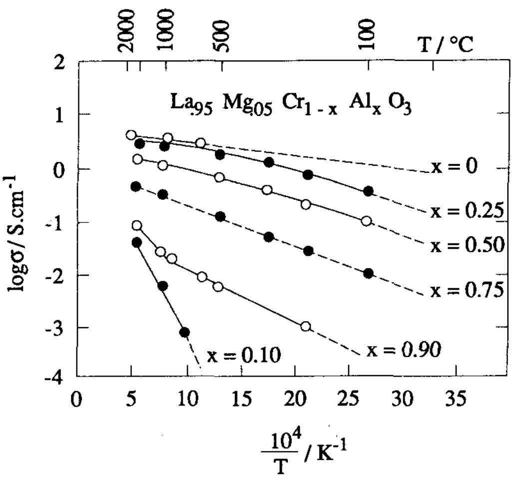

Fig. 31. Temperature dependence of electrical conductivity of $La_{0.95}Mg_{0.05}Cr_{1-x}Al_xO_3$. From ref. [102].

As interconnection materials must be gas tight under the operating conditions of SOFCs, particular attention is paid to sinterability and closed porosity. Generally, the near-full density of chromites is achieved in sintering oxide powders in highly reducing atmospheres at relatively high temperature (~ 1900 K). These conditions are not suitable for sintering the SOFCs as a unit because of the instability of Sr-doped $LaMnO_3$ cathode materials. Low densities and substantial open porosity are obtained for lanthanum chromites when these materials are sintered in air, even at temperatures above 1900 K. As pointed out by Chick et al. [105] from a fabrication stand point, lanthanum chromites and lanthanum manganites appear incompatible if the entire fuel cell components are to be sintered simultaneously as a unit. To resolve this dilemma, Chick et al. [105] proposed the development of Ca or Sr substituted $LaCrO_3$ powders that can be sintered in air to closed porosity at temperatures less than 1823 °K without sintering additives that are likely to diffuse into the adjacent anode and cathode materials. These authors have prepared the composition: $La_{0.82}Sr_{0.15}Cr_{0.85}Al_{0.15}O_3$ by the glycine/nitrate method. Layers up to about 100 µm thick sinter in air to near-full density with closed porosity after 16 hours at 1823 K (see Fig. 32). This composition is considered to be a promising candidate as an interconnection material, taking into account its relatively high conductivity and its thermal expansion coefficient which very closely matches that of the zirconia electrolyte.

Similar investigations have been carried out for the system $LaCr_{1-x}Mn_xO_3$ [106]. A significant improvement in sinterability appears when Mn is substituted for Cr. For example, densities above 95% of theoretical were achieved at 1475 °C in air for $La_{0.9}Sr_{0.1}Cr_{0.3}Mn_{0.7}O_3$. Electrical conductivity and Seebeck coefficient results are interpreted by a small polaron mechanism for all compositions. This is illustrated for conductivity in Fig. 33. It was also demonstrated that the carrier (electron hole) mobility rather than carrier concentration governs the electronic transport.

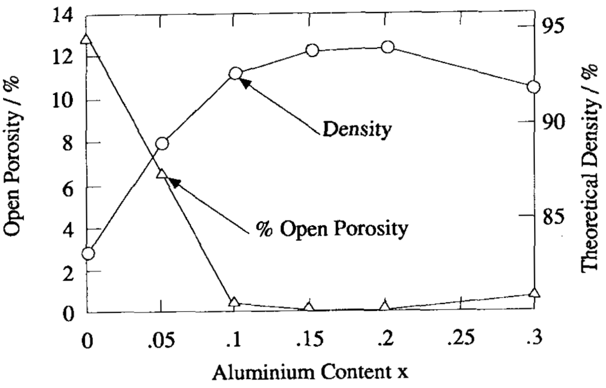

Fig. 32. Percent of open porosity and percent of theoretical density of air sintered samples versus alumina content in the system $La_{0.82}Sr_{0.15}Cr_{1-x}Al_xO_3$. From ref. [105]. This paper was originally presented at the Fall 1989 Meeting of The Electrochemical Society held in Hollywood, Florida.

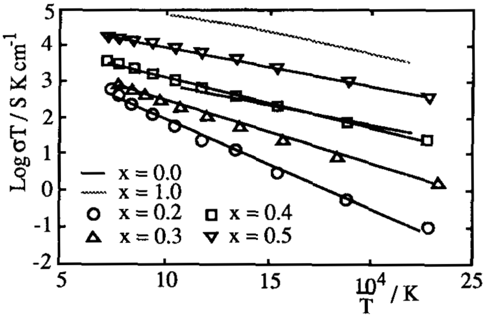

Fig. 33. Arrhenius plots of conductivity in the system $LaCr_{1-x}Mn_xO_3$. From ref. [106].

Several metal alloys have been suggested for use as interconnection materials in SOFCs. It was discovered that the Ni–Cr alloy Inconel could be used. Metal alloys generally satisfy to the required conditions for electrical conductivity and gas tightness. Furthermore, their use is advantageous with regards to their high thermal conductivity which could help to even out the cell temperature. However, the introduction of alloys creates serious problems in bonding them to ceramics and because of the mismatch of thermal expansion coefficients. Long duration tests are to be performed to evaluate their resistance to oxidation, carborization, nitriding and sulfurization. So far, no quantitative results are available to enable valid estimates of the potential use of metallic alloys in SOFCs.

4 Technology for SOFC Generators

4.1 Materials Selection

Although active research efforts are still being carried out to find new materials or to improve the existing ones, there is a general agreement on the use of the following components:

Electrolyte: $(ZrO_2)_{0.92}-(Y_2O_3)_{0.08}$

Cathode: $La_{1-x}Sr_xMnO_3$.

The exact dopant contents may change, depending on the fabrication process and cell configuration. Generally, cathodes with $x = 0.16$ are used and the porosity ranges from 30 to 40%.

Anode: $Ni/(ZrO_2)_{0.92}-(Y_2O_3)_{0.08}$ cermet

with a volume proportion close to 50%.

Interconnection material: M-doped $LaCrO_3$ with M = Mg, Sr.

Arrhenius plots of conductivity for the four components of the elementary cell are shown in Fig. 34. They indicate that electrolyte and interconnection materials are responsible of the main part of ohmic losses. Furthermore, both must be gas tight. Therefore, it is necessary to use them as thin and dense layers with a minimum of microcracks. It has to be said that in the literature not much attention has been paid to electrode overpotentials in evaluating polarization losses. These parameters greatly depend on composition, porosity and current density. Their study must be developed in parallel with the physical properties such as electrical conductivity, thermal expansion coefficient, density, atomic diffusion, etc.

4.2 Cell Design and Performances

4.2.1 Tubular Configuration

Historically, two approaches have been successively adopted in the different development programs for the fabrication of SOFC modules. The first approach involves a relatively thick electrolyte, the cell being arranged in a "bell and spigot" tubular configuration: this technology was adopted initially by Westinghouse and Brown Boveri [107]. The self supporting criterium dictates a minimum thickness of the electrolyte around 0.4 mm, to achieve the mechanical strength. The high thickness value leads to an important ohmic loss under typical operating conditions, estimated as 20% of overvoltage losses.

The second approach involves successive deposition of thick (typically 50–200 μm) layers of electrolyte, electrodes and interconnection materials on a

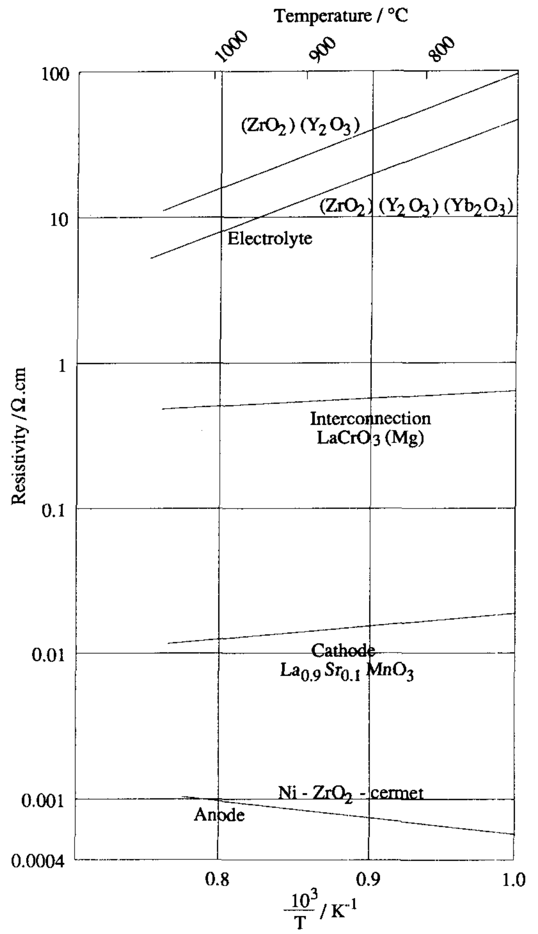

Fig. 34. Arrhenius plots of conductivity for the four main components in SOFCs. From ref. [132].

porous ceramic support [108]. This technology has been adopted by Westinghouse in USA and Electrotechnical Laboratory in Japan. Multicell modules with tubular support or plate-type support have been fabricated. The main weakness of this technology seems to result from the severe cracks due to the thermal expansion coefficient mismatch between interconnection and electrolyte materials. The need to improve either the interconnection material, the fabrication process or the cell design is clear. Over the last fifteen years, a major design change has been introduced by Westinghouse, allowing the fabrication of a simplified assembly suitable for mass production processes [109]. The structure is shown in Fig. 35, formed by a porous support tube of calcia stabilized zirconia, closed at one end. The outside diameter is about 1.5 cm and the length of about 30 cm. The support tube is overlaid with a 0.5 – 1 mm thick porous cathode of $La_{0.9}Sr_{0.1}MnO_3$. A gas-tight layer of yttria stabilized zirconia about 50 μm thick covers the cathode, except for a strip about

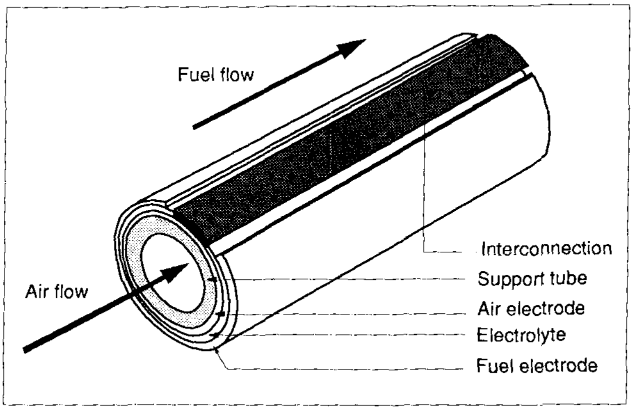

Fig. 35. Arrangement of a single SOFC with tubular design (Westinghouse). From ref. [99]. © 1988 IEEE.

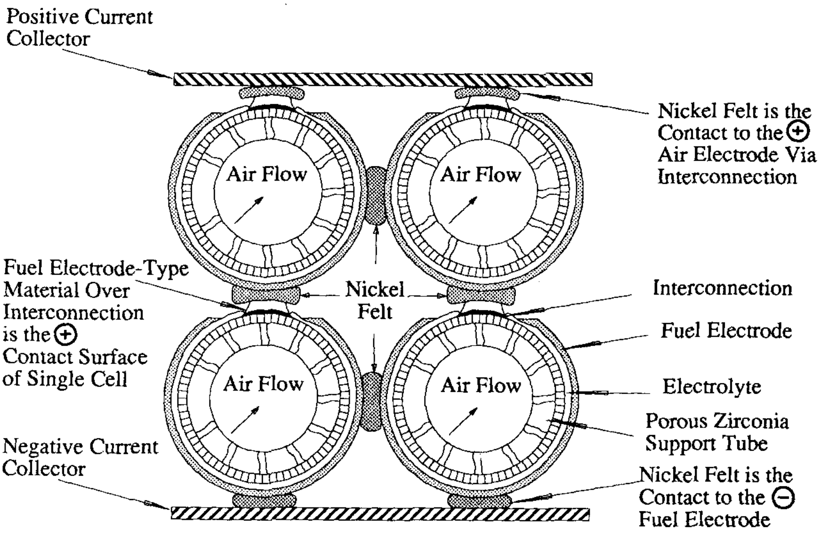

Fig. 36. Cross-section perpendicular to cell axes for a multicell SOFC assembly with tubular design (Westinghouse). From ref. [99]. © 1988 IEEE.

9 mm wide along the active cell length. This cathode strip is covered by a gas-tight layer about 30 μm thick of $La_{0.95}Mg_{0.05}CrO_3$, the interconnection material. The anode is formed by a Ni–YSZ cermet of about 60 weight% Ni, covering the whole electrolyte area, except a narrow zone near the interconnection material to avoid internal short-circuits. The projected surface area is approximately 110 cm^2. Series-parallel arrangements of these tubular single cells are made by connecting cells with ductil nickel felt pads. The latter are in permanent contact with the reducing fuel atmosphere. They are made of nickel fibers sinter-bonded to each other and to the

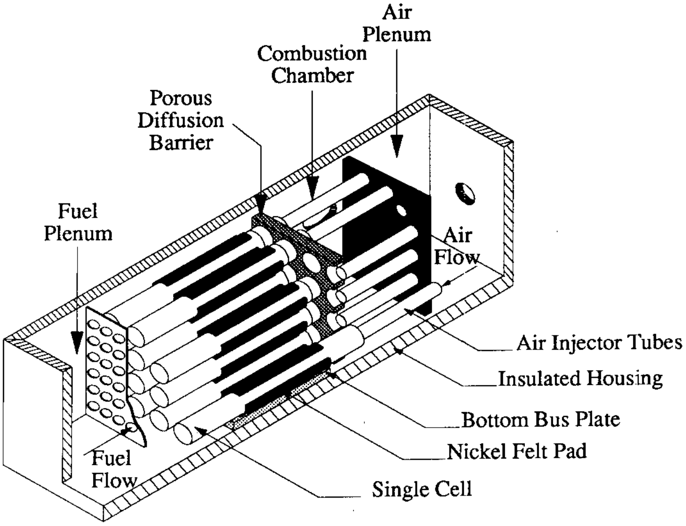

Fig. 37. Design of multicell SOFC assembly (Westinghouse). From ref. [100].

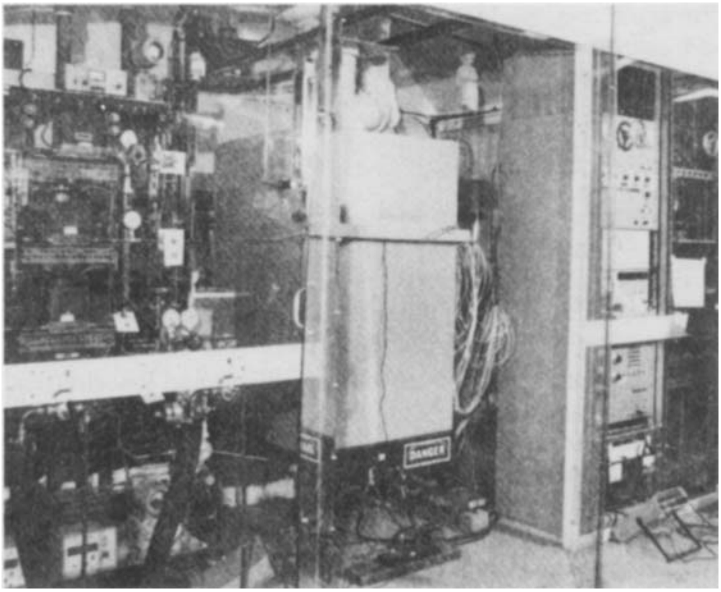

Fig. 38. Photograph of a 5 kW test loop (Westinghouse). From ref. [100].

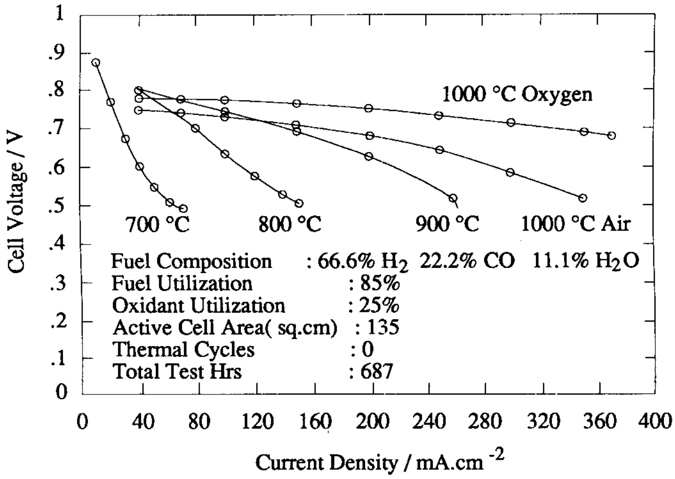

Fig. 39. Current-voltage characteristics of the state-of-the-art single cell SOFC. From ref. [99].

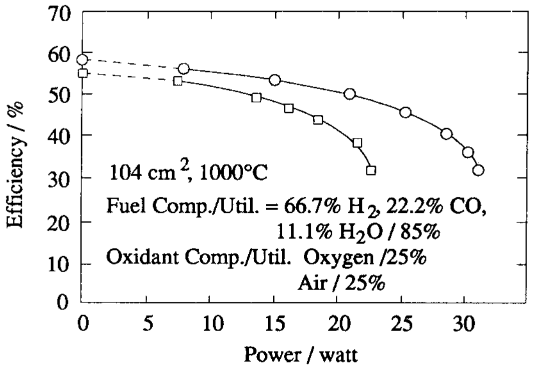

Fig. 40. Efficiency versus power of state-of-the-art SOFC. From ref. [99]. © 1988 IEEE.

nickel metal of the anode and provide a mechanically compliant and low electrical resistance connection between single cells. Bundling single SOFCs together is schematically shown in Fig. 36. In the adopted configuration, air and fuel flow in the same direction, air being injected by a tube inserted into the tubular fuel cell. This makes it easy to burn the depleted fuel gas by the oxygen-depleted air at the open end of tube. The design concept of a generator module is schematically illustrated in Fig. 37. A photograph of a 5 kW test generator built with 324 cells is shown in Fig. 38. Brown [100] has presented a complete set of results concerning single and multicell tubular state-of-the-art SOFCs. Figure 39 shows the current-voltage characteristics of a single cell working under the defined conditions shown. A power density of 0.16 W/cm^2 is obtained at 250 mA/cm^2 which is considered as the typical design point for use of this cell in a generator. Efficiency results for a different single cell are shown in Fig. 40. They mainly indicate the difference in perfor-

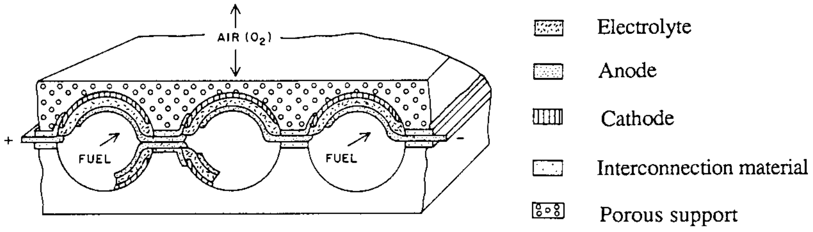

Fig. 41. Cross-section of thin film fuel cell batteries with plate type porous ceramic support. From ref. [110].

mance between air and oxygen, especially at high power values, and a rather low efficiency of about 31% at peak power.

4.2.2 The Self Sustaining Plate Design

The self sustaining plate design is shown in Fig. 41. Its concept is analogous to that of the tubular design, a porous support plate being substituted for the porous support tube [110]. Tubes with semi-circular cross-section extend along one plate axis. The same deposition techniques of the active components of SOFCs can also be used. The electrodes/electrolyte combination on each groove acts as a single fuel cell. Connecting these cells in series and combining two plates to form tubular-shaped twin cells lead to a block of two series-connected cell rows. No known performance data has been published for this configuration.

4.2.3 Monolithic Concepts

The active surface to volume ratio of the tubular arrangements previously described is approximately 1 cm^2/1 cm^3. This parameter could be increased with corresponding increases in both volume power density and area power density. New concepts for solid state electrochemical reactors have been proposed based on more or less planar cell structures which can be integrated to make blocks.

a) Monolithic Modules Design

The concept of monolithic module design is associated with Argonne National Laboratories [111, 112]. Power density of about 8 kW/kg or 4 kW/l and fuel efficiency over 50% are expected to be achieved with monolithic SOFCs. The monolithic structure started with a co-flow version where the cell consists of a honeycomb-like array of adjacent fuel and oxidant channels that look like corrugated paperboard, as shown in Fig. 42. Multilayer laminates of the active cell components (anode-electrolyte-cathode) are appropriately corrugated and stacked alternatively between flat multilayer laminates in the following sequence: anode- interconnection material-cathode. Tape casting [111] and hot-roll calendering [113, 114] are used to fabricate the monolithic structure. A cross-flow version where oxidant and fuel channels are

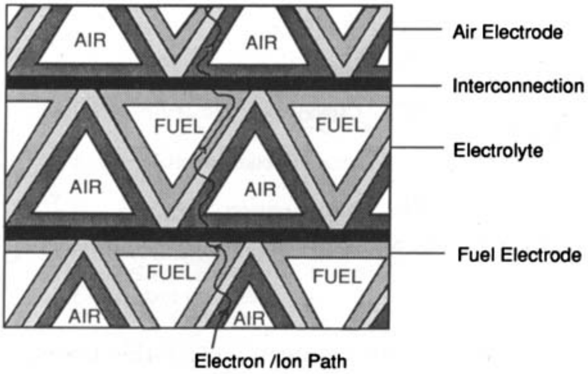

Fig. 42. Coflow monolithic SOFC. From ref. [114].

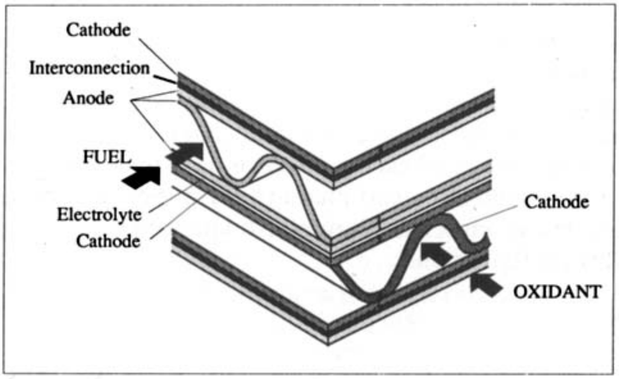

Fig. 43. Crossflow monolithic SOFC. From ref. [114]. This paper was originally presented at the Fall 1989 Meeting of The Electrochemical Society held in Hollywood, Florida.

formed from corrugated anode and cathode layers respectively is represented in Fig. 43. It can be seen that the two laminated structures previously described for the co-flow version are flat and stacked alternatively between the corrugated anode and cathode layers. Green components are co-fired at temperatures of about 1300–1400 °C to sinter the materials and create permanent bonds at the contact points. Figure 44 shows that current densities of 1 A/cm^2 can be achieved with single cells operating at 1000 °C using H_2 as fuel and air as oxidant at a cell potential of about 0.6 V. The percentage of fuel utilization was not reported for this remarkable performance. A 600 hour test on an early four cell stack at about 0.5 V and 50 mA/cm^2 has also been reported [100]. Although satisfactory improvements have been observed for multicell stacks, as can be seen in Fig. 45, their performance remains significantly lower than that of a single cell. According to Myles and McPheeters [115], this is mainly due to interactions among the material during the co-sintering process. The sintering aids introduced to assist densification of the inter-

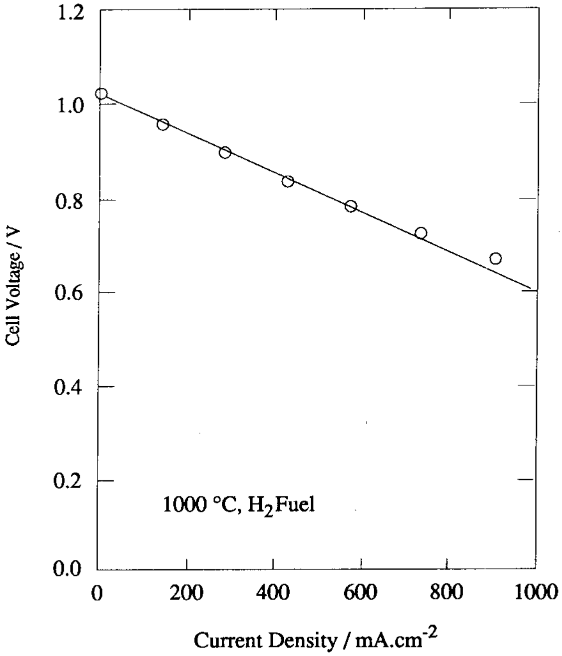

Fig. 44. Current-voltage characteristics of monolithic SOFC at 1000 °C using pure hydrogen. From ref. [100].

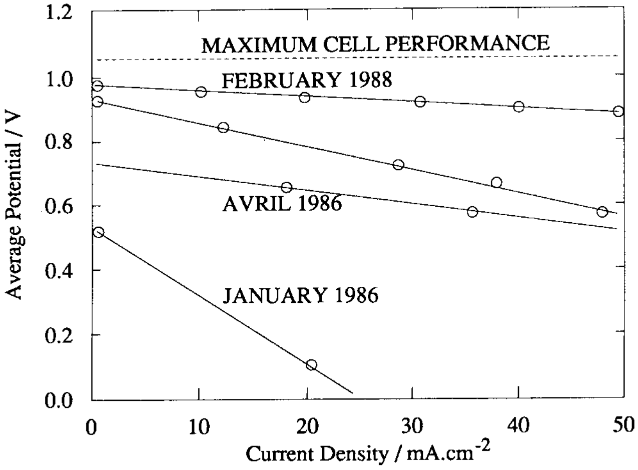

Fig. 45. Improvement in multicell monolithic SOFC. From ref. [115].

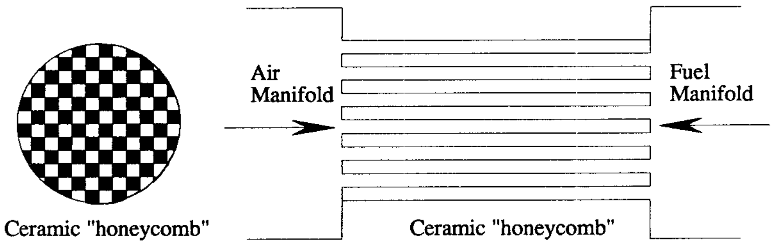

Fig. 46. "Honeycomb" design for SOFCs. From ref. [132].

connection material migrate throughout the monolithic structure and affect the other materials, particularly the cathode. The performance of monolithic SOFCs needs to be greatly improved to compete with tubular ones.

b) Honeycomb Design

The fact that yttria stabilized zirconia can be fabricated into flow-through honeycomb catalyst support, e.g. in automobile exhaust emission control systems, has led Steele [116] to suggest that SOFC systems could use this configuration. A slight modification must be introduced so that adjoining channels are accessible only from opposite ends, as shown in Fig. 46. The oxidant channels are lined with porous cathode materials, fuel channels with porous anode material. The thin and impermeable wall of the solid electrolyte functions as both a structural and active component of the fuel cell. An active surface area to volume ratio as high as $10\,cm^2/cm^3$ can be achieved with the honeycomb configuration. Calculations made with a single cell $3\,cm \times 20\,cm$ with 240 channels 0.5×0.5 cm each, a wall thickness of 300 µm and a channel depth of 1.15 cm result in an active area of $480\,cm^2$. Assuming a moderate current density of $200\,ma/cm^2$, the current amounts to 96 A. Although the honeycomb configuration looks very attractive, severe technological problems make it difficult to produce massively for SOFCs. Among the most critical are the deposition of the electrode material, the thermal management of the cell in operation and the manifold system to feed the gases to the end of each relevant channel.

4.2.4 The Bipolar Plate Design

The bipolar plate design is illustrated in Fig. 47. It consists of a cross-flow arrangement where the gas-tight separation is achieved by dense ceramic or metallic plates with grooves for air and fuel supply to the appropriate electrodes. A porous cathode, a dense and thin electrolyte and a porous anode form a composite flat layer placed at the top of the interconnected grooves. The deposition of the porous electrodes can be achieved by mass production methods. Moreover, the bipolar plate configuration technology makes it possible to check for defaults, independently and prior to assembly of the interconnection plate and the anode-electrolyte-cathode structure.

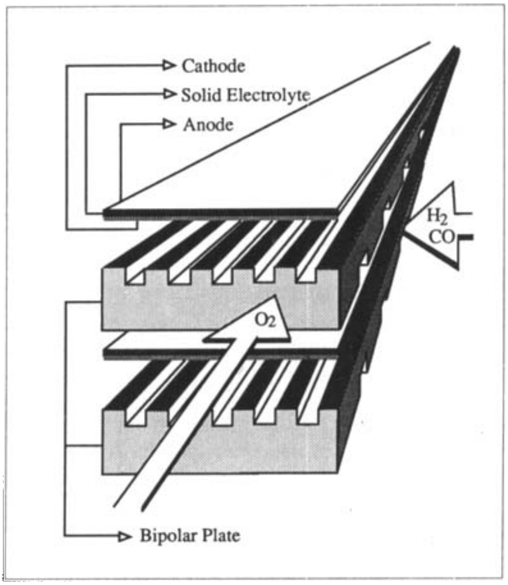

Fig. 47. Bipolar plate design of SOFC. From ref. [132].

However, these advantages may be offset by the use of high temperature seals and the fact that the components will be subject to more stress. Besides mechanical stress due to seals, thermal stresses may appear because of temperature gradients and cycling. Few results related to the performance of this type of SOFCs have been published. An area power density of 0.12 W/cm^2 has been reported without any specification of oxidant and fuel composition and utilization [117].

4.3 Manufacturing Processes

Gas-phase or wet-type processes are usually adopted for the manufacturing of the layers. The gas phase route includes:

- chemical vapour deposition (CVD) and electrochemical vapour deposition (EVD) [118–122],
- plasma spraying [110],
- laser evaporation [123],
- radio frequency sputtering [124],
- electron beam evaporation [125].

4.3.1 The CVD-EVD Technique

The CVD-EVD technique was introduced and developed by Westinghouse, after its conception in 1970 by Isenberg [126]. It has demonstrated the ability to reproducibly

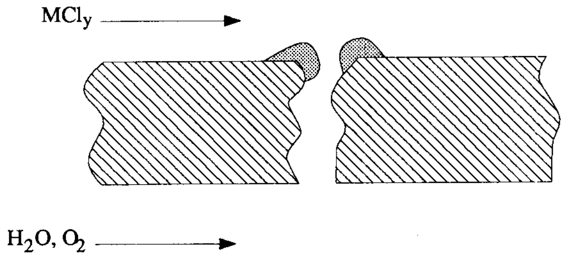

ⓐ CVD Step : Pore Closure

$$2\,MCl_y + y\,H_2O \longrightarrow 2\,MO_{y/2} + 2\,y\,HCl$$
$$4\,MCl_y + y\,O_2 \longrightarrow 4\,MO_{/2} + 2\,y\,Cl_2$$

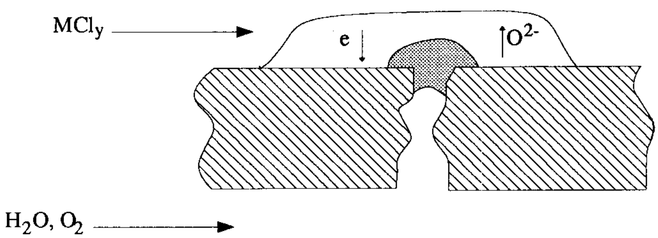

ⓑ EVD Step : Film Growth

$$MCl_y + y/2\,O^{2-} \longrightarrow MO_{y/2} + y/2\,Cl_2 + y\,e$$
$$H_2O + 2\,e \longrightarrow O^{2-} + H_2$$

Fig. 48. Principle of electrochemical vapour deposition. From ref. [121].

deposit relatively thin films of numerous solid electrolytes and interconnection materials on porous supports. This technique will be described here with some details of the manufacturing of gas-tight layers of YSZ in the tubular cell. Its principle is described in Fig. 48. The first stage of this technique is a conventional CVD reaction. To deposit electrolyte films, $ZrCl_4$ and YCl_3 are volatilized in a predetermined ratio and passed over the outer surface of the porous air electrode which covers the calcia stabilized zirconia support tube. The oxygen partial pressure in the gas mixture is about 10^{-18} atm. A stream of water vapour, containing in some cases oxygen at a partial pressure of about 10^{-4} atm, is passed inside the support tube. Molecular diffusion through the porous support tube and air cathode material gives rise to the following reactions:

$$2MCl_y + yH_2O \rightleftharpoons 2MO_{y/2} + 2yHCl$$
$$4MCl_y + yO_2 \rightleftharpoons 4MO_{y/2} + 2yCl_2$$

where M is a metallic cation (M = Zr, Y) and y the valency associated with M.

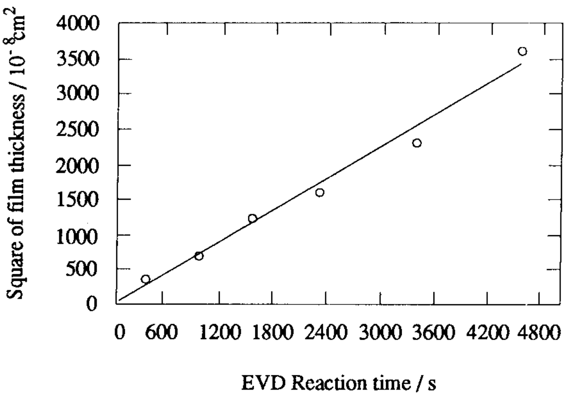

Fig. 49. Square of electrolyte film thickness versus deposition time at 1475 K. From ref. [121]. This paper was originally presented at the Fall 1989 Meeting of The Electrochemical Society held in Hollywood, Florida.

Yttria stabilized zirconia formed by this reaction fills the air electrode pores. The dynamics of this CVD stage has been modeled by Carolan and Michaels [120], who observed that films produced in this manner penetrate the substrate no more than 2–3 pore diameters from the chloride face of the substrate. It has also been shown that the penetration depth is independent of water concentration. The second step of this method is the EVD step. Once pore closure is achieved, the reactants are not longer in contact. Electrochemical semipermeability related to the existence of small electronic conductivity and large gradient of oxygen partial pressure leads to oxygen transport from the steam side to the chloride side through the deposited electrolyte. The electrochemical reactions involved are:

$$MCl_y + y/2\,O^{2-} \rightleftharpoons MO_{y/2} + y/2\,Cl_2 + ye$$

at the chloride side and

$$H_2O + 2e \rightleftharpoons O^{2-} + H_2$$
$$1/2\,O_2 + 2e \rightleftharpoons O^{2-}$$

at the steam side.

Kinetic studies of EVD [121] indicate that the electrolyte layer growth is parabolic with time, as shown in Fig. 49, and the diffusion of both electrons and holes is the limiting step of such electrochemical reactions [122]. The CVD-EVD technique produces fine-grained films of electrolyte with 40–50 μm thickness.

4.3.2 Wet-type Method for Layer Fabrication

In this process, the component powders are first prepared by conventional powder processing, such as co-precipitation, sol-gel, spray-drying and freeze-drying. Binders, plasticizers and organic solvents are introduced to form the green sheet. Numerous processes have been developed for green sheet manufacturing, including extrusion moulding, doctor blade method and calendering technique. The wet-type method has been mainly adopted for the monolithic SOFC structure [115]. The main challenge in manufacturing such structures is to match the sintering shrinkages of the four components: the cathode material, strontium-doped lanthanum manganite, the electrolyte, yttria stabilized zirconia, the anode material, nickel-zirconia cermet and the interconnection material, strontium-doped lanthanum chromite. Shrinkages occur during organic additive burnout around 500 °C and sintering around 1400 °C. It seems that the matching of shrinkages has been accomplished satisfactorily for the monolithic structure [127], resulting in a significant decrease in cracks and cross-leakage.

5 Long Term Behaviour

Working life is an essential criterion for materials selection and cell design for SOFCs. Economic studies based on electricity cost fix a minimum working life at 30000 hours. According to Rohr [107], a period of five to ten years is required for an economically feasible SOFC generator. When working at high temperature, SOFC components are subjected to aging effects. This gradually leads to an increase in resistivity due to the formation of superstructures within the electrolyte and the precipitation of new phases, mainly at grain boundary regions. The interface reactions between the cell components are affected by cation interdiffusion leading to the formation of intermediate new phases whose physical and electrochemical properties are still unknown. Figure 50 shows the performance stability of a tubular-design cell working at 950 °C with 250 mA/cm^2 and 85% H_2 fuel and 25% air consumption

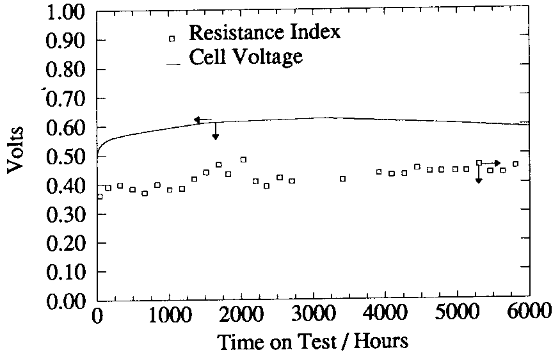

Fig. 50. SOFC voltage versus time at 950 °C, 250 mA/cm^2, 85% fuel utilization and 25% air utilization. From ref. [128]. This paper was originally presented at the Fall 1989 Meeting of The Electrochemical Society held in Hollywood, Florida.

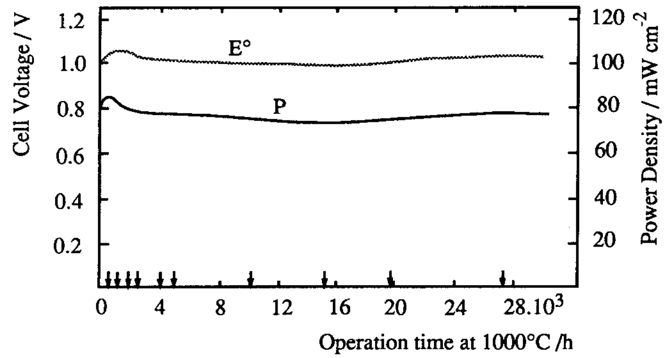

Fig. 51. Life test of the Ni/YSZ/LaNiO$_3$ cell at 1000 °C and 120 mA/cm^2. Fuel/oxidant: H_2(H_2O at 25 °C)/air. ↓ cycling between 1000 °C and room temperature. From ref. [107].

[128]. A constant value of the cell voltage is observed over 6000 hours. Life tests with self-sustaining type cells have shown that open-circuit voltage and power density remain practically constant over a period of more than three years. This is illustrated in Fig. 51. Several cyclings between 1000 °C and room temperature did not affect the performance [107]. On the basis of these results, one may conclude that the tubular concept fulfills the life time requirement quite well.

6 Conclusion

After thirty years of basic research, it was demonstrated that SOFCs potentially have many significant advantages over traditional generators of electricity and other types of fuel cells. These advantages are essentially related to the high operating temperature and to the solid state of the cell components, mainly the electrolyte. They can be summarized as follows:

- high efficiency can be achieved even at reduced loads, in small as well as large units,
- the use of expensive catalysts such as platinum and ruthenium is not necessary,
- the high quality of exhaust heat at relatively high temperatures (600 – 1000 °C), after burning the depleted fuel gas, increases the overall efficiency,
- there are no constraints on carbon monoxide in the fuel,
- electrolyte loss maintenance as well as electrode corrosion are eliminated,
- tolerance to impurities like sulfur in fuel increases the cell's life time and reduces the fuel clean-up cost.

In addition to these characteristics, SOFCs can operate as water vapor electrolysers to produce hydrogen of high quality. Finally, the technology developed for SOFC systems can be applied to the co-generation of electricity and chemicals with high efficiency [129, 130].

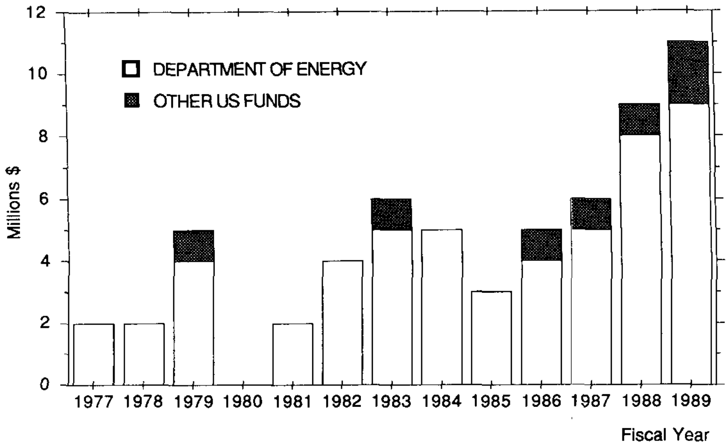

Fig. 52. US R & D expenditures on SOFCs. From ref. [131].

In spite of all these attractive features, improvements must be made in both components and technology. Cathode, electrolyte and interconnection materials which are responsible of the major part of the voltage losses must be improved in terms of electrical conductivity and electrode polarization. Thermal shock resistance and fracture toughness must be increased to reduce cracks which appear during fabrication and thermal cycling, particularly in monolithic designs. Long time tests, for periods exceeding 40000 hours, are to be performed under practical operating conditions to evaluate more precisely the deleterious effect of cation interdiffusion between adjacent components.

Considering that an SOFC is basically a ceramic assembly, one may be optimistic, taking into account the recent developments in ceramic technology. For example, the deposition techniques of thick, thin or multilayers that have been developed in microelectronics technology can be applied. The development of structural ceramics and the recent discovery of high temperature oxide superconductors promises rapid progress in preparing and manufacturing ceramic oxides.

The financial support provided to fuel cell development over the last three years in the USA is shown in Fig. 52 [131]. It indicates that one may be optimistic for the future of SOFCs with regard to their technical aspects. Performance and cost of the modules developed by Westinghouse make it possible to evaluate accurately the real cost of the electricity supplied by this type of generator. It is now time to find commercial markets for them. A definitive answer to this question will very likely be given in the mid 1990s and will determine the commercialization of SOFCs.

Acknowledgements. The author gratefully acknowledges all the scientific edition institutions (Academic Press, American Ceramic Society, Electrochemical Society, Elsevier Sequoia, IEEE Service Center, Office for Official Publications of the European Communities, Pergamon Press, Technip Editions, World Scientific Publishing Co.) and all the authors who granted him the permission to reproduce in this article some of their published figures.

7 References

1. E. Bauer, H.Z. Preis, Z. Elektrochem. 43, 727–732 (1937).
2. C. Wagner, Naturwiss. 22/24, 265–268 (1943).
3. H.S. Isaacs, in: Science and Technology of Zirconia. Advances in Ceramics: A.H. Heuer, L.W. Hobbs (eds.). The American Ceramic Society, Inc., Colombus, Ohio, Vol. 3, 406–418 (1981).
4. C.J. Warde, R.J. Ruka, A.O. Isenberg, in: Fuel Cells for Public Utility and Industrial Power: R. Noyes (eds.). Noyes Data Corporation, 67–98 (1977).
5. M. Warshay, Workshop on High Temperature Fuel Cells: H.S. Isaacs, S. Srinivasan, I.L. Hary, Brookhaven National Laboratory, Upton, New York, 90–94 (1978).
6. J. Weissbart, R. Ruka, in: Fuel Cells, G.J. Young (ed.). Reinhold Publishing Corporation, New York (1963), Vol. 2, pp. 37–49.
7. C. Wagner, Z. Phys. Chem. 21B, 25–41 (1933).
8. J. Besson, C. Deportes, M. Kleitz, in: les Piles à Combustible, Technip (ed.). Paris, 88–102 (1965).
9. D.H. Archer, E.F. Sverdrup, 16th Annual Proceedings Power Sources Conference, 34–36 (1962).
10. H. Binder, A. Kohling, H. Krupp, K. Richter, G. Sandstede, Electrochimica Acta 8, 781–793 (1963).
11. D.H. Archer, R.L. Zahradnik, E.F. Svedrup, W.A. English, I. Elikan, J.J. Alles, in: Proceedings of the 18th Annual Proceedings Power Sources Conference. PSC Publication Committee, Red Bank, New York, pp. 36–40 (1964).
12. D.H. Archer, E.F. Sverdrup, R.L. Zahradnik, Chem. Eng. Prog. 60, 64–68 (1964).
13. T. Takahashi, in: Physics of Electrolytes, J. Hladik (ed.). Academic Press, London (1972), Vol. 2, pp. 989–1049.
14. D.K. Hohnke, in: Fast Ione Transport in Solids, Electrodes and Electrolytes, P. Vashista, J.N. Mundy, G.K. Shenoy (eds.). Elsevier North Holland, Inc., New York, N.Y., pp. 669–672.
15. W. Baukal, Electrochimica Acta 14, 1071–1080 (1969).
16. E.J.L. Schouler, Thesis, Grenoble University (1979).
17. M.V. Inozemtsev, M.V. Perfil'ev, V.P. Gorelov, Electrokhimiya 12, 1231–1235 (1976).
18. H. Bernard, Thesis, Grenoble University (1980).
19. V.S. Stubican, in: Science and Technology of Zirconia, Advances in Ceramics: S. Somiya, N. Yamamoto, H. Yanagida (eds.). The American Ceramic Society, Inc., Westerville, Ohio (1986), Vol. 24B, pp. 71–81.
20. U.C. Subbarao, in: Science and Technology of Zirconia, Advances in Ceramics: N. Clausen, M. Ruhle, A. Heuer (eds.). The American Ceramic Society, Inc., Colombus, Ohio (1984), Vol. 12, pp. 1–24.
21. P.F. Becher, G. Begun, P.D. Funkenbusch, in: Science and Technology of Zirconia, Advances in Ceramics: S. Somiya, N. Yamamoto, H. Yanagida (eds.). The American Ceramic Society, Inc., Westerville, Ohio, Vol. 24B, pp. 645–651 (1986).
22. E.P. Butler, R.K. Slowinski, N. Nonanos, J. Drennan, B.C.H. Steele, in: Science and Technology of Zirconia, Advances in Ceramics: N. Clausen, M. Ruhle, A. Herrer (eds.). The American Ceramic Society, Inc., Colombus, Ohio, Vol. 12, pp. 572–584 (1984).
23. A. El Barhmi, E.J.L. Schouler, A. Hammou, M. Kleitz, in: Science and Technology of Zirconia, Advances in Ceramics: S. Somiya, N. Yamamoto, H. Yanagida (eds.). The Ameican Ceramic Society, Inc., Westerville, Ohio, Vol. 24B, pp. 885–894 (1986).
24. F. Ishizaki, T. Yoshida, S. Sakurada, in: Proceedings of the First International Symposium of Solid Oxide Fuel Cells, S.C. Singhal (ed.). The Electrochemical Society, Inc., Pennington, New Jersey (1989), Vol. 89–11, pp. 3–14.
25. T. Van Dijk, K.J. De Vries, A.J. Burggraaf, Phys. Stat. Sol. (b) 101, 765–774 (1980).

26. T. Van Dijk, K.J. De Vries, A.J. Burggraaf, Phys. Stat. Sol. (a) 58, 115–125 (1980).
27. T. Fournier, J.Y. Nots, J. Muller, J.C. Joubert, Solid State Ionics 15, 71–74 (1985).
28. P.K. Moon, H.L. Tuller, Solid State Ionics 28–30, 470–474 (1988).
29. P.K. Moon, H.L. Tuller, in: Proceedings of the First International Symposium of Solid Oxide Fuel Cells, S.C. Singhal (ed.). The Electrochemical Society, Inc., Pennington, New Jersey, Vol. 89–11, pp. 30–40 (1989).
30. H.L. Tuller, A.S. Nowick, J. Electrochem. Soc. 122, 255–259 (1975).
31. K. El Adham, A. Hammou, J. Chim. Phys. 79, 633–639 (1982).
32. R.V. Coates, J. Appl. Chem. 14, 346–350 (1964).
33. L. Brixner, J. Am. Chem. Soc. 80, 3214–3215 (1958).
34. F. Forrat, G. Dauge, P. Trévoux, G. Danner, M. Christen, C. R. Acad Sci. 259, 2813–2816 (1964).
35. F.K. Patterson, C.W. Moeller, R. Ward, Inorg. Chem. 2, 196–198 (1963).
36. T. Takahashi, H. Iwahara, in: Research in Effective Use of Energy, sp. publ. of the Ministry of Education Science and Culture of Japan, Vol. 3, pp. 727–734 (1982).
37. B.C.H. Steele, B.E. Powell, P.M.R. Moody, Proc. Brit., Cer. Soc. 10, 87–102 (1968).
38. F. Vanbaelinghen, A. Pelloux, C. Déportes, J. Appl. Electrochem. 6, 67–77 (1976).
39. T. Takahashi, H. Iwahara, J. Appl. Electrochem. 3, 65–72 (1973).
40. M.J. Verkerk, A.J. Burggraaf, J. Electrochem. Soc. 130, 78–84 (1983).
41. P. Duran, J.R. Jurado, C. Moure, N. Valverde, B.C.H. Steele, Mater. Chem. Phys. 18, 287–294 (1987).
42. P.J. Dordor, J. Tanaka, A. Watanabe, Solid State Ionics 25, 177–181 (1987).
43. M.J. Verkerk, A.J. Burggraaf, Solid State Ionics 3/4, 463–467 (1981).
44. M.J. Verkerk, K. Keizer, A.J. Burggraaf, J. Appl. Electrochem. 10, 81–90 (1980).
45. H.T. Cahen, T.G.M. Van den Belt, J.W.H. De Witt, J.H.J. Broers, Solid State Ionics 1, 411–423 (1980).
46. E.D. Washman, N. Jiang, D.M. Mason, D.A. Stevenson, in: Proceedings of the First International Symposium on Solid Oxide Fuel Cells, S.C. Singhal (ed.). The Electrochemical Society, Inc., Pennington, New Jersey, Vol. 89–11, pp. 15–21 (1989).
47. F. Honnart, J.C. Boivin, D. Thomas, K.J. De Vries, Solid State Ionics 9–10, 921–928 (1983).
48. M. Dumelié, G. Nowogrocki, J.C. Boivin, Solid State Ionics, 28/30, 524–528 (1988).
49. K. Hu, C. Chen, D. Peng, G. Meng, Solid State Ionics, 28/30, 566–570 (1988).
50. B.C.H. Steele, in: High Conductivity Solid Ionic Conductors, Recent Trends and Applications, T. Takahashi (ed.). World Scientific, Singapore, pp. 402–406 (1989).
51. F. Forrat, G. Dauge, P. Trécoux, G. Danner, M. Christen, Compt. Rend. Acad. Sci. Paris 259, 2813–2816 (1964).
52. S. Stotz, C. Wagner, Ber. Bunsenges. Physik. Chem. 70, 781–788 (1966).
53. D.A. Shores, R.A. Rapp, J. Electrochem. Soc. 119, 300–305 (1972).
54. T. Takahashi, H. Iwahara, Rev. Chim. Miner. 17, 243–253 (1980).
55. H. Iwahara, T. Esaka, H. Uchida, N. Maeda, Solid State Ionics 3/4, 359–363 (1981).
56. H. Uchida, N. Maeda, H. Iwahara, Solid State Ionics 11, 117–124 (1983).
57. H. Iwahara, H. Uchida, N. Maeda, Solid State Ionics 9, 1021–1025 (1983).
58. H. Iwahara, T. Esaka, H. Uchida, T. Yamauchi, K. Ogaki, Solid State Ionics 18/19, 1003–1007 (1986).
59. H. Iwahara, H. Uchida, H. Ono, K. Ogaki, J. Electrochem. Soc. 135, 529–533 (1988).
60. N. Bonanos, B. Ellis, M.N. Mahmood, Solid State Ionics 28–30, 579–584 (1988).
61. E.F. Sverdrup, D.H. Archer, A.D. Glasser, Adv. Chem. Serv. Amer. Chem. Soc. 90, 301–314 (1969).
62. R. Accorsi, E. Bergman, J. Electrochem. Soc. 127, 804–811 (1980).
63. D.W. White, General Electric R & D Rep., p. 254 (1978).
64. W. Fisher, F.J. Rohr, R. Steiner, Brown Bovery Co. Nachr. 54, 4–12 (1972).
65. C.S. Tedmon, H.S. Spacil, S.P. Mittof, J. Eletrochem. Soc. 116, 1170–1175 (1969).
66. Y. Ohmo, S. Nagata, H. Sato, Solid State Ionics 3/4, 439–442 (1981).

67. H.S. Isaacs, L.J. Olmer, J. Electrochem. Soc. 129, 436–443 (1982).
68. B.L. Kuzin, A.N. Vlazov, Electrokhimiya 20, 1636–1642 (1984).
69. M.A. Priestnall, B.C.H. Steele, in: Proceedings of the First International Symposium on Solid Oxide Fuel Cells, S.C. Singhal (ed.). The Electrochemical Society, Inc., Pennington, New Jersey, Vol. 89–11, pp. 157–169 (1989).
70. H.U. Anderson, J.H. Kuo, D.M. Sparlin, in: Proceedings of the First International Symposium on Solid Oxide Fuel Cells, S.C. Singhal (ed.). The Electrochemical Society, Inc., Pennington, New Jersey, Vol. 89–11, pp. 111–1287 (1989).
71. A. Hammouche, E. Siebert, M. Kleitz, A. Hammou, in: Proceedings of the First International Symposium on Solid Oxide Fuel Cells, S.C. Singhal (ed.). The Electrochemical Society, Inc., Pennington, New Jersey, Vol. 89–11, pp. 265–276 (1989).
72. C. Michel, B. Raveau, Rev. Chim. Miner. 21, 407–425 (1984).
73. O. Yamamoto, Y. Takeda, R. Kanno, M. Noda, Solid State Ionics 22, 241–246 (1987).
74. Y. Takeda, R. Kanno, M. Noda, O. Yamamoto, J. Electrochem. Soc. 11, 2656–2661 (1987).
75. O. Yamamoto, Y. Takeda, R. Kanno, M. Noda, in: Science and Technology of Zirconia, Advances in Ceramics: S. Somiya, N. Yamamoto, H. Yanagida (eds.). The American Ceramic Society, Inc., Westerville, Ohio, Vol. 24B, pp. 829–835 (1986).
76. A. Hammouche, Thesis, National Polytechnic Institute Grenoble (1989).
77. P. Fabry, M. Kleitz, Electroanal. Chem. and Interface Electrochem. 57, 165–177 (1974).
78. L.J. Olmer, PhD Columbia University, New York (1980).
79. J.H. Kuo, H.U. Anderson, D.M. Sparlin, J. Solid State Chem. 83, 52–60 (1989).
80. A. Caneiro, private communication.
81. M. Keddam, O.R. Mattos, H. Takenouti, J. Electrochem. Soc. 128, 257–266 (1981).
82. A. Hammouche, A. Caneiro, E. Siebert, A. Hammou, M. Kleitz, to be published in J. Electrochem. Soc.
83. M. Kleitz, Thesis, Grenoble University (1968).
84. H. Schachner, H. Tannenberger, in: First International Symposium Fuel Cells, Brussels, pp. 19–26 (1965).
85. H.H. Eysel, F.J. Rohr, Brown Bovery Company Nachrichten 49, 532–540 (1967).
86. Brown Bovery Company, Final Report on the Project High Temperature Fuel Cells, NT 332 (1975).
87. D.C. Fee, J.P. Ackerman, Fuel Cell Seminar Orlando, 13 Nov. 1983. Abstracts.
88. A.O. Isenberg, Fuel Cell Seminar, Newport Beach, California, Nov. 1982, pp. 154–156.
89. D.W. Dees, T.D. Claar, T.E. Easler, D.C. Fee, F.C. Mrazek, J. Electrochem. Soc. 134, 2141–2146 (1987).
90. P.H. Middelton, M.E. Stirsen, B.C.H. Steele, in: Proceedings of the First International Symposium on Solid Oxide Fuel Cells, S.C. Singhal (ed.). The Electrochemical Society, Inc., Pennington, New Jersey, Vol. 89–11, pp.90–98 (1989).
91. K. Eguchi, T. Inoue, T. Setoguchi, H. Arai, 7th International Conference on Solid State Ionics, Hakone, Japan, Nov. 1989, Abstracts, p. 94.
92. D.O. Hayward, B.M.W. Trapnell, Chimisorption, London, Butterworth (1964).
93. C.S. Tedmon, H.S. Spacil, S.P. Mittof, General Electric, Rep. 69-C-056 (1969).
94. L.J. Olmer, J.C. Viguié, E.J.L. Schouler, Solid State Ionics 7, 23–35 (1982).
95. E.J.L. Schouler, M. Kleitz, J. Electrochem. Soc. 134, 1045–1050 (1987).
96. B.C. Nguyen, T.A. Lin, D.M. Mason, J. Electrochem. Soc. 133, 1807–1815 (1986).
97. B.C.H. Steele, I. Kelly, H. Middelton, R. Rudkin, Solid State Ionics 28/30, 1547–1552 (1988).
98. D.W. Dees, U. Balachandran, S.E. Dorris, J.J. Heiberger, C.C. McPheeters, J.J. Picciolo, in: Proceedings of the First International Symposium on Solid Oxide Fuel Cells, S.C. Singhal (ed.). The Electrochemical Society, Inc., Pennington, New Jersey, Vol. 89-11, pp. 317–321 (1989).
99. J.T. Brown, IEEE Trans. on Energy Conv. 2, 193–197 (1988).

100. J.T. Brown, in: High Conductivity Solid Ionic Conductors, Recent Trends and Applications. T. Takahashi (ed.). World Scientific, Singapore, pp. 630–633 (1989).
101. H.U. Anderson, R. Murphy, S. Semachaibovorn, B. Rossing, A. Aldred, W.L. Precarione, R.J. Ackerman, in: Conference on High Temperature Science Related to Open Cycle, Coal Fired MHD Systems. Argonne, Illinois, pp. 142–147 (1977).
102. H.U. Anderson, R. Murphy, A.K. Fox, B. Rossing, A. Aldred, in: Proceedings of the Workshop on High Temperature Solid Oxide Fuel Cells, H.S. Isaacs, S. Srinivasan, I.L. Harry. Brookhaven National Laboratory, Associated Universities, Inc., Upton, New York, pp. 41–53 (1977).
103. S. Srilomsak, D.P. Schilling, S.U. Anderson, in: Proceedings of the First International Symposium on Solid Oxide Fuel Cells, S.C. Singhal (ed.). The Electrochemical Society, Inc., Pennington, New Jersey, Vol. 89-11, pp. 129–140 (1989).
104. R.J. Ruka, S. Shinaroy, in: Fuel Cell Seminar, Tucson, Arizona (1986), pp. 76–79.
105. L.A. Chick, J.L. Bates, L.R. Pederson, H.E. Kissinger, in: Proceedings of the First International Symposium on Solid Oxide Fuel Cells, S.C. Singhal (ed.). The Electrochemical Society, Inc., Pennington, New Jersey, Vol. 89–11, pp.170–187 (1989).
106. R. Koc, H.U. Anderson, S.A. Howard, in: Proceedings of the First International Symposium on Solid Oxide Fuel Cells, S.C. Singhal (ed.). The Electrochemical Society, Inc., Pennington, New Jersey, Vol. 89-11, pp. 220–241 (1989).
107. F.J. Rohr, in: Solid Electrolytes, P. Hagenmuller, W. Van Gool (eds.). Academic Press, New York, pp. 431–450 (1978).
108. A.O. Isenberg, in: Fall Meeting of the Electrochemical Society, Los Angeles, California, October 1976, abstracts. The Electrochemical Society, Inc., Princeton, New York, pp. 364–365 (1979).
109. A.O. Isenberg, in: Proceedings of the High Temperature Solid Oxide Electrolytes Conference. BNL51728, Brookhaven National Laboratory, Associated Universities, Inc., pp. 5–15 (1983).
110. F.J. Rohr, in: Proceedings of the Workshop on High Temperature Solid Oxide Fuel Cells, H.S. Isaacs, S. Srinivasan, I.L. Harry (eds.). Brookhaven National Laboratory, Associated Universities, Inc., Upton, New York, pp. 122–138 (1977).
111. D.C. Fee, R.K. Steunenberg, T.D. Claar, R.B. Poeppel, J.P. Ackerman, Fuel Cells Seminar, Courtesy Associates, Washington D.C., pp.74–78 (1983).
112. C.C. McPheeters, D.C. Fee, R.B. Poeppel, T.D. Claar, D.E. Busch, B.K. Flandermeyer, T.E. Easler, J.T. Durek, J.J. Picciolo, 1986 Fuel Cell Seminar. Courtesy Associates, Washington D.C., pp. 44–47 (1986).
113. C.C. McPheeters, D.W. Dees, S.E. Doris, J.J. Picciolo, 1988 Fuel Cells Seminar. Courtesy Associates, Washington D.C., pp. 29–39 (1988).
114. N.Q. Minh, C.R. Horne, F. Lin, P.R. Staszak, in: Proceedings of the First International Symposium on Solid Oxide Fuel Cells, S.C. Singhal (ed.). The Electrochemical Society, Inc., Pennington, New Jersey, Vol. 89-11, pp. 307–316 (1989).
115. K.M. Myles, C.C. McPheeters, J. Power Sources 29, 311–319 (1990).
116. B.C.H. Steele, Science of Ceramics 12, 697–707 (1984).
117. M.S. Hsu, Fuel Cells Seminar. Tucson Arizona, p. 84–87 (1986).
118. A.O. Isenberg, Solid State Ionics 3/4, 431–437 (1981).
119. W. Feduska, A.O. Isenberg, J. Power Sources 10, 89–102 (1983).
120. M.F. Carolan, J.N. Michaels, Solid State Ionics 25, 207–216 (1987).
121. U.B. Pal, S.C. Singhal, in: Proceedings of the First International Symposium on Solid Oxide Fuel Cells, S.C. Singhal (ed.). The Electrochemical Society, Inc., Pennington, New Jersey, Vol. 89-11, pp. 41–56 (1989).
122. J.P. Dekker, N.J. Kiwiet, J. Schoonman, in: Proceedings of the First International Symposium on Solid Oxide Fuel Cells, S.C. Singhal (ed.). The Electrochemical Society, Inc., Pennington, New Jersey, Vol. 89-11, pp. 57–66 (1989).

123. H. Nakagawa, S. Kosuge, H. Tsuneizumi, E. Matsuda, H. Mihara, Y. Sato, in: Proceedings of the First International Symposium on Solid Oxide Fuel Cells, S.C. Singhal (ed.). The Electrochemical Society, Inc., Pennington, New Jersey, Vol. 89-11, pp. 71–78 (1989).
124. A. Negishi, K. Nozaki, T. Ozawa, Solid State Ionics 3/4, 443–446 (1981).
125. T.L. Markin, R.J. Bones, R.M. Dell, in: Superionic Conductors, G. Mahan, W. Roth (eds.). Plenum Press, New York, pp. 15–35 (1976).
126. W. Feduska, A.O. Isenberg, J. Power Sources 10, 89–102 (1983).
127. C.C. McPheeters, U. Balachandran, P.E. Blackbirn, D.E. Busch, D.W. Dees, S.E. Dorris, J. Dusck, J.J. Heiberger, H. Leu, S. Majumdar, F.C. Mrazek, K.M. Myles, J.J. Picciolo, R.B. Poeppel, in: Proceedings of the 23rd Intersoc. Energy Conv. Eng. Conf. American Society of Mechanical Engineers, New York, Vol. 2, pp. 279–282 (1988).
128. W.J. Maskalik, in: Proceedings of the First International Symposium on Solid Oxide Fuel Cells, S.C. Singhal (ed.). The Electrochemical Society, Inc., Pennington, New Jersey, Vol. 89-11, pp. 279–287 (1989).
129. C.G. Vayenas, Solid State Ionics 28–30, 1521–1539 (1988).
130. M. Stoukides, C.G. Vayenas, J. Electrochem. Soc. 131, 839–845 (1984).
131. O. Leclerc, in: Piles à Combustibles en 1990 Conf., Grenoble, June 1990.
132. P.D. Lilley, E. Erdle, F. Gross, EUR Report (12249), Office for Official Publications of the European Communities, Luxembourg (1988).

Advances in Electrochemical Science and Engineering
Edited by Heinz Gerischer and Charles W. Tobias

Second Harmonic Generation as an In-situ Probe of Single Crystal Electrode Surfaces

G. L. Richmond

Chemical Physics Institute, University of Oregon, Eugene, OR 97403, USA

Contents

1 Introduction

Over the past decade there has been a growing interest among electrochemists in obtaining a more microscopic picture of the electrochemical interface. To achieve this goal, new techniques are being developed which go beyond simple current-voltage measurements and directly probe double layer properties. On the solution side of the interface, one would like to measure the structure and orientation of molecular adsorbates, to understand the effect of potential bias on these molecular properties and to correlate these adsorbate properties with reactivity. Surface-enhanced Raman spectroscopy (SERS) was the one of the first techniques to provide such information for roughened electrode surfaces [1]. Other spectroscopic techniques [2, 3] have since arisen which are providing a compatible data base on a variety of smooth and roughened substrates. Of equal importance with understanding adsorbate properties is the characterization of electrode surface properties in situ. Although there are a battery of techniques available for studying surfaces in ultra high vacuum (UHV), the tools available for making analogous surface measurements in solution are few. At present, little is known about the electronic structure of the immersed electrode surface, the existence of surface states or the effect of applied potential on the energy of such states. For single crystal electrode surfaces, simple techniques for measuring surface morphology are needed so that one can understand how adsorption and potential bias can stabilize or destabilize the atomic surface structure. Similarly, one would like to measure the structure and order of foreign metal atoms electrodeposited on the surface and how their presence alters the reactivity and electronic properties of the surface. X-ray grazing incidence [4] and scanning tunnelling microscopy [5] are two new in-situ techniques which show promise in measuring surface and overlayer properties. Another new technique, surface second harmonic generation (SHG), is a potential candidate for measuring surface ordering. It has also been found to be very sensitive to surface electronic properties and, for special cases, molecular properties.

Whereas all of these emerging techniques offer exciting opportunities for studies in the future, most noted above are currently in a relatively early stage of development both in theory and in general applicability. Optical second harmonic generation is no exception, although progress in the past decade has been substantial as the unique properties of this nonlinear optical method have been exploited in a number of applications [6, 7]. This review is written to provide a summary of the current state of the field of surface SHG as applied to studying single crystal electrode surfaces. Although most of the work described has been performed with the electrode in solution, the results have direct bearing on studies of metallic surfaces which are being examined in other environments including UHV.

The type of optical second harmonic generation familiar to most scientists is the conversion of infrared frequencies into visible frequencies via the doubling crystal positioned at the end of the laser cavity. In order for this conversion to occur, the doubling media must be noncentrosymmetric. In fact, much of the research today in second harmonic generation is in the development of new noncentrosymmetric materials which are very efficient at making this conversion when the light is passed through the bulk of the material. In *surface* second harmonic generation, one is interested in the SH-light generated at the surface of the medium. The surface inherently provides the broken symmetry necessary for generating the doubled incident frequency. If the medium is centrosymmetric, the surface SHG should be significant relative to the bulk contribution. Numerous studies have appeared which exploit the unique aspect of this nonlinear optical process to study a variety of semiconductor, liquid, polymeric and metallic surfaces [6, 7].

In studies of electrode surfaces, the incident light from the laser is coupled through a window on the electrochemical cell and illuminates the surface. The SH signal is then collected near the reflected angle as the potential is varied across the double layer. For the metallic systems studied in simple electrolytes, the SH response from the metal has been found to dominate over the contribution from the adjacent solution. As will be discussed, the SH response is highly sensitive to changes in surface morphology, surface composition and surface electronic properties as varied by the potential bias. When a single crystal electrode is used, one can not only examine the change in the magnitude of the SH response with applied electric field, but by selecting various optical polarization geometries one can derive detailed information about the nonlinear polarizability of the surface and the symmetry of the surface. By varying the wavelength, one has the option to map surface states and study their bias potential dependence. Phase measurements provide important complementary information to amplitude data, enabling optical resonances to be identified.

The review will begin with a brief description of the progress in the field over the past three decades and will provide a perspective of how the electrochemical measurements have developed in this growing field. This will be followed by a theoretical section which provides some general theoretical principles behind the technique. A description of some of the new microscopic approaches to modelling the nonlinear source currents from metal surfaces will also be presented. An experimental technique section will describe the details involved in making a variety of surface SH measurements. A summary of the results of experimental studies conducted in the past few years on single crystal electrode surfaces in solution will follow. The discussion will draw upon related work performed in UHV and studies on polycrystalline surfaces where comparisons are appropriate. For a more comprehensive discussion of these later two topics, the reader is referred to several other recent reviews [7, 9].

2 Historical Perspective

Directly following the development of the optical laser, in 1961 Frankel et al. [10] reported the first observation of optical harmonics. In these experiments, the output from a pulsed ruby laser at 6943 Å was passed through crystalline quartz and the second harmonic light at 3472 Å was recorded on a spectrographic plate. Interest in surface SHG arose largely from the publication of Bloembergen and Pershan [11] which laid the theoretical foundation for this field. In this publication, Maxwell's equations for a nonlinear dielectric were solved given the boundary conditions of a plane interface between a linear and nonlinear medium. Implications of the nonlinear boundary theory for experimental systems and devices was noted. Experimental substantiation for their theoretical predictions came in the work of Ducuing and Bloembergen in which semiconducting mirrors of tellurium, GaAs and InSb were examined with a ruby laser [12].

Several studies in the 1960s followed which examined the SH response from metallic surfaces. These initial studies were generally focused on understanding the source of the nonlinear polarizability from metals. The first experimental observation of nonlinear optics from a surface was reported by Brown, Parks and Sleeper who examined the SH response from silver [13]. They concluded that, since the substrate was centrosymmetric, the observed harmonic generation must be from the boundary region where symmetry is lacking. Furthermore, their polarization experiments suggested that the observed SH intensity arose from an electric quadrupole type source. In a related theoretical study, Jha [14] attributed the nonlinear polarization source to the conduction electrons and noted the importance of surface terms which arise from the discontinuity of the normal component of the electric field at the boundary. This was followed by a further examination of silver by Brown and Parks [15]. Their work lended support for the dominance of the conduction electron plasma in the SH response. They also provided evidence for the existence of a bulk magnetic dipole source term which had been predicted by Jha [16].

Several other studies noted the importance of bound electrons to the surface nonlinear polarizability. Bloembergen and Shen [17] concluded that the second harmonic radiation observed from a silver surface irradiated at optical frequencies has as its origin the nonlinearity of bound electrons in the ion cores of a monolayer surface layer rather than the plasma electrons. The paper of Bloembergen et al. [18] also asserted that the core electrons were important at optical frequencies by demonstrating the similarity in the SH response from Ag, Au and Cu, to that of Si and Ge, where core electrons are dominant. They provided wavelength dependent data which indicated that the interband contributions are comparable to the plasma or intraband contributions, in agreement with general theoretical considerations for these metals. A later paper by Bloembergen et al. [19] derived expressions for the intensity and polarization of the reflected harmonic radiation as a function of the angle of incidence and the polarization of the incident laser beam. It was concluded therein that the surface contribution was of a quadrupole nature and that this quadrupole term should dominate over the bulk magnetic dipole term which arises from a classical Lorentz force on the conduction electrons. This work also predicted that for high refractive index materials, the SH response should be strong yet insensitive to surface contaminants or adsorbed layers. Important for later single crystal work to be discussed, they predicted that the SH signal from cubic crystals should be independent of crystal orientation. Sonnenberg and Heffner [20] followed with a measurement of the SH intensity as a function of angle of incidence for silver surfaces and found that experimental agreement with theory was only achieved if both bound and free-electron effects were considered. Other studies of significance in this decade include the work of Krivoschekov and Stroganov [21, 22] on silver thin films, and Jha and Warke [23] who showed that the general expression for the nonlinear polarization may be approximated in terms of the complex dielectric constants in the long wavelength limit.

Two studies of SHG from a metal in contact with molecular adsorbates appeared in 1967 and 1968, respectively. In the first work, a silver electrode in a simple aqueous salt solution was examined by SHG as a function of applied voltage [24]. The nonlinear response was found to vary in a quadratic manner relative to the applied voltage. The experiment was relatively crude from an electrochemical standpoint but the work clearly demonstrated the sensitivity of SHG to faradaic processes. Brown and Matsuoka [25] reported the effects of molecular adsorbates on the SH response from silver surfaces examined in vacuum conditions and concluded that, contrary to the results of all prior theoretical and experimental work, adsorbates dramatically reduced the SH response over that observed for atomically clean silver.

As can be seen from the above summary, by the end of the 1960s, the relative importance of interband and intraband contributions to the nonlinear polarizability from Ag and other metal surfaces was controversial. Unfortunately, inadequate sophistication in surface preparation during this and much of the next decade made it difficult to test the theories and also led to much disagreement among groups about whether SHG was sensitive to surface details.

One of the most important theoretical contributions of the 1970s was the work of Rudnick and Stern [26] which considered the microscopic sources of second harmonic production at metal surfaces and predicted sensitivity to surface effects. This work was a significant departure from previous theories which only considered quadrupole-type contributions from the rapid variation of the normal component of the electric field at the surface. Rudnick and Stern found that currents produced from the breaking of the inversion symmetry at the cubic metal surface were of equal magnitude and must be considered. Using a free electron model, they calculated the surface and bulk currents for second harmonic generation and introduced two phenomenological parameters, "a" and "b", to describe the effects of the surface details on the perpendicular and parallel surface nonlinear currents. In related theoretical work, Bower [27] extended the early quantum mechanical calculation of Jha [23] to include interband transitions near their resonances as well as the effects of surface states.

During this time period, several groups investigated the SH response from metallic films using attenuated total reflection techniques (ATR) in which the nonlinear response is enhanced by coupling into surface plasmons (or polaritons) [28–38]. Simon et al. [28] were the first to demonstrate this effect.

At the beginning of the 1980s, studies on surface SHG began to go beyond the very fundamental studies which were directed towards understanding the source of the nonlinear polarizability, to studies which examined the sensitivity of SHG to surface effects. This change in emphasis was largely a result of pioneering studies by Shen and coworkers in 1981 [39–41] in which large enhancements in the SH response from a silver surface were observed during an oxidation/reduction cycle (ORC). The enhancement observed seemed to be similar to the surface-enhanced Raman effect discovered several years earlier. Consequently, much of the initial work in the electrochemical area was directed towards understanding the SH response during an oxidation/reduction cycle [40–53]. Large enhancements in the SH response from silver were observed during an ORC in simple salt solutions. This enhancement was found to occur with and without the presence of an organic adsorbate such as pyridine. It soon became apparent that, whereas SERS could be described in terms of both a chemical and an electromagnetic mechanism [1], the SHG enhancement appeared to be predominantly electromagnetic in nature [41].

Following these studies were a series of works which examined the SH response from polycrystalline and crystalline silver electrode surfaces biased within the ideally polarizable region [42–44, 54–64]. These studies showed the sensitivity of SHG to adsorption of ions to the electrode surface. More importantly, they showed that the sensitivity arose from the changes in the optical properties of the electrode surface itself, and not from the optical properties of the ionic and simple molecular species at the surface. Conversely, the SH response from an adsorbate, such as a dye molecule, can become an important factor if either the fundamental or SH photon energy is resonant with electronic transitions in the adsorbate [65, 66]. For more details on these SH studies of both ORC effects and adsorption phenomena on polycrystalline substrates, the reader is referred to Refs. 7 and 9.

In the past few years, the electrochemical studies have become more sophisticated in both the optical analysis and the experimental parameters measured. A particular area of growth has been the examination of SHG from single crystal electrode surfaces. Following the results of several studies [67–73] on Si single crystals in which the variation of the SH response with rotation about the surface normal was used to measure the surface symmetry and order, Richmond and coworkers performed related studies on metal single crystal electrodes with the goal of using this rotational anisotropy to monitor surface symmetry and order in solution [74–76]. For Ag(111), they found an observable anisotropy in the SH response with rotation which correlated directly with the symmetry of the surface [74, 75]. The appearance of anisotropy from this crystal is nevertheless surprising since the fundamental and harmonic frequencies used were too low to couple to interband transitions in the metal. However, the observed anisotropy from Ag(111) is clearly different than what was reported by Tom and Aumiller for Cu(111) in UHV using similar frequencies [77]. In the copper study, Tom and Aumiller attributed the anisotropy to a resonance between the energy of the harmonic fields and the bulk interband transitions of Cu.

Since that time, numerous experiments on single crystal metal surfaces have been performed in the electrochemical environment and in UHV. How this field has progressed in recent years will be discussed in the following sections. This review will focus on the progress made in the electrochemical area and note the parallel work performed in UHV where appropriate.

3 Theoretical Considerations

Although a theoretical description of second harmonic generation from bulk media is relatively well developed, progress in modeling the surface nonlinear response lags far behind. The difficulty lies in describing the source of the nonlinear polarization at the interface. Once the source is determined, the fields generated by the source can be found. Bloembergen and Pershan in 1962 were the first to solve the problem for a generalized dipole source at an interface [11]. Bloembergen et al. [19] and later Shen [78] updated this work in a manner analogous to classical electrodynamics in linear media. Even though numerous microscopic approaches have been attempted for a range of media, the success has been limited due to the difficulty of the task. This is particularly true for metallic surfaces which have generally been treated with a jellium model.

The approach taken in the following section is to give a brief overview of the concepts used to describe theoretically SHG in reflection from an interface. It will begin with the general solution as developed by Shen [78] and Heinz [79]. This will be followed by extensions of the generalized theory to cubic media, of particular importance to much of the experimental work to be discussed. The section will conclude with a general overview of various theoretical models recently used to describe metallic interfaces on a microscopic level. Several of these studies will be discussed further in the experimental section where comparison with experiment is appropriate.

3.1 General Theory for Surface Second Harmonic Generation

Figure 3.1 shows a simplified picture of an interface. It consists of a multilayer geometry where the surface layer of thickness d lies between two centrosymmetric media (1 and 2) which have two different linear dielectric constants ε_1 and ε_2, respectively. When a monochromatic plane wave at frequency ω is incident from medium 1, it induces a nonlinear source polarization in the surface layer and in the bulk of medium 2. This source polarization then radiates, and harmonic waves at 2ω emanate from the boundary in both the reflected and transmitted directions. In this model, medium 1 is assumed to be linear.

The discontinuity of the interface leads to two contributions to the second order nonlinear polarizability, the electric dipole effect due to the structural discontinuity and the quadrupole type contribution arising from the large electric field gradient at the surface. Under the electric dipole approximation, the nonlinear susceptibility of the centrosymmetric bulk medium 2 is zero. If the higher order magnetic dipole

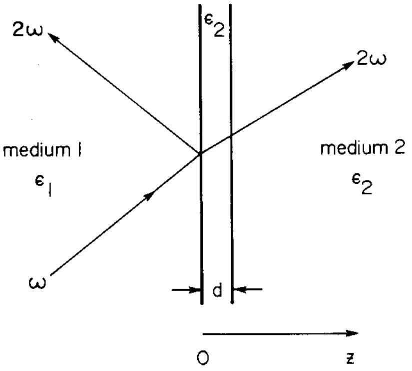

Fig. 3.1. Second harmonic generation from an interface between two isotropic media. The z direction is taken as zero at the interface between the media and is positive going into medium 2. After Ref. 78.

and electric quadrupole source terms are considered, the contribution from the bulk is nonzero. Once the form of the nonlinear polarization for these surface and bulk contributions can be determined, the radiated SH fields are found by solving the wave equation.

The standard method of treating the electric dipole contribution from the surface region is to view the nonlinear polarization as a dipole sheet which can be described by the surface susceptibility tensor, $\chi_s^{(2)}$. This is equivalent to considering the three layer system shown in Fig. 3.1 with the dipole sheet placed just below the surface at $z = 0^+$ and allowing the surface layer thickness, d, to approach zero. The surface contribution to the polarization can then be written as

$$\mathrm{P_s}(2\omega) = \chi_s^{(2)}\delta(z):\mathrm{E}(\omega)\mathrm{E}(\omega) \tag{3.1}$$

where $\delta(z)$ is a δ-function at $z = 0^+$.

The contributions from the bulk, or nonlocal response, of the medium are proportional to the first spatial derivative of the field:

$$\mathrm{P}(2\omega) = \mathrm{Q}(2\omega):\mathrm{E}(\omega)\nabla\mathrm{E}(\omega) \tag{3.2}$$

where Q is a fourth rank tensor of multipole terms. Symmetry dictates the number of independent nonzero tensor elements. For isotropic media there are four nonvanishing tensor elements, three of which are independent. Using the notation of Bloembergen et al [19], the ith component of the induced second order polarization may then be written:

$$\mathrm{P_i}(2\omega) = (\delta-\beta-2\gamma)[\mathrm{E}(\omega)\cdot\nabla]\mathrm{E_i}(\omega)+\beta\mathrm{E_i}(\omega)[\nabla\cdot\mathrm{E}(\omega)]+\gamma\nabla_\mathrm{i}[\mathrm{E}(\omega)\cdot\mathrm{E}(\omega)] \ . \tag{3.3}$$

The coefficients δ, β, and γ relate to the independent tensor elements, and are frequency-dependent material parameters. For cubic media, all four nonvanishing tensor elements are independent and another term, $\zeta\mathrm{E_i}(\omega)\nabla_\mathrm{i}\mathrm{E_i}(\omega)$, appears in this expression. This additional term gives rise to an anisotropy in the SH radiation and will be discussed in more detail later in this review.

By application of Maxwell's equations, the expression in Eq. (3.3) can be transformed to give:

$$\mathrm{P}(2\omega) = (\delta-\beta)[\mathrm{E}(\omega)\cdot\nabla]\mathrm{E}(\omega)+\beta\mathrm{E}(\omega)[\nabla\cdot\mathrm{E}(\omega)]+(2\mathrm{i}\omega/c)\gamma[\mathrm{E}(\omega)\times\mathrm{B}(\omega)] \ . \tag{3.4}$$

The first two terms are electric quadrupole in character while the last term is magnetic dipolar. Under excitation by a single plane wave, the first term vanishes. In a homogeneous medium the second term vanishes by Gauss' Law. The third term describes the induced polarization which is along the propagation direction. It can only radiate at the discontinuity of the surface. The full expression for the second-order nonlinear polarization in an isotropic medium is then written as the sum of the surface and bulk polarizations [78]:

$$P_{s,\mathrm{eff}}(2\omega) = (\delta-\beta)[E(\omega)\cdot\nabla]E(\omega)+\beta E(\omega)[\nabla\cdot E(\omega)]+(2i\omega/c)\gamma[E(\omega)\times B(\omega)] + \chi_s^{(2)}\delta(z):E(\omega)E(\omega)\ . \tag{3.5}$$

This expression can then be used to obtain the radiated SH fields by solving the wave equation [19]:

$$\nabla\times\nabla\times E_2-(4\omega^2/c^2)\varepsilon(2\omega)E_2 = (16\pi\omega^2/c^2)P^{NL}(2\omega) \tag{3.6}$$

given the new boundary conditions imposed by the presence of the dipole layer. $P^{NL}(2\omega)$ has the form given by $P_{\mathrm{eff}}(2\omega)$ in Eq. (3.5).

The intensity of the reflected second harmonic signal from excitation by a plane wave of frequency ω and polarization $\varepsilon(\omega)$ is then found to be [78–80]:

$$I(2\omega) = \left(\frac{32\pi^3\omega^2\sec^2\theta_{2\omega}}{c^3\varepsilon_1(\omega)\varepsilon_1^{1/2}(2\omega)}\right) |e(2\omega)\cdot\chi_{s,\mathrm{eff}}^{(2)}:e(\omega)e(\omega)|^2 I^2(\omega)\ . \tag{3.7}$$

In this equation, $\theta_{2\omega}$ represents the angle of the radiated SH light with respect to the surface normal, $I(\omega)$ is the pump intensity, and $e(2\omega)$ is the polarization at the SH frequency. The vectors $e(\omega)$ and $e(2\omega)$ are related to the unit polarization vectors $\hat{e}(\omega)$ and $\hat{e}(2\omega)$ in medium 2 by Fresnel coefficients. The effective surface nonlinear susceptibility $\chi_{s,\mathrm{eff}}^{(2)}$ incorporates the surface nonlinear susceptibility $\chi_s^{(2)}$ and the bulk magnetic dipole contributions to the nonlinearity. The result simplifies since, for isotropic media, there are only three nonzero independent elements of $\chi_s^{(2)}$. These are $\chi_{s,zii}^{(2)}$, $\chi_{s,izi}^{(2)} = \chi_{s,iiz}^{(2)}$, and $\chi_{s,zzz}^{(2)}$ where $i = x,y$.

3.2 SHG from Cubic Media

A large portion of the SH studies on single crystal electrode surfaces has involved measuring the anisotropy in the SH response as the crystal is rotated 360° about the surface normal, or alternatively, as the polarization of the normal incidence beam is rotated. Early studies of Bloembergen and coworkers [19] suggested that the SH response from the surface of a cubic medium is independent of crystal face or orientation. Later experiments by Guidotti et al. [81] showing SH rotational anisotropy from Si(111) and Ge(111) in air disputed this previous work. This rotational anisotropy was confirmed by Tom, Heinz and Shen for Si(111) using 532 nm excitation and a 10 nsec laser pulse [68]. As an example, Fig. 3.2a shows the variation in the s-polarized SH intensity upon excitation with p-polarized 532 = nm light. The SH output, $I(\|, \perp)$, was monitored as the Si(111) sample was rotated about the surface normal. The notation used, $I(\|, \perp)$, refers to $p(\|)$ and $s(\perp)$ polarized (fundamental, SH) light. For $I(\|, \|)$, anisotropic patterns with threefold and fourfold symmetry were observed from Si(111) (Fig. 3,2b) and Si(100), respectively [68]. The data was fit to a theoretical model in which the symmetry of the crystal and its surface governs the observed anisotropy. The nonlinear response is attributed to the sur-

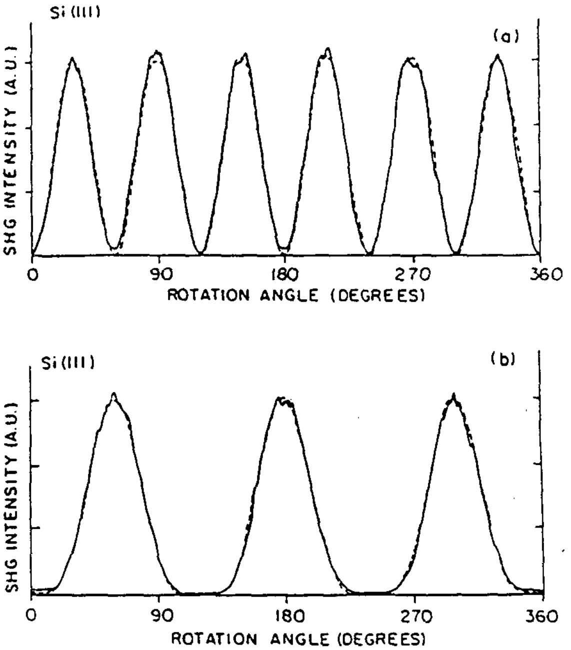

Fig. 3.2. SH rotational anisotropy from a Si(111) surface in air. Excitation was with p-polarized 532 nm light from a Q-switched Nd : YAG laser incident at 45° from the surface normal. The rotation angle lies between the x axis in the plane of incidence and the [100] projection axis on the surface. (a) S-polarized SH data (solid line) and theoretical fit (dashed line) to Eq. (3-10) (with $A = 0$). (b) P-polarized SH data and theoretical fit to Eq. (3-10) (with $B = -A$). From Ref. 67 and also shown in Ref. 68 with a different definition of the angle of rotation.

face electric dipole and bulk electric quadrupole and magnetic dipole contributions in the quiescent crystal. This model, described in more detail below, is an extension of the theory of Shen [78] outlined above for the special case of cubic media under single plane wave excitation.

The model ascribes the effective polarization ($P_{s,\mathrm{eff}}(2\omega)$) of Eq. (3-5) to a linear combination of the bulk nonlinear polarization ($P_i(2\omega)$) of Eq. (3.3) and a surface nonlinear polarization $P^{NS}(2\omega)$. For a cubic medium excited by a single beam of frequency ω, the bulk nonlinear polarization induced by (ω) becomes

$$P_i(2\omega) = \gamma \nabla_i [E(\omega) \cdot E(\omega)] + \zeta E_i(\omega) \nabla_i E_i(\omega) \tag{3.8}$$

where γ and ζ are frequency dependent material parameters and i refers to the crystal principal axes. The first term is isotropic with respect to crystal orientation and the second is anisotropic. Both terms arise from the induced quadrupole and magnetic dipole moments in the bulk. The surface electric dipole term which is caused by the broken inversion symmetry of the boundary region gives rise to a nonlinear polarization $P^{NS}(2\omega)$, such that

$$P^{NS}(2\omega) = \chi_s^{(2)} : E(\omega)E(\omega) \tag{3.9}$$

In this model, the structural symmetry of the boundary region is reflected in the form and magnitude of the tensor elements of the surface nonlinear susceptibility, $\chi_s^{(2)}$, and the bulk anisotropic susceptibility, ζ. For 1.06 μm excitation, the penetration depth of $E(\omega)$ is about 100 Å. The surface electric dipole contribution is thought to arise from the first 10 Å. The electric quadrupole allowed contribution to $E(2\omega)$ from the decaying incident field is attenuated by e^{-2} relative to the surface dipole contribution. Consequently, the symmetry of the SH response should reflect the symmetry of at least the first two topmost layers. For a perfectly terminated (111) surface, the observed symmetry should be reduced from the 6 m symmetry of the topmost layer to 3 m symmetry as additional layers are included. This is consistent with the observations for the centrosymmetric Si(111) surface response shown in Fig. 3.2 [67, 68].

Looking more closely at the various tensor elements for a surface with 3 m symmetry, four independent tensor elements result. Three tensor elements are isotropic and the $\chi_{\xi\xi\xi}$ is anisotropic where the ξ axis is defined as the projection of the [100] crystal axis on the surface. More details regarding the general solutions for the s- and p-polarized SH electric fields using Eqs. (3.8) and (3.9) can be found in Ref. 67.

In recent years, most rotational anisotropic data for both metals and semiconductors have been discussed in light of Tom's model [67, 68] and from the theory of Shen [78]. No assumption is made about the microscopic origin of the bulk and surface nonlinear polarization. This phenomenological model predicts a simple functional dependence of the SH intensity on the angle of rotation of the sample about the surface normal

$$I(2\omega) = |A + B f(\psi)|^2 \tag{3.10}$$

The definition of ψ is arbitrary and varies between researchers although it is usually taken as the angle between an axis in the laboratory frame, such as parallel or perpendicular to the plane of incidence, and a mirror plane or crystal axis direction in the surface. (This angle is labelled in Fig. 4.2b as Φ.) The function $f(\psi)$ in Eq. (3.10) then reflects the 2 mm, 3 m, and 4 mm symmetry of the (110), (111), and (100) surfaces, respectively. The constants A and B represent the isotropic and anisotropic contributions to the SH intensity which depend on the crystal, the experimental geometry, the frequencies used and the fundamental and SH polarizations. The data is then fit to this functional form and relative magnitudes for the phenomenological constants, A and B, determined.

When the data in Fig. 3.2 are fit to Eq. (3.10), the results yield $A = 0$ and $f(\psi) = \sin 3\psi$ for $I(||, \perp)$ [67, 68]. Using p-polarized input and output, the data fits to $|A/B| = 1$ and $f(\psi) = \cos 3\psi$ for $I(||, ||)$. With appropriate choices of the input and output polarizations and separate SH phase measurements, combinations of the four independent surface susceptibility elements and the bulk susceptibilities γ and ζ contributing to A and B for this system were also determined. There is inherent difficulty in separating the bulk surface susceptibilities such that the bulk susceptibility γ is always measured in a linear combination with a surface susceptibility element for any experimental geometry [82–84].

In similar work, Sipe, Moss and Van Driel [84] determined a functional form of the rotational anisotropy for cubic centrosymmetric media. Their derived expressions for the total reflected p- and s-polarized SH fields from perfectly terminated (111) and (100) crystals under p- and s-polarized excitation take the form

$$\mathrm{E}^{(2\omega)}(||,||) \propto a_{||,||} + c^{(\mathrm{m})}_{||,||} \cos(m\phi) \ , \tag{3.11}$$

$$\mathrm{E}^{(2\omega)}(\perp,||) \propto a_{\perp,||} + c^{(\mathrm{m})}_{\perp,||} \cos(m\phi) \ , \tag{3.12}$$

$$\mathrm{E}^{(2\omega)}(||,\perp) \propto b^{(\mathrm{m})}_{||,\perp} \sin(m\phi) \ , \tag{3.13}$$

$$\mathrm{E}^{(2\omega)}(\perp,\perp) \propto b^{(\mathrm{m})}_{\perp,\perp} \sin(m\phi) \ , \tag{3.14}$$

where $m = 4$ and $m = 3$ for the (100) and (111) surfaces respectively. For the (110) surface, the p- and s-polarized SH fields take the form

$$\mathrm{E}^{(2\omega)}(||,||) \propto a + c^{(2)} \cos(2\phi) + c^{(4)} \cos(4\phi) \tag{3.15}$$

$$\mathrm{E}^{(2\omega)}(||,\perp) \propto b^{(2)} \sin(2\phi) + b^{(4)} \sin(4\phi) \ . \tag{3.16}$$

The isotropic coefficient and the anisotropic coefficients $b^{(\mathrm{m})}$ and $c^{(\mathrm{m})}$ can have both bulk and surface contributions and depend on crystal symmetry. The linear and nonlinear dielectric constants of the material, as well as the appropriate Fresnel factors at ω and 2ω, are incorporated into the constants a, $b^{(\mathrm{m})}$ and $c^{(\mathrm{m})}$. Table 3.1 shows the susceptibilities contained in each of these constants. The models of Tom

Table 3.1. Composition of the parameters, a, b, and c in terms of the surface and bulk susceptibility elements. P-polarized (◆) or s-polarized (◇) fundamental field. i = (x, y)

(111) 3*m*	χ_{zzz}	χ_{zii}	χ_{izi}	χ_{xxx}	ζ	γ
a	●	◆, ◇	◆		◆, ◇	◆, ◇
$c^{(3)}$				◆, ◇	◆, ◇	
$b^{(3)}$				◆, ◇	◆, ◇	

(110) *mm*2	χ_{zzz}	χ_{zxx}	χ_{zyy}	χ_{xzx}	χ_{yzy}	ζ	γ
a	◆	◆, ◇	◆, ◇	◆	●	◆, ◇	◆, ◇
$c^{(2)}$		◆, ◇	●	●	●	◆, ◇	
$c^{(4)}$						◆, ◇	
$b^{(2)}$				◆	●	◆, ◇	
$b^{(4)}$						◆, ◇	

(100) 4*mm*	χ_{zzz}	χ_{zxx}	χ_{xzx}	ζ	γ
a	◆	◆, ◇	●	◆, ◇	◆, ◇
$c^{(4)}$				◆, ◇	
$b^{(4)}$				◆, ◇	

[68] and Sipe [84] are equivalent given that $\psi = \phi$. The coefficients a, $b^{(m)}$ and $c^{(m)}$ are defined somewhat differently in each model although the relationship between these constants and A and B in Eq. (3.10) is apparent by inspection.

3.3 SHG from Metallic Surfaces

When modelling the nonlinear response from a metal surface, two source currents are involved. The first and most difficult to describe is the source current from the surface which extends only a few angstroms into the metal. This surface current has components parallel and perpendicular to the surface. The latter is most sensitive to the details of the surface but is also the most difficult to calculate because of the discontinuity at the interface and the rapidly varying normal component of the electric field there. The bulk current is the second and is calculated to extend on the order of the optical skin depth into the metal.

Ideally, one would like to employ models which explicitly contain information about the electronic structure of the metal and its surface. Although this is a relatively difficult task, progress in this direction is being made as described below. The isotropic free-electron gas has been the simplest and most common approach to treating the nonlinear polarizability of the metal surface. Interband effects are ignored by assuming that the excitation energies are well below such resonances. Both classical and quantum mechanical methods have been used [14, 16, 19, 23, 26, 27, 85]. The first attempt at applying quantum mechanics to account for surface electronic structure was done in the cornerstone work of Rudnick and Stern [26]. They showed that their model correctly calculated the parallel current but it failed for the normal component. A new expression was then derived which used a half-infinite medium with a current sheet placed at the surface. They also introduced two adjustable parameters, a and b, to estimate the effects of real surface conditions on the size of the perpendicular and parallel source currents. These phenomenological constants were reported to be on the order of unity.

More recently, a hydrodynamic model has been used to model the electron gas by several groups [31, 86–88]. In this model the electrons are no longer treated as noninteracting and collective electron motions are considered. This model is relatively simple and yet provides a direct link between SHG and media properties such as electron density and surface potential barrier. In the work of Sipe et al. [31], values for the a and b parameters of Rudnick and Stern have been calculated. For the parameter b, a value of -1 has been obtained whereas the parameter a ranges from $+2$ to -2. Corvi and Schaich [87] presented both formal and numerical results for the efficiency of second harmonic generation in a simple reflection geometry. Their theory used the full set of Maxwell equations in combination with the hydrodynamic model to determine the electromagnetic fields. In more recent work, Schaich and Liebsch [88] have extended this work and have shown that similar results can be obtained from an analysis in which the speed of light is at times formally allowed to be infinite. All of the above studies using the hydrodynamic model show that the a parameter for the longitudinal SH response may have some interesting variations at excitation frequencies near or below the bulk plasma frequency.

Several other studies have appeared that are worthy of note. In a series of works by Keller [89–94] and Apell [95], the nonlocal nonlinear response for free-electron-like metals have been examined using various theoretical approaches which are basically extensions of linear theories on the optical response of metals. The results [92] reduce to those obtained by Rudnick and Stern [26] using a similar approach when the free-electron gas is considered to be homogeneous.

Whereas both the free-electron model and the hydrodynamic model are valuable as a starting point, they unfortunately are too crude to give a quantitative description of the dynamics of electrons near a surface [26, 31, 87]. One of the flaws in both models is that the electron distribution is treated as a step function which is constant at the surface and then falls abruptly to zero. In a departure from this model, Weber and Liebsch [96, 97] have used a jellium model treated within a local-density-functional approximation to determine second order induced charge densities at a metal surface in the low frequency limit. The approach is quantum mechanical and takes the smoothness of the electronic density profile in the vicinity of the surface and the nonlocal nature of the response into account. Their results indicate that the longitudinal SH current is located predominantly in the exponential tail of the equilibrium electron density in the vacuum and therefore should lead to the SH signal being highly sensitive to surface conditions. The values calculated for the parameter a range from -28 to -7, values which are significantly different than what is predicted by models based on a single step density profile. Weber and Liebsch [98] have also applied this method to understanding the experimentally observed changes in the intensity of second harmonic radiation caused by adsorption of alkali metal overlayers on a metal substrate [99]. In general they find that the second harmonic intensity is strongly enhanced at low coverages and then decreases again as one monolayer is completed. Where this maxima occurs appears to coincide with the point at which the work function is at a minimum.

The frequency dependence of SHG at simple metal surface has been the focus of a recent theoretical study of Liebsch [100]. Time-dependent density functional theory was used in these calculations. The results suggest that the perpendicular surface contribution to the second harmonic current is found to be significantly larger than had been assumed previously. He also concludes that for 2ω close to the threshold for electron emission, the self-consistently screened nonlinear electronic response becomes resonantly enhanced, analogous to local field enhancement in the linear response near the bulk plasma frequency.

Of relevance to electrochemical measurements, Liebsch and coworkers [101] have applied the density functional method to the metal/electrolyte interface and have compared the results with the potential and angular dependence of the light from a Ag(111) surface. The model is similar to the one used for a clean metal surface with the addition of a uniform static electric field oriented perpendicular to the surface. Interband transitions are neglected for simplicity. The experimental and theoretical results show good correspondence for negative and small positive surface charges but show a large deviation at larger positive charges.

Another study pertinent to electrochemical measurements is the work of Aers and Inglesfield for Ag(100) [102]. This theoretical study examines the screening of an electric field at the surface. The calculation employs a surface embedded Green function method in which the Schroedinger equation is solved explicitly in the true surface region. Although it is primarily directed towards linear electroreflectance, the changing profile of the screening charge with electric field is a nonlinear effect. With a low-frequency field it contributes to the longitudinal second order current normal to the surface. The center of gravity shifts with applied field are calculated and found to be a factor of 3 smaller than the jellium calculations indicate. The Stark shift of surface states in the applied field is also determined but the shifts are found to be too small to explain the spectral shifts in the previous electroreflectance work [103 – 106]. The study opens the way for further calculations of the nonlinear response from a metal surface which are more microscopic in nature.

Several other quantum mechanical studies have also appeared. Hu [107] has used a quantum mechanical approach in which the metal surface is described by a jellium model. The explicit form of the nonlinear current was derived for the high-frequency regime. Chizmeshya and Zaremba [108] have used a generalized Thomas-Fermi (GTF) model to calculate the linear and quadratic responses of a metal surface to an applied electric field. Their results for the normal component of the second harmonic polarization (the a parameter) are found to agree quantitatively with the results of the density functional theory approach [96, 97]. The authors note that the failure of previous hydrodynamic approaches was due to an unrealistic choice of the equilibrium electron density distribution in the boundary region. By using a correct description of ground-state properties, they suggest that their GTF approach may be extended to provide a hydrodynamic description with results similar to those obtained in a fully quantum mechanical approach.

4 Experimental Method

4.1 General Optical Considerations

The conventional geometry for measuring SHG from an electrode surface is shown in Fig. 4.1. Either a pulsed and Q-switched laser, or a mode-locked laser with [45] or without [54] Q-switching, are generally used as a probe source. Although a continuous wave (cw) laser can be employed, the high peak powers of a pulsed laser results in a higher conversion efficiency for the average incident power. Most experiments to date have been done with a Nd : YAG laser which operates on either the fundamental output at 1064 nm (SH at 532 nm), or the doubled fundamental at 532 nm (SH at 266 nm). If tunability of the incident beam is desired, a dye laser or other tunable source coupled to the pump Nd : YAG laser can be used. The polarization of the incident beam can be selected by use of a polarization cube placed in the beam path and prior to the electrochemical cell. Good quality polarization cubes with discrimination factors of 10^4 are recommended to avoid polarization mixing under conditions of low signal levels. The beam is then passed through the window of the electrochemical cell and gently focussed on the electrode surface. Caution

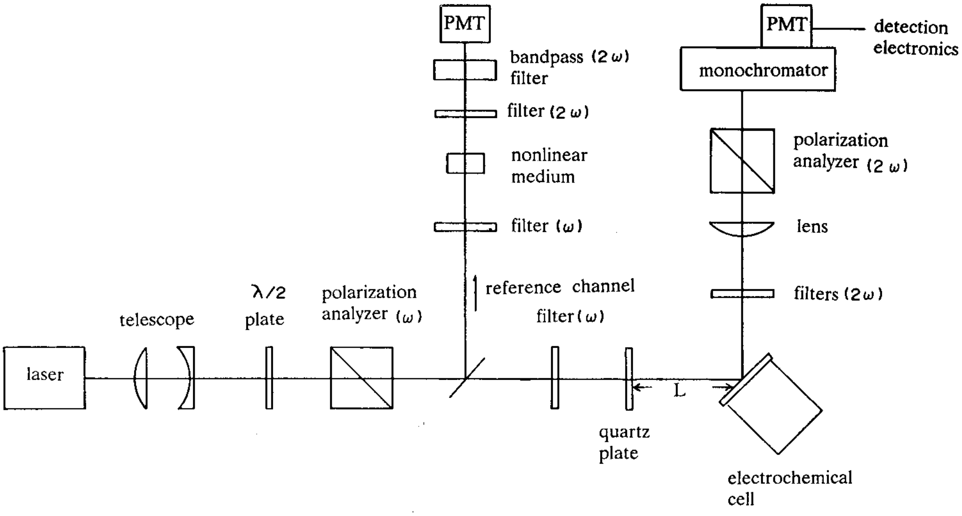

Fig. 4.1. Schematic diagram of the second harmonic generation experimental apparatus with the sample in the reflection geometry. The polarization analyzers are set to transmit p-polarized light at the frequency labeled in the figure. The ($\omega/2\omega$) filters transmit the (fundamental/harmonic) light while blocking the (harmonic/fundamental) light. For phase measurements, a quartz plate is mounted on a translation stage for movement towards the sample at a distance *L*.

must be practiced to avoid surface ablation due to either tight focussing of, or hot spots in, the incident beam. This is particularly a problem when the incident photons are resonant with the optical properties of the electrode surface. Visible damage on the crystal face by inspection under a microscope, or the observation of luminescence accompanying the SH output, are two signs of such damage.

The SH light at frequency 2ω is generated at the surface at an angle near the specular reflection. The exact angle is determined by the frequency dependent Fresnel factors. The harmonic beam is first analyzed for polarization, filtered to eliminate the scattered fundamental and sent through a monochromator for verification before detection using a photomultiplier tube. The monochromator is not essential but is a valuable diagnostic. Gated electronics are generally used for detection with the low repetition rate lasers whereas photon counting is more appropriate for the higher repetition rate mode-locked lasers. As an example of the signal level expected, according to Eq. (3.7), using a 10 Hz Q-switched Nd : YAG laser operating at 20 mJ incident pulse, a sample with $|\chi^{(2)}| \simeq 10^{-15}$ esu would yield 10^4 photons/pulse of 532 nm light [78]. The signal should show a quadratic dependence on the incident power. Normalization of the SH signal against power fluctuations can be achieved by sending a portion of the fundamental beam into a doubling medium and detecting the light in a reference channel.

A complementary approach to the standard reflection geometry described above uses the attenuated total reflection (ATR) geometry which couples surface plasmon waves to the incident electric field and enhances the SH production. Two configurations are possible, the Otto configuration and the Kretschmann method [36]. The incident light launches a surface polariton when the component of the incident wave vector along the surface equals that of the surface polariton. The large enhancement of the surface electromagnetic fields associated with surface plasmons is well suited for nonlinear optics [109].

The ATR geometry has been employed in numerous alkali and noble metal thin film studies [28–38, 55, 110–112]. For a more comprehensive review of ATR experiments, consult Ref. 36. A waveguide structure has also been proposed that uses phase matching of the interacting waves and leads to a predicted surface SHG enhancement of five orders of magnitude [113]. Enhancements of several orders of magnitude due to coupling to the long range surface plasmon mode has been predicted [114] and observed [115].

4.1.1 Time Resolved Measurements

The most convenient means of making time-resolved SH measurements on metallic surfaces is to use a cw laser as a continuous monitor of the surface during a transient event. Unfortunately, in the absence of optical enhancements, the signal levels are so low for most electrochemical systems that this route is unattractive. A more viable alternative is to use a cw mode-locked laser which offers the necessary high peak powers and the high repetition rate. The experimental time resolution is typically 12 nsec, which is the time between pulses. A Q-switched Nd: YAG provides 30 to 100 msec resolution unless the repetition rate is externally controlled. The electrochemical experiments done to date have involved the application of a fast potential step with the surface response to this perturbation followed by SHG [54, 55, 116, 117]. Since the optical technique is instantaneous in nature, one has the potential to obtain a clearer picture than that obtained by the current transient. The experiments have also been applied to multistep processes which are difficult to understand by simple current analysis [54, 117].

Measurements of dynamics in the subnanosecond regime are possible using pump-SH probe experiments where an initial pulse causes either a photo- or thermal excitation of the sample and the SH probe beam monitors the transient surface properties [69, 72, 73, 118–120]. Although experiments of this type have yet to be reported for an electrochemical system, experiments on Si samples excited under ambient and vacuum conditions have been published [69, 72, 73, 120].

4.1.2 Rotational Anisotropy Measurements

Of particular value to the study of single crystal electrodes in solution are experiments which measure the variation in SH response as the surface is rotated azimuthally about the surface normal (Fig. 4.2). In this experiment the incoming beam has a fixed polarization and the outgoing SH beam is monitored for the two different polarizations, s and p. The modulation in the SH intensity as the angle between the plane of incidence and a crystal axis or direction is changed is referred to

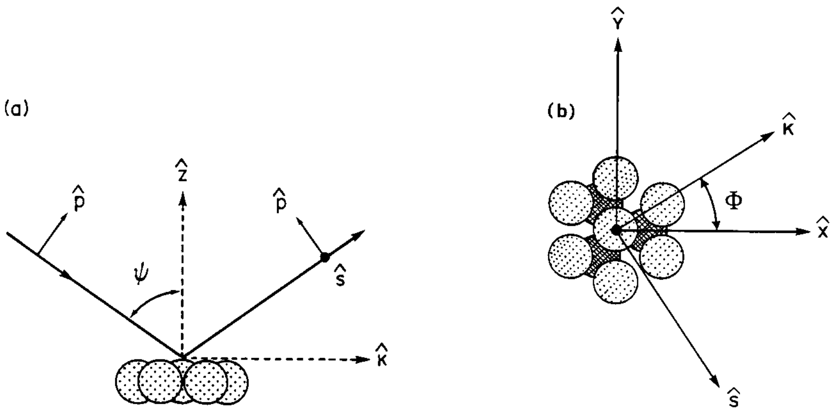

Fig. 4.2. Diagrammatic representation of the experimental crystal and beam geometries for p-polarized radiation incident upon the (111) crystal face as viewed (a) from the side and (b) from the top including the second atomic plane (#). The crystal coordinates are labeled x, y, z with the z direction along the $[2\bar{1}\bar{1}]$ crystal direction. The beam coordinates are labeled s, k, z. From Ref. 122.

as rotational anisotropy. An alternate means of obtaining the same information is to fix the electrode surface and illuminate the sample at normal incidence (e.g. Ref. 71). The polarization of the incoming beams is rotated and the SH light generated is analyzed along two orthogonal directions. In both experiments it is necessary to know the absolute orientation of the crystal axes as can be determined by various surface techniques. The utility of using such rotational anisotropy experiments to explore surface symmetry and order will be discussed in detail later. In theory, one has the possibility of also monitoring adsorbate surface order by such a method. In the absence of optical resonances with the molecular adsorbate, the metal surface response often dominates over that of the molecular adsorbate and thus one merely monitors the perturbation of the electronic properties of the surface upon adsorption rather than the molecular overlayer itself.

In the above experiments in which an electrode surface is examined, the electrode potential is fixed as the electrode surface is rotated and the SH anisotropy recorded. In a useful variation of this procedure, one can fix the angle of rotation and measure the SH response as a function of potential. Since the absolute orientation of the crystal is known, information can be derived about the various tensor elements describing the nonlinear polarizability from these crystalline surfaces. By fixing the angle and applying a transient potential pulse, one can perform time resolved measurements and watch the evolution of various adsorption and deposition processes along specific crystal axes.

In the Richmond laboratory, the single crystal disc electrode is mounted on the end of a hollow Kel-F shaft which extends outside of the electrochemical cell. The shaft is connected to a stepping motor and is interfaced to a computer. All parts of the electrochemical cell are constructed from either Kel-F, teflon, or high density polyethylene. The edges and back of the electrode are sealed from contact with the solution by a mask fabricated from Kel-F. An optical window is securely sealed to the front of the cell. The choice of material for the window is dependent upon the wavelengths used in the experiments. The reference electrode is contained in a separate compartment and is connected to the cell through a salt bridge. The counter electrode is a Pt ring. Prior to running an experiment, the cell and all flow tubes are cleaned with Nochromix in sulfuric acid and rinsed extensively with ultrapure water. The cell is operated in a flow geometry with the aid of a peristaltic pump. The solution is purged with nitrogen which is scrubbed free of O_2 prior to performing the experiments. In addition, freshly purged electrolyte flows through the cell at a slow rate (1 ml/min) to retard diffusion of oxygen into the cell. All electropolishing and subsequent mounting of the electrode in the cell are performed in an oxygen free glove box.

4.1.3 Phase Measurements

In the experiments described above, the variation of the amplitude of the harmonic fields is monitored as a function of various parameters. The surface nonlinear response, described by $\chi^{(2)}$ is, in the case of adsorbing media, a complex quantity. Hence, the phase of the nonlinear reflectance is related to the magnitude of $\chi^{(2)}$. When resonant optical transitions are involved, phase measurements can provide valuable complementary information to observed amplitude changes in the harmonic field. The phase measurements that have been performed in an electrochemical cell have used an interferometric geometry [121]. As shown in Fig. 4.1, a quartz plate is placed within the beam path close to the sample. The SH field generated at the quartz plate reflects off the electrode surface and interferes with the harmonic field generated at the electrode surface. The plate is then translated along the beam path a distance L, and the SH interference pattern monitored. The experiment is then repeated after an alteration of the electrode surface and compares the two waveforms. The relative phase shift due to the surface perturbation is then measured. By knowing the absolute orientation of the crystal relative to rotation of the azimuthal angle, one can monitor the relative phase shift in particular tensor elements which describe the polarizability from the surface. These phase measurement experiments are particularly valuable in detecting changes in surface electronic properties as a function of adsorption, potential variation or overlayer depositions.

4.2 Electrochemical Considerations

As with all surface analytical methods, surface preparation is critical to obtaining reproducible SHG from metallic surfaces and single crystals in particular. For surfaces prepared in UHV and then transferred to an electrochemical cell, sputtering and heating or annealing followed by Auger analysis of impurities should proceed inert transfer. Low energy electron diffraction (LEED) can also be used to check surface order. Metal electrode surfaces, particularly for the rotational anisotropy experiments, should be cut with an accuracy of < 1° in order to minimize polarization mixing. If UHV preparation is not performed, Laue backscattering is a good way to obtain the orientation of the principal axes and to have an additional, albeit qualitative, check of the maintenance of crystallinity after surface polishing. Mechanical polishing and, in most cases, electrochemical polishing to remove the damage layer and oxides, should be performed. Metal electrodes subject to oxidation should be prepared in an inert atmosphere and placed in a purged spectroelectrochemical cell. Extreme care must be practiced to remove all impurities, particularly trace residues from the electropolishing solutions. The SH response from the electrode surface is highly sensitive to submonolayer levels of impurities that can alter the electronic (optical) properties of the surface.

5 Experimental Results for Single Crystal Electrode Surfaces

5.1 Ag(111), Ag(110), and Ag(100)

5.1.1 Rotational Anisotropy Measurements

The first studies to be described examine the variation in the optical nonlinearity from single crystal metal surfaces as the crystal axis is rotated relative to the incident beam. Referred to as "rotational anisotropy", this behavior was first observed for Si(111) and Ge(111) single crystals [81]. Fig. 3.2 shows the results for Si(111) in air as obtained in a later study by Tom, Heinz and Shen [68]. Rotational anisotropy in the SH response is somewhat intuitive for semiconductors if one assumes that the electrons, which are polarized by the incident beam, reside in localized orbitals which are directionally aligned with the atoms in the crystal. For metals, the variation of SH intensity with azimuthal rotation is not as intuitive since one has generally viewed the source of the SH response from a metal to be free electron-like in character. Such behavior would lead to an isotropic response. As the energy of ω and 2ω approach the energy of electronic states of the metal and the light couples to these states in the metal, the response would more likely display anisotropy with rotation. Tom and Aumiller [77] were the first to demonstrate this effect for a metal in their studies of Cu(111) examined in UHV. They attributed the observed rotational anisotropy to interband transitions, or more specifically, a resonance between the nonlinear response at 2ω (532 nm, 2.3 eV) and the d bands of copper near 2.0 eV. The rotational anisotropy from a Ag(111) surface in solution was subsequently reported [74, 122]. This work is significant since bulk interband transitions can not be invoked to describe the anisotropy. The energy of the 1064 nm (1.1 eV) incident and the 532 nm (2.3 eV) SH photons lie far below the bulk d bands of Ag at 3.8 eV. How this anisotropy has been examined in the electrochemical cell, what impact the results have on our understanding of the nonlinear polarizability from metal surfaces, and

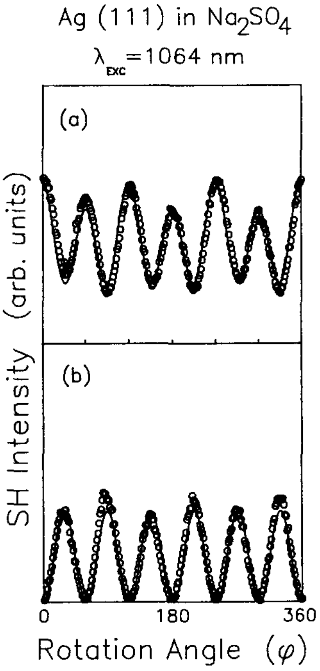

Fig. 5.1. Second harmonic intensity as a function of angle of rotation for Ag(111) in 0.25 M NaClO$_4$, pH = 5.0 at −0.72 V vs. Ag/AgCl (PZC) with p-polarized 1064 nm illumination. Angle of incidence (ψ) is 10°. The solid lines are fits to the data generated from the theoretical expressions given in the text (Eqs. (3-11) and (3-13)). (a) p-polarized SH intensity, $a/c^{(3)} = 1.2e^{i86°}$. (b) s-polarized SH intensity. The constant $b^{(3)}$ is taken to be unity. From Ref. 124.

what these rotational anisotropy experiments can tell us about the structure of metal single crystal surfaces in solution are the subjects of this section.

Figure 5.1 shows the SH rotational anisotropy obtained from Ag(111) biased in NaClO$_4$ which was first reported by Richmond and coworkers [74, 123]. A more complete presentation of the results later appeared [122, 124]. The incoming beam is 1064 nm light of p-polarization which is incident on the sample at an angle of 45°. Fig. 5.1 a and b correspond to the p- and s-polarized SH output, respectively. The 3-fold symmetry of the SH rotational plots clearly reflect the symmetry of the bulk crystal structure reduced at the boundary by the removal of the inversion symmetry (C_{3V}). The p-polarized results show a maximum when the electric field vector of the incident light, E(ω), is parallel to the [$2\bar{1}\bar{1}$] direction and a mimimum when E(ω) is parallel to the [$11\bar{2}$] direction. Fitting the data in Fig. 5.1 a to Eq. (3.11), the authors find a phase shift of $\pi/2$ between the a and $c^{(3)}$ terms (see Fig. 5.1 caption). The s-polarized data (Fig. 5.1 b) shows a good fit to the theoretical form given in Eq. (3.13). The authors suggest that the observation of any nonzero signal at the minima in the s-polarized output may be due to experimental factors such as surface roughness. An applied potential near the potential or zero charge (PZC) at −0.72 V

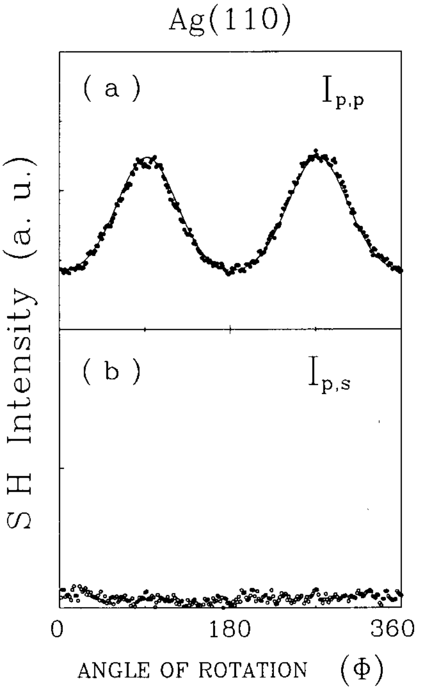

Fig. 5.2. Second harmonic intensity at 532 nm as a function of angle of rotation for Ag(110) in 0.25 M Na_2SO_4, pH = 5.8 at −0.2 V vs. Ag/AgCl. A p-polarized 1064 nm pump beam at a $\psi = 31°$ incident angle was used. (a) p-polarized SH intensity. The theoretical curve (solid line) is generated from Eq. (3-15) in the text by setting $a = 3.1$, $c^{(2)} = -0.83$, and $c^{(4)} = 0.08$. (b) s-polarized SH intensity. From Ref. 122.

was selected for these experiments to minimize the effect of the surface *dc* electric field on the SH response.

Rotational anisotropy has also observed at this wavelength for the Ag(110) surface examined under similar electrochemical conditions [122]. Fig. 5.2a and b correspond to the respective p- and s-polarized 532 nm SH response using an incident beam of p-polarization. Negligible anisotropy in the SH signal is observed for the s-polarized output within the sensitivity of this experiment. The p-polarized output (Fig. 5.2a) fits the theoretical form of Eq. (3.15) with several results of significance. Similar to Ag(111), a phase shift is observed between the isotropic coefficient, a, and the anisotropic coefficient, $c^{(2)}$. The relative magnitude of the $c^{(4)}$ term is found to be small and nonzero. The authors note that the relatively small magnitude of the $c^{(4)}$ term, which contains only bulk factors, is suggestive of the dominance of the surface contribution over the bulk.

Bulk interband transitions are not expected to contribute appreciably to the nonlinear response at the wavelengths discussed above. However, the results presented in these early studies by this group [74, 122, 123] clearly indicate that the anisotropic susceptibilities of Ag(111) and Ag(110) do not vanish even though the d bands for silver lie energetically higher than either the probe or SH photons. Several explanations for the observed behavior were offered [122]. Either the anisotropy indicates a deviation of the conduction band electrons from Drude-like behavior, or, surface states, possibly created by the double layer, exist and are resonant with the incident or outgoing beams. The authors discount the possibility that oxides were responsible for the anisotropy based on experimental tests and observations [122].

To verify the anisotropy observed on the silver surface and to attempt to understand the effect of the electrochemical solution on the surface electronic and structural properties, Bradley et al. [124] have examined the SH response from a Ag(111) surface in UHV. The experiments on this crystal were then repeated after an inert transfer to the electrochemical cell. The SH experiments performed in the electrochemical cell were again conducted at the PZC to minimize the effect of the *dc* electric field on the surface properties. Fig. 5.3 a and b show the results for the crystal examined in UHV for p- and s-polarized output at 532 nm. The solution data is consistent with the previous in-situ results of Koos et al. [122] shown in Fig. 5.1. More importantly, when the fits to the UHV data are compared to the subsequent results performed in solution, nearly identical values for the relative magnitudes of the *a* and $c^{(3)}$ coefficients are found (see Fig. 5.5 for comparison). Bradley et al. [124]

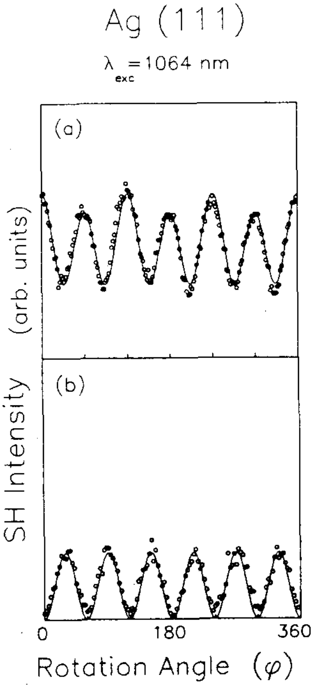

Fig. 5.3. SH rotational anisotropy from clean Ag(111) in UHV at 3×10^{-10} torr under p-polarized excitation at 1064 nm. The open circles represent the p-polarized (a) and s-polarized (b) SH data. Theoretical fits using Eqs. (3-11) and (3-13) are indicated with the solid line. From Ref. 124.

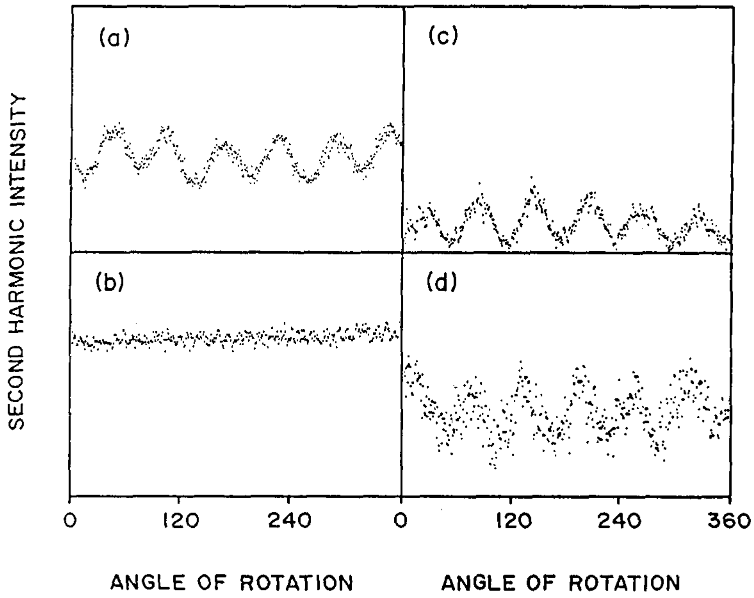

Fig. 5.4. p-polarized (a, b) and s-polarized (c, d) 532 nm SH intensity as a function of angle of rotation for an electrochemically roughened Ag(111) electrode. The data in (a) and (c) are for the unroughened surface; (b) and (d) were taken after several ORC's in a KBr solution. From Ref. 125.

conclude that the alteration of the surface optical dielectric properties at 1064 nm (532 nm SH) due to the presence of the water layer is negligible and that the SH measurements in solution are a good approximation of the properties of the surface prepared and analyzed in UHV [124].

The UHV results confirm the anisotropy from Ag but also raise the issue of the degree of sensitivity of SHG to defects and imperfections on the surface of the silver crystal. Although quantitative measurements of these effects have not been performed, the effects of surface roughening have been examined in both environments [124, 125]. In the solution, the roughening experiments were conducted by monitoring the rotational anisotropy after successive oxidation/reduction cycles [125]. Fig. 5.4 shows the results obtained for p-polarized excitation and p-polarized SHG (Fig. 5.4a and b) and s-polarized SH light (Fig. 5.4c and d). With successive ORCs in KBr the p-polarized output becomes progressively isotropic in nature. The effect on the anisotropy is observable in the p-polarized output after several monolayers of surface oxidation whereas the s-polarized output requires more vigorous oxidation. After oxidation and reduction of 15–20 monolayers of oxidation, the isotropic response shown in Fig. 5.4b for the p-polarized output is obtained. Fig. 5.4d shows the response from the s-polarized output after this amount of roughening. The isotropic *a* coefficient is most affected by the roughening which is consistent with the fact that the *a* coefficient contains tensor elements (Table 3.1) which have components normal to the surface (i.e. χ_{zzz}, χ_{zii} and χ_{izi}). The s-polarized SH response eventually becomes isotropic but the surface requires a more rigorous roughening procedure, corresponding to 20 – 30 monolayers of oxidation and reduction in KBr. Both the anisotropic coefficients $c^{(3)}$ (Eq. 3.11) and $b^{(3)}$ (Eq. 3.13) contain tensor element χ_{xxx} which lies within the plane of the surface and does not appear to be as surface sensitive as *a*. In the UHV experiments [124], when surface order is intentionally disrupted by ion sputtering, a decrease in the overall SH response is observed. The maxima and minima in the rotational scans become irregular in form and periodicity. Subsequent annealing of the crystal followed by slow cooling restores the originally observed anisotropy and the intensity increases.

In the studies discussed thus far, the potential has been maintained at the PZC in order to minimize the additional dc electric field contribution to the polarizability which can arise through the third order polarizability $\chi^{(3)}$ [24, 126] where

$$P_{dc}(2\omega) = \chi^{(3)} E_{dc} E(\omega) E(\omega) \ . \tag{5.1}$$

In general, $\chi^{(3)}$ is several orders of magnitude smaller than $\chi^{(2)}$ [78]. However, this contribution can be comparable to the second-order response when the dc field is large (i.e. $10^4 - 10^5$ V/cm) as is the case for a metal electrode in solution held at a bias on either side of the PZC. The SH fields can be viewed as arising from a sum frequency mixing process where two incident ac fields at frequency ω are mixed with a dc field at frequency $\omega = 0$ to produce a reflected and transmitted wave at frequency 2ω.

This additional contribution was first noted by Lee et al. [24] for polycrystalline silver and examined in more detail later by several groups on polycrystalline silver [44, 54, 58 – 60], single crystal bulk silver electrodes [7, 42, 43, 56, 127], and on thin silver films [55, 57, 101, 128]. For the early single crystal work [42, 43, 56] the studies were performed at a fixed electrode geometry with the crystal axis direction unknown relative to the incident beam.

How this additional field will alter the magnitude of the various tensor elements and the form of the rotational anisotropy has been examined by Koos et al. [122]. $\chi^{(3)}$ has the properties of a fourth-rank tensor such that the third order polarization has the form

$$P_i(2\omega) = \chi^{(3)}_{ijkl} : E_j E_k E_l \quad \text{where} \quad E_l = E_{dc} \ . \tag{5.2}$$

Making the appropriate transformations from surface to beam coordinates, Koos et al. [122] note that $\chi^{(3)}_{ijkl}$ has the same form as the second-order surface tensor $\chi^{(2)}_{ijk}$ as a result of the applied field being parallel to the surface normal. Because the field is localized at the surface, the $\chi^{(3)}$ effect should mimic the dipolar surface response with an effective susceptibility of

$$\chi^{(2)}_{eff} = \chi^{(2)}_{ijk} + \chi^{(3)}_{ijkl} E_l (l = 0) \tag{5.3}$$

where there is a one-to-one correspondence between the elements of $\chi^{(2)}$ and $\chi^{(3)}$. As a result, the application of an applied field should not be expected to change the symmetry observed in the rotational anisotropy, but the magnitude of the individual tensor elements, $\chi^{(2)}$ and $\chi^{(3)}$, may vary with potential. The phase of the tensor

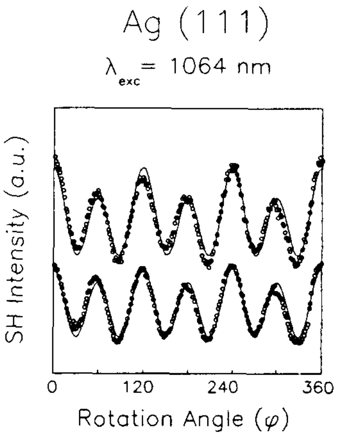

Fig. 5.5. Second harmonic intensity, $I_{\mathrm{p,p}}$, as a function of angle of rotation for Ag(111) in 0.25 M Na_2SO_4, pH = 5.0. An excitation wavelength of 1064 nm at an angle of incidence (ψ) of 45° was used. Lower trace: at −0.7 V (PZC), $c^{(3)}/a = 1.2\,e^{i86°}$; Upper trace: at −0.2 V (vs. Ag/AgCl), $c^{(3)}/a = 0.8\,e^{i86°}$. The solid lines are fits to the data generated from the theoretical expressions given in the text (Eq. (3.11)). From Ref. 174 and similar to that obtained in Ref. 122.

elements may also change if a potential dependent optical resonance at the surface is involved.

The experimental results for the potential dependence of the SHG from Ag(111) are consistent with this analysis [122]. As shown in Fig. 5.5 for the p-polarized input and output polarizations, the symmetry of the rotational anisotropy for Ag(111) in Na_2SO_4 is preserved as the potential is ramped from near the PZC at −0.7 V to the point where the surface has a large dc field at −0.2 V. However, the amplitude is clearly potential dependent as indicated by the change in the values for $c^{(3)}/a$ derived from the fit of Eq. (3.11) to the data. $I_{\mathrm{p,s}}$ gives little or no change in amplitude with positive bias. Earlier experiments from this group had shown a much stronger potential effect for $I_{\mathrm{p,p}}$ that appeared after the electrode was biased at the PZC for several hours [125]. The initial 6 maxima and minima pattern was found to convert to 3 maxima and minima with a nearly zero baseline. This was later attributed to traces of organic impurity ($\Theta < 1$ ML) that concentrates at the surface after extended potential bias (hours). Additional investigations into this effect showed that the change to a seemingly more "ordered" anisotropy pattern is merely a reflection of the changing electronic properties of the surface upon adsorption and not on the ordering of the molecular overlayer. A similar conclusion about the dominance of the metal in the presence of simple adsorbates has come from UHV studies by Hall and coworkers [8].

Further analysis of the SH potential dependence with 1064 nm excitation has been performed on these two electrode surfaces at fixed azimuthal angles of 30° for Ag(111), and 45° for Ag(110) [122]. With the appropriate choice of input and output polarizations, this allows the separation of the potential dependent behavior of the isotropic and anisotropic susceptibilities. The results are shown in Fig. 5.6a and b

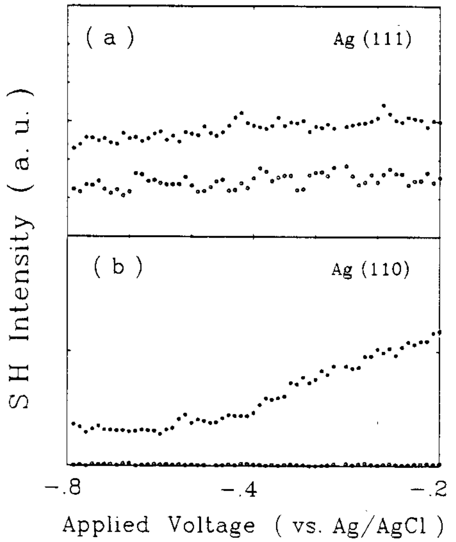

Fig. 5.6. p-polarized (upper) and s-polarized (lower) second harmonic intensity as a function of applied voltage for silver single crystals in 0.25 M Na_2SO_4, pH = 3.5. An excitation wavelength of 1064 nm and an incident angle of 45° was used. (a) Ag(111), $\Phi = 30°$; (b) Ag(110), $\Phi = 45°$. From Ref. 122.

where the potential dependence in the p-polarized (isotropic) and s-polarized (anisotropic) SH responses from Ag(111) and Ag(110) are shown. In the case of Ag(111) at an incident angle of 31°, a 30% increase in both the isotropic and anisotropic susceptibilities is observed (Fig. 5.6a). When the incident angle is varied, the change in the relative magnitude of the ratio of $c^{(3)}/a$ correlates with the angular dependence in the Fresnel coefficients. For the Ag(110) crystal (Fig. 5.6b), a 3.2 fold increase is seen in the isotropic response with no discernible effect on the anisotropic response. The authors note that reports of the relative change in SH amplitude with potential must be viewed with caution since the measurement is very sensitive to slight surface alterations such as surface roughness.

The potential dependence of silver evaporated films in electrolyte solution has been examined recently by Guyot-Sionnest et al. [101] as a function of angle of incidence. Although the SH variation with potential reported here has been previously examined in numerous studies [see Ref. 7], this work is a more extensive experimental and theoretical treatment of simple intensity changes from silver films. The films were assumed to be predominantly (111) orientated with unknown crystal orientation relative to the incident beam. Although no rotational anisotropy was measured, results pertinent to this summary were obtained. Fig. 5.7 shows the angular scans of the square root of the normalized SH response as a function of incident angle. The four curves represent different potentials examined. In accordance with previous work [7, 43, 55], they found that the surface contribution to the harmonic polarization is significant. Microscopic calculations based on the time-dependent density

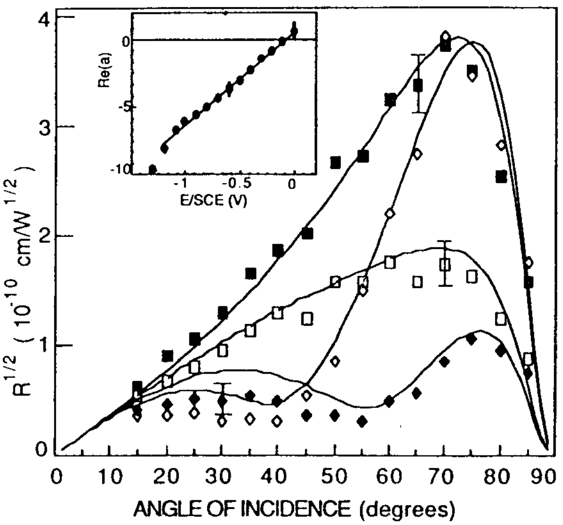

Fig. 5.7. $R^{1/2} = I(2\omega)^{1/2}/I(\omega)$ as a function of the angle of incidence for Ag(111) at 1064 nm for various potentials. The lines are fits as described in the text. Filled squares, 0 V (vs. SCE); open squares, -0.4 V; filled diamonds, -1 V; open diamonds, -1.3 V. Inset: The variation of Re $a(\omega)$ with potential. From Ref. 101.

functional approach applied to a jellium model shows qualitative agreement with the data as indicated by inspection of the data and fits in Fig. 5.7.

In much of the above analysis, the relative magnitude of the surface and bulk contribution to the nonlinear response has not been addressed in any detail. As noted in Section 3.1, in addition to the surface dipole terms of Eq. (3.9), there are also nonlocal electric-quadrupole-type nonlinearities arising from the bulk medium. The effective polarization is made of a combination of surface nonlinear polarization, $\mathrm{P}^{\mathrm{NS}}(2\omega)$ (Eq. (3.9)), and bulk nonlinear polarization (Eq. (3.8)) which contains bulk terms γ and ζ. The bulk term γ is isotropic with respect to crystal rotation. Since it appears in linear combination with surface terms (e.g. Eq. (3.5)), its separate determination is not possible under most circumstances [83, 129, 130, 131]. It mimics a surface contribution but its magnitude depends only upon the dielectric properties of the bulk phases. For a nonlinear medium with a high index of refraction, this contribution is expected to be small since the ratio of the surface contribution to that from γ is always larger than $\chi_S \varepsilon_2(2\omega)/\gamma$. The magnitude of the contribution from ζ depends upon the orientation of the crystal and can be measured separately under conditions where the anisotropic contribution of χ_s vanishes.

Estimates of the relative surface/bulk response have recently been made for Ag(100) and Ag(110) [131]. For a (110) surface, the bulk term ζ can be isolated in the anisotropic response using appropriate polarizations. For example, the anisotropic coefficient, $c^{(4)}$ in the expression for the p-polarized response from a (110) crystal is comprised solely of bulk terms (Table 3.1). By measuring $I_{\mathrm{p,p}}^{(110)}$ and fitting the data, the value for $c^{(4)}$ is found to be small relative to the magnitude of

$c^{(2)}$ which contains both surface and bulk terms. In a related experiment [131], $I_{p,s}^{(100)}$ and $I_{s,s}^{(100)}$ were measured as a function of rotation angle. For the (100) crystal face, the SH fields take the form of Eqs. (3.11) – (3.14) with m = 4. Referring to Table 3.1, the only contribution to $c^{(4)}$ and $b^{(4)}$ is from ζ, the bulk anisotropic response. Therefore, if any anisotropy in the signal is measured from the signal in $I_{p,s}^{(100)}$ or $I_{s,s}^{(100)}$, the signal must arise solely from the bulk. The authors find that using the experimental set-up and surface preparation conditions of previous studies [e.g. 74, 122], no anisotropic response above the background for these measurements can be observed. However, with more elaborate surface preparation and improvement in their optics, they have measured a very weak anisotropy in $I_{p,p}^{(100)}$. A fit to the data estimates $a/c^{(4)} = 0.028$ (± 0.003) where, again, $c^{(4)}$ contains only the bulk susceptibility, ζ. The authors caution that the situation may be different for other surfaces (e.g. the (111) face) due to the linear Fresnel coefficients which scale with the susceptibilities.

5.1.2 Wavelength Dependent Studies

All of the studies discussed above for silver have been done with an incident beam of 1064 nm. These studies have proven that the anisotropy in the nonlinear polarizability from the silver surface is not purely free-electron-like at these wavelengths, that the anisotropy can be correlated with surface symmetry, and that the SH response measured in situ is nearly identical to that measured in UHV. The issue of the sensitivity of the rotational anisotropy to surface electronic properties has been the topic of very recent work which has been conducted by variation of the incident wavelengths to where optical resonances in the bulk or surface electronic structure can be accessed.

The first studies to demonstrate the effect of optical resonance on the rotational anisotropy from a native metal were reported for Ag(111) and Ag(110) in solution [132], and Ag(111) in UHV [124]. Both sets of experiments were performed with incident 532 nm light and the SH photons collected at 266 nm. Fig. 5.8 a and b show the p- and s-polarized SH response from a Ag(111) electrode biased in solution at the PZC using an incident beam of p-polarized 532 nm photons [132]. The SH response at 266 nm for the two different output polarizations clearly reflects the C_{3v} symmetry of the surface. The p-polarized output (Fig. 5.8 a) is significantly different than what is obtained at the longer wavelength (see Fig. 5.1 a). Relative to the 532 nm SH response where the ratio $c^{(3)}/a$ is found to be $1.2e^{i86^\circ}$, at 266 nm a value of 0.7 is observed. The authors conclude that at the higher incident energy, the phase shift in the parameter $c^{(3)}/a$ as the wavelength varies is indicative of a resonance process where 2ω accesses interband transitions in the metal [132]. At 1064 nm excitation, both the fundamental and the second harmonic photon energies are well below the silver bulk interband transitions (3.8 eV) while at 532 nm excitation, the SH photon energy is 4.66 eV, well above the interband transition energy. In earlier work [75] the importance of interband transitions was proposed to explain the difference in rotational anisotropy at 1064 nm (SH 532 nm) between Ag(111), and the two other noble metals examined at the same wavelength, Cu(111) [77, 133] and Au(111)

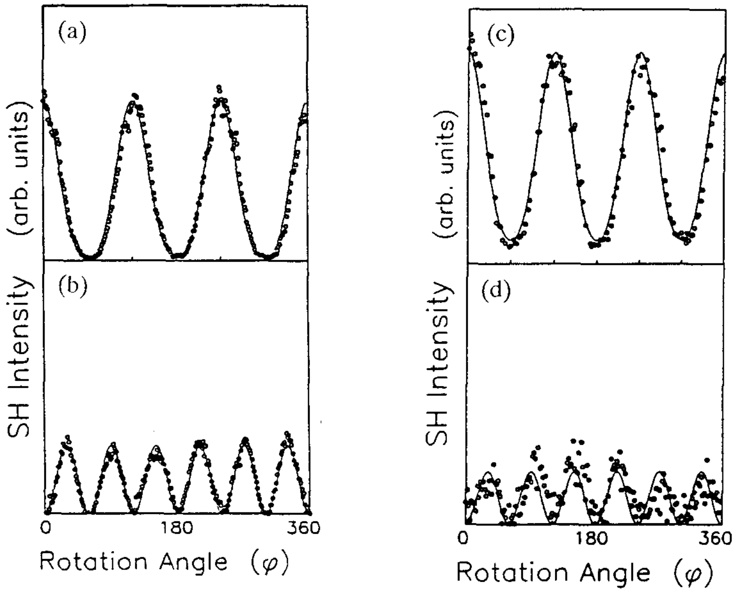

Fig. 5.8. Second harmonic intensity at 532 nm as a function of angle of rotation for Ag(111). An angle of incidence (ψ) of 45° was used with p-polarized incident radiation. The solid lines are fits to the data generated from the theoretical expressions given in the text (Eqs. (3.11) and (3.13)). (a) p-polarized SH response for Ag(111) biased in 0.25 M Na_2SO_4 (pH = 5.0) near the PZC, $c^{(3)}/a = 1.2(\pm 0.1)$. (b) s-polarized (SH) response from Ag(111) biased in 0.25 M Na_2SO_4, (pH = 5.0) near the PZC. (c) p-polarized SH response from Ag(111) in UHV, $c^{(3)}/a = 1.0(\pm 0.1)$. (d) s-polarized SH response from Ag(111) in UHV. The constant $b^{(3)}$ for (b) and (d) is taken to be unity. From Ref. 132.

[134]. The d bands of the latter two are in resonance with the 532 nm SH photons. These results are the first experimental evidence to support this early hypothesis.

Pertinent to this discussion is the examination of the rotational anisotropy from Ag(111) examined in UHV with 532 nm excitation by Bradley et al. [124]. The results are shown in Fig. 5.8c and d and can be compared with those measured in solution on the same crystal in solution (Fig. 5.8a and b). As with the longer wavelengths studied in both environments, the rotational anisotropy observed in UHV at 266 nm is nearly identical to that obtained in solution both in the magnitude and the phase of the coefficients used to fit the data (see figure caption).

In light of these wavelength dependent effects described above, Richmond and coworkers have recently completed a more extensive wavelength dependent study of the rotational anisotropy on Ag(111) [136, 137]. One set of experiments has involved the use of photons of lower energy in the infrared in an attempt to see if the rotational anisotropy would change as the incident and SH photons are more energetically removed from surface or bulk resonances [136]. They used the 1.53 μm output from an optical parametric oscillator which was pumped by the 1064 nm output of

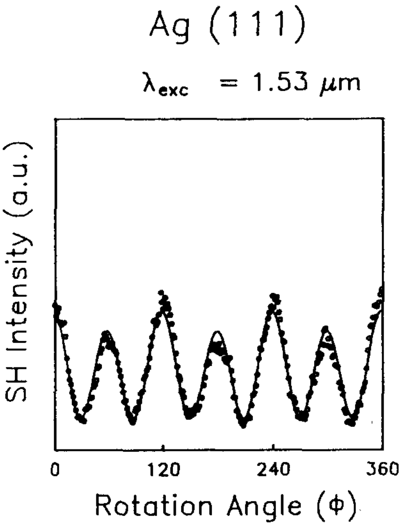

Fig. 5.9. p-polarized second harmonic intensity as a function of angle of rotation for Ag(111) in 0.25 M Na_2SO_4 in D_2O. Data was taken with p-polarized 1.53 μm illumination. Angle of incidence (ψ) was 45°. The solid lines are fits to the data generated from the theoretical expressions given in the text (Eq. (3.11)). From Ref. 136.

a 10 Hz Nd : YAG laser. To avoid absorption of the infrared light by the aqueous electrolyte solution, D_2O was used as the solvent. The results are shown in Fig. 5.9 for the p-polarized SH response from Ag(111) at 765 nm. The surface was biased at the PZC. Rotational anisotropy continues to be observed at this longer wavelength. The data collected was found to be remarkably similar to the results at 1064 nm in both form and fit to the theory. The readily observable anisotropy at incident wavelengths as long as 1530 nm is not easy to explain in terms of the known electronic band structure of silver and certainly is in contradiction with describing silver as a free electron gas even at these infrared wavelengths. While one can not *a priori* discount the possibility that the anisotropy observed at 1530 nm is due to the presence of the dipole layer, the striking similarity in the SH response from Ag(111) in solution and in UHV at other excitation wavelengths, including 1064 nm, leads the authors to believe that this anisotropy would also be present in UHV at 1530 nm in UHV. The persistence of SH anisotropy for Ag(111) at infrared wavelengths strongly suggests that theoretical approaches which go beyond the jellium model are needed. Although a simple surface charge density model [55, 56], which also presumes free electron behavior, can qualitatively fit the potential dependence (see below) of the SH response, it remains only an approximation of the behavior at best.

A second set of wavelength dependent measurements from Ag(111) have recently been reported by Georgiadis and Richmond [137]. These experiments have involved the collection of SH rotational anisotropy scans from Ag(111) at three fixed incident

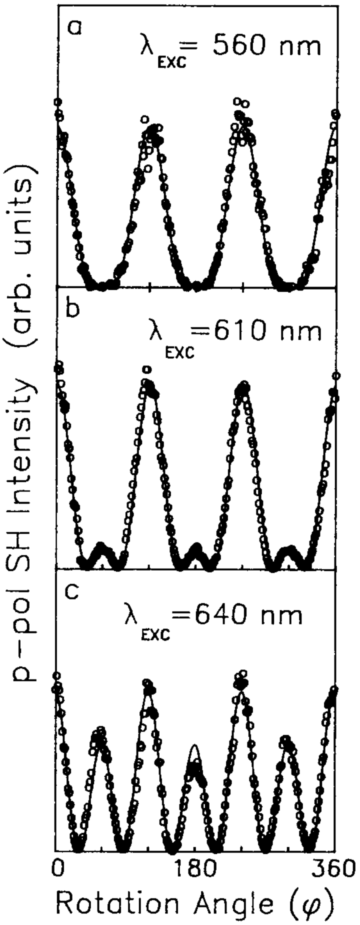

Fig. 5.10. p-polarized SH intensity as a function of azimuthal angle of rotation for Ag(111) in 0.1 $NaClO_4$ under p-polarized excitation at the wavelengths indicated. See Table 5.1 for fits to the data (solid lines). From Ref. 137.

wavelengths in the visible (560 nm, 610 nm and 640 nm) in addition to repeating the 1064 nm and 532 nm incident work. These wavelengths were chosen to determine if the SH photons generated at 320 nm (3.87 eV), 305 nm (4.06 eV) and 280 nm (4.42 eV), would show a progressive trend of coupling to surface resonances with increasing photon energy. Figure 5.10 shows the dramatic variation in the rotational anisotropy in the p-polarized intensity as the excitation wavelength is varied. All measurements were made at the PZC. The 3m symmetry is retained throughout and, as with previous wavelengths discussed, the data fit well to the functional form of Eq. (3.11). The results indicate that as the incident wavelength is shortened, the rotational anisotropy scans, and the derived values for the isotropic and anisotropic coef-

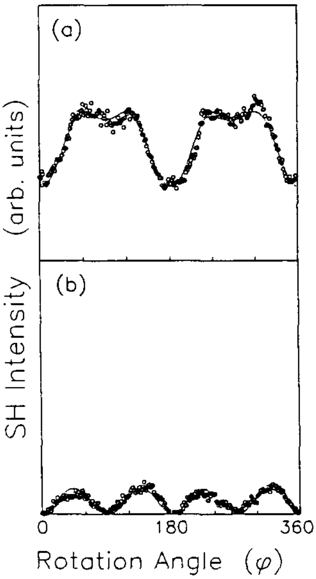

Fig. 5.11. Second harmonic intensity as a function of angle of rotation for Ag(110) in 0.25 M Na_2SO_4, pH = 5.0 near the PZC. A p-polarized 532 nm excitation beam was used at an incident angle (ψ) of 45°. The solid lines are fits to the data generated from the theoretical expressions given in the text (Eqs. (3.15 and 3.16)). (a) p-polarized SH intensity from Ag(110) with $a/c^{(2)} = -6.8$; $a/c^{(4)} = -15$. (b) s-polarized SH intensity from Ag(110) with $b^{(2)}/b^{(4)} = -24$. From Ref. 132.

ficients, show a progressive change from that observed at 1064 nm (Fig. 5.1 a) to that measured at 532 nm (Fig. 5.8 a). Table 5.1 summarizes the values derived from the fits to the data and shows that the magnitude of the ratio $c^{(3)}/a$ changes with incident photon energy, indicating different contributions from the in-plane anisotropic response relative to the isotropic response. More importantly, the phase difference between $c^{(3)}$ and a also varies as a function of photon energy, approaching 90° at the long wavelength limit. The convergence of $c^{(3)}/a$ to 90° is consistent with calculations of this ratio using the appropriate values for the linear Fresnel coefficients in the long wavelenght limit. The change in the phase between these coefficients at the shorter wavelengths is an indication that the SH susceptibility tensor, $\chi^{(2\omega)}$ passes into resonance as the SH frequency approaches electronic transition of the metal. While for a single susceptibility element this might be expected to result in as much as a 180° phase shift as a resonance is approached, the situation is more complicated for a ratio containing a number of elements in the numerator and denominator as in the case of $c^{(3)}/a$. In an extension of this study, Bradley et al. [135] have examined the rotational anisotropy from Ag(111) in UHV at the same wavelengths as the solution data. The anisotropies observed are nearly identical to those obtained in solution at the PZC.

These wavelength dependent effects are consistent with increased optical coupling to surface resonances with increasing photon energy. Georgiadis and Rich-

Table 5.1. Wavelength dependence of the rotational anisotropy from Ag(111) electrodes held at the PZC. Aqueous electrolyte (either 0.25 M Na_2SO_4) was used for all experiments. D_2O was used as a solvent for the 1.53 μm experiment. From Ref. 137. Fitting parameters from Eq. (3.11).

SH Photon Energy (eV)	λ_{exc} (nm)	Fitting parameters $c^{(3)}/a$
4.60	532	0.7
4.43	560	1.0
4.06	610	$1.85\, e^{i18^\circ}$
3.87	640	$5.4\, e^{i57^\circ}$
2.33	1064	$1.2\, e^{i86.5^\circ}$
1.62	1530	$1.2\, e^{i90(6)^\circ}$

mond also find that there is an abrupt change in the rotational anisotropy patterns and the magnitude and phase of $c^{(3)}/a$, in the region between 610 to 640 nm, a change of only 0.2 eV in the SH photon energy. They attribute this to additional structure such as a surface state. This is based on the expectation that transitions involving surface bands would be broader in energy than electronic transitions involving only surface electronic states. When the SH response is measured as a function of wavelength with a fixed azimuthal angle, a peak is observed near 3.85 eV ($\lambda_{exc} = 640$ nm) which is potential dependent. When the identical measurement is performed in UHV, the peak is also readily observable [135]. Georgiadis and Richmond [137] discuss these resonances in terms of the electronic band structure of Ag(111) and possible surface states near the interband threshold, which has an onset at about 3.9 eV.

Wavelength dependent studies have also been performed on Ag(110) at 532 nm incident wavelengths [132] and at intermediate wavelengths [138] and the results compared with the data at 1064 nm. The SH response at 532 nm is shown in Fig. 5.11 a and b for p- und s-polarized output, respectively [132]. Similar to the (111) surface, as the incident wavelength is lowered, there is a noticeable difference in the rotational anisotropy for the p-polarized output. Furthermore, comparison of the values of the coefficients derived from fitting the data to Eq. (3.15) shows that a phase shift has occurred between the isotropic (a) and anisotropic ($c^{(4)}$) coefficient with increased incident energy. The form of the rotational anisotropy for the s-polarized data is invariant at both wavelengths although the relative magnitudes of the SH response at 532 nm and 266 nm were not measured. At intermediate wavelengths, the rotational anisotropy scans show a progression suggestive of increased coupling to electronic resonances as the incident energy is increased [137]. Hicks et al. [139] have measured a sharp resonance in the SH response at about 320 nm for Ag(110) in UHV which they attribute to the Ag interband transition.

As described above, there is a strong wavelength dependence in the SH response from Ag(111) and Ag(110) in the visible region when the surface is biased at the

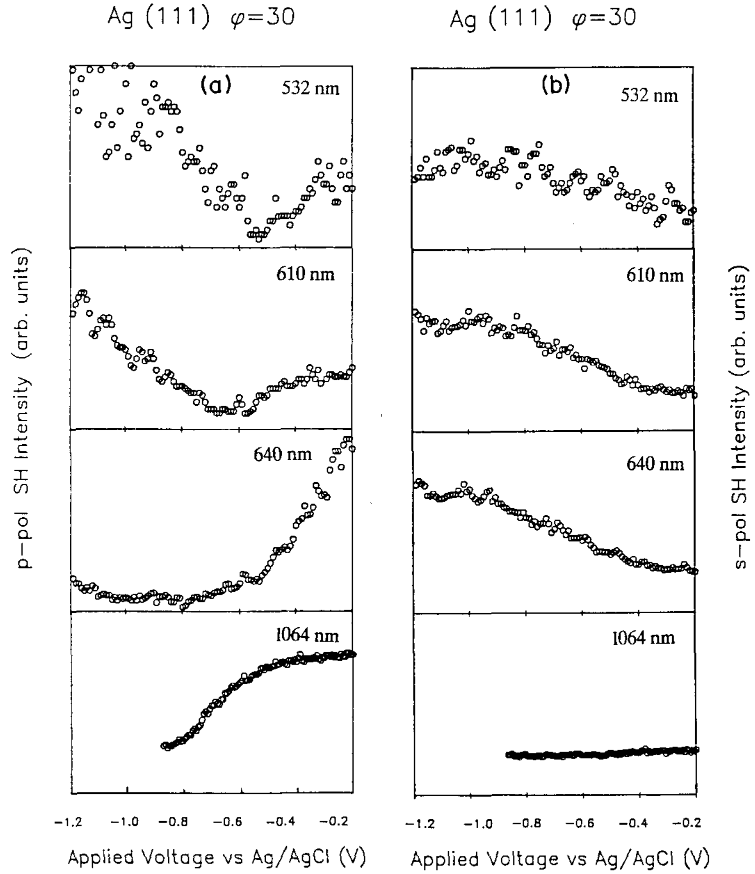

Fig. 5.12. Comparison of the potential dependence in isotropic (a) and anisotropic (b) components to the second harmonic intensity from Ag(111) at the indicated incident wavelengths. The solution was 0.25 M Na_2SO_4 at a pH of 3.5. An incident angle of 45° was used. From Ref. 132 and 137.

PZC. The effect of applied potential on the SH response has also been found to be very wavelength dependent. Richmond and coworkers have examined how this potential dependence in the SH response from Ag(111) [132, 137] and Ag(110) [132, 138] varies as the energy of the incident beam is increased. As the incident wavelength is changed, the rotational anisotropy with p-in and p-out polarizations show a dramatic variation as the voltage is biased by several hundred millivolts around the PZC. For example, with 610 nm excitation, the ratio changes from $c^{(3)}/a = 1.8\,e^{i86°}$ (−0.2 V) to $c^{(3)}/a = 1.1\,e^{i30°}$ (−1.2 V). These changes can more easily be monitored by fixing the rotational angle to isolate the respective anisotropic and isotropic response and varying the potential. Fig. 5.12 shows this large variation in the potential dependence in the SH response from Ag(111) as the incident wavelength is altered. The data has been collected at the appropriate angles to isolate the potential dependence in the isotropic (Fig. 5.12a) and the anisotropic (Fig. 5.12b) contributions to the overall response. At the longest wavelengths (1530 nm and 1064 nm), well below the interband threshold, the isotropic response shows the behavior which is consistent with nonresonant coupling of the optical field to the static applied field at the surface which increases as the surface becomes more positively charged. At the highest excitation energy the potential dependence deviates very strongly from such behavior, showing an overall decrease with positive charging. For intermediate energies, at 640 nm, the potential dependence is qualitatively similar to the behavior observed in the infrared, while at 610 nm and 560 nm excitation (not shown), the potential dependence resembles the behavior observed for 532 nm excitation.

The anisotropic contribution to the response with 1064 nm excitation is consistent with previous studies and the expectation that χ_{xxx} does not couple with the dc field in the z direction. For visible wavelength excitation, however, a significant potential dependence is observed. Although the potential dependence is qualitatively similar at these visible wavelengths, the relative magnitude of the isotropic and anisotropic response changes from 10:1 for 640 nm to 0.5:1 for 532 nm. Variation in magnitude of the anisotropic response with applied potential is suggestive of a resonant contribution arising from χ_{xxx}. These striking changes in both the isotropic and anisotropic response when the excitation wavelength is varied from 640 nm to 610 nm provides further evidence for the existence of a surface state in this region, a surface state which shifts in energy with potential.

Georgiadias and Richmond [137] have also performed phase measurements of the isotropic and anisotropic components of the response to verify the potential dependence of these resonances. For 1064 nm excitation they observe no significant phase shift in either the isostropic or anisotropic contribution to response as the potential is varied between -1.2 V and -0.2 V vs Ag/AgCl. This is consistent with what was observed in the potential dependence of the anisotropy for 1064 nm excitation in which there is almost no change in the imaginary component of the fitting parameter $c^{(3)}/a$ as a function of potential (see Fig. 5.5). For 532 nm excitation, a potential induced phase shift in both the anisotropic and isotropic components is observed, again consistent with the large change in $c^{(3)}/a$ as the potential is varied.

Similar potential-dependent experiments were performed on Ag(110) at various visible wavelengths. Unlike the results at 1064 nm (Fig. 5.6b), where the isotropic response is at a minimum at the PZC, a maximum in both the isotropic and anisotropic response is observed near the PZC followed by a rapid decline as the surface is charged positively. Although the analysis is somewhat more complicated for the Ag(110) due to additional parameters in the fit relative to Ag(111), the results are qualitatively similar to Ag(111) in that one observes increased coupling to surface resonances with increased photon energy. These resonances are also potential dependent.

Strongly potential dependent spectral features observed in the optical linear electroreflectance spectroscopy of various single crystal noble metal electrodes have been attributed to Stark shifts in surface states [105, 106, 140]. For the Ag(111)/electrolyte interface, an energy state is presumed to shift from about 5 eV at -0.20 V bias potential to about 4 eV at -0.80 V. An analogous explanation is suggested to account for the behavior of Ag(110), which is reported to have two surface states [105, 140] in the range of these experiments. These electronic states are not accessed at 1064 nm where the potential dependence is different and more reflective of the free-electron character of the metal. However, they suggest that a more complete theoretical treatment beyond the simple jellium or surface charge density model is needed which considers the effect of applied fields on the surface electronic band structure of the metal interface such as that recently reported by Aers and Ingelsfeld for Ag(001) at the vacuum interface [102].

Guyot-Sionnest and Tadjeddine have published related work on silver electrode surfaces [128]. The work was performed on silver evaporated films which are presumed to be of predominantly (111) orientation and the data was collected at a fixed and undefined crystal orientation. They also find that there is a distinct difference in the potential dependence in the overall magnitude of the SH response under unspecified polarization conditions for their Ag samples at 1064 nm and 532 nm incident wavelengths. They conclude that the response is free-electron in nature at the longer wavelength but that the nonlinear susceptibility of the d-electrons is dominant for the shorter wavelengths [128].

5.1.3 Underpotential Deposition Systems

Underpotential deposition (UPD) is the electrochemical adsorption and (partial) reduction of a submonolayer or monolayer of cations on a foreign metal substrate at potentials more positive than the reversible potential of the deposited metal [141]. The UPD phenomenon is used in many fundamental and applied studies because it offers a means of controlling coverages during electrodeposition in a very concise manner. Until recently, most of the information obtained about the structure of the overlayers deposited on single crystal surfaces has come from indirect means such as current-voltage analysis or by analysis of the deposited films after transfer to a UHV chamber [141].

Several studies have recently appeared which combine UPD and SHG on single crystal Ag, Cu (Section 5.2.3) and Au (Section 5.3.3). Ideally, one would like to be able to characterize the physical structure, the electronic properties and the growth dynamics of the interfacial region by SHG as deposition occurs. On the more fundamental side, one would like to gain further insight into the nonlinear polarizability at metal surfaces by taking advantage of the unique alterations in the surface properties that can be done easily by UPD. All of these issues have been addressed in the studies described below.

When an adsorbate is present at the surface of a metal, the interfacial region can be viewed as having an effective nonlinear susceptibility, $\chi^{(2)}_{\mathrm{eff}}$ where

$$\chi^{(2)}_{\mathrm{eff}} = \chi^{(2)}_{\mathrm{m}} + \chi^{(2)}_{\mathrm{a}}(\Theta) + \chi^{(2)}_{\mathrm{i}}(\Theta) \ . \tag{5.4}$$

In this expression, $\chi^{(2)}_{\mathrm{m}}$ corresponds to the underlying metal substrate, $\chi^{(2)}_{\mathrm{a}}(\Theta)$ represents the adsorbate susceptibility and $\chi^{(2)}_{\mathrm{i}}(\Theta)$ refers to the interaction region where bonding between the substrate and adsorbate exists. If there is a strong interaction between the substrate and adsorbate, and $\chi^{(2)}_{\mathrm{m}} \neq \chi^{(2)}_{\mathrm{a}}$, one would expect to see changes in the SH response corresponding to the interfacial region as the deposition begins. If one tunes to a frequency in resonance with the electronic properties of this interaction region, one might be able to map out interfacial states. A recent study has demonstrated this very convincingly for CaF_2 on Si(111) [142, 143]. For adsorption of simple molecules and ions on metal surfaces where $\chi_m^{(2)}$ is generally greater than $\chi_a^{(2)}$, the change in SHG upon adsorption can again be viewed as the adsorption causing a perturbation of the native metal, described in terms of $\chi_i^{(2)}$.

When foreign metals are adsorbed, one might expect that at coverages less than a monolayer, $\chi_m^{(2)}$ or $\chi_i^{(2)}$, would dominate. The interesting aspect of UPD systems is the relatively strong metallic bond that forms between the adatom and the substrate. This strong adsorption in fact plays an important role in electrochemical deposition since the work function change that this imparts on the surface region prohibits further adsorption without excursion to more reductive potentials. As deposition proceeds, one should eventually reach the point at which the overlayer takes on bulk properties and $\chi_a^{(2)}$ would start to be a factor. Ideally, if the optical properties of these regions corresponding to $\chi_a^{(2)}$, $\chi_m^{(2)}$ and $\chi_i^{(2)}$ are distinct, one could probe particular portions of the interface by simple wavelength variation.

In the one of the first nonlinear optical studies of UPD, Koos et al. examined the deposition of Pb and Tl on Ag(111) and Ag(110) [122, 144]. Fig. 5.13a and b

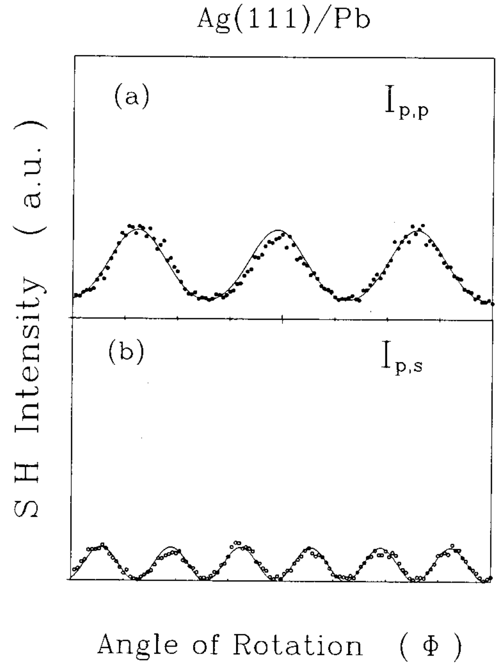

Fig. 5.13. SH intensity at 532 nm as a function of angle of rotation for Ag(111) in $NaClO_4$ containing Pb^{2+} at a lead coverage of one monolayer, E = −0.46 V (vs. Ag/AgCl). Solid lines are fits to the data using Eqs. (3.11) and (3.15) found in the text. (a) p-polarized SH, $c^{(3)}/a = -0.37$. (b) s-polarized SH, $b^{(3)} = 0.65$. From Ref. 122.

shows the respective p- and s-polarized SH response at 532 nm during deposition of Pb^{2+} on Ag(111). The corresponding CV shows a sharp peak corresponding to one monolayer as measured by integration of the current under the peak. The sharpness of the CV is generally assumed to be indicative of an ordered (111) substrate surface [141]. Prior to deposition, the native Ag(111) surface was found to give an anisotropy pattern similar to that shown in Fig. 5.1. A significant change in the p-polarized nonlinear response is observed upon adsorption. A change in the magnitude of the SH response had previously been observed on silver films [55]. The data in Fig. 5.13 indicates that the interfacial region retains 3 m symmetry upon deposition. When the p-polarized data is fit to Eq. (3.11), the ratio of $c^{(3)}/a$ has undergone a phase shift relative to the native surface. The s-polarized data shows a minor change in intensity only. An optical resonance between 2ω and electronic states of the Ag/Pb interface is presumed to be responsible for this phase shift.

Thallium deposition proceeds in a more complex manner but leads to some very interesting SH results [122]. The CV for the system is shown in Fig. 5.14 with the corresponding SH response during the various stages of deposition shown in Fig. 5.15 a–e. The first three deposition peaks in the CV (A_1–A_3) are assumed by previous studies to correspond to the sequential formation of two intertwined

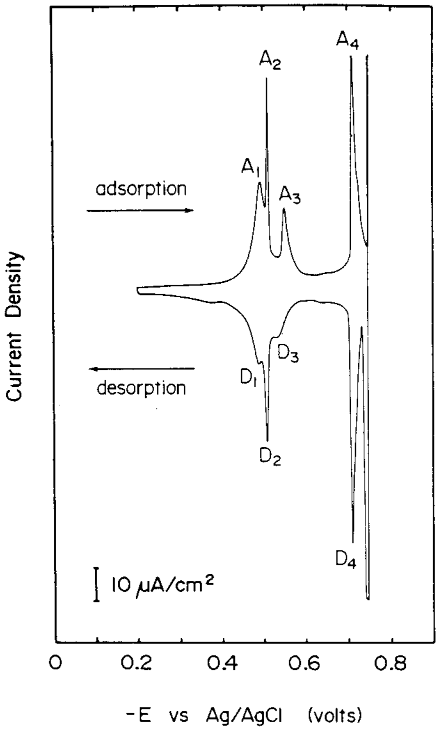

Fig. 5.14. Cyclic voltammogram for Ag(111) in 0.25 M Na_2SO_4 and 5 mM Tl_2SO_4, pH = 3.2, sweep rate = 10 mV/s. From Ref. 122.

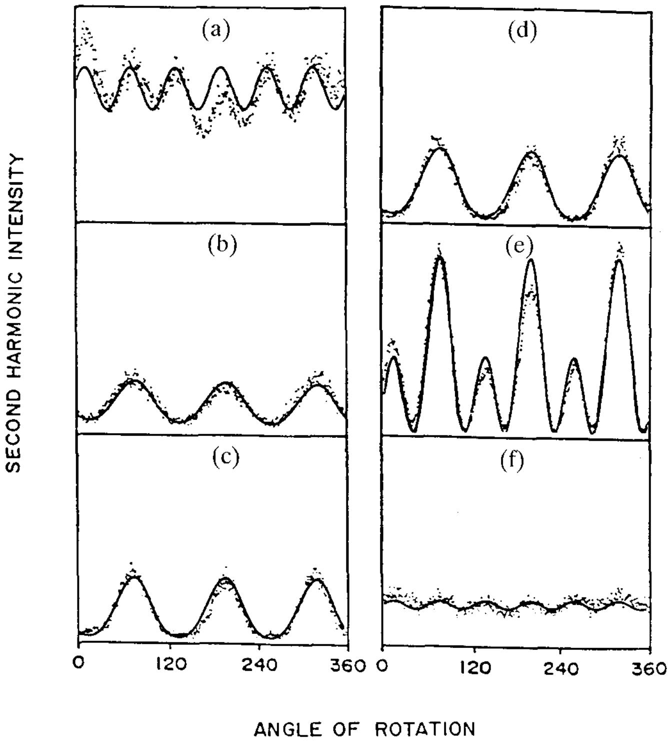

Fig. 5.15. Dependence on Tl coverage (Θ) of the p-polarized SH intensity as a function of angle of rotation for Ag(111) electrode in 1.0 mM Tl_2SO_4/0.25 M Na_2SO_4 at: (a) 0.00 V (vs. Ag/AgCl); (b) -0.52 V (A_1); (c) -0.57 V (A_2); (d) -0.67 V (A_3); (e) -0.85 V (A_4); (f) -0.90 V (bulk region). From Ref. 144.

$p(\sqrt{3}\times\sqrt{3})R\,30°$ overlayers that are subsequently filled in to form a complete monolayer before bulk deposition occurs [4]. A second monolayer (A_4) is also formed before bulk deposition occurs (-0.8 V vs. Ag/AgCl). Deposition of the first monolayer modifies the p-polarized response observed in the rotational scan in the same way as lead. The 3 m symmetry expected from the (111) surface is retained, and a phase shift is introduced between a and $c^{(3)}$. Upon adsorption of the second monolayer, the relative magnitudes of the susceptibility elements change from $|c^{(3)}/a| < 1$ to $|c^{(3)}/a| > 1$ and the intensity levels are enhanced significantly.

Although the rotational anisotropy scans are informative, considerably more information can be obtained by separate determination of changes in the isotropic and anisotropic components of the surface susceptibility tensor as done by Koos et al. [122]. The experiments consist of monitoring the SH intensity at a fixed angle of $\phi = 30°$ where $I^{SH}_{p,p} \propto |a|^2$ and $I^{SH}_{p,s} \propto |b^{(3)}|^2$. The results shown in Fig. 5.16 are displayed in terms of thallium coverage. The data has been fitted to a simple linear Langmuir isotherm model of Heinz [79] where the adsorbate contribution to $\chi^{(2)}$ varies linearly with coverage such that

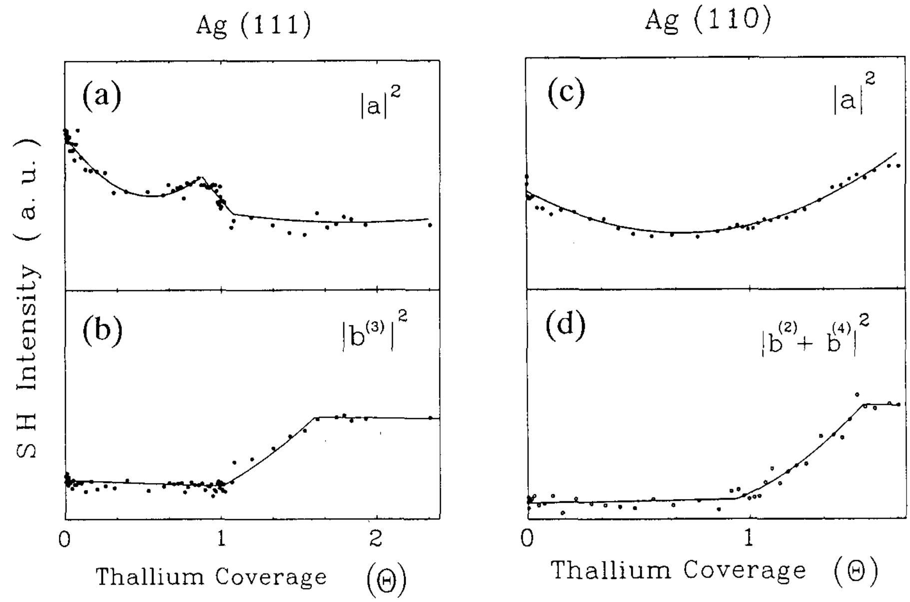

Fig. 5.16. Second harmonic response for Ag(111) (a,b) and Ag(110) (c,d) in 5 mM Tl_2SO_4 as a function of thallium coverage (Θ). Incident wavelength = 1064 nm. (a) p-polarized signal at $\Phi = 30°$ where $I^{SH} \propto |a|^2$ (Eq. (3.11)); (b) s-polarized signal at $\Phi = 30°$ where $I^{SH} \propto |b^{(3)}|^2$ (Eq. (3.13)); (c) p-polarized signal at $\Phi = 45°$ where $I^{SH} \propto |a|^2$; (d) s-polarized signal at $\Phi = 45°$ where $I^{SH} \propto |b^{(2)} + b^{(4)}|^2$. The solid lines are fits to the data using a Langmuir model. From Ref. 122.

$$\chi_{\mathrm{eff}}^{(2)} = \chi_{\mathrm{m}}^{(2)} + \chi_{\mathrm{a}}^{(2)}(\Theta)_{\mathrm{l}} \ . \tag{5.5}$$

Due to the strong bond between the metal and adatom for UPD systems, a more appropriate model at the low coverage might be $\chi_{\mathrm{a}}^{(2)} = \chi_{\mathrm{i}}^{(2)}$. At higher coverages of $\Theta > 1$, a third susceptibility was added to account for changes in the adsorption site due to adatom interactions which change the optical response of the interface, or,

$$\chi_{\mathrm{eff}}^{(2)} = \chi_{\mathrm{m}}^{(2)} + \chi_{\mathrm{a}}^{(2)}\Theta_1 + \chi_{\mathrm{a}}^{(2)\prime}(\Theta_2 - \Theta_1) \ . \tag{5.6}$$

The ratio of susceptibilities and their phase differences are used as fitting parameters.

For the isotropic response, discrete changes are observed up to approximately one monolayer whereas further adsorption has no effect. This might be viewed simplistically as the localization of electrons as the electronegative thallium atoms bond to the silver surface. According to the best fitting parameters, $\chi_{\mathrm{a}}^{(2)}$ makes a significant contribution at coverages up to 0.87 ML with $\chi_{\mathrm{a}}^{(2)}/\chi_{\mathrm{m}}^{(2)} = 0.94$. An abrupt change in the isotropic response is then observed between 0.87 and 1.0 ML. For the anisotropic response, a large change occurs upon formation of the second monolayer. The authors [122] attribute this large change to a resonance between

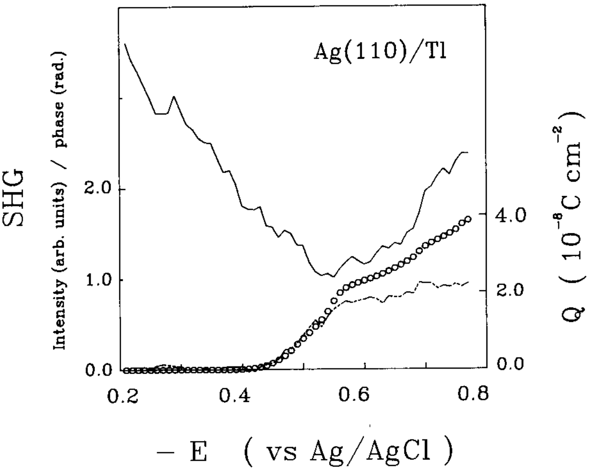

Fig. 5.17. Changes in the SH intensity (solid line), phase (broken line), and cathodic charge passed (open circles) as a function of applied bias potential. Ag(110) in 0.25 M Na_2SO_4, 5 mM Tl_2SO_4, pH = 3.0. Incident wavelength = 1064 nm. From Ref. 146.

either ω and 2ω with eigenstates in the overlayer, which beyond one monolayer approaches three-dimensional bulk thallium structure. Bulk interband transitions are predicted by theory and observed experimentally for thallium in this wavelength region [145]. A similar analysis beyond two monolayers of deposited Tl was not performed.

The electrodeposition of thallium on Ag(110) is similar to that which takes place on the (111) face of silver [122]. The voltammogram shows well-defined structure in the formation of the first monolayer, and further deposition occurs before formation of the bulk deposit. Fig. 5.16c and d display the results for the isotropic and anisotropic response respectively. The magnitude and phase of $|a|^2$ were modeled by a constant contribution from the adatoms throughout the adsorption process (Eq. (5.4)). Values of $\chi_a^{(2)}/\chi_m^{(2)} = 0.94$ and a phase shift of 131° were obtained. As with Ag(111), an enhancement in the anisotropic response was observed beyond 1 monolayer and was attributed to a similar resonance effect.

The model used to describe this data is a good starting point but a more accurate means of measuring the relative substrate/adatom interaction is to combine the results with a direct phase measurement during the deposition. This type of a measurement was performed recently by Koos and Richmond for Tl/Ag(110) [146] in an experimental geometry described in Section 4.3. Fig. 5.17 shows changes in the relative phase of the isotropic SH response, as well as the SH intensity and cathodic charge passed, as thallium is plated onto the Ag(110) by varying the bias potential. The sensitivity of phase measurement to the deposition process as opposed to charging effects is evident in the figure. A complete picture of the nonlinear response can be gained by presenting the phase and intensity data in a phasor plot which is shown in Fig. 5.18. In this representation, the square root of the SH intensity corresponds

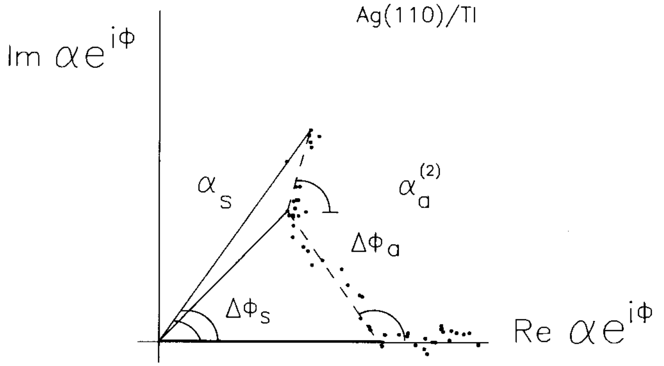

Fig. 5.18. Phasor diagram for the components of the SH polarizability as a function of thallium coverage (Θ) on Ag(110) where $\alpha e^{i\phi} = \Sigma_{j=x,z} \Sigma_{kl} F_{jkl}\chi^{(2)}_{jkl}$ and F_{jkl} are the Fresnel coefficients. Incident wavelength = 1064 nm. Solid lines are vectors representing $\sqrt{I_{SH}}$, and phase, $\Delta\phi_s$, for coverages of $\Theta = 0$, 1 ML and 2 ML. Broken lines are vectors representing the adsorbate contribution to $\sqrt{I_{SH}}$ and phase, $\Delta\phi_a$, at coverages of $\Theta = 1$ ML and 2 ML. Data at intermediate coverages are represented by the filled circles. From Ref. 146.

to the length of a vector whose orientation is determined by the measured phase. The zero of the angular scale is arbitrarily defined as the phase measured for the native surface. While intensity changes can be adequately modeled by coverage dependence in a single component of $\chi^{(2)}_{\text{eff}}$ (Fig. 5.16a), the phasor plot shows that at higher coverages an additional component is involved [146].

Thallium deposition on Ag(111) has also been studied by Miragliotta and Furtak using a continuous wave Nd:YAG laser [145]. In this study and a related study of the UPD of Zn and Cd on Ag(111) [147], the anisotropy from the native substrate surface was not observable. However, the sensitivity to the deposition in all cases is evident. For thallium deposition, the intensity in the SH response is significantly enhanced at 2 ML as mentioned previously [122, 147]. A 3m rotational symmetry is observed in the SH response. By using a thin-layer cell, they were able to extend the deposition in a controlled manner to up to 4.1 monolayers. The symmetry observed was similar to that obtained at the lower coverage. They propose that Tl grows with a coincidence lattice that is (6×6)-25 for all coverages. Significant to this and the previous analysis was the report of reflectivity measurements during deposition. A peak at 1.5 eV was observed upon formation of 1 ML of thallium on the surface [145].

Several other studies have appeared for Tl deposition on polycrystalline Ag which are pertinent to this discussion. The work of Furtak et al. [148] shows the sensitivity to the deposition of thallium on mechanically polished silver surfaces. They attribute a decrease in observed intensity prior to Tl deposition to a physisorbed state of Tl on the silver surface. In another study, Robinson and Richmond [54] performed time-resolved measurements on the deposition of Tl on electrochemically polished polycrystalline silver. Sharper UPD peaks were observed in this study compared to the previous work. The interesting aspect of this work was the sequential nature by which the deposition occurs following a fast potential step into the UPD region. The kinetics of growth of the first A_1 and A_2 peaks of Fig. 5.14 were modelled and the kinetic results compared to their current transient analysis. It is most likely that a similar sequential growth also occurs on single crystal silver surfaces and would be interesting to examine in angularly resolved studies similar to those discussed later for Cu(111).

The UPD of Cd [147] and Zn [145, 147] on Ag(111) were also examined by Furtak and coworkers using a cw laser. Both metal adsorbates were found to produce significant increases in the SH response upon adsorption. For Zn, where the symmetry of the SH pattern is of C_{3v} initially, the symmetry is found to change to twofold with further coverage. The results are consistent with an epitaxial 8.6% expanded hexagonal monolayer for Zn, followed by a return to the Zn lattice constant at higher coverage. The enhancement is attributed to resonance with interband transitions which occur in crystal zinc. For Cd, they have reported resonant SHG from Cd as the monolayer is formed in a three-step process. Each step is presumed to be associated with one-third of a monolayer having $(\sqrt{3}\times\sqrt{3})\mathrm{R}\,30°$ symmetry. The overlayer is assumed to be epitaxial and buckled below two monolayers. Above two monolayers the entire overlayer appears to become incommensurate and close packed.

5.2 Cu(111) and Cu(100)

5.2.1 Rotational Anisotropy Measurements

The SH response from Cu(111) has been examined in two studies, one in UHV and one in the electrochemical cell. The study by Tom and Aumiller [77] was the first to demonstrate rotational anisotropy from a metallic surface. The study involved excitation at 1064 nm with the SH response monitored at 532 nm. The anisotropy has been attributed to the excitation of interband transitions since the energy of the SH photons (2.3 eV) is large enough to promote d electrons into the sp conduction bands. Similar SH experiments on Cu(111) measured in the electrochemical cell were later reported [133]. Fig. 5.19 shows the variation in the p- and s-polarized second harmonic intensities upon excitation with 1064 nm. The 1064 nm data correlates well with that observed in UHV [77]. Although the fits give a ratio of $a/c^{(3)}$ which is slightly higher than that obtained in vacuum, the anisotropy is qualitatively the same. Shannon et al. [133] attribute the difference in the ratio to sample preparation and experimental geometry, both of which would affect the isotropic coefficient a. The same measurements were recently performed in solution with 532 nm excitation [149]. The results show that there is little variation in the anisotropy as the wavelength is shortened. Based on the conclusions at 1064 nm, one would expect that resonance effects would be even stronger at the shorter wavelengths since both the fundamental and the SH fields can couple to electronic bands in the metal. This is in contrast with the Ag(111) results where there was a distinct difference between the 1064 nm and 532 nm data. Recall from above that the anisotropy observed for

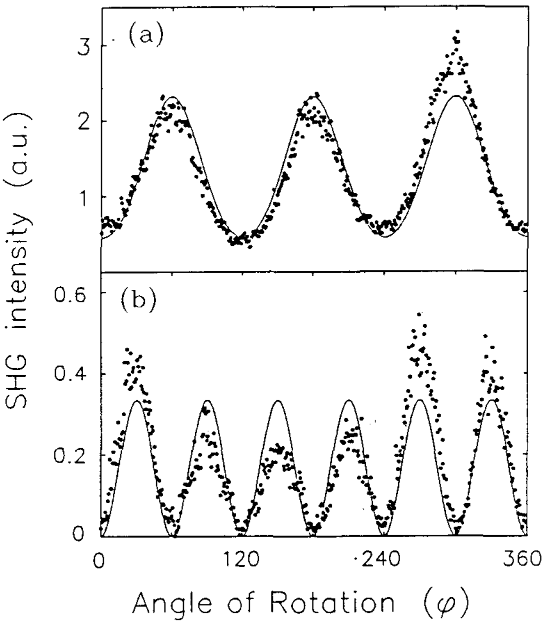

Fig. 5.19. Second harmonic intensity (p-polarized input) as a function of angle of rotation for a Cu(111) electrode in 0.25 M Na_2SO_4 solution at open circuit. Incident wavelength = 1064 nm. The solid lines are fits to the data using Eqs. (3.11) and (3.13); (a) p-polarized SH intensity at 532 nm, $c^{(3)}/a = -0.50$ and (b) s-polarized SH intensity at 532 nm. From Ref. 133.

Ag(111) with 532 nm (Fig. 5.11) where interband transitions were proposed to play an important role, is similar to that obtained for Cu(111) at both wavelengths.

The potential dependence of the SH response from Cu(111) electrode has also been examined [133]. The symmetry in the anisotropy is found to be invariant with potential in agreement with what is expected theoretically for an applied field parallel to the surface normal, assuming that no potential induced morphological changes in the surface occur [122]. In addition, no significant changes in either the p- or s-polarized SH intensity are observed as the potential is varied between the anodic limit at −0.2 V (also the PZC) and the cathodic limit at −0.8 V. The authors believe that this constancy in the response indicates that the electron density is not significantly altered with potential variation. They cite previous ATR and electroreflectance studies which found this invariance with potential in this region [150]. Note that the double layer charging region resides primarily negative to the PZC for Cu(111) whereas the strong potential dependence observed for Ag(111) (0.0 V to −1.0 V) was found positive to the PZC (−0.79 V). Sampling the SH response for Cu when the electrode is positively charged is difficult due to the onset of oxidation which occurs just positive of the PZC.

The nonlocal response from Cu was examined for Cu(100) in experiments similar to those described for Ag(100) above [131]. The s-polarized SH intensities from either p- or s-polarized excitation at 1064 nm showed very low signal levels. Any response above the background did not vary periodically as the crystal was rotated. The authors concluded that the data is consistent with a dominance of the surface terms over the bulk at this incident and SH wavelength.

5.2.2 Underpotential Deposition

The underpotential deposition of Tl on Cu(111) has been examined by Shannon et al. [133] under static conditions, and Richmond and Robinson in the time domain [117]. A large mismatch between the copper and the thallium lattice constants makes it an interesting case for comparison with the Tl/Ag(111) SH study described above [122] where the lattice constants are more closely matched and the overlayer has been shown to form in an ordered manner. From strictly geometrical considerations, the silver lattice is able to accommodate a thallium overlayer without buckling. On the copper substrate, a close-packed thallium overlayer must be either buckled or rotated with respect to the substrate lattice.

The SH analysis of the copper system is a bit more complicated from several perspectives. The electrochemistry is not as well known for copper and trace amounts of oxygen can disrupt the deposition process [151]. The integrated deposi-

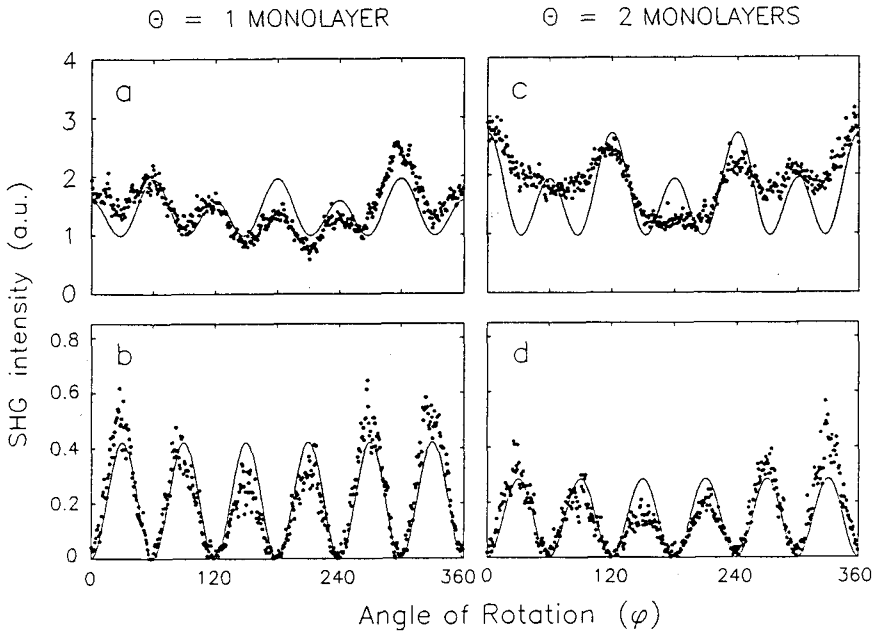

Fig. 5.20. p-polarized (a,c) and s-polarized (b,d) SH intensity vs. angle of rotation for one and two monolayers of thallium deposited on Cu(111). Incident wavelength = 1064 nm. Theoretical curves (solid lines) are generated by using Eqs. (3.11) and (3.13). (a) $c^{(3)}/a = -0.9\,e^{i84°}$ and (c) $c^{(3)}/a = 1.15\,e^{i80°}$. From Ref. 133.

tion currents in this study for the various peaks in the UPD curves can not be easily correlated with any kind of an ordered overlayer on the underlying substrate. The stripping CV curves are found to be considerably different than the deposition results. Minor changes in the voltammetric data were observed when the electrode was held at a bias potential where one or two monolayers of thallium were present on the electrode surface for several minutes. Such behavior is indicative of surface reconstructions or structural transformations [141]. Although conclusions about overlayer properties based on CV curves should be viewed with caution, the electrochemical results reinforce the idea that the thallium grows in an incommensurate, or possibly disordered, manner in this study [133].

The rotational anisotropy in the SH response observed for Tl coverages of one and two monolayers on Cu(111) is shown in Fig. 5.20a–d [133]. The p-polarized SH response is clearly sensitive to the various stages of deposition as is determined by the changing intensity patterns. Although the patterns for the p-polarized data become irregular in form with increasing deposition, the 3-fold symmetry is retained. The analysis also included measurements of the relative changes in the isotropic and anisotropic contributions to the polarizability by judicious choice of azimuthal angles which simplify the sinusoidal functions. Any possible changes in the anisotropic coefficients were found to be within the S/N for these experiments. If the lateral interactions between Tl atoms became significant, this would be expected to appear in changes in the anisotropic coefficients. In contrast with Tl on Ag(111) [122], no enhancement was observed in the anisotropic response corresponding to a development of a distinct thallium overlayer. The changes in the isotropic response observed with coverage were confirmed to be responsible for the varying anisotropy in the p-polarized output of Fig. 5.20a and c.

5.2.3 Time Resolved Measurements

A later study of thallium deposition on Cu(111) has been performed by Robinson and Richmond [117] with the intention of monitoring the growth of the overlayer in the time domain. The experiments involved measuring the rotational anisotropy at various stages of deposition, followed by monitoring the time evolution of the deposition at a fixed rotation angle. A Nd:YAG mode-locked laser was used in these studies. Appropriate angles were chosen to allow the separate isotropic and anisotropic temporal SH responses to be monitored. The static rotational anisotropic response from the native Cu(111) surface was qualitatively similar to that obtained by Shannon et al. [133]. The 3m symmetry was retained throughout the deposition. However, in the later study, variations in the anisotropic component ($I_{p,s}$) were observed as the thallium was deposited up to 2 ML. There was also no evidence of a disordered overlayer as was seen in the previous work [133]. Robinson and Richmond [117] suggest that these differences between the two studies could be due to several factors, the most likely being either different surface preparations or the presence of trace amounts of oxygen in the initial study which is known to disrupt the deposition process [151]. It is interesting to compare these two studies with the x-ray scattering work of Materlik et al. [151] in which Tl adsorption on Cu(111) has been ex-

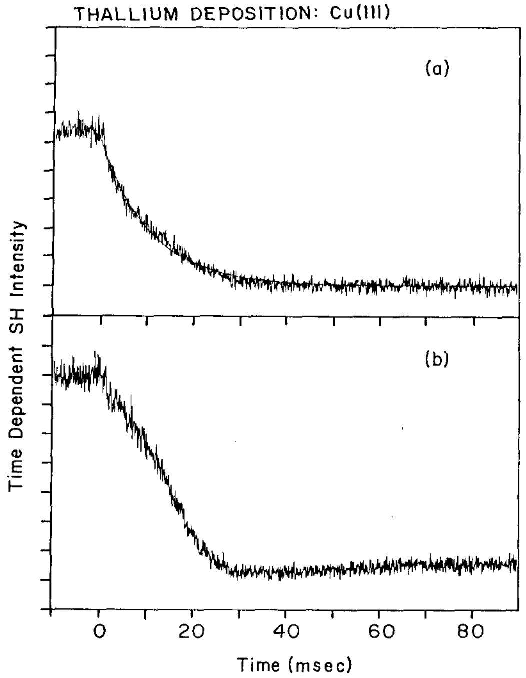

Fig. 5.21. Transient SH response of a Cu(111) electrode during thallium underpotential deposition. Incident wavelength = 1064 nm. (a) Isotropic SH signal, $I_{p,p}(t)$. The solid line is a single exponential fit to the entire transient with time constant, $\tau = 10.7 \pm 0.3$ msec. (b) Anisotropic SH signal, $I_{p,s}(t)$. The intensity scale is 2X more sensitive than in (a). From Ref. 117.

amined using x-ray standing waves. They performed this experiment under oxygen-free and oxygen-rich solution conditions. In the absence of oxygen, they found that Tl adsorption takes place at twofold sites together with a contraction of the Tl radius by 3% relative to the oxygen-containing electrolyte. Adsorption of thallium in the presence of oxygen was concluded to occur at threefold sites. Although the effect of oxygen on the position of the topmost Cu layer is controversial, an inward shift of the Cu layer by about 0.3 Å has been deduced from other scattering data [152]. Theoretical calculations suggest that the oxygen atoms build in below the top layer, thereby pushing the Cu atoms out of the surface and opening a larger threefold hole for the Tl atom binding [153]. No conclusions regarding the lateral structure of the overlayer could be deduced from this x-ray scattering data.

The results for the time-resolved measurements of Richmond and Robinson for Tl adsorption on Cu(111) are shown in Figs. 5.21 and 5.22 [117]. Fig. 5.21 shows the time dependent SH response of a Cu(111) electrode as thallium is deposited to a coverage of 0.87 ML. The plane of incidence is fixed at 30 degrees with respect to the $[2\bar{1}\bar{1}]$ crystal direction and the 1064 nm incident laser beam. The response time of the cell was 2 msec. Fig. 5.21 a shows the transient behavior of the isotropic contribution to the SH response, $I_{p,p}(t) \propto [a^{(3)}(t)]^2$. Fig. 5.21 b contains the correspond-

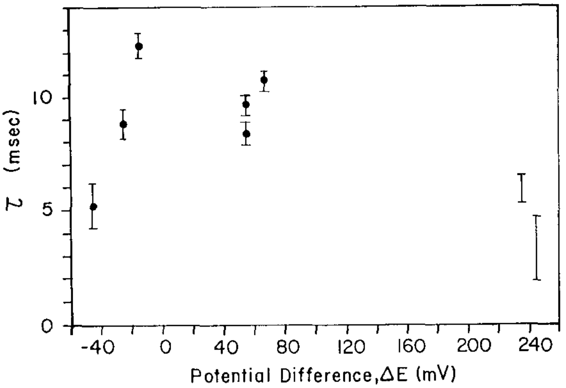

Fig. 5.22. The variation in τ for fits to various $I_{p,p}(t)$ signals obtained for potential steps cathodic (overpotential, $\Delta E > 0$) and anodic of the potential of the peak current for single monolayer formation. The error bars for data at $\Delta E < 80$ mV are two standard deviations. The error bars at $\Delta E = 235$ and 245 mV are the range of τ that fit different time segments of the decaying signal. From Ref. 117.

ing time dependent anisotropic contribution, $I_{p,s}(t) \propto [b^{(3)}(t)]^2$. For the potential step from −0.20 V to −0.55 V shown, both the isotropic and the anisotropic components of $\chi^{(2)}$ initially decrease and reach a minimum near 30 msec, where the coverage is about 2/3 ML. Further thallium deposition, as evidenced by the current transients obtained concurrently (not shown), produces no change in $I_{p,p}(t)$ whereas $I_{p,s}(t)$ increases. These SH results demonstrate that the completion of the overlayer at coverages exceeding 2/3 ML affects only the anisotropic elements of $\chi^{(2)}$.

Although both SH transients in Fig. 5.21 fall to a minimum at about the same time, their form is quite different and qualitative comparisons are useful. The isotropic contribution, $I_{p,p}(t)$, decays as a single exponential, in agreement with previous measurements of submonolayer thallium deposition on polycrystalline electrodes [54]. The solid line in Fig. 5.21 a is an exponential fit with $\tau = 10.7$ msec. The exponential form suggests that the deposition occurs by an absorption, rather than a nucleation, mechanism [154]. The transient anisotropic response is not as simple. In fact, the initial fall in $I_{p,s}(t)$ in Fig. 5.21 b is not a simple decaying exponential. The differing time dependencies for the isotropic and anisotropic responses suggests that ζ, the bulk anisotropic susceptibility element which is the only common element, is not the main source of the nonlinear response in either case.

Robinson and Richmond [117] also found that the time constant for adsorption of the first thallium overlayer depends on the final potential, E_f, of the potential step. They investigated the effect of underpotential and overpotential steps on the best fit values of τ for exponential fits to $I_{p,p}(t)$. The under- and overpotentials, ΔE, are defined with respect to the maximum of the current peak, E_p, in the CVs for the first monolayer deposition. Fig. 5.22 displays the results for seven different potential steps. The time required to form the deposit increases at anodic potentials ($\Delta E < 0$) closest to E_p, indicating that more time is required to deposit successively larger coverages. The form of the data suggests that τ would reach a maximum near

$\Delta E = 0$. In the overpotential region, where the final coverage should be independent of E_f, the overlayer is formed faster as the overpotential increases. The result suggests that activation energy is supplied by the overpotential. Similar results were reported in related SHG measurements of the UPD kinetics of thallium deposition on polycrystalline electrodes within the overpotential region [54].

5.3 Au(111), Au(110), and Au(100)

5.3.1 Rotational Anisotropy Measurements

Several studies have appeared which examine the SH response from bulk single crystals of gold under potential control. The first study reported was that of Koos [134] in which both the native and underpotential deposition of thallium was studied. This was later examined in more detail for a series of different metals on Au(111) [155]. Fig. 5.23 shows the SH intensity from Au(111) in $HClO_4$ as a function of the azimuthal angle Φ. The SH response using a 1064 nm incident beam was collected for p-polarized input and p- and s-polarized output (Fig. 5.23 a and c) and s-polarized input and p-polarized output (Fig. 5.23 b). The responses are consistent

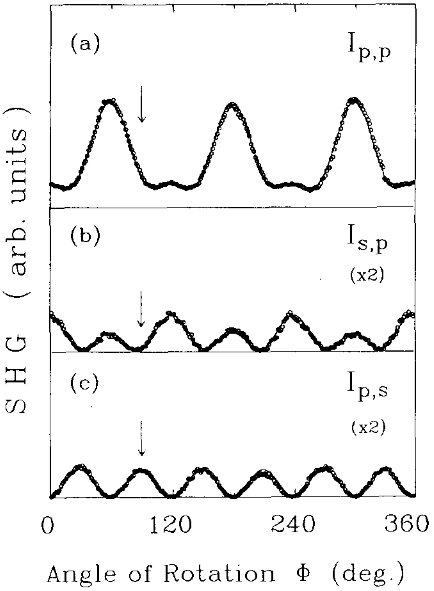

Fig. 5.23. Second harmonic intensity at 532 nm for Au(111) as a function of rotation angle, Φ. Incident wavelength = 1064 nm. The electrode was in 0.01 M $HClO_4$ and biased at +0.8 V (vs. SCE). The solid lines are fits to the data using Eq. (3.10)–(3.14) in the text: (a) p-pol SH, p-pol excitation, $c^{(3)}/a = 1.0\,e^{i51°}$; (b) p-pol SH, s-pol excitation; (c) s-pol SH, p-pol excitation, $a = 0$. From Ref. 121 and 155.

with a surface of 3m symmetry and can be fit well the theoretical expressions of Eq. (3.11) – (3.14). The observed anisotropy is somewhat intermediate between that obtained for Ag(111) and Cu(111). This suggests a contribution from interband transitions, although anisotropy experiments need to be performed on either side of this wavelength to understand the observed resonance effect more directly. For gold, the d-bands are at 2.5 eV, close to the 2.3 eV SH field. These scans were taken at +0.8 V, positive of the PZC which occurs at 0.23 V (vs. SCE) in ClO_4^- media. The p-polarized SHG shows a strong potential dependence which increases as the surface is biased positive of the PZC. The symmetry of the surface was preserved in these studies as the potential was varied within the double layer charging region.

Both the Au(100) and the Au(111) surfaces were examined in studies aimed at measuring the relative surface/bulk response from gold surfaces [131]. For the Au(100) surface and a p-polarized incident pulse at 1064 nm, anisotropy in the p- and s-polarized responses were found to be minimal. The potential dependence for this surface was also examined. The p-polarized response was found to increase by a factor of 4 when the voltage was swept positive of the PZC from −0.1 V to +0.8 V. The s-polarized response which was very small and isotropic showed no change with bias voltage. All of the data from this surface is consistent with a dominance of the surface response relative to the bulk.

The potential dependence of Au films evaporated on mica substrates have recently been investigated by Guyot-Sionnest and Tadjeddine [128]. The films were assumed to be of predominantly (111) orientation and were performed without regard to the crystal axis orientation relative to the incident beam. In these studies, the potential dependence of the gold films was examined at two incident wavelengths, 1064 nm and 532 nm, and fit to a surface charge density model [7]. They found that at the longer wavelengths, the surface acted in accordance with a free electron model, or surface charge density model, whereas at 532 nm incidence, the model does not reproduce the data. They attributed this deviation at the shorter wavelengths to the importance of resonant coupling to the d-bands of Au.

5.3.2 Surface Reconstruction Measurements

In the first study of its kind, second harmonic generation has been used to study potential induced reconstruction on Au(111) and Au(100) by Kolb and coworkers [156]. These surfaces have been known to reconstruct in UHV when they are clean [153, 157]. Surface reconstruction occurs when the surface atoms of a solid rearrange themselves in a structure different from that expected from simple termination of the bulk lattice. Various studies by cyclic voltammetry, electroreflectance spectroscopy and ex situ electron diffraction have suggested that flame-treated crystals form stable reconstructions in solution. Unfortunately, due to the lack of in situ probes, very little direct evidence for this reconstruction has been available.

In the work by Kolb and coworkers [156], a change in the symmetry in the SH anisotropy has been observed for both of these crystals in regions where previous studies have suggested that the reconstruction occurs. Fig. 5.24 shows the rotational anisotropy that they obtained for Au(111) at two different electrode potentials.

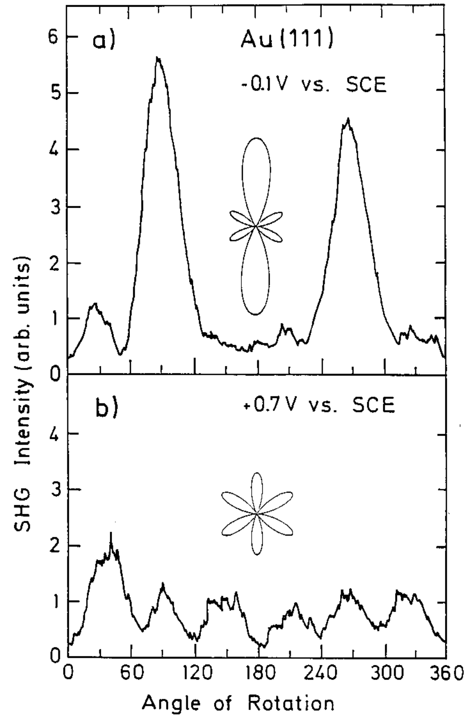

Fig. 5.24. Second harmonic intensity at 532 nm as a function of angle of rotation for Au(111) in 0.01 M H_2SO_4 at (a) -0.1 V and (b) $+0.7$ V vs. SCE. s-polarized excitation and s-polarized SHG detection in both cases. For comparison purposes the calculated polar plots of the rotational anisotropies for s/s-polarization of a threefold symmetry surface with (a) and without (b) a onefold symmetry superimposed are also shown. From Ref. 156.

Fig. 5.24a corresponds to a freshly prepared (flame-treated) surface which was immersed at -0.4 V (vs. SCE) and then potentiostated at -0.1 V. Under these conditions, the Au(111) has been presumed to be reconstructed into the (1×23) structure where the surface atoms show a 4% compression in the [110] direction. The pattern appears to be onefold in symmetry with two dominant peaks at 90° and 270° with the other four peaks markedly reduced in intensity. The authors fit the data to a mixture of one-fold and threefold symmetry elements. The observations are distinctly different when the electrode is ramped negatively. The data in Fig. 5.24b was collected after the electrode in the above figure was biased at $+0.7$ V. In the figure, the threefold symmetry of the unreconstructed Au(111)-(1×1) surface is observed. Both sets of data were collected with s-polarized incident light at 1064 nm and the s-polarized output at 532 nm. Transient SH signals collected at an azimuthal angle of 90° indicate that the lifting and reestablishment of the reconstruction followed first order kinetics with respective decay times of 22.7 s and 15.3 s. This reconstruction was not observed by Richmond and coworkers [134, 155], where the samples were not cleaned in UHV by alternating cycles of ion-bombardment and annealing. Such a preparation appears essential to obtaining the reconstructions observed in these studies.

The more in depth analysis of the SH reconstruction data of Kolb and coworkers [156] on Au(111) has recently been performed by Lupke et al. [158]. In this work, the second order susceptibility tensor has been split into contributions due to 1-fold, 2-fold, 3-fold and ∞-fold axes for a surface of C_s symmetry. Their results suggest that the SH rotational patterns cannot be completely analyzed by theoretical models without knowledge of the distribution of domains present in the reconstruction of the surface. They also conclude that rotation axes of lower symmetry create additional contributions via "overtones" or "harmonics". Their symmetry analysis of the SH rotational patterns from Au(111) reveals contributions from a 3-fold axis with a regular (1×1) structure and simultaneously from a 1-fold and a 2-fold axis due to the (1×23) reconstruction.

Au(100) offers another interesting case for reconstruction [156]. Previous studies on this electrode surface with LEED and RHEED have shown that the reconstructed Au(100)-(5×20) surface is stable in a potential range where no anion adsorption is present [104]. In the presence of anions, the reconstruction is presumed to be lifted to a (1×1) structure. However, at negative potentials, the (5×20) structure is regenerated. The authors observed a difference in the SH rotational anisotropy at these two potentials and attributed it to the reconstruction and lifting of the reconstruction [156].

5.3.3 Underpotential Deposition

The first SH study of underpotential deposition of a foreign metal on Au has been done by Koos for thallium on Au(111) [134]. The rotational anisotropy during deposition is found to be very sensitive to deposition of the overlayer. Using p-polarized 1064 nm incident light and detecting the s-polarized harmonic, Koos has found that the anisotropy which appeared with 3m symmetry initially is reduced after UPD of one monolayer. With the continued deposition to two monolayers, the anisotropic response increases to a level approximately equal to that of the adsorbate-free surface. The author suggested that the decrease in the anisotropic response is due to a lack of long range order upon the formation of an incommensurate overlayer.

This system has been examined in more detail in the first studies performed on metal surfaces in which changes in the phase of the SH response are explicitly examined. Since the previous studies showed that the anisotropic response is strongly affected by the overlayer, phase shifts in the anisotropic terms was specifically sought [146]. The experiment involved examining the s-polarized response from this (111) surface which allows isolation of the term $c(\chi^{(2)}_{\mathrm{xxx}} - a\zeta)$, where a and c represent Fresnel factors and ζ is the nonlocal bulk response. The x direction is in the plane of the surface along the [211] crystallographic axis. The phase was then measured by the interference method discussed in section 4.1.3. Fig. 5.25 shows the intensity and the phase of $c(\chi^{(2)}_{\mathrm{xxx}} - a\zeta)$ as a function of coverage. A 1064 nm p-polarized incident beam was used. The charge deposition measured in the first set of UPD peaks

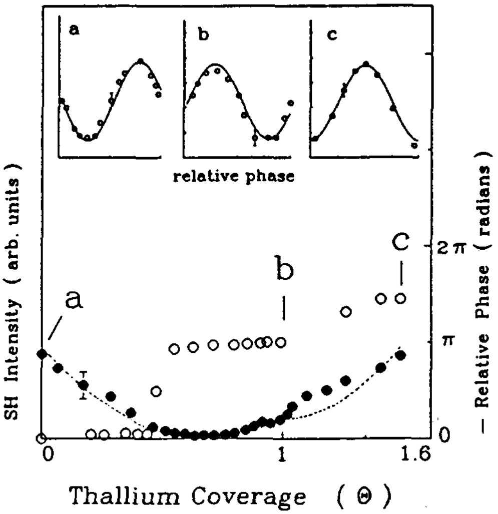

Fig. 5.25. s-polarized SH intensity (●) and phase (○) for Au(111) as a function of thallium coverage (Θ) in monolayers. The inserts in the upper part of the figure represent the actual phase data for coverages of $\Theta = 0.0$, 1.0, 1.5 monolayers labeled a, b, and c, respectively. Incident wavelength = 1064 nm. The solid and dotted lines represent fits to the data (see text). From Ref. 121.

was 183 $\mu C/cm^2$. It was assumed that this corresponded to the formation of a monolayer. Examples of the phase data for three coverages are shown at the top of the figure. The solid lines are the sinusoidal fits to the form of the interference of the two plane waves.

The results show that as the magnitude of the SH response decreases and passes through a minimum at $\Theta = 0.6$ ML, the relative phase of $c(\psi^{(2)}_{xxx} - a\zeta)$ is seen to shift 180 °C relative to that from the native surface. The authors attribute the initial phase shift to a possible flipping of the dipole at the surface. As the second layer forms, an increase in magnitude is observed as is a phase shift of −258°. A similar intensity increase was reported for Tl on Ag(111) (above) when coverages exceeded 1 ML [122]. The measured phase changes show that perturbations to the nonlinear optical properties of the interface at coverages less than a monolayer are strikingly different from those affected by further deposition. This is not obvious if only intensity measurements are made.

A more recent study has examined the SH response from a Au(111) electrode during UPD of a variety of metals, Ag, Cu, Pb, Tl and Sb [155]. In situ x-ray diffraction techniques have examined Ag, Cu and Pb on this substrate [159–161]. Silver is shown to form an epitaxial overlayer with Ag atoms sitting in 3-fold hollow sites forming a (1 × 1) commensurate overlayer. The lattice mismatch between lead and the substrate is shown to prevent formation of a commensurate overlayer but forms a hexagonal close-packed overlayer contracted by 0.7% from bulk lead. Although Tl and Sb on Au(111) have not been examined by x-ray diffraction, a close packed structure would necessitate an incommensurate overlayer due to the lattice mismatch.

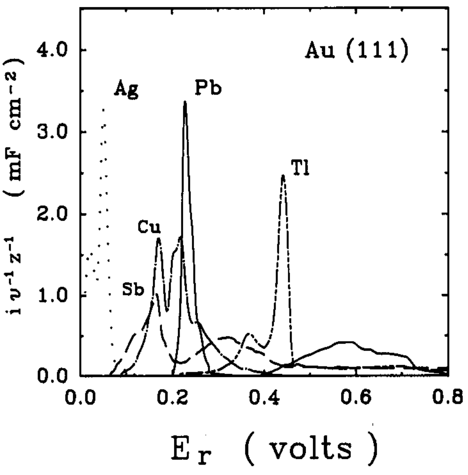

Fig. 5.26. Potentiodynamic desorption spectra for the deposition of Cu (—●—), Ag (· · ·) Sb (– – –), Pb (———), and Tl (· · – · ·) on Au(111). The electrode was in 0.01 M $HClO_4$, with 10 mM Me^{2+}. Sweep rate of 10 mV/s for Cu, Ag, Sb and Tl and 5 mV/s for Pb. From Ref. 155.

The stripping voltammetry and the SH response for each adatom is shown in Figs. 5.26 and 5.27, respectively. The electrochemical results of Fig. 5.26 are in good agreement with earlier reported voltammetry [162]. Fig. 5.27a and b shows changes in the total surface isotropic response, $I_{p,p}$, and the term χ_{zxx} respectively, during the deposition of each of the metal overlayers. The greatest change shown in both the isotropic intensity and the term χ_{zxx} occurs for Sb, Tl and Pb. This change occurs in coverages greater than $\Theta = 0.4$ ML. Silver, copper and lead deposition produce only small changes in the total isotropic signal.

When anisotropic response is monitored as a function of deposition (Fig. 5.27c), the 3m symmetry is found to be retained for all of the metal overlayer/Au(111) systems even though there is a significant mismatch in the lattice parameters for the larger adatoms, thallium, antimony, and lead [155]. When these three larger adatoms are deposited, a corresponding decrease in the anisotropic term is found which is not seen for the other adatoms. The authors concluded from these results that local site symmetry is dictating the symmetry of the SH response. This questions the earlier conclusion that the anisotropic SH response represents the longer range order of the adsorbate/substrate interface. They suggest that the SH response at low coverages may be sensitive to the interaction of the individual atoms with the substrate and hence does not provide information about the overall structure of the overlayer as earlier proposed.

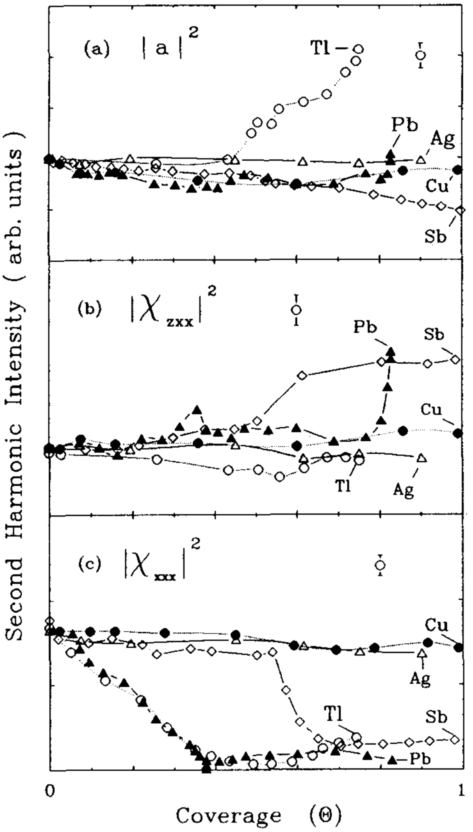

Fig. 5.27. SH intensity as a function of surface coverage Θ taken at an azimuthal angle of $\Phi = 90°$. (a) $I_{p,p} \propto |a|^2$; (b) $I_{s,p} \propto |\chi_{zxx}|^2$; (c) $I_{p,s} \propto |\chi_{xxx}|^2$. Data is given for Cu(●), Ag(△), Sb(◇), Pb(△) and Tl(○) deposition. Lines are drawn between data points as a guide to the eye. From Ref. 155.

5.4 Other Metals

As shown above, most of the work to date on SH studies of electrode surfaces has been on noble metals. This is not to suggest that the technique is restricted to these surfaces alone. In fact a wide variety of other metals and semiconductors produce measureable SH signals [163]. There have been a number of metallic single crystal surfaces studied in UHV including Ni(111) [8, 164–166], Pt(111) [8, 165], Rh(111) [167–169], and, Al(111) and (110) [170]. A few of these studies have involved rotation of the crystal surface about the surface normal [166]. Of pertinence to electrochemical studies, two recent papers have appeared, one on Pt(111) [171] and the other on Fe(110) [172]. Both have involved measuring the rotational anisotropy from the metal surface.

Lynch and Corn have reported the measurement of rotational anisotropy from a Pt(111) electrode surface [171]. Pt(111) has been studied extensively by Hubbard and coworkers by immersion studies [173]. In these previous studies, it has been found that flame annealing procedures can produce a single crystal surface which has identical electrochemical behavior as a Pt(111) crystal prepared in UHV. Through UHV-transfer studies, they have demonstrated that the immersed surface retains this order in solution. Lynch and Corn have measured the Pt(111) SH rotational anisotropy in solution and have found it to have a surface symmetry of either C_{3v} or C_3. The Pt(111) electrodes were transferred to solution with an iodine overlayer and cleaned through an iodine-CO exchange reaction and subsequent CO oxidation electrochemistry. They concluded that oxidation of the CO monolayer creates a well-ordered Pt(111) surface with a potential dependent SH response that suggests the presence of an adsorbed hydrogen species over a range of potentials. In contrast to the noble metals discussed above, in the potential regions examined in these studies, adsorbates other than the solvent are always present at the surface of Pt(111). Previous studies of SHG from Pt(111) in UHV have shown the strong sensitivity of SHG to adsorbates such as CO, O_2 and H_2 on the surface [166]. In addition, a striking frequency dependence of the SH response is observed suggesting the participation of surface states or resonant effects associated with interband transitions [166].

Over the past several years, Gruen and coworkers have examined the SH response from iron electrodes in alkaline solutions [45, 53, 172]. In their work on polycrystalline iron, they concluded that the potential dependent SH response which was observed during surface oxidation could be attributed to two intermediate phases on the electrode surface between the passive film at oxidative potentials and the reduced metal at hydrogen evolution potentials [53]. They have recently extended this work to Fe(110). In this study [172], they examined the SH rotational anisotropy from this crystal under ambient conditions. They found that the experiments reveal the presence of both twofold and threefold symmetric species at the metal/oxide interface. When their data is fit to the theory of Tom et al. [68], they conclude that the measured three-fold symmetric oxide is found to be tilted by 5° from the Fe(110) plane. The two-fold symmetric structure is aligned with the Fe(110) surface.

6 Summary and Conclusions

Over the past decade there have been extensive advances in the understanding of optical surface SHG. During this time there has been nearly a tenfold increase in the number of papers published in this area. Parallel to the progress made in our understanding of this nonlinear process on a fundamental level has been the growing application of the method to a variety of interfaces including metals, semiconductors, liquids and polymers [6]. This review has summarized the progress of surface SHG as applied to metals, and more specifically, metals in an electrochemical environment.

Although there is much fundamental work remaining to be done before surface SHG can be used in a purely analytical sense, the potential for obtaining unique information about the electrochemical interface is already apparent. One area which holds particular promise is in the measurement of the electronic properties of the electrode surface by wavelength dependent SH studies. Identification of surface states and their potential dependence by resonant SHG is one example where the technique could be very valuable. Recent work from this laboratory has demonstrated this for Ag(111) and Ag(110) [137]. The unique advantage that one has over other optical or electron techniques for making such measurements in solution or in other environments is the inherent surface specificity. Under conditions where the metal nonlinear response dominates over the adsorbing molecular layer, one can study how these electronic properties are altered by the presence of the adsorbate. Surface physical structure and chemical reactivity is usually governed by the electronic properties of the surface but little is known about this correlation in solution because of the paucity of in situ techniques for making such measurements.

A second area where SHG has particular potential for providing unique information is in the time domain. Depending upon the capabilities of the laser used, one has the potential to perform pump probe measurements down to fractions of a picosecond. Where this might be applicable for electrochemical studies is in the study of photoinduced effects and carrier dynamics at the semiconductor/liquid interface. Under the appropriate polarization and wavelength conditions, one has the advantage over other optical transient techniques, such as luminescence or reflectivity, of being surface specific. As described above, SHG has been shown in previous studies to be very sensitive to surface charge density on both metal and semiconductor surfaces. One has the advantage over current transient measurements in not being hampered by time constants in the circuitry.

Studies have shown how SHG has been used to verify reconstruction of surfaces in solution via changes in the rotational symmetry. In this area SHG can provide complementary information to STM or x-ray grazing incidence measurements with SH studies being more generally applicable. Whereas the reconstruction seen for Au(111) is quite striking, it is difficult to obtain a quantitative measure of the degree of reconstruction [158]. Also, changes in the geometrical structure of the surface can be accompanied by changes in the electronic properties which can alter not only the relative intensity but also the phase of the SH response. Performing these experiments at several wavelengths and making phase measurements should help decouple these effects.

For monitoring thin film growth of metals on metals or semiconductors, the SH method provides complementary information to STM or x-ray grazing incidence measurements if one is interested in the geometrical structure of the overlayer. SHG is somewhat more versatile in that it can be applied to nearly any metal or semiconductor surface; however, one must again be aware that optical resonance effects can play a role in the changing rotational anisotropy patterns. For semiconductors, the bulk may have a significant SH response and therefore must be considered. Both x-ray scattering and SHG probe macroscopic behavior whereas STM gives a microscopic picture of the geometric properties of the surface. All three techniques currently suffer from the lack of a full understanding of fundamental issues behind each method. Where SHG has an advantage is in being able to probe electronic properties of the overlayer, and, possibly the buried interfacial region as has been done by Heinz and coworkers for the $CaF_2/Si(111)$ interface [142, 143]. Another advantage is the use of SHG to monitor thin film growth dynamics as has been shown with studies described from this laboratory by Robinson et al. [54, 116].

For organic thin films on metals, one might be able to monitor the order of the underlying substrate if the metallic response dominates over the overlayer nonlinearity. One generally assumes that the overlayer does not perturb the underlying surface of the substrate but there are currently no other direct experimental probes to verify this. As with the reconstruction data, it is always important to consider how the electronic properties of the surface may be altered by the overlayer in addition to the geometrical structure as measured by the symmetry of the response.

Nearly all of the studies described in this review have focussed on the properties of the electrode surface because of the fact that the response from the highly conductive metal generally dominates over that of the adjacent water layer or the ions or molecules which reside therein. The exception is the use of model systems such as dyes adsorbed at the surface where optical resonance effects are large and the electronic structure of the adsorbed molecular can be probed. Obtaining an infrared vibrational spectrum of an adsorbed molecule by resonant SHG is possible, but difficult. The better alternative is to use a related nonlinear optical method, sum-difference frequency generation. In these experiments, two different incident frequencies lead to a nonlinear polarization at the interface at the sum and difference frequencies of the incoming beams. One of the incident beams is from a tunable infrared source with frequencies corresponding to vibrational modes of the adsorbate. The second is a fixed visible frequency. As the infrared beam tunes to a resonance in the molecule, enhancement in the SF response is observed. The overall result is the measurement of the infrared spectrum of the molecule with detection at visible frequencies. A number of studies have appeared which have demonstrated the feasibility of this technique on surfaces in UHV and for surfaces in the presence of a nonaqueous solvent [6, 8]. Since like SHG, this is a second order optical effect, it therefore inherently interface specific. However, one still has to worry about the absorption of the incident infrared beam by the solvent prior to illumination of the surface. To minimize this one can use a thin layer cell, a transparent electrode and couple through the back side of the electrode, or use nonadsorbing solvents.

Acknowledgements. Appreciation is expressed to my postdoctoral associates, Dr. Jeanne Robinson, Dr. Rosina Georgiadis, and my graduate students, Pam Fischer, Grace Ann Neff, Rick Bradley, Eric Wong and Dan Koos for help with this manuscript. Helpful discussions with Prof. Stephen Kevan are also acknowledged. Financial support for the work from this laboratory has been provided by the Office of Naval Research (N00014-89-J-1261), the Army Research Office (26191-CH), the Petroleum Research Fund of the American Chemical Society (ACS 24180) and the National Science Foundation (CHE 8801348) and the Department of Energy Basic Energy Sciences for the time resolved studies (DE-FG06-86ER45273). The author is an NSF PYI Awardee, an Alfred P. Sloan Fellow and a Camille and Henry Dreyfus Teacher Scholar.

7 References

1. R.K. Chang, T.E. Furtak, Surface Enhanced Raman Scattering. Plenum Press, New York, 1982 and references therein.
2. See for example, J.K. Foley, S. Pons, Anal. Chem. 57, 945 A (1985) and references therein.
3. D.B. Chase, B.A. Parkinson, Appl. Spec. 42, 1186 (1988).
4. M.G. Samant, M.F. Toney, G.L. Borges, L. Blum, O.R. Melroy, J. Phys. Chem. 92, 220 (1988).
5. R. Sonnenfeld, J. Schneir, P.K. Hansma, in: Modern Aspects of Electrochemistry, Vol. 21, J.O'M. Bockris (ed.), in press; Dennis J. Trevor, C.E.D. Chidsey, D.N. Loiacono, Phys. Rev. Lett. 62, 929 (1989).
6. Y.R. Shen, Nature 337, 519 (1989)
7. *G.L. Richmond, J.M. Robinson, V.L. Shannon.* Prog. in Surf. Sci. 28, 1 (1988)
8. R.B. Hall, J.N. Russell, J. Miragliotta, P.R. Rabinowitz, Chem. and Phys. of Surfaces, Vol. VII. Springer Verlag, 1990, in press.
9. G.L. Richmond, in: Electroanalytical Chemistry, A.J. Bard (ed.), Vol. 17. Marcel Dekker, Inc., New York.
10. P.A. Franken, A.E. Hill, C.W. Peters, G. Weinreich, Phys. Rev. Lett. 7, 118 (1961).
11. N. Bloembergen, P.S. Pershan, Phys. Rev. 128, 606 (1962).
12. J. Ducuing, N. Bloembergen, Phys. Rev. Lett. 10, 474 (1963).
13. F. Brown, R.E. Parks, A.M. Sleeper, Phys. Rev. Lett. 14, 1029 (1965).
14. S.S. Jha, Phys. Rev. 140, A2020 (1965).
15. F. Brown, R.E. Parks, Phys. Rev. Lett. 16, 507 (1966).
16. S.S. Jha, Phys. Rev. Lett. 15, 412 (1965).
17. N. Bloembergen, Y.R. Shen, Phys. Rev. 141, 298 (1966).
18. N. Bloembergen, R.K. Chang, C.H. Lee, Phys. Rev. Lett. 16, 986 (1966).
19. N. Bloembergen, R.K. Chang, S.S. Jha, C.H. Lee, Phys. Rev. 174, 813 (1968).
20. H. Sonnenberg, H. Heffner, J. Opt. Soc. Am. 58, 209 (1968).
21. G.V. Krivoshchekov, V.I. Stroganov, Sov. Phys. – Solid State 9, 2856 (1968).
22. G.V. Krivoshchekov, V.I. Stroganov, Sov. Phys. – Solid State 11, 89 (1969).
23. S.S. Jha, C.S. Warke, Phys. Rev. 153, 751 (1967).
24. C.H. Lee, R.K. Chang, N. Bloembergen, Phys. Rev. Lett. 18, 167 (1967).
25. F. Brown, M. Matsuoka, Phys. Rev. 185, 985 (1969).
26. J. Rudnick, E.A. Stern, Phys. Rev. B 4, 4274 (1971).
27. J.R. Bower, Phys. Rev. B 14, 2427 (1976).
28. H.J. Simon, D.E. Mitchell, J.G. Watson, Phys. Rev. Lett. 33, 1531 (1974).
29. H.J. Simon, R.E. Benner, J.G. Rako, Opt. Comm. 23, 24.
30. M. Fukui, V. So, G.I. Stegeman, Phys. Rev. B 18, 2484 (1978).
31. J.E. Sipe, V.C.Y. So, M. Fukui, G.I. Stegeman, Phys. Rev. B 21, 4389 (1980).
32. M. Fukui, G.I. Stegeman, Solid State Comm. 26, 239 (1978).
33. Y.J. Chen, E. Burstein, Il Nuovo Cimento, 39B, 807 (1977).
34. H.J. Simon, D.E. Mitchell, J.G. Watson, Opt. Comm. 13, 294 (1975).
35. M. Fukui, V.C.Y. So, J.E. Sipe, G.I. Stegeman, J. Phys. Chem. Solids 40, 523 (1979).
36. J.E. Sipe, G.I. Stegeman, in: Surface Polaritons, V.M. Agranovich, D.L. Mills (eds.). North-Holland Publishing Company, New York (1982), p. 661.
37. Y.R. Shen, F. DeMartini, in: Surface Polaritons, V.M. Agranovich, D.L. Mills (eds.). North-Holland Publishing Company, New York (1982), p. 629.
38. D.L. Mills, Solid State Comm. 24, 669 (1977).
39. C.K. Chen, A.R.B. deCastro, Y.R. Shen, Phys. Rev. Lett. 46, 145 (1981).
40. C.K. Chen, T.F. Heinz, D. Ricard, Y.R. Shen, Phys. Rev. Lett. 46, 1010 (1981).
41. C.K. Chen, T.F. Heinz, D. Ricard, Y.R. Shen, Phys. Rev. B 27, 1965 (1983) and references therein.

42. G.L. Richmond, H.M. Rojhantalab, J.M. Robinson, V.L. Shannon, J. Opt. Soc. Am. B 4, 228 (1987).
43. G.L. Richmond, Langmuir 2, 132 (1986).
44. G.L. Richmond, Chem. Phys. Lett. 106, 26 (1984).
45. B.M. Biwer, M.J. Pellin, M.W. Schauer, D.M. Gruen, Surf. Sci. 176, 377 (1986).
46. G.L. Richmond, in: Modern Techniques for In Situ Characterization, H. Abruna (ed.). VCH Publishers, Brooklyn, New York, 1990, Chapt. 6.
47. G.L. Richmond, Surf. Sci. 147, 115 (1984).
48. D.V. Murphy, K.U. von Raben, T.T. Chen, J.F. Owen, R.K. Chang, B.L. Laube, Surf. Sci. 124, 529 (1983).
49. C.D. Marshall, G.M. Korenowski, J. Chem. Phys. 85, 4172 (1986).
50. C.D. Marshall, G.M. Korenowski, J. Phys. Chem. 91, 1289 (1987).
51. T.T. Chen, K.U. von Raben, D.V. Murphy, R.K. Chang, Surf. Sci. 143, 369 (1984).
52. P. Chu, G.L. Richmond, J. Electroanal. Chem. 29, 203 (1990).
53. B.M. Biwer, M.J. Pellin, M.W. Schauer, D.M. Gruen, Langmuir 4, 121 (1988).
54. J.M. Robinson, G.L. Richmond, Chem. Phys. 141, 175 (1990).
55. R.M. Corn, M. Romagnoli, M.D. Levenson, M.R. Philpott, J. Chem. Phys. 81, 4127 (1984).
56. G.L. Richmond, Chem. Phys. Lett. 110, 571 (1984).
57. R.M. Corn, M. Romagnoli, M.D. Levenson, M.R. Philpott, Chem. Phys. Lett. 106, 30 (1984).
58. H.M. Rojhantalab, G.L. Richmond, J. Phys. Chem. 93, 3269 (1989).
59. H.M. Rojhantalab, G.L. Richmond, in: Advances in Laser Science – II, AIP Conference Proceedings Series No. 180, W.C. Stwalley, M. Lapp, G.A. Kenney-Wallace (eds.). AIP, New York (1987).
60. J.M. Robinson, H.M. Rojhantalab, V.L. Shannon, D.A. Koos, G.L. Richmond, Pure and Appl. Chem. 59, 1263 (1987).
61. D.F. Voss, M. Nagumo, L.S. Goldberg, K.A. Bunding, J. Phys. Chem. 90, 1834 (1986).
62. D.J. Campbell, R.M. Corn, J. Phys. Chem. 91, 5668 (1987).
63. D.J. Campbell, R.M. Corn, J. Phys. Chem. 92, 5796 (1988).
64. G.L. Richmond, Chem. Phys. Lett. 113, 359 (1985).
65. D.J. Campbell, D.A. Higgins, R.M. Corn, J. Phys. Chem., in press.
66. F.W. Gordon, S.A. Cresswell, J.K. Steehler, Langmuir 5, 286 (1989).
67. H.W.K. Tom, Ph. D. Dissertation, University of California, Berkeley, 1984.
68. H.W.K. Tom, T.F. Heinz, Y.R. Shen, Phys. Rev. Lett. 51, 1983 (1983).
69. C.V. Shank, R. Yen, C. Hirlimann, Phys. Rev. Lett. 51, 900 (1983).
70. T.F. Heinz, M.M.T. Loy, W.A. Thompson, J. Vac. Sci. Technol. B 3, 1467 (1985).
71. T.F. Heinz, M.M.T. Loy, W.A. Thompson, Phys. Rev. Lett. 54, 63 (1985).
72. H.W.K. Tom, in: Advances in Laser Science – II, AIP Conference Proceedings Series No. 180, W.C. Stwalley, M. Lapp, G.A. Kenney-Wallace (eds.). AIP, New York (1987).
73. H.W.K. Tom, G.D. Aumiller, C.H. Brito-Cruz, Phys. Rev. Lett. 60, 1438 (1988).
74. V.L. Shannon, D.A. Koos, G.L. Richmond, J. Chem. Phys. 87, 1440 (1987).
75. V.L. Shannon, J.M. Robinson, G.L. Richmond, Spectroscopy 3, 4 (1988).
76. G.L. Richmond, FAACS Meeting, Detroit, MI, Sept. 1986.
77. H.W.K. Tom, G.D. Aumiller, Phys. Rev. B 33, 8818 (1986).
78. Y.R. Shen, The Principles of Nonlinear Optics. Wiley, New York (1984).
79. T.F. Heinz, Ph. D. Dissertation, University of California, Berkeley (1982).
80. V. Mizrahi, J.E. Sipe, J. Opt. Soc. Am. B 5, 660 (1988).
81. D. Guidotti, T.A. Driscoll, H.J. Gerritsen, Solid State Comm. 46, 337 (1983).
82. P. Guyot-Sionnest, W. Chen, Y.R. Shen, Phys. Rev. B 33, 8254 (1986).
83. J.E. Sipe, V. Mizrahi, G.I. Stegeman, Phys. Rev. B 35, 9091 (1987).
84. J.E. Sipe, D.J. Moss, H.M. van Driel, Phys. Rev. B 35, 1129 (1987).
85. Hung Cheng, P.B. Miller, Phys. Rev. 134, A683 (1964).
86. J.E. Sipe, V.C.Y. So, M. Fukui, G.I. Stegeman, Solid State Comm. 34, 523 (1980).
87. M. Corvi, W.L. Schaich, Phys. Rev. B 33, 3688 (1986).

88. W.L. Schaich, A. Liebsch, Phys. Rev. B 37, 6187 (1988).
89. O. Keller, J. Opt. Soc. Am. B 2, 367 (1985).
90. O. Keller, Phys. Rev. B 31, 5028 (1985).
91. O. Keller, Phys. Rev. B 33, 990 (1986).
92. O. Keller, Opt. Acta 33, 673 (1986).
93. O. Keller, K. Pedersen, J. Phys. C: Solid State Phys. 19, 3631 (1986).
94. O. Keller, Phys. Rev. B 34, 3883 (1986).
95. P. Apell, Physica Scripta 27, 211 (1983).
96. M. Weber, A. Liebsch, Phys. Rev. B 35, 7411 (1987).
97. M. Weber, A. Liebsch, Phys. Rev. B 37, 1019 (1988).
98. M.G. Weber, A. Liebsch, Phys. Rev. B 36, 6411 (1987).
99. K.J. Song, D. Heskett, H.L. Dai, A. Kiebsch, E.W. Plummer, Phys. Rev. Lett. 61, 1380 (1988).
100. A. Liebsch, Phys. Rev. Lett. 61, 1233 (1988).
101. P. Guyot-Sionnest, A. Tadjeddine, A. Liebsch, Phys. Rev. Lett. 64, 1678 (1990).
102. G.C. Aers, J.E. Inglesfield, in press.
103. D.M. Kolb, J. Phys. (Paris) 44, C10-137 (1983); D.M. Kolb, J. Schneider, Electrochim. Acta 31, 929 (1986); J. Schneider, D.M. Kolb, Surf. Sci. 193, 579 (1988).
104. D.M. Kolb, J. Schneider, Electrochim. Acta 31, 929 (1986); J. Schneider, D.M. Kolb, Surf. Sci. 193, 579 (1988).
105. W. Boeck, D.M. Kolb, Surf. Sci. 118, 613 (1982).
106. T.E. Furtak, D.W. Lynch, Phys. Rev. Lett. 35, 960 (1975).
107. C.C. Hu, Phys. Rev. B 40, 7420 (1989).
108. A. Chizmeshya, E. Zaremba, Phys. Rev. B 37, 2805 (1988).
109. G.I. Stegeman, J.J. Burke, D.G. Hall, J. Opt. Soc. Am. 72, 1613 (1982).
110. J.C. Quail, H.J. Simon, Phys. Rev. B 31, 4900 (1985).
111. C.-C. Tzeng, J.T. Lue, Surf. Sci. 192, 491 (1987).
112. E.M. Schmidlin, H.J. Simon, Appl. Opt. 28, 3323 (1989).
113. H.A. Haus, G.A. Reider, Appl. Opt. 26, 4576 (1987).
114. R.T. Deck, D. Sarid, Appl. Phys. Lett. 41, 906 (1982).
115. J. Quail, J.G. Rako, H.J. Simon, R.T. Deck, Phys. Rev. Lett. 50, 1987 (1970).
116. J.M. Robinson, G.L. Richmond, Electrochim ACTA 34, 1639 (1989).
117. J.M. Robinson, G.L. Richmond, Time Resolved SH Rotational Anisotropy Measurements of Thallium Deposition on Cu(111), in preparation.
118. T.F. Heinz, G. Arjavalingam, M.T. Loy, J.H. Glownia, in: Proceedings of the XIV International Quantum Electronics Conference, June 9–13, 1986, San Francisco, CA. Paper THII1.
119. G. Arjavalingam, T.F. Heinz, J.H. Glownia, in: Ultrafast Phenomena V, G.R. Fleming, A.E. Siegman (eds.). Springer-Verlag, Berlin (1986), p. 370.
120. H.W.K. Tom, G.D. Aumiller, C.H. Brito-Cruz, Proc. SPIE-Int. Soc. Opt. Eng. 2, 152 (1988).
121. D.A. Koos, G.L. Richmond, J. Chem. Phys. 93, 869 (1990).
122. D.A. Koos, V.L. Shannon, G.L. Richmond, J. Phys. Chem. 94, 2091 (1990).
123. V.L. Shannon, D.A. Koos, G.L. Richmond, Appl. Opt. 26, 3579 (1987).
124. R.A. Bradley, S. Arekat, R. Georgiadis, J.M. Robinson, S.D. Kevan, G.L. Richmond, Chem. Phys. Lett. 168, 468 (1990).
125. V.L. Shannon, D.A. Koos, G.L. Richmond, J. Phys. Chem. 91, 5548 (1987).
126. Second harmonic generation observed in transmission from crystalline calcite, which also possesses a center of inversion, had been previously reported: R.W. Terhune, P.D. Maker, C.M. Savage. Phys. Rev. Lett. 8, 404 (1962).
127. V.L. Shannon, D.A. Koos, J.M. Robinson, G.L. Richmond, Chem. Phys. Lett. 142, 323 (1987).
128. P. Guyot-Sionnest, A. Tadjeddine, J. Chem. Phys. 92, 1 (1990).
129. P. Guyot-Sionnest, Y.R. Shen, Phys. Rev. B 35, 4420 (1987).
130. P. Guyot-Sionnest, Y.R. Shen, Phys. Rev. B 38, 7985 (1988).
131. D.A. Koos, V.L. Shannon, G.L. Richmond, Phys. Rev. B, in press.

132. R.A. Georgiadis, G.A. Neff, G.L. Richmond, J. Chem. Phys. 92, 4623 (1990).
133. V.L. Shannon, D.A. Koos, S.A. Kellar, G.L. Richmond, J. Phys. Chem. 93, 6434 (1989).
134. D.A. Koos, J. Electrochem. Soc. 136, 218C (1989).
135. R. Bradley, R. Georgiadis, G.L. Richmond, to be submitted.
136. E.K.L. Wong, G.L. Richmond, submitted.
137. R. Georgiadis, G.L. Richmond, J. Phys. Chem. 95, 2895 (1991).
138. R. Georgiadis, G.L. Richmond, to be submitted.
139. J.M. Hicks, L.E. Urbach, E.W. Plummer, H.-L. Dai, Proc. of the SPIE, Los Angeles, CA 1990; J.M. Hicks, L.E. Urbach, E.W. Plummer, H.-L. Dai, Phys. Rev. Lett. 61, 2588 (1988).
140. K.-M. Ho, C.L. Fu, S.H. Liu, D.M. Kolb, G. Piazza, J. Electroanal. Chem. 150, 235 (1983).
141. See for example, D.M. Kolb, in: Advances in Electrochemistry and Electrochemical Engineering. Vol II, H. Gerischer, C.W. Tobias (eds.). Wiley, New York (1978), p. 125.
142. T.F. Heinz, F.J. Himpsel, E. Palange, E. Burstein, Phys. Rev. Lett. 63, 644 (1989).
143. F.J. Himpsel, T.F. Heinz, A.B. McLean, E. Palange, E. Burstein, J. Vac. Sci. Technol. B7, 879 (1989).
144. V.L. Shannon, D.A. Koos, J.M. Robinson, G.L. Richmond, in: Chemically Modified Surfaces, Vol. 2, Gordon and Breach Science Publishers, New York (1988), p. 485.
145. J. Miragliotta, T.E. Furtak, Surf. Interface Anal. 14, 53 (1989).
146. D.A. Koos, G.L. Richmond, to be submitted.
147. J. Miragliotta, T.E. Furtak, Phys. Rev. B 37, 1028 (1988).
148. T.E. Furtak, J. Miragliotta, G.M. Korenowski, Phys. Rev. B 35, 2569 (1987).
149. J.M. Robinson, R. Georgiadis, G.A. Neff, G.L. Richmond, unpublished.
150. R. Kotz, D.M. Kolb, Z. Phys. Chem. N.F. 112, 69 (1978).
151. G. Materlik, M. Schmah, J. Zegenhagen, W. Uelhoff, Ber. Bunsenges. Phys. Chem. 91, 292 (1987).
152. H. Niehus, Surf. Sci. 130, 41 (1983).
153. M.A. van Hove, R.J. Koestner, P.C. Stair, J.P. Biberian, L.L. Kesmodel, I. Bartos, G.A. Somarjai, Surf. Sci. 103, 189 (1981).
154. A. Bewick, J. Jovicevic, B. Thomas, Faraday Symp. Soc. 12, 24 (1977).
155. D.A. Koos, G.L. Richmond, J. Phys. Chem., in press.
156. A. Friedrich, B. Pettinger, D.M. Kolb, G. Lüpke, R. Steinhoff, G. Marowsky, Chem. Phys. Lett. 63, 123 (1989).
157. D.G. Fedak, N.A. Gjostein, Surf. Sci. 8, 77 (1967).
158. G. Lupke, G. Marowsky, R. Steinhoff, A. Friedrich, B. Pettinger, D.M. Kolb, Phys. Rev. B 41, 6913 (1990).
159. J.H. White, M.J. Albvarelli, H.D. Abruna, L. Blum, O.R. Melroy, M.G. Samant, G.L. Borges, J.G. Gordon, II, J. Phys. Chem. 92, 4432 (1988).
160. M.P. Green, K.J. Hanson, R. Carr, I. Lindau, J. Electrochem. Soc. 137, 168C (1990).
161. O.M. Magnussen, J. Hotlos, R.J. Nichols, D.M. Kolb, R.J. Behm, Phys. Rev. Lett. 64, 2929 (1990).
162. J.W. Schultze, D. Dickertmann, Surf. Sci. 54, 489 (1976).
163. G.T. Boyd, Th. Rasing, J.R.R. Leite, Y.R. Shen, Phys. Rev. B 30, 519 (1984).
164. X.D. Zhu, Th. Rasing, Y.R. Shen, Phys. Rev. Lett. 61, 2883 (1988).
165. S.G. Grubb, A.M. DeSantolo, R.B. Hall, J. Phys. Chem. 92, 1419 (1988).
166. R.J.M. Anderson, J.C. Hamilton, Phys. Rev. B 38, 8451 (1988); R.J.M. Anderson, J.C. Hamilton, Chem. Phys. Lett. 151, 455 (1988).
167. H.W.K. Tom, C.M. Mate, X.D. Zhu, J.E. Crowell, T.F. Heinz, G.A. Somorjai, Y.R. Shen, Phys. Rev. Lett. 52, 348 (1984).
168. H.W.K. Tom, C.M. Mate, X.D. Zhu, J.E. Crowell, Y.R. Shen, G.A. Somorjai, Surf. Sci. 172, 466 (1986).
169. C.C. Mate, G.A. Somorjai, H.W. K. Tom, X.D. Zhu, Y.R. Shen, J. Chem. Phys. 88, 441 (1988).

170. R. Murphy, M. Yeganch, K.J. Song, E.W. Plummer, Phys. Rev. Lett. 63, 318 (1989).
171. M.L. Lynch, R.M. Corn, J. Phys. Chem., in press.
172. M.W. Schauer, M.J. Pellin, D.M. Gruen, Chem. Mater. 1, 101 (1989).
173. M. Wasberg, L. Palaikis, S. Wallen, M. Kamrath, A. Wieckowski, J. Electroanal. Chem. 256, 51 (1988).

Advances in Electrochemical Science and Engineering
Edited by Heinz Gerischer and Charles W. Tobias

Flow Modulation Techniques in Electrochemistry

C. Deslouis and B. Tribollet

U.P.R. 15 du C.N.R.S., Physique des Liquides et Electrochimie, Université
Pierre et Marie Curie, tour 22, 4 Place Jussieu, 75252 Paris Cédex 05, France

Contents

List of Symbols

a	constant (= 0.51023)
a_i	solid state activity of species i
A_1	defined by Eq. (6-20)
B	constant = $\left(\frac{3}{\mathrm{a}^4}\right) 1/3$
c	concentration (mole/cm^3)
C_1 C_2	coefficients defined Eq. (5.1)
C_D	double layer capacitance (F)
C_{LF}	low frequency capacitance of the polymer layer (F)
d	diameter of circular probe (cm)
D	diffusion coefficient (cm^2 s^{-1})
D_E	diffusion coefficient of electrons (cm^2 s^{-1})
E	overall potential (V)
F	Faraday number (96487 C/equiv.)
F	steady dimensionless function corresponding to the radial velocity component
f	unsteady dimensionless function corresponding to the radial velocity component
G	steady dimensionless function corresponding to the tangential velocity component
g	unsteady dimensionless function corresponding to the tangential velocity component
G	dimensionless instantaneous tangential velocity
H	steady dimensionless function corresponding to the normal velocity component
h	unsteady dimensionless function corresponding to the normal velocity component
i	$\mathrm{i}^2 = -1$
I	current (A cm^{-2})
Im	imaginary part of a complex quantity
J	overall mass flux (mole/cm^2)
j	local mass flux (mole/cm^2)

K_1 K_2	integration constants
K_A K_x	reaction rates
K	consistency
k_E, k_0	see Eqs. (6-8) and (6-9)
$k^{\circ}_{f1}, k^{\circ}_{b1}, k^{\circ}_{f2}, k^{\circ}_{b2}$	see Eqs. (6-14) and (6-17)
L	ratio of the steady current Eq. (6-1)
M	integration constants see Eqs. (5-14) and (6-25)
n	number of electrons fluidity index Eq. (6-3)
N	integration constant see Eqs. (5-14) and (6-25)
p	dimensionless frequency ($= \omega/\bar{\Omega}$)
Q	constant ($= 0.8058\ Sc^{-1/3}$)
Q	constant defined by Eq. (5-9)
r	radial coordinate (cm)
R	radius (cm)
R	universal gas constant (8.3143 J/mole·K)
Re	real part of a complex quantity
Re	generalized Reynolds number
R_D	convective diffusion resistance ($= Z_{DS}(0)$) (ohm)
R_E	electrolyte resistance (ohm)
R_t	charge transfer resistance (ohm)
Sc	Schmidt number
s_i	stoechiometric coefficient
s	slope defined in Section 6.1
t	time (s)
t_3, t_4, t_5, t_6	coefficients for *Sc* correction see Eq. (3-16)
U	surface overpotential (V)
$\vartheta_r, \vartheta_\theta, \vartheta_y$	velocity components ($\mathrm{cm \cdot s^{-1}}$)
W	defined by Eq. (3-4)
w_1, w_2	see Eq. (4-23)
X	adsorbate
$X(t)$	time dependent quantity
Y	general term for perturbation
y	coordinate (cm)
Z_{ac}	ac impedance (ohm)
Z_D	convective diffusion impedance (ohm)
Z_{EHD}	electrohydrodynamical impedance (C)
Z_{HD}	hydrodynamic impedance
Z_c	transfer function corresponding to mass transport
Z_F	faradaic impedance (ohm)
Z_{w1}, Z_{w2}	impedances defined by Eq. (4-23)
α	wall velocity gradient ($\mathrm{s^{-1}}$)
α_1, α_2	kinetic parameters see Eqs. (6-14) and (6-17)
β_L	coefficient Eq. (4-14)
γ_i	see Eq. (4-24)
γ	coefficient of $\vartheta_y : \vartheta_y = \gamma(t)y^2$

Γ	gamma function
δ	diffusion layer thickness (cm)
ε	flow modulation amplitude see Eq. (6-35)
η	axial dimensionless distance (= y/δ)
θ	solution of homogeneous Eq. (3-2)
Θ	coverage fraction
λ	defined by Eq. (6-2)
υ	kinetic viscosity ($cm^2 \cdot s^{-1}$)
ξ	dimensionless frequency
ϱ	density
Φ	angular phase see Eq. (6-1)
χ	axial dimensionless distance $\left(= y \sqrt{\frac{\Omega}{\upsilon}} \right)$
ψ	phase shift
Ψ	blocked fraction of the surface
ω	pulsation
Ω	angular velocity

Superscript

–	mean value
~	complex quantity of small amplitude independent of time
*	complex quantity, dependent of time

1 Introduction

1.1 Foreword

During the past thirty years, the study of interfacial kinetics has been greatly improved by use of transient techniques. They basically imply the controlled perturbation with time of an electrical quantity (potential or current) at the electrochemical interface and the response analysis of the other electrical quantity. Among the different existing techniques, the electrochemical impedance spectroscopy (EIS) [1–3] occupies an outstanding place mainly because the frequency analysis of the system response, performed in a wide frequency range, provides a deep insight into the different elementary steps. Though the current for most of the electrochemical systems primarily depends on potential, other physical quantities such as pressure, temperature or fluid flow can also affect its value and therefore may be used as perturbations. The influence of flow on the current was the starting idea of the hydrodynamic modulated rotating disk electrode technique (HMRDE) proposed at the beginning of the seventies by Bruckenstein et al. [4–6]. Very early, these authors suggested to apply sinusoidal hydrodynamic modulations (SHM) and derived the first theoretical analysis of the problem [7] by considering the response of the mass transfer rate to a modulation of the angular velocity of a rotating disk electrode such that $\Omega^{1/2} = \bar{\Omega}^{1/2}(1+\varepsilon \cos \omega t)$.

The fact of modulating the square root of Ω was naturally supported by the results of the Levich theory in steady-state conditions [8]. With the increasing development of impedance techniques, aided by a sophisticated instrumentation [2], the authors of the present work promoted the use of impedance concept for this type of perturbation and introduced the so-called electrohydrodynamic (EHD) impedance [9, 10]. A parallel approach has been also investigated by use of velocity steps in both theoretical and experimental studies [5, 11, 12]. More recently, Schwartz et al. considered the case of hydrodynamic modulations of large amplitude for increasing the sensitivity of the current response and also for studying additional terms arisen with non linearities [13–15].

Another variant devised by Martem'Yanov et al. [16] ensures strong electrolyte stirring for generating turbulent fluctuations in solution. Assuming a pseudo hydrodynamical white noise, the responding current can be analyzed in the frequency domain to provide the same information as that obtained from any of the techniques mentioned above.

Since most electrode processes are non-linear, this requires the use low level signals for a linear analysis, and though all types of perturbation are equivalent from the viewpoint of signal processing, harmonic analysis provides the best compromise between the time of measurement and the accuracy [17].

At present flow modulation techniques have received many improvements from both the theoretical or instrumental sides. In addition, many applications have demonstrated their specific interest. However, though several review articles or monographs devoted as a whole or in part to hydrodynamic methods in Electrochemistry appeared in recent years [18–28], no complete presentation about the state of the art concerning flow modulation techniques has been given so far. This work is precisely aimed at reaching this goal. More emphasis will be put in the theoretical presentation on the EHD impedance technique, showing that not only a better knowledge of mass transport characteristics can be obtained but also a detailed analysis of electrode processes is possible. Therefore the EHD impedance will appear as a companion of the classical electrochemical impedance technique.

1.2 Symbolic Notation

A time-dependent quantity $X(t)$ responding to the sine wave modulation of some low level perturbation $\mathrm{d}Y \cos \omega t$ and frequency $\omega/2\pi$, is generally written in linear conditions as:

$$X(t) = \bar{X} + \mathrm{d}X \cos(\omega t + \psi)$$

The resulting impedance is defined as the complex quantity $\frac{\mathrm{d}X}{\mathrm{d}Y} \exp \mathrm{i}\psi$. ψ is the phase shift between Y and X signals.

An alternative treatment consists in using the complex notation:

$$X^*(t) = \bar{X} + \mathrm{d}X^* \quad \text{with} \quad \mathrm{d}X^* = \tilde{X} \exp \mathrm{i}\omega t$$

$\tilde{X}$ is a complex quantity which contains amplitude $\mathrm{d}X$ and phase shift ψ.

$$\tilde{X} = \mathrm{d}X \cdot \exp \mathrm{i}\psi$$

As the phase reference is taken with respect to that of the perturbation, then $\tilde{Y} = \mathrm{d}Y$.

$\tilde{X}$ also represents the Fourier transform of $X^*(t)$. Therefore the impedance can also be defined as $\tilde{X}/\tilde{Y}$.

1.3 Relation between Impedances

When the current at a rotating disk electrode (RDE) depends partly on mass transport, the instantaneous state of the electrochemical system can be characterized by an implicit functional relationship such as:

$$\mathrm{F}(I(t), E(t), \Omega(t)) = 0 \tag{1-1}$$

In a particular case of a sine wave modulation of low amplitude, a similar relation can be written with the complex quantities. Differentiating Eq. (1-1) for each frequency and considering the fact that I^*, E^* or Ω^* are independent variables two by two, one obtains:

$$\mathrm{d}I^* = \left(\frac{\partial I^*}{\partial E^*}\right)_{\Omega} \mathrm{d}E^* + \left(\frac{\partial I^*}{\partial \Omega^*}\right)_{E} \mathrm{d}\Omega^* \tag{1-2}$$

$$\mathrm{d}E^* = \left(\frac{\partial E^*}{\partial I^*}\right)_{\Omega} \mathrm{d}I^* + \left(\frac{\partial E^*}{\partial \Omega^*}\right)_{I} \mathrm{d}\Omega^* \tag{1-3}$$

and then:

$$\left(\frac{\partial E^*}{\partial I^*}\right)_{\Omega} = -\left(\frac{\partial E^*}{\partial \Omega^*}\right)_{I} \left(\frac{\partial \Omega^*}{\partial I^*}\right)_{E} \tag{1-4}$$

$\left(\frac{\partial E^*}{\partial I^*}\right)_{\Omega} = \left.\frac{\mathrm{d}E^*}{\mathrm{d}I^*}\right|_{\Omega} = \left.\frac{\tilde{E}}{\tilde{I}}\right|_{\Omega}$ is the usual ac impedance Z_{ac}.

Therefore, two other new quantities are introduced:

$\left.\dfrac{\tilde{E}}{\tilde{\Omega}}\right|_I$ is the electrohydrodynamical (EHD) impedance under galvanostatic control denoted $Z_{\mathrm{EHD,G}}$. In the same way:

$\left.\dfrac{\tilde{I}}{\tilde{\Omega}}\right|_E = Z_{\mathrm{EHD,P}}$ is the EHD impedance under potentiostatic control.

For simplifying the notations, impedances in the following will be written without vertical bars and the subscript defining the fixed variable.

Eq. (1-4) shows that only two quantities are needed, the third one being determined from the two first. Eq. (1-4) was directly verified by measuring Z_{ac}, $Z_{\mathrm{EHD,G}}$ and $Z_{\mathrm{EHD,P}}$ with the ferri/ferrocyanide system in KCl (M) at the half-wave potential [29]. Experimental Z_{ac} values were shown to be in good agreement with the calculated ones deduced from experimental $Z_{\mathrm{EHD,G}}$ and $Z_{\mathrm{EHD,P}}$ values, and application of Eq. (1-4) written as: $Z_{\mathrm{ac}} = -Z_{\mathrm{EHD,G}}/Z_{\mathrm{EHD,P}}$ (see Fig. 1-1).

From Eq. (1-2) one can still write:

$$\tilde{I} = \frac{\tilde{E}}{Z_{\mathrm{ac}}} + Z_{\mathrm{EHD,P}}\tilde{\Omega} \qquad (1\text{-}5)$$

Obtaining Eq. (1-5) in an explicit form provides a complete solution. This result can be properly achieved by splitting the problem in elementary steps which can be separately considered [11, 30] as schematized below:

$$\tilde{\Omega} \xrightarrow{1} \tilde{\alpha}_{\mathrm{i}} \xrightarrow{2} \begin{matrix} \tilde{c}(0) \\ \left.\dfrac{\partial \tilde{c}}{\partial y}\right|_0 \end{matrix} \xrightarrow{3} \begin{matrix} \tilde{E} \\ \tilde{I} \end{matrix}$$

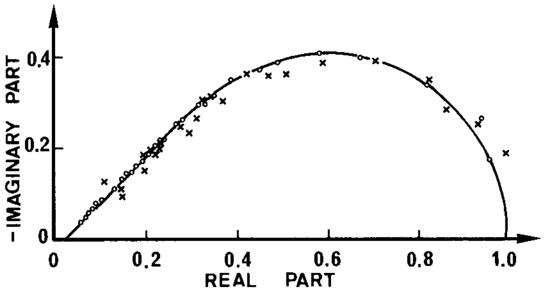

Fig. 1.1. Electrochemical impedance (×) obtained from Eq. (1-4) with the experimental measurements of $Z_{\mathrm{EHD,G}}$ and $Z_{\mathrm{EHD,P}}$. Electrochemical impedance (○) directly measured at the half wave potential. Curve in full line represents the theoretical variation. The coordinates are normalized by the electrochemical impedance value at zero frequency $Z_{\mathrm{ac}}(0)$. The parameter is the dimensionless frequency $pSc^{1/3}$. After [29].

- Step 1 is purely hydrodynamic and relates the perturbation $\tilde{\Omega}$ to the velocity near the wall which is the only relevant quantity for the mass transfer response. $\tilde{\alpha}_i$ are either wall velocity gradients or coefficients involved in the velocity expansion near the wall. This step requires the use of Navier-Stokes equations and will be treated in Chapter 2.
- Step 2 regards the mass transfer problem and needs to solve the mass balance equation, in order to obtain the concentration field and in particular the concentration and the concentration gradient at the electrode. This is the topic of Chapter 3.
- Step 3 which addresses the kinetic problem is performed to test the electrode process mechanism under study. The general procedure for achieving this task is detailed in Chapter 4.

A consequence of these elementary steps is that the observable quantities $\tilde{I}/\tilde{\Omega}$ or $\tilde{E}/\tilde{\Omega}$ can be generally written as the product of three elementary transfer functions, except for some cases where, for example, the problem is depending upon two velocity components.

2 Periodic Flow at a Rotating Disk

A periodic flow generated by small oscillations of a body in a fluid at rest involves non-linearities either in the mass transport problem or in the secondary flow, and is therefore out of range of this presentation.

The steady flow field created by an infinite disk rotating at a constant angular velocity in a fluid with constant physical properties was first studied by Von Karman [31].

The solution was sought by a separation of variables using an axial dimensionless distance $\chi = y\sqrt{\bar{\Omega}/\upsilon}$ which transforms the fluid velocity vector as follows:

$$\bar{\vartheta}_r = r\bar{\Omega}F(\chi)\ ,\quad \bar{\vartheta}_\theta = r\bar{\Omega}G(\chi)\ ,\quad \bar{\vartheta}_y = \sqrt{\upsilon\bar{\Omega}}H(\chi)$$

The overbar designates the steady-state values.

Hence, the time independent Navier-Stokes equations are put in form of three coupled, nonlinear, ordinary differential equations, functions of η only:

$$\begin{cases} 2F+H' = 0 & (2\text{-}1) \\ F^2-G^2+HF'-F'' = 0 & (2\text{-}2) \\ 2FG+HG'-G'' = 0 & (2\text{-}3) \end{cases}$$

Not listed in the set of Eqs. (2-1, 2-3) is the axial component of momentum which provides an additional equation for the hydrodynamic pressure that can be calculated once H is determined.

The boundary conditions are:

$$\left|\begin{array}{l} F(0)=H(0)=0\\ G(0)=1\\ F(\infty)=G(\infty)=0 \end{array}\right.$$

For the unsteady situation, the instantaneous value Ω is defined by:

$$\Omega=\bar{\Omega}+\mathrm{Re}\{\tilde{\Omega}\exp \mathrm{i}\omega t\} \quad \text{with} \quad \tilde{\Omega}=\Delta\Omega$$

$\omega/2\pi$ is the modulation frequency.

Large amplitude modulations induced a nonlinear flow response which has been studied by few authors [15, 32].

The impedance concept is developed here following the work of Tribollet and Newman [30], which means that the system response is linear and corresponds to low amplitude modulation ($\Delta\Omega \ll \bar{\Omega}$).

Therefore:

$$\vartheta_{\mathrm{r}}=r\bar{\Omega}\left[F(\chi)+\frac{\Delta\Omega}{\bar{\Omega}}\mathrm{Re}\{\tilde{f}(\chi)\exp \mathrm{i}\omega t\}\right] \tag{2-4}$$

$$\vartheta_{\theta}=r\bar{\Omega}\left[G(\chi)+\frac{\Delta\Omega}{\bar{\Omega}}\mathrm{Re}\{\tilde{g}(\chi)\exp \mathrm{i}\omega t\}\right] \tag{2-5}$$

$$\vartheta_{\mathrm{y}}=r\bar{\Omega}\left[H(\chi)+\frac{\Delta\Omega}{\bar{\Omega}}\mathrm{Re}\{\tilde{h}(\chi)\exp \mathrm{i}\omega t\}\right] \tag{2-6}$$

where $\tilde{f}$, $\tilde{g}$, and $\tilde{h}$ are complex functions.

The equation of continuity and the unsteady Navier-Stokes equations are linearized, i.e. the quadratic terms, proportional to $(\Delta\Omega/\bar{\Omega})^2$ are neglected.

The resulting equations may be written:

$$\begin{cases} 2\tilde{f}+\tilde{h}'=0 & (2\text{-}7)\\ \mathrm{i}\,\tilde{f}p+2F\tilde{f}-2G\tilde{g}+H\tilde{f}'+F'\tilde{h}=\tilde{f}'' & (2\text{-}8)\\ \mathrm{i}\,\tilde{g}p+2G\tilde{f}+2F\tilde{g}+\tilde{h}G'+H\tilde{g}'=\tilde{g}'' & (2\text{-}9) \end{cases}$$

where $p=\omega/\bar{\Omega}$ is the dimensionless modulation frequency.

The boundary conditions are:

$$\begin{cases} \tilde{f}(0)=\tilde{h}(0)=0\\ \tilde{g}(0)=1\\ \tilde{f}(\infty)=0 \end{cases}$$

Table 2-1. Values of $\left.\frac{d\tilde f}{d\chi}\right|_0$ and of $\left.\frac{d\tilde g}{d\chi}\right|_0$ versus the dimensionless frequency.

p	f_1'	f_2'	g_1'	g_2'
0.0631	0.7652	−0.0130	−0.9241	−0.0233
0.1000	0.7650	−0.0206	−0.9241	−0.0368
0.1585	0.7645	−0.0329	−0.9243	−0.0583
0.2512	0.7630	−0.0527	−0.9244	−0.0922
0.3981	0.7579	−0.0849	−0.9241	−0.1467
0.6310	0.7410	−0.1356	−0.9243	−0.2371
1.0000	0.6943	−0.2035	−0.9367	−0.3899
1.5849	0.6020	−0.2642	−0.9993	−0.6280
2.5119	0.4832	−0.2842	−1.1573	−0.9388
3.9811	0.3748	−0.2652	−1.4193	−1.2969
6.3095	0.2906	−0.2297	−1.7770	−1.7067
10.0000	0.2272	−0.1922	−2.2359	−2.1933

Each complex function may be written as the sum of a real function (index 1) and an imaginary function (index 2). The set of the three coupled Eqs. (2-7), (2-8), (2-9) becomes then a set of six coupled linear ordinary differential equations.

By using Newman's method [33, 34], the solution of the set of six equations is derived for each dimensionless frequency.

Cochran [35] has shown that the system of Eqs. (2-1), (2-2, (2-3) can be satisfied by two sets of series expansions for small and large values of η. The series solutions for small values of χ are especially relevant to the mass transfer problem. In particular the derivatives at $\chi = 0$, obtained from Eqs. (2-7), (2-8), (2-9) and given in Table 2-1 are essential in order to determine the first coefficients of the series expansions. The other coefficients are deduced from the first one by using the set of Eqs. (2-7), (2-9). In particular:

$$H = -0.51023\,\chi^2 + \frac{\chi^3}{3} \qquad (2\text{-}10)$$

$$\tilde h = -\tilde f'(p)\chi^2 + \frac{2}{3}\chi^3 \qquad (2\text{-}11)$$

As the frequency modulation tends towards zero, $r\tilde f_1$ tends towards the derivative of $\bar\vartheta_r$ with respect to $\bar\Omega$ (see Eq. (2-4)) and $\tilde f_2'$ tends towards zero. Therefore, $\tilde f'(0) = \frac{3}{2}\left.\frac{dF}{d\chi}\right|_0 = 0.765345$ and in the same way $\tilde g'(0) = \frac{3}{2}\left.\frac{dG}{d\chi}\right|_0 =$ -0.923883.

With an axisymmetric electrode (like a disk or ring) only $\bar\vartheta_y$ and/or $\bar\vartheta_r$ are involved in the mass balance equation. Hence, according to Eq. (2-4) or (2-11) only the $\tilde f'$ variations are useful for mass transfer measurements.

But for a nonaxisymmetric electrode (like a microelectrode off the rotation axis), the velocity component parallel to the wall $\vartheta_x = \sqrt{\vartheta_r^2 + \vartheta_\theta^2}$ appears also in the mass balance equation, and $\left.\frac{d\vartheta_x}{d\chi}\right|_0$ is proportional to $\sqrt{\tilde{f}'F' + \tilde{g}'G'}$.

By using the result of Sparrow and Gregg [36] who solved the unsteady flow problem, the low frequency expressions of $\tilde{f}'$ and $\tilde{g}'$ can be obtained following our notation:

$$\tilde{f}' = (0.765345 - 0.023112\,p^2) - 0.204835\,p\mathrm{i} \tag{2-12}$$

$$\tilde{g}' = (-0.923883 - 0.021185\,p^2) - 0.36922\,p\mathrm{i} \tag{2-13}$$

For the high frequencies, Sharma [37] obtained an asymptotic solution which can also be expressed in terms of $\tilde{f}'$ and $\tilde{g}'$:

$$\tilde{f}' = \frac{1}{\sqrt{2p}} - \mathrm{i}\left(\frac{1}{\sqrt{2p}} - \frac{0.313}{p}\right) \tag{2-14}$$

$$\tilde{g}' = -\sqrt{\frac{p}{2}} - \mathrm{i}\left(\sqrt{\frac{p}{2}} - \frac{3}{2}\,\frac{0.510}{p}\right) \tag{2-15}$$

The expressions (2-12) and (2-13) may be used with an accuracy better than 1% for $p \leq 0.1$.

The expressions (2-14) and (2-15) may be used with an accuracy better than 1% for $p \geq 7$.

3 Mass Transport on a Uniformly Accessible Electrode

The method was first introduced by Bruckenstein et al. at the beginning of the seventies [4].

Tokuda et al. 1975 [7], considered first the response of the limiting current to a modulation of the square root of the rotation speed. In their calculation, they took into account the second harmonic of the response, but gave the solution only for the first one in a limiting range of p and for discrete Sc values. This pioneering work is at the origin of all the other theoretical treatments.

Deslouis et al. [9] in 1977 measured experimentally with a high performance apparatus the response of the limiting current in a large frequency domain and for a large range of Schmidt number. In particular, they showed experimentally that the phase shift tends towards 180° in the high frequency range.

Later, Albery et al. 1979 [11] presented a theoretical treatment for both potentiostatic and galvanostatic regulations. These solutions are given as series expansions.

Deslouis et al. [10, 38], at the beginning of the eighties gave an analytical treatment for both potentiostatic and galvanostatic regulations by using Airy functions.

In 1983, Tribollet and Newman [30] derived a quantitative treatment by considering the hydrodynamic and mass transport problems together. They also found a relation linking the fluctuating concentration and its gradient at the interface, for use in kinetic studies.

3.1 Theoretical Analysis on Rotating Disk Electrode

The concentration distribution in the diffusion layer is governed by the one-dimensional unsteady equation of convective diffusion:

$$\frac{\partial c}{\partial t} + \vartheta_y \frac{\partial c}{\partial y} = D \frac{\partial^2 c}{\partial y^2} \tag{3-1}$$

The expansion of ϑ_y is obtained from Eqs. (2-10) and (2-11) and is limited to the first term in χ^2. The effect of the second term which appears as a Schmidt number correction will be evaluated in the next paragraph.

By putting: $c = \bar{c} + \mathrm{Re}\{\tilde{c} \exp \mathrm{i}\omega t\}$ and by using the dimensionless variables and parameters:

$$\mathrm{a} = 0.51023$$

$$\delta = \left(\frac{3D}{\mathrm{a}\upsilon}\right)^{1/3} \sqrt{\upsilon/\bar{\Omega}}$$

$$\eta = \frac{y}{\delta} = 0.554\, Sc^{1/3} \chi$$

$$\xi = \frac{\omega \delta^2}{D} = 3.258\, p Sc^{1/3}$$

where $Sc = \dfrac{\upsilon}{D}$ is the Schmidt number

The equivalent Nernst diffusion layer thickness is $\Gamma(4/3)$ times δ.

Eq. (3-1) becomes:

$$\frac{\mathrm{d}^2 \tilde{c}}{\mathrm{d}\eta^2} + 3\eta^2 \frac{\mathrm{d}\tilde{c}}{\mathrm{d}\eta} - \mathrm{i}\xi\tilde{c} = -\frac{\Delta\Omega}{\bar{\Omega}} \frac{3\tilde{\mathrm{f}}'(p)}{\mathrm{a}} \eta^2 \frac{\mathrm{d}\bar{c}}{\mathrm{d}\eta} \tag{3-2}$$

where

$$\frac{\mathrm{d}\bar{c}}{\mathrm{d}\eta}=\frac{c_\infty-c(0)}{\Gamma(4/3)}\exp-\eta^3$$

c_∞ being the concentration in the bulk and $c(0)$ the concentration at the interface.

Let $\theta_0(\chi)$ be a solution of the homogeneous Eq. (3-2) satisfying the boundary conditions:

$$\theta_0\rightarrow 0 \quad \eta\rightarrow\infty$$

and

$$\theta_0\rightarrow 1 \quad \eta=0$$

Integration gives:

$$\tilde{c}=K_2\theta_0+K_1\theta_0\int_0^\eta\frac{\exp-\eta'^3}{\theta_0^2(\eta')}\mathrm{d}\eta'-\frac{\Delta\Omega}{\bar{\Omega}}\left.\frac{\mathrm{d}\bar{c}}{\mathrm{d}\eta}\right|_0\theta_0\int_0^\eta\frac{\exp-\eta'^3}{\theta_0^2(\eta')}$$
$$\left[\int_0^{\eta'}\frac{3\tilde{\mathrm{f}}'(p)}{\mathrm{a}}\eta''^2\theta_0(\eta'')\mathrm{d}\eta''\right]\mathrm{d}\eta' \tag{3-3}$$

Where K_1 and K_2 are two integration constants. K_2 can be identified with $\tilde{c}(0)$, the value of the concentration at $\eta=0$. K_1 can be obtained from the boundary condition at infinity:

$$K_1=\frac{\Delta\Omega}{\bar{\Omega}}\left.\frac{\mathrm{d}\bar{c}}{\mathrm{d}\eta}\right|_0 W_0 \quad \text{with} \quad W_0=\int_0^\infty\frac{3\tilde{\mathrm{f}}'(p)}{\mathrm{a}}\eta^2\theta_0\mathrm{d}\eta \tag{3-4}$$

The general result is a relationship between the concentration and the concentration derivative, both evaluated at the electrode interface:

$$\left.\frac{\mathrm{d}\tilde{c}}{\mathrm{d}y}\right|_0=\frac{\tilde{c}(0)}{\delta}\theta_0'(0)+\frac{\Delta\Omega}{\tilde{\Omega}}\left.\frac{\mathrm{d}\bar{c}}{\mathrm{d}y}\right|_0 W_0 \tag{3-5}$$

where

$$\theta_0'(0)=\left.\frac{\mathrm{d}\theta_0}{\mathrm{d}\eta}\right|_0$$

The numerical calculation of W_0 requires the calculation of the homogeneous solution θ_0 which is necessary for the determination of the diffusion (or convective

Table 3-1. Variation of $Z_c = \left[\dfrac{\frac{3}{a}\int_0^\infty \eta^2\theta_0\,d\eta}{0.6533}\right]$ versus $pSc^{1/3}$

Coefficients for the Schmidt number correction corresponding to Eq. (3-16).

$pSc^{1/3}$	Re (Zc)	Im (Zc)	t_3	t_4	t_5	t_6
0.0	1.0	0.0	1.1921	0.0000	−0.9124	0.0000
0.1000	0.9970	−0.0607	1.1830	−0.1270	−0.9091	0.0624
0.1585	0.9925	−0.0958	1.1693	−0.2000	−0.9042	0.0985
0.2512	0.9812	−0.1505	1.1355	−0.3118	−0.8921	0.1546
0.3981	0.9536	−0.2334	1.0543	−0.4742	−0.8624	0.2394
0.6310	0.8889	−0.3507	0.8719	−0.6792	−0.7930	0.3584
1.0000	0.7508	−0.4904	0.5211	−0.8481	−0.6457	0.4967
1.5849	0.5090	−0.5929	0.0384	−0.793	−0.3912	0.5869
2.5119	0.2113	−0.5633	−0.2916	−0.4337	−0.0897	0.5269
3.9811	−0.0055	−0.3943	−0.2581	−0.0636	0.1016	0.3216
6.3095	−0.0740	−0.2069	−0.0860	.0511	0.1205	0.1236
10.0000	−0.0590	−0.0918	−0.0082	0.0259	0.0666	0.0299
15.8488	−0.0333	−0.0403	0.0013	0.0054	0.0272	0.0053
25.1187	−0.0171	−0.0186	0.0005	0.0009	0.0104	0.0009
39.8104	−0.0086	−0.0090	0.0001	0.0001	0.0040	0.0002
63.0952	−0.0043	−0.0044	0.0000	0.0000	0.0016	0.0000
100.0000	−0.0022	−0.0022	0.0000	0.0000	0.0006	0.0000

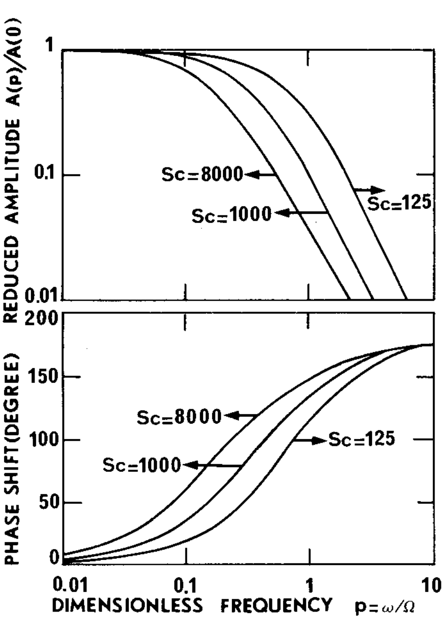

Fig. 3-1. Variation of W_0 versus the dimensionless frequency p for different Sc values. In the high frequency range the amplitude is proportional to p^{-2}.

Warburg) impedance, where potential or current is modulated instead of rotation speed.

W_0 can be written as:

$$W_0 = 0.5\, Z_{\mathrm{HD}} \cdot Z_c \quad \text{where} \quad Z_{\mathrm{HD}} = \frac{\tilde{\mathrm{f}}(p)}{\tilde{\mathrm{f}}'(0)}$$

$$\text{and} \quad Z_c = \frac{\frac{3}{\mathrm{a}} \int_0^{\infty} \eta^2 \theta_0 \mathrm{d}\eta}{0.6533} \quad \text{with} \quad Z_c \xrightarrow[\omega \to 0]{} 1 \,. \tag{3-6}$$

The hydrodynamic transfer function Z_{HD} can be obtained from Table 2-1 and Eqs. (2-12) and (2-14). The transfer function corresponding to mass transport, Z_c, is given in Table 3-1 for $0.1 \le p Sc^{1/3} \le 100$. For $p Sc^{1/3}$ larger than 60, the asymptotic value of Z_c can be analytically derived [39] (see Section 3.1).

The variation of W_0 is plotted on Fig. 3-1 versus the dimensionless frequency p for different Sc values.

3.2 Asymptotic Solution in High Frequency Range

Since the frequency is large, the distance over which a concentration wave proceeds is small, then $\exp(-\eta^3)$ can be considered as equal to one and the velocity modulation being rapidly damped close to the wall, the convective term can be disregarded in the homogeneous part of Eq. (3-2) which becomes:

$$\frac{\mathrm{d}^2 \tilde{c}}{\mathrm{d}\eta^2} - \mathrm{i}\xi \tilde{c} = \frac{\Delta\Omega}{\bar{\Omega}} \frac{3 \tilde{\mathrm{f}}'(p)}{\mathrm{a}} \eta^2 \left. \frac{\mathrm{d}\bar{c}}{\mathrm{d}\eta} \right|_0 \tag{3-7}$$

The solution of the homogeneous equation is $\theta = \exp(-(\mathrm{i}\xi)^{1/2}\eta)$ and the solution of Eq. (3-7) may be written as:

$$\tilde{c} = \theta(\eta) \left[\int_0^{\eta} \theta^{-2}(\chi') \left[-\int_0^{\eta'} \frac{\Delta\Omega}{\bar{\Omega}} \frac{3 \tilde{\mathrm{f}}'(p)}{\mathrm{a}} \eta''^2 \theta(\eta'') \left. \frac{\delta \bar{c}}{\mathrm{d}\eta} \right|_0 \mathrm{d}\eta'' + K_1 \right] \mathrm{d}\eta' + \tilde{c}(0) \right] \tag{3-8}$$

where

$$K_1 = \frac{\Delta\Omega}{\bar{\Omega}} \frac{3 \tilde{\mathrm{f}}'(p)}{\mathrm{a}} \left. \frac{\mathrm{d}\bar{c}}{\mathrm{d}\eta} \right|_0 \int_0^{\infty} \eta^2 \theta(\eta) \mathrm{d}\eta$$

and

$$\left. \frac{\mathrm{d}\tilde{c}}{\mathrm{d}y} \right|_0 = \frac{\Delta\Omega}{\bar{\Omega}} \frac{\tilde{\mathrm{f}}'(p)}{\mathrm{a}} \left. \frac{\mathrm{d}\bar{c}}{\mathrm{d}y} \right|_0 \frac{6}{(\mathrm{i}\xi)^{3/2}} \tag{3-9}$$

$$Z_c = \frac{18}{(\mathrm{i}\xi)^{3/2}} = \frac{3.061}{(\mathrm{i}pSc^{1/3})^{3/2}} \tag{3-10}$$

3.3 Schmidt Number Correction

The development of ϑ_y is now limited to the first two terms: Eq. (3-1) becomes:

$$\frac{\mathrm{d}^2\tilde{c}}{\mathrm{d}\eta^2} + \left(3\eta^2 - \frac{\mathrm{B}\eta^3}{Sc^{1/3}}\right)\frac{\mathrm{d}^2\tilde{c}}{\mathrm{d}\eta} - \mathrm{i}\xi\tilde{c} = -\frac{\Delta\Omega}{\bar{\Omega}}\left(\frac{3\tilde{\mathrm{f}}'(p)}{\mathrm{a}} - \frac{2\mathrm{B}\eta^3}{Sc^{1/3}}\right)\frac{\mathrm{d}\bar{c}}{\mathrm{d}\eta}$$

where

$$\mathrm{B} = \left(\frac{3}{\mathrm{a}^4}\right)^{1/3} \tag{3-11}$$

Following the same procedure, an equation similar to Eq. (3-4) is obtained but where θ and W are depending on Schmidt number:

$$W = \int_0^\infty \left(\frac{3\tilde{\mathrm{f}}'(p)}{\mathrm{a}}\eta^2 - \frac{2\mathrm{B}\eta^3}{Sc^{1/3}}\right)\theta\,\mathrm{d}\eta \tag{3-12}$$

As proposed by Levart and Schuhmann [40], θ was expressed as a series expansion in $Sc^{-1/3}$:

$$\theta(\eta, Sc, \xi) = \theta_0(\eta, \xi) + \frac{\theta_1(\eta, \xi)}{Sc^{1/3}} + \ldots \tag{3-13}$$

where θ_0 is the solution of:

$$\frac{\mathrm{d}^2\tilde{c}}{\mathrm{d}\eta^2} + 3\eta^2\frac{\mathrm{d}\tilde{c}}{\mathrm{d}\eta} - \mathrm{i}\xi\tilde{c} = 0 \tag{3-14}$$

as mentioned previously and θ_1 is the solution of:

$$\frac{\mathrm{d}^2\tilde{c}}{\mathrm{d}\eta^2} + 3\eta^2\frac{\mathrm{d}\tilde{c}}{\mathrm{d}\eta} - \mathrm{i}\xi\tilde{c} = \mathrm{B}\eta^3\frac{\mathrm{d}\theta_0}{\mathrm{d}\eta} \tag{3-15}$$

Finally W becomes:

$$W = 0.5\,Z_{\mathrm{HD}}Z_c + \frac{1}{Sc^{1/3}}[\tilde{\mathrm{f}}(p)(t_3 + \mathrm{i}t_4) + t_5 + \mathrm{i}t_6] \tag{3-16}$$

where

$$t_3 = \frac{3}{0.6533\,\mathrm{a}} \int_0^\infty \eta^2 \,\mathrm{Re}\{\theta_1\} \mathrm{d}\eta \ , \quad t_4 = \frac{3}{0.6533\,\mathrm{a}} \int_0^\infty \eta^2 \,\mathrm{Im}\{\theta_1\} \mathrm{d}\eta$$

$$t_5 = \frac{-2\mathrm{B}}{0.6533} \int_0^\infty \eta^3 \,\mathrm{Re}\{\theta_0\} \mathrm{d}\eta \ , \quad t_6 = \frac{-2\mathrm{B}}{0.6533} \int_0^\infty \eta^3 \,\mathrm{Im}\{\theta_0\} \mathrm{d}\eta$$

Im denoted the imaginary part of a complex quantity. t_3, t_4, t_5, t_6 are given in Table 3-1.

We verify that for $p Sc^{1/3} = 0$, the correction term is zero and W = 0.5.

4 Influence of Overall Kinetics

In the previous section, the velocity and concentration distributions have been established and two transfer functions were considered. The explicit form of the third function which relates the fluctuating interfacial concentration or concentration gradient to the potential or the current at the interface, requires to make clear the kinetic mechanism composed of elementary steps with at least one of them being in part or wholly mass transport controlled.

This section will demonstrate the advantage of treating the modulation flow problem in terms of impedance.

4.1 Analysis

We shall now describe the general procedure for getting Eq. (1-5) linking $\tilde{I}, \tilde{E}$ and $\tilde{\Omega}$.

To start with, it is necessary to consider the simplest equivalent circuit with the unique assumption of faradaic and capacitive branches (Fig. 4-1).

The following relations link the observable $\tilde{I}, \tilde{E}$ to the quantities $\tilde{U}$ and $\tilde{I}_\mathrm{F}$:

$$\tilde{I} = \tilde{I}_\mathrm{F} + C_\mathrm{D} \frac{\mathrm{d}\tilde{U}}{\mathrm{d}t} \qquad \left(\frac{\mathrm{d}\tilde{U}}{dt} = \mathrm{i}\omega \tilde{U} \quad \text{in sine wave regime} \right) \tag{4-1}$$

$$\tilde{E} = R_\mathrm{E} \tilde{I} + \tilde{U} \tag{4-2}$$

$\tilde{U}$ is the overpotential at the metal/electrolyte interface.

To this set of equations, we add Eq. (3-5) linking the complex concentration and concentration gradient at the electrode.

Now, the relevant kinetic mechanism will lead to a kinetic equation of the general shape:

$$I_\mathrm{F} = \mathrm{f}(U, c_\mathrm{i}(0), \Theta_\mathrm{j}, \ldots) \tag{4-3}$$

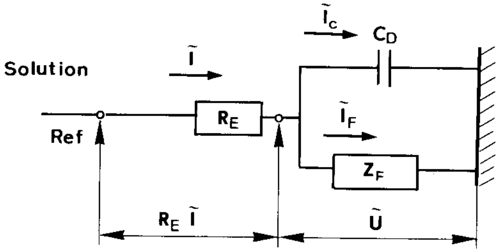

Fig. 4-1. Equivalent electrical circuit.

where Θ_j terms represent the possible coverage fractions by intermediate species j adsorbed at the electrode.

For species i, whose kinetic is partly or wholly mass transport controlled, one has:

$$D_i \frac{\partial \tilde{c}_i}{\partial y}\bigg|_0 = \frac{s_i}{nF} \tilde{I}_i \tag{4-4}$$

where s_i are the stoechiometric coefficients of the electrochemical reaction and $\tilde{I}_i$ is a partial current appearing in the mechanism.

It is, of course, impossible to provide an exhaustive catalog containing the EHD impedance expressions with all possible mechanisms. We will, only, in the next section illustrate the general procedure to follow, by some examples.

4.2 Reversible Redox Reaction in Mixed Kinetics

This is the simplest case which involves that partial current $\tilde{I}_i$ in Eq. (4-4) identifies itself with the overall faradaic current $\tilde{I}_F$. The faradaic current is ruled out by a Butler-Volmer kinetics:

$$I_F = I_0 \left[\frac{c_{ox}(0)}{c_{ox\infty}} \exp\left(\frac{\alpha_a F}{RT} U\right) - \frac{c_{red}(0)}{c_{red\infty}} \exp\left(-\frac{\alpha_c F}{RT} U\right) \right] \tag{4-5}$$

where symbols in Eq. (4-5) have their usual meaning, index i of Eq. (4-3) stands for ox and red in Eq. (4-5).

From Eq. (4-3):

$$\tilde{I}_F = \frac{\partial f}{\partial U}\bigg|_{c_i(0)} \tilde{U} + \sum_i \frac{\partial f}{\partial c_i(0)}\bigg|_{U, c_j(0)} \tilde{c}_i(0) \tag{4-6}$$

with

$$\left.\frac{\partial f}{\partial U}\right|_{c_i(0)} = R_t^{-1} .$$

R_t is the usual charge transfer resistance.

By subsequent use of Eqs. (3-5) and (4-4) one substitutes $\frac{\partial \tilde{c}_i}{\partial y}$ – hence $\tilde{I}_F$ – and $\tilde{\Omega}$ to $\tilde{c}_i(0)$.

Therefore Eq. (4-6) becomes:

$$\tilde{U} = (R_t + Z_D)\tilde{I}_F + \frac{\tilde{\Omega}}{\bar{\Omega}} \frac{\bar{I} R_t}{nF} \sum_i \left.\frac{\partial f}{\partial c_i(0)}\right|_{U,c_j(0)} \frac{W_i \delta_i}{\theta_i'(0)} \frac{s_i}{D_i} \tag{4-7}$$

$$Z_D = -R_t \sum_i \left.\frac{\partial f}{\partial c_i(0)}\right|_{U,cj(0)} \frac{\delta_i s_i}{nFD_i \theta_i'(0)} \tag{4-8}$$

Z_D is the convective diffusion impedance with its dimensionless form $-1/\theta_i'(0)$ [41].

Considering now Eqs. (4-1) and (4-2), one obtains the relation between observable quantities corresponding to the general form of Eq. (1-5):

$$\tilde{E} = Z_{ac}\tilde{I} + \frac{\tilde{\Omega}}{\bar{\Omega}} \frac{1}{1+i\omega C_D(R_t+Z_D)} \frac{\bar{I} R_t}{nF} \sum_i \left.\frac{\partial f}{\partial c_i(0)}\right|_{U,c_j(0)} \frac{W_i \delta_i}{\theta_i'(0)} \frac{s_i}{D_i} \tag{4-9}$$

where

$$Z_{ac} = R_E + \frac{R_t + Z_D}{1+i\omega C_D(R_t+Z_D)} \tag{4-10}$$

Z_{ac} represents the ac impedance of the usual Randles equivalent circuit.

With the simplifying assumption that the overpotential is large and mainly concentration-controlled and that the current is defined by the gradient of one species, the potentiostatic impedance can be expressed as:

$$\frac{\tilde{I}}{\tilde{\Omega}} = 0.5 \frac{\bar{I}}{\bar{\Omega}} Z_{HD} Z_c \frac{Z_D}{Z_{ac}} \frac{1}{1+i\omega C_D(R_t+Z_D)} \tag{4-11}$$

when $\omega \to 0$, $\tilde{I}/\tilde{\Omega}$ tends to $0.5\,\bar{I}/\bar{\Omega}$ as the derivative of the Levich current versus $\bar{\Omega}$.

The EHD impedance appears clearly as the product of three transfer fonctions: hydrodynamical Z_{HD}, mass transport Z_c and kinetic $Z_D/Z_{ac}\,[1+i\omega C_D(R_t+Z_D)]$.

In addition, by assuming purely diffusion control (i.e. at the diffusion plateau), R_E and $R_t \ll |Z_D|$ whatever ω, and by assuming $R_E C_D \ll 1$, hence $Z_D/Z_{ac} \to 1$, Eq. (4-11) becomes

$$\frac{\tilde{I}}{\tilde{\Omega}} = \frac{\bar{I}}{\bar{\Omega}} W = 0.5 \frac{\bar{I}}{\bar{\Omega}} Z_{\mathrm{HD}} Z_{\mathrm{c}} \tag{4-12}$$

Thus, under limiting current conditions, the measured quantity $\tilde{I}/\tilde{\Omega}$ has the same properties as W, in particular, the reducibility versus p, because $\tilde{c} = 0$, as $\bar{c} = 0$.

4.3 Heterogeneous Reaction with Adsorption

This mechanism involves the adsorption of an intermediate species. Consider indeed the two electrochemical elementary steps:

$$\begin{cases} \mathrm{A} \xrightarrow{\mathrm{K_A}} \mathrm{X} + \mathrm{e}^- \\ \mathrm{X} \xrightarrow{\mathrm{K_x}} \mathrm{P} + \mathrm{e}^- \end{cases} \tag{4-13}$$

Species A arrives at the interface by convective diffusion, adsorbs and reacts, producing species P (see Fig. 4-2).

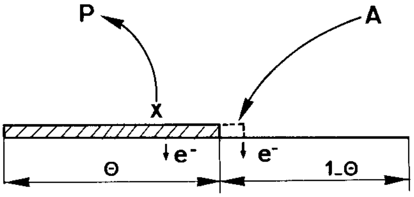

Fig. 4-2. Model of exchange of two electrons with adsorption of an intermediate species X.

The impedance expression is calculated with the following assumptions:

(i) Adsorption of reaction intermediate X obeys a Langmuir isotherm and is characterized by a surface coverage Θ. Areas Θ and $1 - \Theta$ are macroscopically distributed.

(ii) Reactions are governed by heterogeneous kinetics and reaction rates are exponentially potential dependent, following a Tafel's law instead of Butler-Volmer, corresponding then to irreversible conditions:

$$K_{\mathrm{i}} = k_{\mathrm{i}} \exp b_{\mathrm{i}} \eta$$

(iii) Maximum number of available sites per surface unit for adsorbate X is characterized by a coefficient β depending on the substrate nature.

Mass and charge balances give:

$$\begin{cases} \beta_{\mathrm{L}} \dfrac{\mathrm{d}\Theta}{\mathrm{d}t} = K_{\mathrm{A}} c_{\mathrm{A}} (1 - \Theta) - K_{\mathrm{x}} \Theta \beta_{\mathrm{L}} \\ I_{\mathrm{F}} = F\{K_{\mathrm{A}} c_{\mathrm{A}} (1 - \Theta) + K_{\mathrm{x}} \Theta \beta_{\mathrm{L}}\} \end{cases} \tag{4-14}$$

Solution of these equations for $\frac{\mathrm{d}\Theta}{\mathrm{d}t} = 0$ leads, after elimination of Θ, to the equation of the steady-state current voltage curve:

$$\bar{\Theta} = \frac{K_A c_A}{K_x \beta_L + K_A c_A} \tag{4-15}$$

$$\bar{I}_F = \frac{2FK_A K_x c_A \beta_L}{K_A c_A + K_x \beta_L} \tag{4-16}$$

Under a flow modulation of amplitude $\tilde{\Omega}$ and frequency $\omega/2\pi$, subsequent complex responses $\bar{I}_F, \tilde{U}, \tilde{c}_A$ and $\tilde{\Theta}$ take place, determined by linearized Eq. (4-14):

$$(K_A \bar{c}_A + K_x \beta_L + \mathrm{i}\omega\beta_L)\tilde{\Theta} = \{\bar{c}_A(1-\bar{\Theta}) b_A K_A - \beta\bar{\Theta} b_x K_x\}\tilde{U} + K_A(1-\bar{\Theta})\tilde{c}_A \tag{4-17}$$

$$\tilde{I}_F = \{\bar{c}_A(1-\bar{\Theta}) b_A K_A + \Theta\beta_L b_x K_x\}\tilde{U} + (K_x\beta - K_A\bar{c}_A)\tilde{\Theta} + K_A(1-\bar{\Theta})\tilde{c}_A \tag{4-18}$$

and also

$$\tilde{I}_F = nFD_A \left.\frac{\partial \tilde{c}_A}{\partial y}\right|_0 \tag{4-19}$$

If we consider the general Eq. (4-18), one can eliminate $\frac{\partial \tilde{c}_A}{\partial y}$, $\tilde{c}_A$, $\bar{\Theta}$ and $\tilde{\Theta}$ and obtain the following relation:

$$\tilde{I}_F = \frac{\tilde{U}}{Z_{ac}} + \frac{\bar{I}}{\bar{\Omega}}\left(\frac{W}{[D_A\theta'(0)]/\delta}\,\frac{(K_x\beta_L + K_A c_A)(K_A c_A + K_x\beta_L + \mathrm{i}\omega\beta)}{K_A K_x \beta_L(2K_x\beta_L + \mathrm{i}\omega\beta_L)} - 1\right)\tilde{\Omega} \tag{4-20}$$

with

$$Z_{ac} = \frac{(K_x\beta_L + K_A c_A)(K_x\beta_L + K_A c_A + \mathrm{i}\omega\beta_L) - \frac{\delta}{D_A\theta'(0)}\cdot K_A K_x \beta_L(2\mathrm{K}_x\beta_L + \mathrm{i}\omega\beta_L)}{K_A c_A K_x \beta_L\{2b_A K_x\beta_L + 2b_x K_A c_A + (b_A + b_x)\mathrm{i}\omega\beta_L\}} \tag{4-21}$$

This expression of Z_{ac} was earlier proposed by Epelboin et al. [42] and the relevant impedance diagrams, when assuming an infinitely fast diffusion process, contain a low frequency loop of either capacitive or inductive nature, depending on the values assigned to the different kinetics constants.

It is worth noting that even in a situation where the interface overpotential $\tilde{U}$ is zero, the EHD impedance $\tilde{I}_F/\tilde{\Omega}$ contains the relaxation effect of adsorbed species X.

By use of Eqs. (4-21) and (4-2), the general relation between the observables can be obtained:

$$\tilde{I} = \frac{\tilde{E}}{Z_{\mathrm{ac}}} + \frac{Z_{\mathrm{ac}} - R_{\mathrm{E}}}{Z_{\mathrm{ac}}} \frac{\bar{I}}{\bar{\Omega}} \frac{W}{\dfrac{D_{\mathrm{A}}\theta'(0)(K_{\mathrm{x}}\beta_{\mathrm{L}} + K_{\mathrm{A}}c_{\mathrm{A}})(K_{\mathrm{A}}c_{\mathrm{A}} + K_{\mathrm{x}}\beta_{\mathrm{L}} + \mathrm{i}\omega\beta)}{\delta K_{\mathrm{A}}K_{\mathrm{x}}\beta_{\mathrm{L}}(2K_{\mathrm{x}}\beta_{\mathrm{L}} + \mathrm{i}\omega\beta_{\mathrm{L}})} - 1} \tilde{\Omega} \qquad (4\text{-}22)$$

where Z_{ac} contains R_{E} and C_{D} as shown in Fig. (4-1).

From Eq. (4-22), the impedances $\frac{\tilde{I}}{\tilde{\Omega}}$ or $\frac{\tilde{E}}{\tilde{\Omega}}$ can be easily deduced.

4.4 Alternative Treatment of Martem'Yanov and Grafov

In a recent work [43], Martem'Yanov and Grafov, envisaged also the effect of hydrodynamic fluctuations on the electrochemical current, proposing to call it a hydroelectrochemical impedance, with the same definitions as those given above (see Section 1.3). Their approach is basically the same as that described in Section 1.3 in that they consider the hydrodynamic and electrical perturbations from a unified position. More precisely, for the kinetic situation described in Section 4.2 they show that an equation such as Eq. (4-7), obtained in a simplified version (i.e. no convective diffusion and a qualitative analysis of the fluctuating flow field) can be written as

$$(R_{\mathrm{t}} + Z_{\mathrm{w1}} + Z_{\mathrm{w2}})\tilde{I}_{\mathrm{F}} = \tilde{U} + \tilde{w}_1 + \tilde{w}_2 \qquad (4\text{-}23)$$

By doing so, they introduced in the electrical circuit explicit hydrodynamic current generators $\tilde{y}_{\mathrm{i}}$ or additional tension generators $\tilde{w}_{\mathrm{i}}$ which are placed either in parallel or in series to the relevant Warburg impedances Z_{w1} or Z_{w2} for each form of the redox couple. One has:

$$\tilde{w}_{\mathrm{i}} = Z_{\mathrm{wi}}\tilde{y}_{\mathrm{i}} \quad \text{and} \quad \tilde{y}_{\mathrm{i}} = (-1)^{\mathrm{i}} nFD_{\mathrm{i}}k\tilde{\vartheta}_{\mathrm{i}} \qquad (4\text{-}24)$$

with the notation of Chapter 3:

$$k = \frac{I}{\bar{\Omega}} W \frac{\tilde{\vartheta}}{\tilde{\Omega}} \qquad (4\text{-}25)$$

$\tilde{\vartheta}$ represents the flow modulation intensity in the y direction, equal to

$$\tilde{\vartheta} = -\tilde{f}'(0,p)\frac{\bar{\Omega}}{\upsilon} \qquad (4\text{-}26)$$

Thus, the only limitation when using this technique is that one needs to know explicitely the decomposition in single elements required by the use of an equivalent electrical circuit, which is not always possible.

5 Characterization of the Interface with an Additional 2-D or 3-D Insulating Phase

Uniform accessibility and reactivity of the electrode interface are the main hypotheses for developing the EHD impedance theory. However, in many cases a real interface deviates from this ideal picture due for example either to incomplete monolayer adsorption leading to the concept of partial blocking (2D adsorption) or to the formation of layers of finite thickness (3D phenomena).

These effects do not involve the interfacial kinetics on bare portions of the metal which, for simplification, will be assumed to be inherently fast. The changes will affect only the local mass transport conditions towards the reaction sites.

Before presenting some applications of practical interest, the theoretical EHD impedance for partially blocked electrodes and for electrodes coated by a porous layer will be analyzed.

5.1 Partially Blocked Electrodes

The first theoretical analysis of this problem was proposed by Landsberg et al. [44–46] following a concept developed in electrical engineering and formely used by Smythe [47]. The calculation was carried out for an interface composed of purely insulating and purely conducting areas, the latter being small disks of diameter d arranged in a two-dimensional periodic array.

The first contribution, which led to an approximate analytical solution, was then improved in further studies by Levart et al. [48]. For moderate blocked ratio values ($0.5 < \Psi < 1$), (Ψ blocked fraction of the surface), some contributions, such as that of Filinovsky [49], attempted to consider the convective terms for two-dimensional concentration fields but disregarded the diffusion terms in direction parallel to the electrode plane.

It turns out that the information issued from the steady-state technique can not be unambiguously unravelled in general, and that a comprehensive description of the topography leading to a defined (Ψ, d) couple is questionable. In fact, all the predictions put forward could be summarized for moderate Ω by a relation of the form:

$$I_d^{-1} = C_1 \Omega^{-1/2} + C_2 \qquad (5\text{-}1)$$

where C_1 and C_2 related to the blocking ratio Ψ and to the characteristic site dimension d.

A first problem is that, there is not a one-to-one relation between the measured (C_1, C_2) and (Ψ, d) couples. Secondly, equation such as (5-1) can be found for other processes, for example diffusion through a porous layer [50] and coupling with a preceding chemical reaction of first order [51].

To overcome these drawbacks, Landsberg and Thiele [44] recommended, in 1966 the use of transient techniques. Recently, these techniques, such as chronopotentiometry and amperometry [52], linear potential sweep and cyclic voltammetry [53], ac impedance [54] and EHD impedance [55] have been applied with increasing frequency.

In some applications where adsorption is involved, the blocking ratio Ψ can depend on the overpotential. The EHD impedance technique under potentiostatic conditions seems therefore the most appropriate technique.

A thorough numerical integration of the complete mass balance equation was developed for predicting the transient mass flux on a unique small active microelectrode placed in the trailing region of a large electrode [56]. It has the advantage of offering a validation of the theory with an easy-to-build experimental model.

5.1.1 Statement of the Problem

A unique small active site close to a uniformly accessible rotating disk electrode is considered in this derivation. For the sake of simplification, the geometry of the active site is rectangular with its length perpendicular to the streamline of the flow (Fig. 5-1). By neglecting diffusion in the z direction, the mathematical problem is locally reduced to two dimensions, and the complete mass balance equation is formulated as follows:

$$\frac{\partial c}{\partial t} + \vartheta_{\mathrm{x}} \frac{\partial c}{\partial x} + \vartheta_{\mathrm{y}} \frac{\partial c}{\partial y} = D \left(\frac{\partial^2 c}{\partial y^2} + \frac{\partial^2 c}{\partial x^2} \right) \tag{5-2}$$

The series expansions of the velocity components ϑ_{x} and ϑ_{y} are limited to the first term only (see Chapter 2)

$$\vartheta_{\mathrm{x}} = \sqrt{\vartheta_{\mathrm{r}}^2 + \vartheta_{\theta}^2} = \alpha(r,t)y$$

$$\vartheta_{\mathrm{y}} = \gamma(t)y^2$$

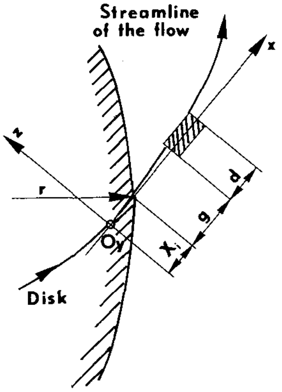

Fig. 5-1. Coordinate system for integration of Eq. (5-2). Flux is calculated for the rectangular active site in the vicinity of a RDE.

where r is the disk radius and under stationary conditions $\bar{\alpha} = 0.8\, r\bar{\Omega}^{3/2}\upsilon^{-1/2}$ and $\bar{\gamma} = -0.51023\,\bar{\Omega}^{3/2}\upsilon^{-1/2}$.

a) Steady-state Solutions

Integration of non-stationary mass balance equation requires that the steady-state concentration distribution $\bar{c}$ be known. This is achieved by solving the steady-state part of Eq. (5-2).

The details of the numerical calculation based on the Newman's method are given in [56].

The steady-state iso-concentration lines, deduced from the numerical treatment are plotted in Fig. 5-2. The effect of the x diffusion term ($\partial^2\bar{c}/\partial x^2$) of Eq. (5-2) is important at the leading edge of the microelectrode: when this term is dropped, all the isoconcentration lines start from this same point.

In Fig. 5-2 is displayed the effect of two neighbouring microelectrodes. Such an arrangement would describe locally a periodical distribution of active and passive sites with an active fraction of the whole area of 43%.

It appears that the concentration profiles of the two leading edges coincide reasonably well and one may assume that the memory effect on the concentration distribution is lost over one or few active sites. This last result hence justifies the procedure of considering one site located in the wake of a macroelectrode.

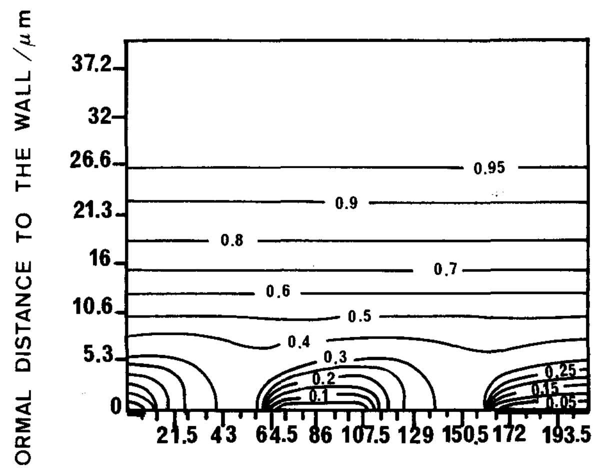

Fig. 5-2. Concentration field over the outer edge of a disk and over two controlled microelectrodes for a gap of 57 μm and two microelectrodes of 43 μm. From [56].

b) Unsteady-state Solutions (EHD Impedance)

Integration of nonsteady part of Eq. (5-2), was performed, the fluctuating concentration being split, at each mesh point, into a real and an imaginary part:

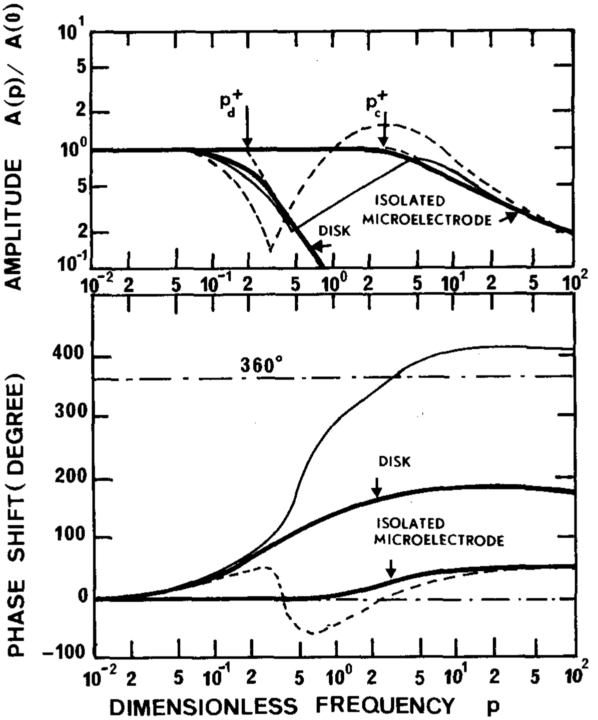

Fig. 5-3. Numerical integration of the complete mass balance Eq. (5-2) for a uniform disk electrode, an isolated microelectrode and two microelectrodes of same dimension but with two different gaps: (--------) $g = 40\ \mu\mathrm{m}$, (– – –) $g = 22.5\ \mu\mathrm{m}$.

$$\tilde{c} = \mathrm{Re}\,(\tilde{c}) + \mathrm{i}\,\mathrm{Im}\,(\tilde{c})$$

The calculated impedance $\tilde{I}/\tilde{\Omega}$ is represented in Fig. 5-3. The curves in solid line correspond to the behaviour previously calculated for the rotating disk electrode (see Section 3.1) and in reference [57], for the isolated microelectrode. The different curves in dots and dashes were obtained for the microelectrode in the wake of the large electrode. The first two curves (solid line) show only a monotonic decrease with increasing frequency. The controlled microelectrode curves display, at variance, non-monotonic evolutions with two characteristic frequency domains:

1. At low frequencies, it approaches the macroelectrode behaviour. Indeed the steady-state solution shows that the microelectrode can be considered as a simple extension of the macroelectrode. In this quasi steady-state regime, the frequency is small enough to allow the concentration wave to propagate over the whole diffusion layer thickness.
2. At high frequencies, the curves are close to those of the isolated microelectrode in normalized amplitude and the phase shift can be 2π higher for the controlled microelectrode with respect to the isolated one. At these frequencies, indeed the

concentration perturbation concerns only the first isoconcentration lines which exhibit close to the leading edge the same curvature as that found with an isolated microelectrode.

The first frequency response of the function $\tilde{I}/\tilde{\Omega}$ (disk response) follows an asymptotic power law dependence $|\tilde{I}/\tilde{\Omega}| \propto p^{-2}$ and the second response (controlled isolated microelectrode $|\tilde{I}/\tilde{\Omega}| \propto p^{-1/2}$.

Two cut-off frequencies p^+ can be defined as the intercept of the horizontal LF behavior ($A(p)/A(0) = 1$) and the "relevant" HF behavior (disk p_d^+ or controlled microelectrode p_c^+).

From Section 3.1, one can write

$$2.4 = p_d^+ Sc^{1/3} \tag{5-3}$$

and from [57]

$$0.79 = (0.963/2\pi) p_c^+ Sc^{1/3} (d/R)^{1/3} \tag{5-4}$$

Rearranging Eqs. (5-3) and (5-4) finally yields:

$$p_c^+/p_d^+ = 2.1\,(R/d)^{2/3}$$

An alternative presentation is to give dimension d versus the frequency lag which is the experimental quantity measured:

$$d = 2.1^{3/2} R (p_c^+/p_d^+)^{-3/2} \tag{5-5}$$

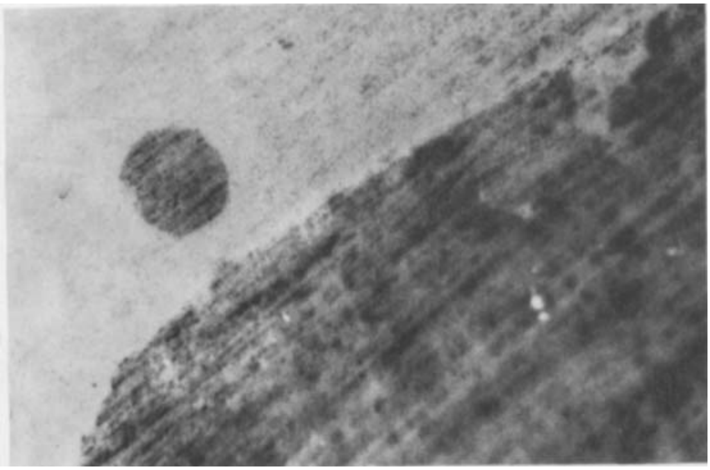

Fig. 5-4. Photograph of the experimental disk electrode and controlled microelectrode. $d = 105\ \mu$m the estimated gap value is 40 μm.

5.1.2 Confirmation with an Experimental Model

The electrode arrangement and dimensions are displayed in Fig. 5-4. The two rotating electric contacts (disk and microelectrode) are ensured by two mercury contactors [58], allowing the EHD impedance to be measured under satisfactory signal-to-noise conditions. The system $\mathrm{Fe(CN)_6^{3-}/Fe(CN)_6^{4-}}$ in the reduction direction was used.

The general aspect of these EHD impedance diagrams reproduces the theoretical variations depicted in Fig. 5-3. By applying the p_c^+/p_d^+ criterion (Eq. 5-5), one finds a value of the microelectrode diameter which falls within the range of 100–150 μm. This gives a reasonable estimate of the actual diameter value of 105 μm.

The phase shifts are wholly reducible versus p and are displayed in Fig. 5-5. The response of the controlled microelectrode increases monotonically with the frequency and equals the $\pi/4$ limiting value of the isolated microelectrode [57] increased by 2π, a case theoretically predicted for a small gap.

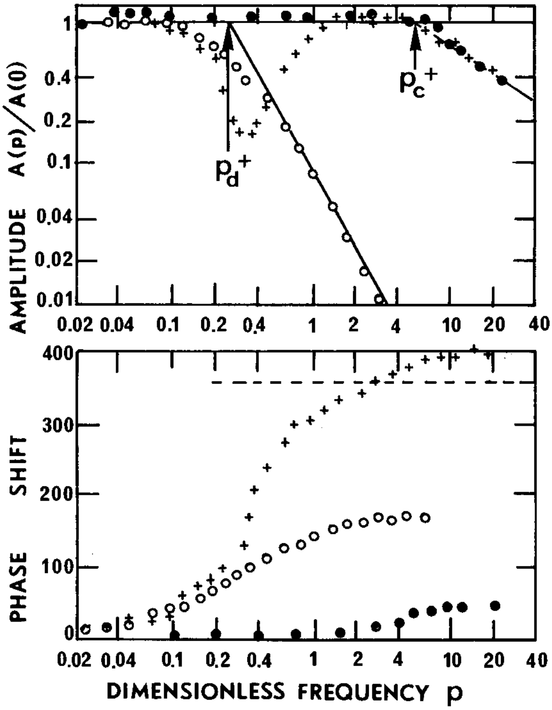

Fig. 5-5. Experimental EHD impedance in Bode coordinates for the microelectrode shown in Fig. 5-4. (●) Isolated microelectrode, (+) controlled microelectrode, (○) disk electrode.

5.2 Coated Disk Electrode

Porous nonreacting layers covering reacting metallic interfaces may slow down the mass transfer rate of diffusing species. This decrease includes the effect of the diffusivity D_F, as well as that of the layer thickness δ_F; steady-state techniques yield only the ratio D_F/δ_F [59].

5.2.1 Theoretical Analysis

The system under investigation is schematized in Fig. 5-6. The concentration gradient is distributed between the fluid and the porous layer. In addition, the metal layer interface is assumed to be uniformly reactive.

Two mass balance equations can be written:

i) In the porous layer, the concentration distribution c_1 is only determined by molecular diffusion:

$$\frac{\partial c_1}{\partial t} = D_F \frac{\partial^2 c_1}{\partial y^2} \tag{5-6}$$

ii) In the fluid, the concentration distribution c_2 is governed by convective diffusion:

$$\frac{\partial c_2}{\partial t} = D \frac{\partial^2 c_2}{\partial y_f^2} - \vartheta_y \frac{\partial c_2}{\partial y_f} \tag{5-7}$$

For simplicity, the origin of the coordinate y is taken at the metal/layer interface and that of y_f at the layer/fluid interface ($y_f = y - \delta_F$). c_1, c_2 and ϑ_y contain a steady-state component and a sinusoidal time dependent component of small amplitude when the angular velocity of the disk is modulated.

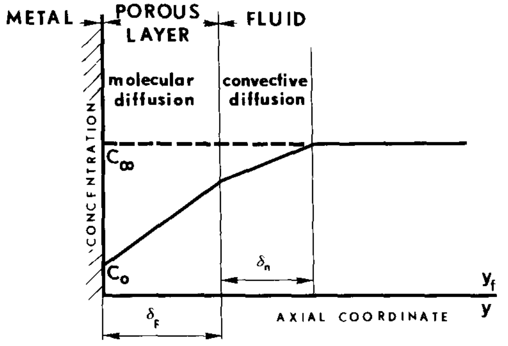

Fig. 5-6. Concentration distribution versus the axial coordinate in the presence of a porous layer.

Associated with Eqs. (5-6) and (5-7), are the boundary conditions which express the continuity of the concentration fields and of the fluxes for the steady-state as well as for the time dependent quantities:

– for $y = \delta_F (y_f = 0)$ $c_1(\delta_F) = c_2(0)$

$$D_F \frac{\partial c_1}{\partial y} = D \frac{\partial c_2}{\partial y}$$

– for $y_f = 0$ $\vartheta_y = 0$

– for $y_f \to \infty$ $c_2 \to c_\infty$ (then $\bar{c}_2 \to c_\infty$ and $\tilde{c}_2 \to 0$)

Finally the diffusing species are consumed at the metal-porous layer interface in a very fast electrochemical reaction. For simplification, diffusion control will be assumed (i.e. $\bar{c}_1(0) = 0$).

It is now convenient to split up Eqs. (5-6) and (5-7) into their steady-state and fluctuating components to get the corresponding solutions.

a) Steady-state Solutions

Eq. (5-6) is reduced to the simple form:

$$\frac{\partial^2 c_1}{\partial y^2} = 0 \tag{5-8}$$

which leads to

$$c_1(y) = Q \cdot y \tag{5-9}$$

The constant Q will be determined with the boundary conditions at $y = \delta_F$ and $y = 0$

$$Q \cdot \delta_F = \bar{c}_2(0)$$

$$Q \cdot D_F = D \frac{c_\infty - \bar{c}_2(0)}{\delta} \Gamma\,(4/3) \quad \text{(Nernst approximation)} \tag{5-10}$$

Therefore the steady-state flux is given by:

$$\bar{J} = \frac{c_\infty}{\dfrac{\delta}{D\Gamma(4/3)} + \dfrac{\delta_F}{D_F}} \tag{5-11}$$

Or by considering the reciprocal quantities, as is usually done for processes occurring in series:

$$\bar{J}^{-1} = \bar{J}_{\mathrm{L}}^{-1} + \bar{J}_{\Omega\to\infty}^{-1} \tag{5-12}$$

The physical meaning of the quantities appearing in Eq. (5-12) is obvious: $\bar{J}_{\mathrm{L}} = c_\infty D\Gamma(4/3)/\delta$ is the limiting diffusion flux at $\bar{\Omega}$ on the metallic surface, free from porous layer and $\bar{J}_{\Omega\to\infty} = c_\infty D_{\mathrm{F}}/\delta_{\mathrm{F}}$ is the limiting flux when the entire concentration gradient is located within the porous layer, i.e. when $\Omega\to\infty$.

The interest of using reciprocal values as in Eq. (5-12) is that an experimental plot of J^{-1} vs $\Omega^{-1/2}$ must be a straight line parallel to the Levich linear variation, which passes through the origin. The ordinate value of the intercept of this straight line at $\Omega^{-1/2} = 0$ is $J_{\Omega\to\infty}^{-1}$, and hence provides the layer permeability $D_{\mathrm{F}}/\delta_{\mathrm{F}}$.

b) Unsteady-state Solutions

In the porous layer, the fluctuating part of Eq. (5-6) may be written as:

$$\frac{\partial^2 \tilde{c}_1}{\partial y^2} - \frac{\mathrm{i}\omega}{D_{\mathrm{F}}}\tilde{c}_1 = 0 \tag{5-13}$$

The solution contains two constants M and N

$$\tilde{c}_1 = M\exp\left\{\frac{\mathrm{i}\omega}{D_{\mathrm{F}}}y^2\right\}^{1/2} + N\exp-\left\{\frac{\mathrm{i}\omega}{D_{\mathrm{F}}}y^2\right\}^{1/2} \tag{5-14}$$

At the fluid-porous layer interface ($y_{\mathrm{f}} = 0$), the relationship (3-5) can be applied since there is no additional process in the fluid:

$$\left.\frac{\partial \tilde{c}_2}{\partial y_{\mathrm{f}}}\right|_{y_{\mathrm{f}}=0} = \frac{\tilde{c}_2(0)}{\delta}\theta'(0) + \frac{\Delta\Omega}{\bar{\Omega}}\left.\frac{\mathrm{d}\bar{c}_2}{\mathrm{d}y}\right|_{y_{\mathrm{f}}=0} W \tag{5-15}$$

Then, from the boundary conditions at $y = \delta_{\mathrm{F}}$, Eq. (5-15) becomes

$$\left.\frac{\partial \tilde{c}_2}{\partial y_{\mathrm{f}}}\right|_{y_{\mathrm{f}}=0} = \frac{D_{\mathrm{F}}}{D}\left.\frac{\partial \tilde{c}_1}{\partial y}\right|_{\delta_{\mathrm{F}}} = \frac{\tilde{c}_1(\delta_{\mathrm{F}})}{\delta}\theta'(0) + \frac{\Delta\Omega}{\bar{\Omega}}\frac{D_{\mathrm{F}}}{D}\left.\frac{\mathrm{d}\bar{c}_1}{\mathrm{d}y}\right|_{0} W \tag{5-16}$$

Using Eq. (5-14) and the different boundary conditions, the constants M and N may be eliminated and Eq. (5-16) becomes:

$$\left.\frac{\partial \tilde{c}_1}{\partial y}\right|_0 = \tilde{c}_1(0)\,\frac{\dfrac{\xi_F^{1/2}\,\mathrm{th}\,\xi_F^{1/2}}{\delta_F}+\dfrac{D}{D_F}\,\dfrac{({}^{-1}/\theta'(0))}{\delta}}{1+\dfrac{D}{D_F}\,\dfrac{\delta_F}{({}^{-1}/\theta'(0))\delta}\,\dfrac{\mathrm{th}\,\xi_F^{1/2}}{\xi_F^{1/2}}}$$

$$+\Delta\Omega\,\frac{\dfrac{1}{\mathrm{ch}\,\xi_F^{1/2}}\left.\dfrac{\mathrm{d}\bar{c}_1}{\mathrm{d}z}\right|_0\dfrac{W}{\bar{\Omega}}}{1+\dfrac{D}{D_F}\,\dfrac{\delta_F}{\delta}\,\dfrac{1}{({}^{-1}/\theta'(0))}\,\dfrac{\mathrm{th}\,\xi_F^{1/2}}{\xi_F^{1/2}}} \qquad (5\text{-}17)$$

where $\xi_F = \mathrm{i}\omega \dfrac{\delta_F^2}{D_F}$

It may be easily verified that when the layer effect is gradually decreased (i.e. $\delta_F \to 0$ and $D_F \to D$) one finds again the relation (3-5).

The EHD impedances corresponding to a constant concentration ($\tilde{c}_1(0) = 0$) were simulated and the results were compared to those valid for a bare electrode.

In Fig. 5-7, the amplitude and phase shift corresponding to Eq. (5-17) for different angular velocities show that in contrast with the simple behavior of a bare electrode, the data are no longer reducible by the dimensionless frequency p. In fact $\left.\dfrac{\partial \tilde{c}_1}{\partial y}\right|_0 / \Delta\Omega$ contains W and $({}^{-1}/\theta'(0))$ which depend on p, for a given Schmidt num-

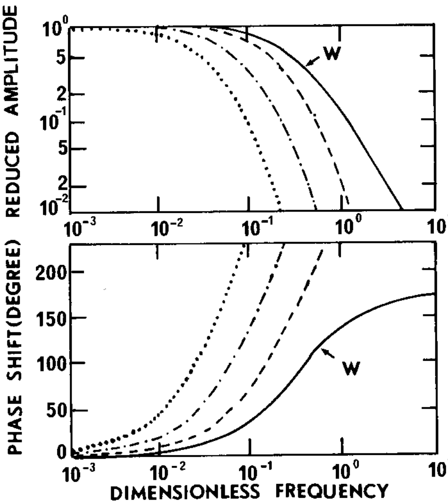

Fig. 5-7. From Eq. (5-17), EHD impedance versus the dimensionless frequency p for different rotation speeds (— — — 10.47 rd·s^{-1}, — · — · — 65.4 rd·s^{-1}, · · · · · · 262 rd·s^{-1}). $D_F/\delta_F = 5\cdot10^{-3}$ cm·s^{-1}, $\delta_F^2/D_F = 1$ s, $Sc = 10^3$. W is the EHD impedance on a bare electrode. After [59].

ber, but it is also a function of ξ_F. And so, an increase of $\bar{\Omega}$ produces a shift of the Bode diagrams toward smaller p values, other parameters being kept constant.

Thus, frequency analysis provides the diffusion time constant δ_F^2/D_F. Combining that value with the steady state determination of D_F/δ_F yields a separate estimate of δ_F and D_F.

6 Applications

6.1 Measurement of Molecular Diffusion Coefficients

The measurement of a molecular diffusion coefficient D by electrochemical techniques is generally done with a rotating disk electrode in the limiting diffusion current condition and application of the Levich's equation [8].

However, using this technique for measuring the diffusion coefficient requires an accurate knowledge of the electrode area A, the bulk concentration c_∞ of the diffusing species, the number n of electrons transferred in the reaction, and the kinematic viscosity υ of the electrolyte. Errors in measuring these quantities can cause a substantial error in determining D.

Transient methods nearly overcome this disadvantage and measure directly the Schmidt number υ/D so that the only unknown parameter is the kinematic viscosity υ. This is true for the flow modulation technique (EHD, HMRDE, velocity steps) and for the ac electrochemical impedance method [1, 60] which lead both to a dependence on $Sc^{1/3}$ of the transient data. However, in order to obtain a detectable alternating current at moderate or low frequencies, the ac measurement must be made on the slope below the limiting plateau. In this instance, the concentration and the surface overpotential are depending on r the radial coordinate over the surface of the electrode [33]. This complexity is not reflected in the boundary conditions imposed for the calculation of the diffusion impedance, and has not been so far considered for a quantitative analysis under transient conditions. In addition, surface relaxation of adsorbed species can be triggered by the potential modulation and give rise to a capacitive coupling, able to shift the apparent diffusion time constant and hence alter the Sc determination. From the very beginning, flow modulation techniques were claimed to be the appropriate tool to this end because the measurements are performed in the plateau conditions. Different versions of the flow modulation technique have been used:

6.1.1 Angular Velocity Steps

S. Brukenstein et al. proposed in 1973 [5] this technique as an alternative to the sine-wave modulation technique. Their approach was based on the Benton's analysis of fluid flow near an impulsively started disk from rest [61]. They assumed that the solution to this problem could also apply to a small velocity step between Ω_1 and Ω_2, both different from zero.

The solution to the time dependent Eq. (3-1) was derived by use of the method of Moments with the main assumption of the existence of a time dependent Nernst layer.

They established the following relationships between the angular phase $\Phi = \Omega_2 t$ and the potential current $Y = (I)_{t\to\infty}/(I)_t$:

$$\Phi = \mathrm{F}(Y) - \mathrm{F}(L) \tag{6-1}$$

L being the ratio of the steady currents for $\Omega = \Omega_2$ and $\Omega = \Omega_1$, respectively:

$$\mathrm{F}(\lambda) = \frac{1.3125}{3\mathrm{Q}}\left\{\frac{1}{2}\ln\frac{1-\lambda^3}{(1-\lambda)^3} - \sqrt{3}\tan^{-1}\left(\frac{2\lambda+1}{\sqrt{3}}\right)\right\} \tag{6-2}$$

with $\mathrm{Q} = 0.8058\, Sc^{-1/3}$.

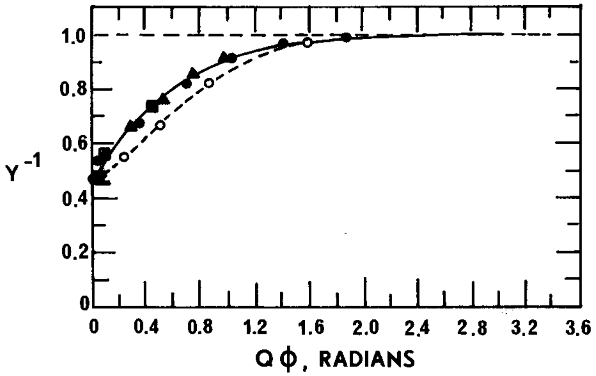

Fig. 6-1. Comparison of normalized theoretical and experimental Levich-Levich curves for Fe^{3+}, Hg_2^{2+}, and Ag^+ reductions. Solid curves are computer calculated. Experimental points are plotted as Y^{-1} vs. $\mathrm{Q}\cdot\Phi$ for normalization (see text) and have been shifted horizontally by $\mathrm{Q}\cdot\Delta\Phi$. Values of L, final speed Ω_2, $(D/\upsilon)^{1/3}$, and $\mathrm{Q}\cdot\Delta\Phi$ are as follows:

	species	L*	Ω_2 (rad/sec)	$(D/\upsilon)^{1/3}$	$\mathrm{Q}\cdot\Delta\Phi$ (rad)
□	Hg^{2+}	2.118	114.26	0.102	−0.18
▲	Ag^+	2.148	113.42	0.121	−0.04
●	Fe^{3+}	2.151	114.03	0.079	−0.18
○	Fe^{3+}	2.151	114.03	0.079	0.0

* calculated from $I_{t=\infty}/I_{t=0}$.

The respective solutions and disk surfaces were: 4 mM Hg_2^{2+} in 1 M $HClO_4$ (amalgamated gold), 2 mM Ag^+ in 1 M $HClO_4$ (Pt), and 2.17 mM Fe^{3+} in 1 M H_2SO_4 (Pt). From [5].

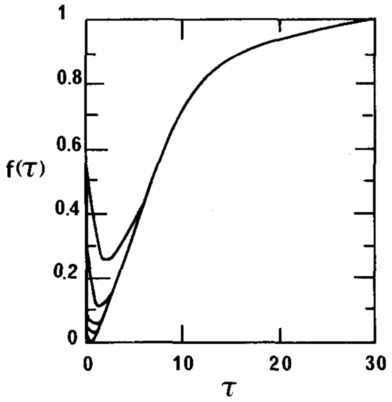

Fig. 6-2. Fractional change in current with dimensionless time τ for a step to higher rotation rate, calculated as an expansion of exponentials by the collocation technique. From the bottom to the top curve 2, 4, 6, 8 and 10 exponential terms were utilized in the calculation with $Sc = 1500$ and $\varepsilon = 0.3$. After [12].

Comparison between different redox couples are best made by plotting Y^{-1} versus $Q\Phi$ since, only one curve is obtained at the same L value. This is illustrated in Fig. 6-1 for Hg_2^{2+}, Ag^+, Fe^{3+}.

This technique was further improved by Albery et al. [11] and later by Blauch and Anson [12] who used the orthogonal collocation technique for numerical resolution of Eq. (3-1). In this last case, the effects of hydrodynamic relaxation and of imperfect motor response were taken into account, but the unsteady hydrodynamic flow was basically that described by Sparrow and Gregg [36].

The fractional change in current $f(\tilde{\tau})(\equiv Y(t))$ was obtained theoretically for different number of exponential terms in orthogonal collocation; four terms were enough (see Fig. 6-2) for ensuring good accuracy when the rotation rate is stepped to either lower or higher values.

Experimentally, they measured for $Fe(CN)_6^{4-}$ in 1 M KCl solution at 25 °C a Schmidt number $Sc = 1260 \pm 40$.

6.1.2 EHD Impedance Determination

It follows from the Section 3-1 that the potentiostatic EHD impedance $\tilde{I}/\tilde{\Omega}$ is depending only on $pSc^{1/3}$ with an additional Schmidt number correction. Even, in the range $Sc \sim 1000$ this correction is necessary because the error on Sc is approximately three times that on $Sc^{1/3}$ directly measured.

No other approximation was made and, in particular, the hydrodynamic transfer function was quantitatively calculated (see Chapter 2). In [62] measurements were done with the same system as that of Blauch and Anson [12]. The results obtained for $0.1\ \text{Hz} \leq \omega/2\pi \leq 10\ \text{Hz}$ and $\Omega = 400$ rpm were used to fit the theoretical response (see Section 3.1) and determine Sc. The agreement shown in Fig. 6-3 is very satisfactory.

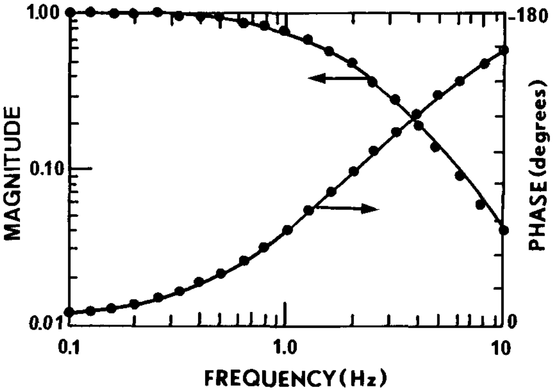

Fig. 6-3. Magnitude (left scale) and phase (right scale) of EHD impedance (at 400 rpm and 0.0 V/SCE) vs. log frequency. *The dots are the measured values, and the curve is the best theoretical* fit of Eq. (3-16). From [62].

The Schmidt numbers for ferri and ferrocyanide were respectively

$$Sc_{\text{ferri}} = 1153 \pm 35 \ ; \quad Sc_{\text{ferro}} = 1252 \pm 21$$

This last value compares very well to that given by Blauch and Anson [12].

An extension of this application was proposed by Deslouis and Tribollet to the diffusivity measurement in non-Newtonian fluids [63, 64]. They considered a power-law fluid characterized by a rheological law:

$$\tau = K(\partial \vartheta_x / \partial y)^n \qquad (6\text{-}3)$$

τ is the shearing stress, K the consistency and n the fluidity index.

It was shown that the mass transfer problem is identical to that for a newtonian fluid when adequate dimensionless quantities are used. In particular, a generalized dimensionless frequency ξ can be defined:

$$\xi = p Sc^{1/3} Re^{n-1/(3n+1)} \qquad (6\text{-}4)$$

where Sc and Re are generalized Schmidt and Reynolds numbers with:

$$Sc = \frac{K\Omega^{n-1}}{\varrho D} \quad \text{and} \quad Re = \frac{R^2 \Omega^{2-n} \varrho}{K}$$

Impedance data plotted in such coordinates in the case of solutions of ferri/ferrocyanide with KCl(M) in polyethylene oxide of various concentrations display a very good reducibility (Fig. 6-4) versus the reduced frequency. This allowed to show that for those solutions, the diffusivity of small species remains unchanged even for highly vis-

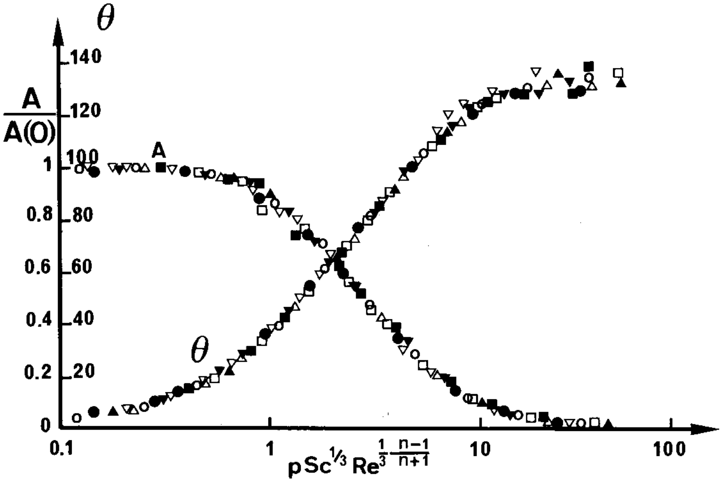

Fig. 6-4. Reduced amplitude A/A(0) and phase shift θ of the EHD impedance $\tilde{I}/\tilde{\Omega}$ as functions of the reduced frequency $pSc^{1/3}\,\mathrm{Re}^{(n-1)/3(n+1)}$. After [63].

Symbols	concen./ ppm	n	K	$10^5\,D/$ $\mathrm{cm^2\,s^{-1}}$	Sc	Re	∅/cm	Ω/rpm
○	500	0.966	0.0196	0.75	2226	230	0.5	600
▼	1000	0.918	0.063	0.75	3435	150	0.5	600
●	1500	0.895	0.037	0.75	5332	96.2	0.5	600
▽	2000	0.88	0.08	0.75	6363	80.7	0.5	600
△	3000	0.82	0.2	0.75	12408	41.37	0.5	600
▲	4000	0.75	0.52	0.75	23860	21.5	0.5	600
■	5000	0.7	0.7	0.5	49772	31.6	1	300
□	7000	0.63	2.25	0.3	137000	12.5	1	300

cous solutions. Also due to this high viscosity, the influence of the hydrodynamic transfer function was negligible, and the limiting phase shift of $\tilde{I}/\tilde{\Omega}$ was rather close to 135° (Fig. 6-4).

6.1.3 EHD Impedance in the Low Frequency Range

This method, first proposed by Smyrl [65] to determine the Schmidt number from ac impedance measurements, was furtherly extended by Tribollet et al. [66] to the EHD impedance. By taking a Taylor expansion of W to the first order, they showed that the slope $s = \dfrac{\mathrm{d}(\mathrm{Re}\,(W))}{\mathrm{d}(p\,\mathrm{Im}\,(W))_{p\to 0}}$ provides an intrinsic determination of Sc.

In potentiostatic mode one has:

$$0.4989\,Sc^{2/3} + (0.432 - s)\,Sc^{1/3} - 0.191 = 0 \tag{6-5}$$

In galvanostatic mode, a slope s_1 is defined as:

$$s_1 = \frac{\mathrm{d}(\mathrm{Re}\{(^{-1}/\theta'(0))\,W\})}{\mathrm{d}(p\,\mathrm{Im}\{(^{-1}/\theta'(0))\,W\})}$$

and:

$$1.3202\,Sc^{2/3} + (0.9405 - s_1)\,Sc^{1/3} + 0.531 = 0 \tag{6-6}$$

The flow modulation technique, in general, appears therefore very well suited for this specific purpose of quantitative diffusivity measurement. However, it also reveals any deviation from a purely diffusion controlled kinetics more clearly than do steady state measurements when, for example, a slow series process is concealed in an apparent diffusion plateau.

6.2 Analytical Chemistry

6.2.1 Submicromolar Trace Analysis with HMRDE

The development of a sophisticated form of dropping mercury electrode (DME) polarography in analytical chemistry has extended its sensitivity to micromolar and submicromolar levels. When there is minimal interference from surface and supporting electrolyte redox processes, direct voltammetry at a RDE is generally capable of equaling or bettering the sensitivity of refined polarographic methods. In the past, complications associated with solid electrode surfaces (adsorption of pollutants, ...) have restrained the realization of these analytical potentialities. At the beginning of the seventies, Miller and Bruckenstein demonstrated [67, 68], though the technique had not reached at that time a quantitative state of development, that the use of HMRDE can frequently overcome those surface processes and thereby extract usable voltammetric waves. They also assumed that the HMRDE with phase sensitive detection of the convective-diffusion component of the disk current, eliminates the charging current associated with the conventional scanning mode of dc voltammetry.

The method consists in imposing a modulation of the form $\Omega^{1/2} = \bar{\Omega}^{1/2} + \frac{\tilde{\Omega}^{1/2}}{2}\sin\omega t$ at a constant (and low) frequency while performing a voltage scanning. The sinusoidal component of the convective diffusion current is recovered from the total current by synchronous phase sensitive detection to yield its peak to peak value $|\tilde{I}|$ such that:

$$\frac{|\tilde{I}|}{\bar{I}} = \frac{\tilde{\Omega}^{1/2}}{\bar{\Omega}^{1/2}} \tag{6-7}$$

The elimination of double layer charging components, as stated by Bruckenstein et al., results firstly from an almost constant charging current in a linear potential

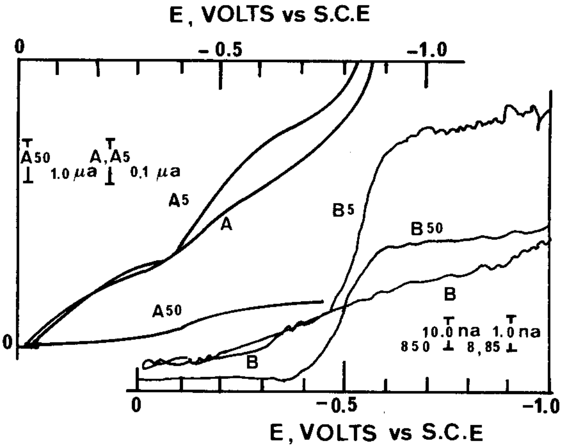

Fig. 6-5. RDE and HMRDE cathodic scans of nitrobenzene in 0.01 M $HClO_4$ at an amalgamated gold rotating disk. All A traces are RDE curves, all B traces are HMRDE curves. A, B are residual currents; A5, B5 are for 5.0×10^{-8} M; and A50, B50 are for 49.2×10^{-8} M. Scan rate for A, B, B5 is 1 mV/s; for A50, B50, 3 mV/s. Current sensitivities indicated by markers. Upper potential scale refers to B traces, lower to A. Zero current of A on right ordinate, zero current of B is upper abscissa. Modulation and speed conditions: $\bar{\Omega}^{1/2} = 60\ \mathrm{rpm}^{1/2}$, $\Delta\Omega^{1/2} = 6\ \mathrm{rpm}^{1/2}$, $f = 3$ Hz. Averaging time constant is 10 s for A, B, A5, B5, and 3 s for A50, B50. From [67].

scan due to a slowly charging differential double layer value with potential. Second, another charging current component arises because of uncompensated ohmic potential drop (see Eq. (4-9) in Section 4.1). The latter is also eliminated by phase sensitive detection as being $\pi/2$ out of phase with $\tilde{I}$.

A more refined analysis based on the developments of the theoretical part Chapter 4, shows that these statements are correct in a first approximation when the following conditions are realized:

(i) $p \ll 1$ (quasi steady state) which imposes also slow scan rates.
(ii) The kinetics is diffusion controlled (Eq. (4-12) of Chapter 4). In fact, in mixed kinetics conditions, general Eq. (4-9) shows that the separation is not so obvious.

From comparison between $\bar{I}/\bar{E}$ and $|\tilde{I}|/\tilde{E}$ scans for different electrochemical systems, the above base assumptions were proved well founded [67, 68].

As a first example, curves in Fig. 6-5 reproduce RDE and HMRDE experiments for nitrobenzene on an amalgamated gold electrode at the same nitrobenzene concentrations.

Clearly, the HMRDE curve gives a cleaner polarographic wave than does the RDE, the latter showing, in particular, a larger slope in the region of the limiting current, an effect directly connected to the double layer charging.

This leads to a detection limit of nitrobenzene of about $2\cdot10^{-9}$ M, that is 10 times lower than the usual value with the RDE method.

The second example illustrating the advantage of a flow modulation technique concerns the platinum electrode, for which reduction or oxidation processes of the

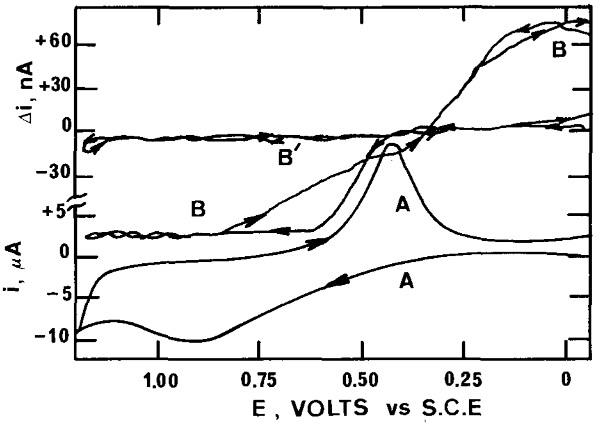

Fig. 6-6. RDE and HMRDE curves for quinhydrone at platinum. Curve A, RDE traces for cyclic potential scan of 1.00 μM quinhydrone in 0.02 M H_2SO_4 at platinum disk electrode. Curve B, HMRDE traces for the solution in curve A. Curve B′, HMRDE residual in 0.02 M H_2SO_4. Conditions: $\bar{\Omega}^{1/2} = 60\ \text{rpm}^{1/2}$. $\Delta\Omega^{1/2} \approx 6\ \text{rpm}^{1/2}$. $f = 3$ Hz, scan rate is 5 mV/s, averaging time constant is 3 s. From [67].

surface may severely interfere, which was not the case for amalgamated gold. In Fig. 6-6, RDE curves for quinhydrone oxidation exhibit a large hysteresis which almost vanishes in the HMRDE curves. In RDE curves, the major part of the current is not diffusion controlled.

As pointed out by Miller and Bruckenstein [67], performing HMRDE method with small sample volumes of solution without meaningful deviation from theory, really makes competitive the flow modulation technique with modern DME techniques in both trace and microanalysis.

6.2.2 Application of HMRDE to Kinetics Diagnostics

Very early, Miller and Bruckenstein [6] had felt that for an electrochemical system under mixed kinetic control, HMRDE was able to derive information about the kinetic parameters and give more valuable interpretation than by conventional RDE technique. At that time, they developed a theoretical analysis, restricted to quasi steady state, and which is now presented in a more quantitative way and over a large frequency domain with the formalism of EHD impedance (see Chapter 4).

However, their simplified analysis offers the interest of a fast criterion about the kinetics control. They considered a Butler-Volmer equation such as Eq. (4-5) where Ω and the limiting currents explicitly appear, and expressed the derivative of this steady current with respect to Ω (which represents, in fact, the zero frequency limit of the EHD impedance).

Then one has:

$$\frac{\mathrm{d}I}{I}=\frac{\mathrm{d}\Omega^{1/2}}{\bar{\Omega}^{1/2}}\left\{\frac{k_{\mathrm{E}}}{k_E+\bar{\Omega}^{1/2}}\right\} \tag{6-8}$$

with

$$k_{\mathrm{E}}=\frac{k_0}{0.62\,\upsilon^{-1/6}}\left\{\frac{\exp\left(\dfrac{-\alpha_{\mathrm{c}}FU}{RT}\right)}{D_{\mathrm{ox}}^{2/3}}+\frac{\exp\left(\dfrac{\alpha_{\mathrm{a}}FU}{RT}\right)}{D_{\mathrm{red}}^{2/3}}\right\} \tag{6-9}$$

Therefore $\dfrac{\mathrm{d}I}{I}=\dfrac{\tilde{I}}{\bar{I}}\Big|_{p\to 0}$

For any couple with reasonably symmetrical parameters ($\alpha_{\mathrm{a}} \sim \alpha_{\mathrm{c}}$), k_{E} will be a minimum for E around E°. Then, three limiting cases can be envisaged:

(i) For limiting diffusion current conditions:

$$\frac{\tilde{I}_{\mathrm{L}}}{\bar{I}_{\mathrm{L}}}=\frac{\tilde{\Omega}^{1/2}}{\bar{\Omega}^{1/2}} \tag{6-10}$$

(ii) If $k_0 \gg 1$ then $k_{\mathrm{E}} \gg \bar{\Omega}^{1/2}$ and Eq. (6-10) applies without subscript L everywhere. Then, normalized plots $\bar{I}/\bar{I}_{\mathrm{L}}$ and $\tilde{I}/\tilde{I}_{\mathrm{L}}$ versus E would superimpose (reversible reaction).

(iii) For totally irreversible reaction one has:

$$(\tilde{I}_{\mathrm{L}}/\tilde{I})^{1/2}=\bar{I}_{\mathrm{L}}/\bar{I} \tag{6-11}$$

since the equation for the irreversible wave of the Ox/Red couple is given by:

$$E=E_{1/2}\pm RT/\alpha F\ln\left[(\bar{I}_{\mathrm{L}}/\bar{I})-1\right] \tag{6-12}$$

It results that:

$$E^{1/2}-E_{1/2}^{\mathrm{mod}}=\pm 0.02265/\alpha \quad \text{volts} \tag{6-13}$$

where $E_{1/2}^{\mathrm{mod}}$ is the HMRDE half-wave potential.

The shift in potential is about 45 mV when $\alpha=1/2$. The various relationships that exist between the RDE and HMRDE curves for the completely reversible and irreversible extremes are summarized in Fig. 6-7.

Those predictions were improved later [69] and have been verified for the case of the totally irreversible limit, using the Pd/Pd(II) couple, for the case of fast elec-

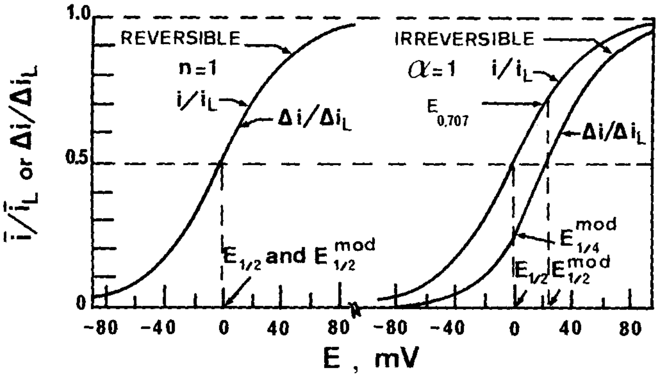

Fig. 6-7. Normalized current plots of $\bar{I}/\bar{I}_L$ and $\Delta I/\Delta I_L$ vs. potential for the cases of a reversible one-electron reaction and an irreversible reaction with an α of one. From [6].

tron transfer, using the $Fe(CN)_6^{3-}/Fe(CN)_6^{4-}$ couple at gold in 1 M KCl, and for the case of mixed kinetics and convective diffusion control using the Fe^{3+}/Fe^{2+} couple at gold in 1 M HCl. With this last system, values of $k_0 = 5.6\ 10^{-3}\ cm \cdot s^{-1}$ and $\alpha \sim 0.48$ have been obtained [70].

After this preliminary approach, further improvements, either used concurrently or separately, were recently proposed for a better sensitivity and enhanced facility in the data treatment. Such was the rapid potential scan with HMRDE.

As to the rejection of charging and interfacial current contributions, Rosamilia and Miller [71, 72] were able to extend the scan rate: this required also to increase the modulation frequency but ensuring always $p < 1$. Also the determination of $|\tilde{I}|$ involves one band passfilter, one RC filter, and a full wave rectifier which leads to a lag in the $|\tilde{I}|/E$ curve relative to that of the corresponding I/E curve.

As an example, this procedure was applied to dopamine oxidation (Fig. 6-8) with a scan rate of 80 mV/s and $\omega/2\pi = 15$ Hz.

A second improvement was also proposed with the use of derivative mode of HMRDE [73]. Indeed, as for any classical polarographic method, a derivation of the $|\tilde{I}|$ signal with respect to E can be envisaged to provide peak current outputs for clearer separation of successive components in solution. The relationships between I, $|\tilde{I}|$ and E have been given earlier for mixed mass transfer-charge transfer case (see Eq. (6-8)) and the relevant relations in the derivative mode can be deduced for the reversible or for the irreversible cases respectively.

6.3 Corrosion

One of the earlier application of the EHD impedance method was aimed at finding the mechanisms of corrosion and in particular to evaluate the role of developing layers of insoluble corrosion products which are known to be formed at neutral pH.

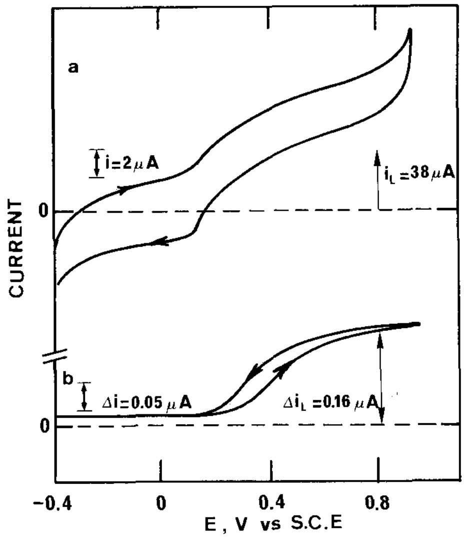

Fig. 6-8. Average current (i) and modulated current (Δi) versus potential for 10^{-5} M dopamine at carbon electrode. Scan rate 80 mV/s $\Delta\Omega^{1/2} = 4.2$, $\bar{\Omega}^{1/2} = 60$, $f = 15$ Hz, 2% ripple. From [71].

The role of those layers on the course of corrosion is essential since the main cathodic process involved is the reduction of dissolved oxygen which is at least partly diffusion controlled at usual corrosion potentials. Thus, the existence of an additional solid phase at the electrode generally decreases the diffusion rate of oxygen and therefore modifies the corrosion potential and the corrosion rate as well.

Several systems have been considered in former works but all theoretical treatment of the effects analyzed in Chapter 5 and relevant to this topics were not available in that period, so that only qualitative analysis were used for identifying the concerned mechanism.

Partial blocking effect was first identified for pure iron in contact with aerated sulphuric acid medium [55]. Corrosion of carbon steel in sodium chloride media clearly showed the porous layer effect (see Section 5.2) [74]. The same effect was found for zinc corrosion in sodium sulphate [75] and the properties of the layer which was demonstrated to be formed of an oxide/hydroxide mixture were further used for building a general kinetic model of anodic dissolution [76], usable for measurement of the corrosion rate from impedance data.

Recently, an exhaustive study of copper in sodium chloride medium was carried out on the basis of porous layer and partial blocking effects involving Cu_2O and CuCl and also a kinetic model of dissolution was proposed, following the procedure of Chapter 4 [77].

Corrosion inhibition by organic compounds was also investigated and either 2-D adsorption [78] or more often 3-D adsorption, particularly with film forming compounds [79–81], or both effects [82] were observed.

6.4 Electrocrystallization [83]

Electrodeposition of metals is very often evolving under mixed kinetic conditions which deeply influence the resulting structure and aspect of the surface. The following example shows how the EHD technique gives an in-situ information about some geometrical characteristics of the growing electrodeposit in the case of tellurium.

Tellurium is a constituent common to several definite compounds having semiconducting properties which can be obtained by electrolytic deposition (e.g. CdTe, ZnTe, . . .). The low solubility of tellurium oxide in acidic aqueous solutions explains why its kinetics of electrodeposition, in the binary of tertiary alloys involved, is mainly controlled by mass transport.

Tellurium was deposited under the same conditions as those used for cadmium telluride, i.e. from an aqueous solution of 0.2 M K_2SO_4 saturated with TeO_2. The pH was adjusted to 2.2, and the temperature maintained at 85 °C.

The EHD measurements were performed at constant potential (−0.7 V/SSE) at the beginning of or just below the diffusion plateau and are presented in Fig. 6-9. These diagrams reveal two limiting behaviors according to the angular velocity range:

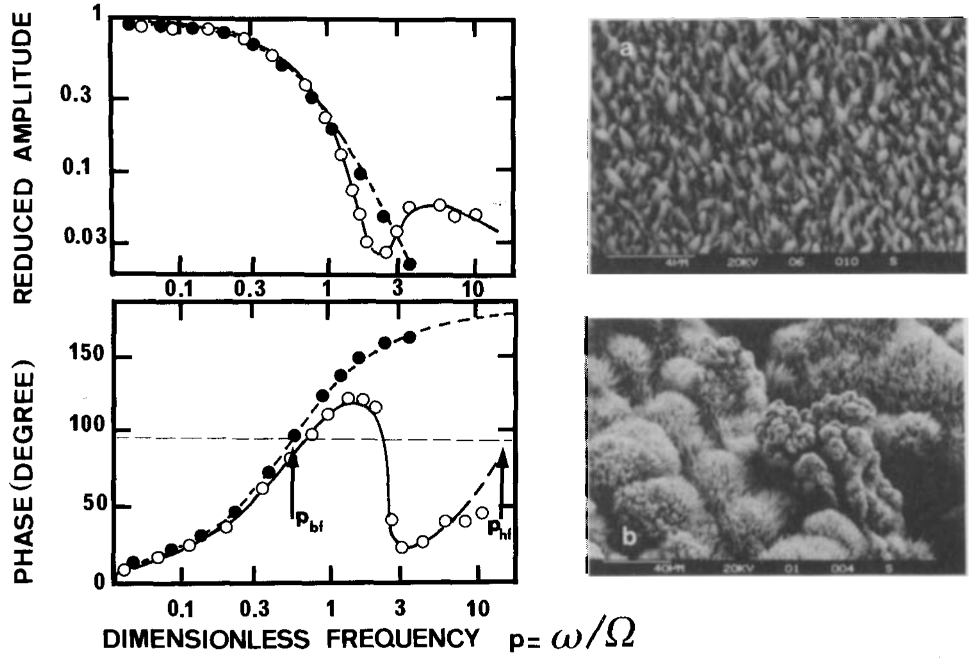

Fig. 6-9. (●) corresponds to the S.E.M. micrograph (a) obtained at $\bar{\Omega} = 1200$ rpm and $E = -0.7$ V/SSE. (○) corresponds to the SEM micrograph (b) obtained at $\bar{\Omega} = 64$ rpm and $E = 0.675$ V/SSE. From [83].

i) At higher values ($\bar{\Omega} = 600$, 900, 1200 rpm), the data fall on a single dashed curve corresponding to a fitted Schmidt number of 125. This unusually low value results from the high temperature. The system can then be considered as ideal, i.e. the interface is uniformly accessible from the view point of mass transport. This result is confirmed by the morphological aspect of the interface depicted in the Fig. 6-9a, characterized by a regular and short cut "lawn" where the elementary structures have lateral dimensions of about 50 nm. No larger scale structures appear.

From these data, the molecular diffusion coefficient of $HTeO_2^+$, taking into account a kinematic viscosity of $0.33\ 10^{-2}\ cm^2 \cdot s^{-1}$ was calculated as $D = 2.6\ 10^{-5}\ cm^2 \cdot s^{-1}$.

ii) At lower values ($\bar{\Omega} = 60$, 120 rpm) the phase shifts and amplitudes follow the theoretical disk response only in the low frequency domain (i.e. for $p < 1$). At higher frequencies a significant divergence is observed, the properties of this new behaviour being very similar to those of a partial blocking of the interface. From

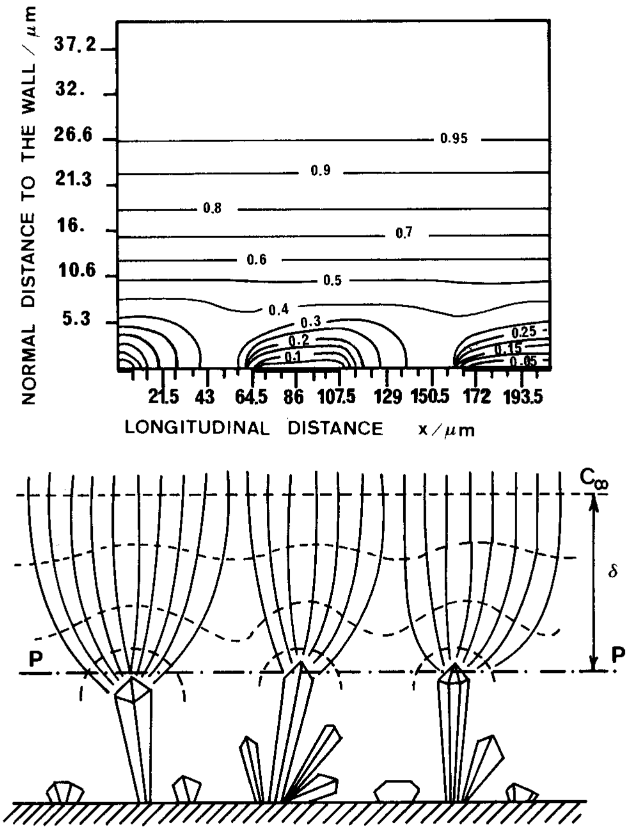

Fig. 6-10. Scheme of current and concentration distribution around the tips of growing dendrites. From [84].

the p_c^+/p_d^+ value deduced by considering the diagrams in Fig. 6-9, an average characteristic size around 40 μm can be estimated by use of Eq. (5-5). The deposit aspect in these conditions (Fig. 6-9b) shows the same microstructure as those of Fig. 6-9a. However, in addition, macrostructures with a "bush-like" shape now emerge and display an average characteristic dimension of about 40 μm.

The analysis of these measurements obtained on a 3-D system (dendritic growth) by applying a theoretical treatment elaborated for a 2-D geometry was justified in [84] as follows: in all cases the dendrite height is small with respect to the hydrodynamic boundary layer. Secondly, it is known that the dendritic growth is primarily limited at the very tips where the current density is large and mass transport controlled. On the contrary, between dendrites there are dead zones where the local mass flux is negligible. Then, one may represent a plane P, parallel to the interface and crossing the dendrite tips, which acts as a reference plane for the flow and the electrical current and has the same boundary conditions as a partially blocked area. The aspect of the isoconcentration lines given in Fig. 6-10 is similar to those in Fig. 5-2.

6.5 Modified Electrodes

6.5.1 Theory of EHD Impedances for a Mediated Reaction on a Redox Polymer Modified Electrode [85]

a) Steady-state Solutions

A redox polymer can be described as immobile redox centers covalently bound to an insulating polymer network and capable of performing a change of oxidation state between an oxidized (Q) and a reduced (P) form: $Q + e^- \rightleftarrows P$.

The presence of a redox substrate, causing the steady-state current to be non-zero, greatly increases the complexity of the problem because the electron transfer between the polymer and the substrate may take place either at the polymer solution interface or in the polymer layer. The model presented below corresponds to the limiting situation where the reaction site is the polymer-electrolyte interface and is based on the EHD method. The HMRDE variant defined by Bruckenstein et al., involving modulation of the angular velocity at a single frequency and detection of the modulated current during a potential sweep, has been applied recently by Cassidy and Vos [86, 87] to the study of redox polymer modified electrodes, with the aim of enhancing the response of the soluble redox couple in solution with respect to that of the redox couple confined to the polymer film. However, their analysis of the data was performed with the theory established for a bare electrode.

The model was developed with the following hypothesis (Scheme in Fig. 6-11): At the metal polymer-interface ($y = 0$), we assume a Butler-Volmer kinetics for the polymer confined redox couple P/Q.

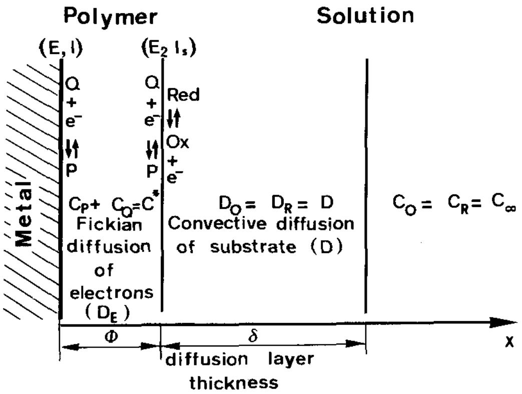

Fig. 6-11. Scheme of the modified electrode (polymer film thickness ϕ) in contact with a solution containing a redox substrate. δ is the Nernst layer thickness defined for a rotating disc electrode. From [85].

$$I = c_P(0)k^\circ_{f1}\exp\left(\frac{\alpha_1 F}{RT}E\right) - c_Q(0)k^\circ_{b1}\exp\left(\frac{-(1-\alpha_1)F}{RT}E\right) \tag{6-14}$$

Within the polymer layer we assume "Fickian diffusion of electrons" which results in an apparent diffusion of immobile P and Q centers with the same diffusivity D_E.

$$\frac{\partial c_Q}{\partial t} = D_E\frac{\partial^2 c_Q}{\partial y^2} \tag{6-15}$$

$$\frac{\partial c_P}{\partial t} = D_E\frac{\partial^2 c_P}{\partial y^2} \tag{6-16}$$

$$c_P(y) + c_Q(y) = c_T$$

At the polymer-electrolyte interface ($y = \Phi$), where no penetration of the substrate is assumed to occur, we split the usual mediation reaction $Q + Red \rightleftarrows P + Ox$ into two half-reactions: $Q + e^- \rightleftarrows P$ and $Ox + e^- \rightleftarrows Red$, where electrons appears explicitly, in order to use the formalism of electrochemical kinetics.

For the P/Q couple:

$$-I_s = c_P(\Phi)k^\circ_{f2}\exp\left(\frac{\alpha_2 FE_2}{RT}\right) - c_Q(\Phi)k^\circ_{b2}\exp\left(\frac{-(1-\alpha_2)FE_2}{RT}\right) \tag{6-17}$$

where E_2, the polymer potential in $y = \Phi$ is generally different from E and is not measurable. The current I_s due to the redox couple in solution is identical to I under steady-state conditions but not under transient conditions ($\tilde{I} \neq \tilde{I}_s$, the difference arising from the charging current due to counterions crossing the polymer/solution interface and not considered in the model).

For the Red/Ox couple, we assume that both species are transported in solution by a convective diffusion process:

$$I_s = f(E_2, \Omega)$$

This relation represents implicitly the $E-I$ characteristics for the substrate redox processes occurring at an ideally active electrode.

b) Unsteady-state Solutions

Following the usual way for impedance calculation from Eqn. (6-14) we may write:

$$\tilde{I} = A_1 \tilde{c}_P(0) + R_{t_1}^{-1} \tilde{E} \tag{6-18}$$

Where R_{t_1}, the charge-transfer resistance of the P/Q redox system at the metal-polymer interface, is

$$R_t^{-1} = (F/RT)\{\alpha_1 \overset{\circ}{k}_{f1} \bar{c}_P(0) \exp(\alpha_1 F\bar{E}/RT) + (1-\alpha_1)\overset{\circ}{k}_{b1} \bar{c}_Q(0) \exp-[(1-\alpha_1)F\bar{E}]/RT\} \tag{6-19}$$

$$A_1 = \overset{\circ}{k}_{f1} \exp[\alpha_1 F\bar{E}/RT] + \overset{\circ}{k}_{b1} \exp-[(1-\alpha_1)F]\bar{E}/RT] \tag{6-20}$$

At the polymer-solution on the polymer side, one has, following Eq. (6-17)

$$-\tilde{I}_s = A_2 \tilde{c}_P(\Phi) + R_{t_2}^{-1} \tilde{E}_2 \tag{6-21}$$

R_{t_2}, is the charge-transfer resistance of the P/Q redox system at the polymer-solution interface and has the same definition as in Eq. (6-19) by replacing the subscript 1 by 2 and the location "0" by "Φ". A_2 has the same definition as in Eq. (6-20) by replacing the subscript 1 by 2.

This kinetic current balances a diffusion flux in the polymer:

$$\tilde{I}_s = FD_E \left.\frac{\partial \tilde{c}_P}{\partial y}\right|_{\Phi} \tag{6-22}$$

On the solution side, this current is equal to the one due to the redox substrate which can be written explicitly as:

$$\tilde{I}_s = \tilde{E}_2/Z_s + Z_{EHD,P}\tilde{\Omega} \tag{6-23}$$

Z_s is the faradaic impedance due to the substrate; for a redox system it consists of a series combination of a charge-transfer resistance R_{t_s} and a convective diffusion impedance Z_{DS} ($Z_s = R_{t_s} + Z_{DS}$).

$$Z_{DS} = \frac{R_D}{\Gamma(4/3)}\left(-\frac{1}{\theta'(0)}\right) \tag{6-24}$$

$Z_{EHD,P}$ is the EHD impedance of the substrate under potentiostatic conditions, i.e. when $\tilde{E}_2 = 0$, and measured without polymer layer.

The solution of Eqs. (6-15) and (6-16) with $\tilde{c}_P(y) + \tilde{c}_Q(y) = 0$ yields:

$$\tilde{c}_P(y) = M \exp (j\omega y^2/D_E)^{1/2} + N \exp - (j\omega y^2/D_E)^{1/2} \tag{6-25}$$

where M and N are integration constants.

By eliminating $\tilde{E}_2$ between Eqs. (6-21) and (6-23) and considering Eq. (6-22) we obtain the boundary condition $y = \Phi$.

Writting at the metal-polymer interface that the current $\tilde{I}$ balances a diffusion flux:

$$\tilde{I} = FD_E \left.\frac{\partial \tilde{c}_P}{\partial y}\right|_0 \tag{6-26}$$

we obtain the second boundary condition at $y = 0$ and we are able to calculate M and N and then the desired general expression:

$$\tilde{I} = \tilde{E}/Z_{ac} + Z_{EHD}\tilde{\Omega} \tag{6-27}$$

with

$$Z_{ac} = R_E + R_{t1} + \left[\frac{\dfrac{A_1 R_{t1}}{A_2 R_{t2}}(R_{t2} + Z_s) + \dfrac{1}{C_{LF}}\left(\dfrac{\Phi^2}{D_E}\right)\dfrac{\tanh \xi_1^{1/2}}{\xi_1^{1/2}}}{1 + C_{LF}\left(\dfrac{D_E}{\Phi^2}\right)\dfrac{A_1 R_{t1}}{A_2 R_{t2}}(R_{t2} + Z_s)\xi_1^{1/2} \tanh \xi_1^{1/2}}\right] \tag{6-28}$$

$$\begin{aligned} Z_{EHD} = \frac{A_1 R_{t1}}{A_2 R_{t2}} Z_s Z_{EHD,P} \Bigg\{ &\cosh \xi_1^{1/2} \left[(R_E + R_{t1}) \left(1 + C_{LF}\left(\frac{D_E}{\Phi^2}\right) \frac{A_1 R_{t1}}{A_2 R_{t2}} \right.\right. \\ &\left.\left. \cdot (R_{t2} + Z_s)\xi_1^{1/2} \tanh \xi_1^{1/2} \right) \right] + \frac{A_1 R_{t1}}{A_2 R_{t2}}(R_{t2} + Z_s) \\ &+ \frac{1}{C_{LF}} \left(\frac{\Phi^2}{D_E} \frac{\tanh \xi_1^{1/2}}{\xi_1^{1/2}} \right) \Bigg\}^{-1} \end{aligned} \tag{6-29}$$

where

$$C_{\mathrm{LF}} = \frac{F\Phi}{A_1 R_{\mathrm{t}1}} \quad \text{and} \quad \xi_1 = \frac{\mathrm{i}\omega\Phi^2}{D_{\mathrm{E}}}$$

c) Discussion

First of all, it is interesting to check the validity of Eq. (6-28) yielding $\tilde{E}/\tilde{I}$ in the conditions investigated earlier by Gabrielli et al. [88], i.e. without a redox substrate: then $Z_{\mathrm{s}} \to \infty$ and Eq. (6-28) becomes

$$Z_{\mathrm{ac}} = R_{\mathrm{E}} + R_{\mathrm{t}} + \frac{1}{C_{\mathrm{LF}}} \frac{\Phi^2}{D_{\mathrm{E}}} \frac{1}{\xi_1^{1/2} \tanh \xi_1^{1/2}} \tag{6-30}$$

which is identical to the expression found in [88]:

Another analogy can be realized in the high frequency range even if now the redox substrate concentration is not zero. Indeed when ω (or ξ_1) $\to \infty$, Eq. (6.28) is equivalent to

$$Z_{\mathrm{ac}}(\xi_1 \to \infty) \to R_{\mathrm{E}} + R_{\mathrm{t}} + \frac{1}{C_{\mathrm{LF}}} \frac{\Phi^2}{D_{\mathrm{E}}} \frac{1}{\xi_1^{1/2}} \tag{6-31}$$

which is the limit of Eq. (6-30) when $\xi_1 \to \infty$.

The EHD impedance, defined in Eq. (6-29), takes a very simple form when the steady-state current $\bar{I}_{\mathrm{s}}$ is diffusion-controlled, i.e. at the diffusion plateau, and is generally analyzed under those conditions when possible.

As a matter of fact, at the diffusion plateau, on the one hand, Z_{S} becomes infinite, and on the other, $Z_{\mathrm{EHD,P}}$ is proportional to W (see Section 4.2), so that one has:

$$Z_{\mathrm{EHD}} = \frac{\bar{I}}{\bar{\Omega}} \frac{W}{\cosh \xi_1^{1/2} \{1 + (R_{\mathrm{E}} + R_{\mathrm{t}}) C_{\mathrm{LF}} (D_{\mathrm{E}}/\Phi^2) \xi_1^{1/2} \tanh \xi_1^{1/2}\}} \tag{6-32}$$

As previously mentioned, W which is the major term of the response and is found on a uniformly reactive interface without a polymer layer, is expressed as a function of $pSc^{1/3}$. The two other contributions to Z_{EHD}, i.e. ξ_1 (or Φ^2/D_{E}) and $(R_{\mathrm{E}} + R_{\mathrm{t}})$ C_{LF}, are closely coupled for significant values of ξ_1. They obviously cause a lack of reducibility vs $pSc^{1/3}$ of the overall impedance, as displayed in Fig. 6-12 by curves 2 and 4 plotted in Bode coordinates and corresponding to $\bar{\Omega} = 2400$ and 120 rpm respectively for $\Phi^2/D_{\mathrm{E}} = 10^{-2}$ s. However, these two contributions vary with ω in rather different ways:

a) When Φ^2/D_{E} is large, the main contribution is due to $\cosh \xi_1^{1/2}$ and a monotonic and diverging increase of the phase shift (toward negative values) is observed when the frequency increases. This is demonstrated in curve 1 of Fig. 6-12.

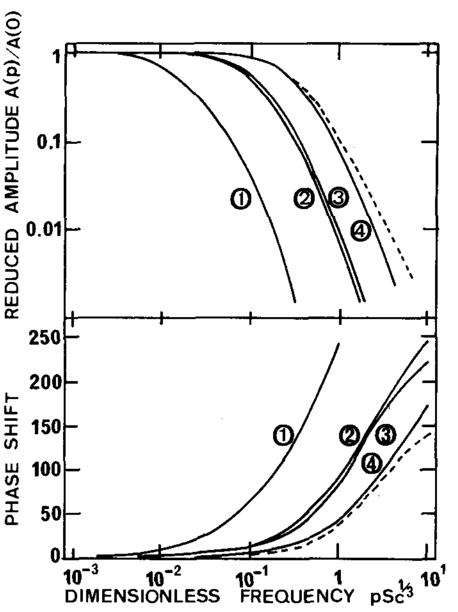

Fig. 6-12. Potentiostatic EHD impedance at the diffusion plateau in Bode coordinates calculated according to Eq. (6-32). $R_E = 5\ \Omega$ cm, $R_T = 0$, $C_{LF} = 10^{-2}$ F cm^{-2}. $\bar{\Omega} = 2400$ rpm; $\phi^2/D_E = 1$ s (1); 10^{-2} s (2); 10^{-6} s (3). $\bar{\Omega} = 120$ rpm, $\phi^2/D_E = 10^{-2}$ s (4). The dashed curve is the response without a polymer film. From [85].

b) On the contrary, for very small values of Φ^2/D_E (10^{-6} s in the simulation), ξ_1 remains close to zero and therefore Eq. (6-32) is reduced to

$$Z_{EHD} \sim \frac{\bar{I}}{\bar{\Omega}} W/[1 + i\omega C_{LF}(R_E + R_t)] \tag{6-33}$$

Thus, when ω increases, the phase shift increases faster than for W, attaining asymptotic value of $\frac{3\pi}{2}$ i.e. $\frac{\pi}{2}$ higher than that of W. This trend is observed between the phase shifts of curve 3 and the dashed curve.

c) Finally, when $\frac{\Phi^2}{D_E} \to 0$ then $\xi_1 \to 0$ in the whole frequency range, Eq. (6-32) can be replaced by an expansion of the different functions around zero. One has

$$\cosh \xi_1^{1/2} \sim 1 + \xi_1/2$$

and

$$\tanh \xi_1^{1/2} \sim \xi_1^{1/2}(1 - \xi_1/3)$$

Then by neglecting terms of the second order in ω, one finds

$$Z_{\mathrm{EHD}} \sim \frac{\bar{I}}{\bar{\Omega}} \frac{W}{1+\mathrm{i}\omega\left(\dfrac{\Phi^2}{2D_{\mathrm{E}}}+(R_{\mathrm{E}}+R_{\mathrm{t}})C_{\mathrm{LF}}\right)} \tag{6-34}$$

and therefore, a simple frequency analysis is not enough to evaluate the relative importance of the two effects.

Below are reported comparisons of the model with some experimental systems. We consider successively the behaviour of a highly conductive polymer like polyaniline in contact with solutions containing redox couples ($\mathrm{Fe(CN_6)^{3-}/Fe(CN_6)^{4-}}$) and the oxidation of hydroquinone (HQ) mediated by a moderately conductive polymer (pECBZ) film.

6.5.2 Redox Processes at Polyaniline-coated Electrodes

For a conductive polymer the description of charge transport in terms of "Fickian diffusion of electrons" is not fully satisfactory, since it implies that electrons can only be transported by hopping from reduced centres to oxidized ones in a self-exchange process, $\mathrm{Q+e^- \rightleftarrows P}$, driven by concentration gradients [89]. Conductive polymers are characterized over conjugated domains generally smaller than the film thickness by free intramolecular electron transport, while hopping processes ensure intermolecular and interparticle transport [90]. Therefore, straightforward application of the model developed for redox polymers to conductive ones is questionable. However, this inadequacy of the model might appear only if the transport of charge is accessible experimentally, i.e. not infinitely fast on the time scale of the experiments. Conversely, if charge transport is very fast, whatever its mechanism, it will not be detectable. Polyaniline is likely to correspond to the latter situation. Indeed, if we tentatively use the relation $\sigma = D_{\mathrm{E}}\varrho$ (where ϱ is the redox capacitance and σ is the conductivity) derived for redox polymers [91] for estimating the D_{E} value of polyaniline, we obtain a value of $\sim 3\cdot 10^{-3}\,\mathrm{cm^2\,s^{-1}}$ in the range of potentials and pHs where it is conductive ($\sigma \approx 1\,\Omega^{-1}\,\mathrm{cm}^{-1}$ [92]). Therefore, for films ≤ 500 nm thick, Φ^2/D_{E} is $\leq 10^{-6}$ s. Thus, in the range of frequencies used in our experiments no effect of charge transport in the film must be detectable and only the capacitive effects will appear and the simplified expression (6-33) can be used.

On both Pt and polyaniline-coated electrodes, diffusion-limited currents are observed at $E < 250$ mV for $\mathrm{Fe(CN)_6^{3-}}$ reduction, and at $E > 500$ mV for $\mathrm{Fe(CN)_6^{4-}}$ oxidation. Potentiostatic EHD impedance was measured on both diffusion plateaux (50 mV and 550 mV), using Pt electrodes coated with polyaniline films of various thickness: 50 and 130 nm. As an example, the results obtained on the cathodic plateau are shown in Fig. 6-13; those observed on the anodic plateau were very similar [93].

All experimental diagrams were fitted with Eq. (6-33) using the product $(R_{\mathrm{E}}+R_{\mathrm{t1}})\,C_{\mathrm{LF}}$ as the sole adjustable parameter. The results of the fitting are summarized in Table 6-1 and the fitted curves are shown in Fig. 6-13 as dashed lines.

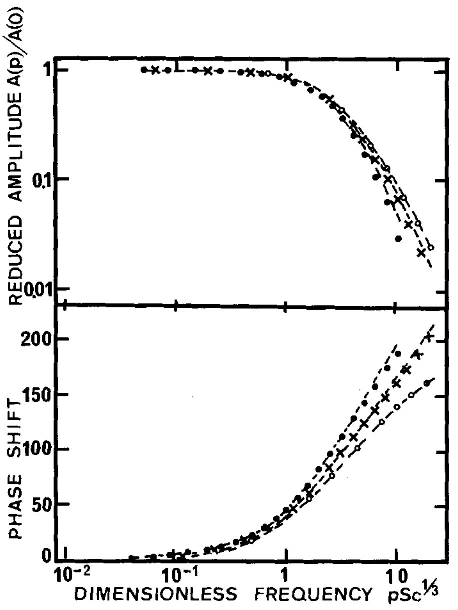

Fig. 6-13. Potentiostatic EHD impedance plots for a 130 nm thick film. (○) 120 rpm; (×) 900 rpm; (●) 2400 rpm. From [93].

Table 6-1. Potentiostatic EHD impedance experiments on diffusion plateaux. From [93].

Thickness/nm	E/mV (vs. SCE)	$\bar{\Omega}$/rpm	$10^3\ C_{LF}\ (R_{tl}+R_E)/s$
50	50	120	7.3
50	50	900	3.0
50	50	2400	2.3
50	550	120	10.0
50	550	900	2.7
50	550	2400	3.6
130	50	120	4.6
130	50	900	6.1
130	50	2400	6.3
130	550	120	4.3
130	550	900	7.5
130	550	2400	8.0

The terms iω $C_{LF}(R_E+R_t)$ in the denominator of the potentiostatic EHD expression (6-33) explain why all the experimental diagrams are shifted towards lower p values with respect to the one obtained on a uniformly accessible Pt electrode, which matches the theoretical predictions and is independent of $\bar{\Omega}$. The non-reducibility of the experimental diagrams is caused by the existence of a modulated current due to charging and discharging of the polymer redox capacitance. Since this capacitive modulated current is independent of $\bar{\Omega}$, curves obtained at higher $\bar{\Omega}$ are found at lower p (for the same film thickness). For low $\bar{\Omega}$, the experimental curves are close to the one obtained in the absence of polyaniline and therefore the $(R_E+R_{t1})C_{LF}$ value, which is a corrective term describing the deviation from W, is poorly defined. The best precision is obtained at high $\bar{\Omega}$, where $(R_E+R_{t1})C_{LF}$ becomes almost independent of it.

Eq. (6-29) provides a linear variation of $(R_E+R_{t1})C_{LF}$ with the polymer film thickness Φ. If only the data obtained at $\bar{\Omega} = 2400$ are considered, such a dependence is followed very strictly. Taking into account that for polyaniline, R_{t1}, is negligible with respect to R_E, and $R_E = 6.5\ \Omega$ in our experiments, C_{LF} for a film 50 nm thick becomes $2.9\ \mathrm{mF\,cm^{-2}}$ at $E = 550$ mV and $1.8\ \mathrm{mF \cdot cm^{-2}}$ at 50 mV, in good agreement with independent ac impedance measurements. In this particular case, like the double layer capacitance C_D for ordinary electrodes, the redox capacitance C_{LF} may be considered in parallel with the faradaic impedance, which in the present case, is that of the redox system in solution.

6.5.3 Mediated Oxidation of Hydroquinone on Poly(*N*-Ethylcarbazole) (pECBZ) [94]

It must be expected that a polymer material having a much lower conductivity than polyaniline will give impedance responses revealing the effect of the three time constants obtained in the model. The system investigated was chosen for this reason since pECBZ conductivity and redox capacity [94] correspond to $D_E = 10^{-7}\ \mathrm{cm^2 \cdot s^{-1}}$ and therefore, for the same layer thickness (500 nm), the diffusion time constant would be 0.025 s. "Electron diffusion" should therefore be detectable in the a.c. and even in the EHD frequency domain.

EHD impedances have been measured on the diffusion plateau at 0.7 V/SCE. The mass transport time constant of the redox couple in solution, which is one of the terms implied in the impedance expression is independent of the interface nature. The Schmidt number *Sc* was first determined on a bare electrode, and this value of 1540 is further used as a fixed parameter in the analysis of the diagrams obtained on pECBZ films at different $\bar{\Omega}$ (Fig. 6-14). The different diagrams are analyzed in the light of the theoretical model predicted by expression (6-34).

The fitted parameters are the amplitude at zero frequency $(\bar{I}/2\bar{\Omega})$, the diffusion time constant through the film ϕ^2/D_E, and the capacitive time constant $(R_E+R_{t1})C_{LF}$ (Table 6-2).

The $\bar{I}/2\bar{\Omega}$ value varies as expected, proportionally to $\bar{\Omega}^{-1/2}$. The product $(R_E+R_{t1})C_{LF}$ is independent of the main rotation speed $\bar{\Omega}$ for each thickness, and nearly proportional to ϕ: the latter result is consistent with the constant value of R_E and of R_{t1} which only depends on the active area and on the potential.

Finally, very small values were obtained for ϕ^2/D_E. They were not reliable because the available frequency range covered by the EHD measurements is too narrow (mechanical modulation frequencies cannot exceed some tens of Hz). Indeed, following the simulations of EHD diagrams performed in [85], ϕ^2/D_E cannot be

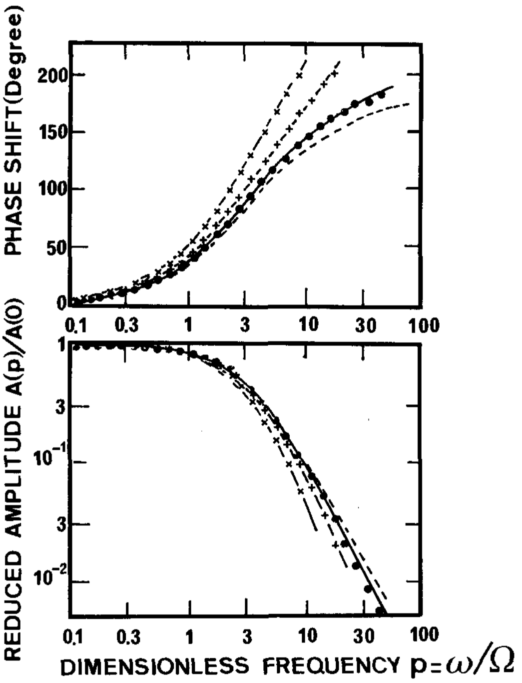

Fig. 6-14. Potentiostatic EHD impedance plots, in Bode representation (reduced amplitude $A(pSc^{1/3})/A(\text{O})$ and phase shift, versus dimensionless frequency $pSc^{1/3}$) for the oxidation of hydroquinone on a 360 nm thick poly(*N*-ethylcarbazole) film at $E = 0.7$ V (diffusion plateau). $\bar{\Omega} = 120$ rpm (●); 900 rpm (+); 2400 rpm (×); (– – –) fitting with Eq. (6-34), for the different velocities. Dashed line corresponds to theory on a bare electrode for $Sc = 1540$. From [94].

Table 6-2. Potentiostatic EHD impedance results at E = 0.7 V (diffusion plateau). *Sc* was fixed at 1540. From [94].

ϕ, nm	Ω, r.p.m.	$\bar{i}/2\bar{\Omega}$, μC	$(R_E+R_{t1})C_{LF}$, s
120	900	1.07	2.02×10^{-3}
120	2400	0.644	1.83×10^{-3}
360	120	3.16	7.04×10^{-3}
360	900	1.13	8.60×10^{-3}
360	2400	0.676	7.15×10^{-3}

estimated if it is lower than 10^{-2} s, and in this instance the simplified expression (6-33) can be used.

In the high frequency range, the approximation is of the order $\xi_1/6$ which corresponds to a deviation of the phase angle of around 5° for 10 Hz.

In these diagrams, the main effect of the polymer film is to introduce a phase shift due to $C_{LF}(R_E+R_{t1})$. The quality of the data fitting is illustrated by Fig. 6-14 for a thickness of 360 nm. The excellent agreement in the whole frequency range at all velocities gives an indirect indication that the pECBZ interface behaves an ideal surface for electron exchange of the HQ/Q system and that it offers, in particular, a uniform reactivity.

Similar behavior was obtained with other systems such as Ru^2/Ru^3 in polyvinylpyridine or polyhydroxyphenazine on glassy carbon electrodes [95].

6.6 Miscellaneous

As mentioned at the beginning of this review, most electrochemical systems are at least partly diffusion controlled and flow modulation techniques in general can be applied. Thus, to the list of applications analyzed in detail here, it is interesting to quote other fields of interest which illustrate different possibilities of this technique. Among them, mass transport in biological suspensions with rheological information [96], analysis of passive layers [97], effect of magnetic field on mass transport [98] and photoelectrochemical cells under mass and light flux modulation [99, 100] were studied.

Recently, Schwartz et al. [13–15], treated the nonlinear hydrodynamic problem involving large amplitude modulations of the angular velocity.

They proposed hence to apply this technique for improving the electrodeposition of composition modulated alloys (CMA) [101]. They showed that combining potential and flow modulations it is possible to control the symmetry of concentration distribution of the element in the alloy which is electrodeposited under mass transport conditions [102].

One outstanding feature of the technique which deserves a particular emphasis is that mass transport properties coupled with interfacial kinetics can be analyzed without (or with a minimal) perturbation of the interface potential, particularly for systems presenting locally high nonlinearities.

7 Experimental Set-up

According to the variant of the flow modulation technique envisioned for application (HMRDE, EHD, ...), appropriate modulation signals and relevant instrumentation must be used (phase detection, harmonic analysis).

An example of the experimental set up for HMRDE measurements with phase detection is described by Miller and Bruckenstein in [103].

In fact, the crucial point in the set-up, common to all variants, is the electromechanical part which must deliver at the output (i.e. at the RDE) a noise free modulation of the angular velocity: indeed, regarding the theoretical requirements for some applications (e.g. partial blocked electrodes), well performing motors and servosystems are necessary.

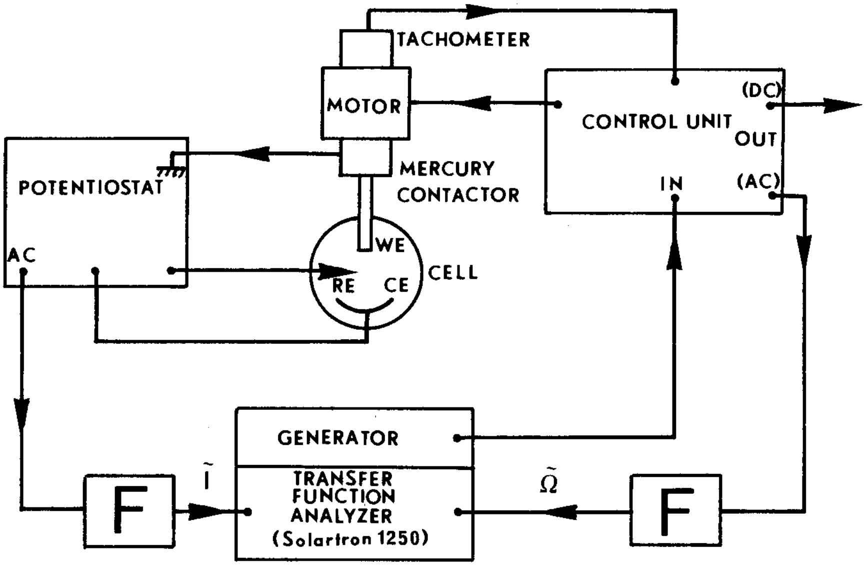

Fig. 7-1. Experimental set-up.

As an example, we present below a typical experimental arrangement suited for EHD measurements in a wide frequency range, with a frequency response analyzer as for any impedance measurement.

The analysis of the EHD impedance is done in the framework of a linear theory $(\Delta\Omega \ll \bar{\Omega})$. A typical modulation level of 10% is used; then the amplitude response of a Levich current in the low frequency range, is about 5% of the value of the dc current $(I \propto \Omega^{1/2})$. In the high frequency range, the amplitude of the response decreases rapidly. Generally, the amplitude of the EHD impedance is analyzed over three decades, so the minimum amplitude to be measured is about $5 \cdot 10^{-5}$ times the value of the dc current. It is clear that this measurement must be performed with a high performance apparatus which provides a very good signal to noise ratio.

The experimental set-up is shown in Fig. 7-1: an electrochemical interface with low level noise and a transfer function analyzer (TFA) were used for measurements of the EHD impedance. A matched two-channels 24 db/octave low pass filter (F) was used to remove HF noise and the ripple due to electric network supply, this analog filtering allows the TFA to operate with an increased sensitivity. These instruments were controlled by a computer, which recorded the data.

The signal/noise ratio of the current channel can be improved by amplifying the signal, the minimum amplification being imposed by the range of TFA (generally larger than 10 mV).

The disk is rotated by a low inertia motor with a tachometer mounted on its shaft. The response of the motor to modulation of its speed is flat within ± 1 db up to 100 Hz, and the average speed is reproducible within 1 or 2 parts in 10000 from day to day, independent of the temperature of the motor and its control electronics.

This reproducibility is important for a high accuracy in measuring diffusivity (see Section 6.1.2).

The rotating disk is secured to the motor shaft with a collet, which ensures an eccentricity of less than 4%. The mercury contactor which allows the current to be measured, has a very low contact resistance due to its large wetted area ($\sim \mathrm{cm}^2$) and so provides a cleaner signal than usual solid-solid contactors.

8 References

1. D.D. MacDonald, Transient Techniques in Electrochemistry, Plenum Press, N.Y. (1977).
2. C. Gabrielli, Identification of Electrochemical Processes by Frequency Response Analysis, Techn. report n° 004/83. Schlumberger. Farnborough (1980).
3. Proceeding of the First International Symposium on Electrochemical Impedance Spectroscopy, C. Gabrielli (ed.), in Electrochimica Acta 35, 1483 (1990).
4. B. Miller, M.I. Bellavance, S. Bruckenstein, Analytical Chem. 44, 1983 (1972).
5. S. Bruckenstein, M.I. Bellavance, B. Miller, J. Electrochem. Soc. 120, 1351 (1973).
6. B. Miller, S. Bruckenstein, J. Electrochem. Soc. 121, 1558 (1974).
7. K. Tokuda, S. Bruckenstein, B. Miller, J. Electrochem. Soc. 122, 1316 (1975).
8. V.G. Levich, Physicochemical Hydrodynamics, Prentice Hall, New Jersey (1962).
9. C. Deslouis, I. Epelboin, C. Gabrielli, B. Tribollet, J. Electroanal. Chem. 82, 251 (1977).
10. C. Deslouis, C. Gabrielli, Ph. Sainte-Rose Fanchine, B. Tribollet, J. Electrochem. Soc. 129, 107 (1982).
11. W.J. Albery, A.R. Hillman, S. Bruckenstein, J. Electroanal. Chem. 100, 687 (1979).
12. D.N. Blauch, F.C. Anson, J. Electroanal. Chem. 259, 1 (1989).
13. D.T. Schwartz, J. Electrochem. Soc. 136, 33c (1989).
14. D.T. Schwartz, P. Stroeve, B.G. Higgins, J. Electrochem. Soc. 136, 1755 (1989).
15. D.T. Schwartz, T.J. Rehg, P. Stroeve, B.G. Higgins, Phys. Fluids A4, 2, 167 (1990).
16. S.A. Martem'Yanov, B.M. Grafov, T.N. Khomchenko, L.N. Nekrasov, Elektrokhimiya 26, 498 (1990).
17. C. Gabrielli, F. Huet, M. Keddam, J.F. Lizee, J. Electroanal. Chem. 138, 201 (1982).
18. A.J. Bard, L.R. Faulkner, Electrochemical Methods, Fundamentals and Applications, John Wiley and Sons, New York (1980).
19. C.M.A. Brett, A.M.C.F. Brett, Hydrodynamic Electrodes, in: Comprehensive Chemical Kinetics, C.H. Bamford, R.G. Compton (eds.), Elsevier (1986); Vol. 26, pp. 355–343.
20. C.M.A. Brett, Portugaliae Electrochimica Acta 3, 259 (1985).
21. B. Miller, in: Physicochemical Hydrodynamics, V.G. Levich Festschrift ed. by B. Spalding Advance Publication limited, London (1977); Vol. 2, pp. 973–987.
22. C. Deslouis, I. Epelboin, M. Keddam, L. Viet, O. Dossenbach, N. Ibl, in: Physicochemical Hydrodynamics, V.G. Levich Festschrift ed. by B. Spalding Advance Publication limited, London (1977); Vol. 2, pp. 939–971.
23. C. Deslouis, B. Tribollet, in: I. Chem. E. Symposium Series, Hemisphere Publishing Corporation (1989), n° 112, pp. 29–45.
24. C. Deslouis, B. Tribollet, in: Actes du 2e Forum sur les impédances électrochimiques, Montrouge, France, C. Gabrielli (ed.) (1987), pp. 3–41.
25. C. Deslouis, B. Tribollet, in: Electrochemical Methods in Corrosion Research, M. Duprat (ed.). Materials Science Forum (1986), Vol. 8, pp. 1–12.
26. J. Wang, Talanta 28, 369 (1981).
27. C. Deslouis, B. Tribollet, Electrochimica Acta 35, 1637 (1990).

28. B. Tribollet, ATB Metallurgie XXIX 77–84 (1989).
29. C. Deslouis, I. Epelboin, C. Gabrielli, Ph. Sainte-Rose Franchine, B. Tribollet, J. Electroanal. Chem. 107, 193 (1980).
30. B. Tribollet, J. Newman, J. Electrochem. Soc. 130, 2016 (1983).
31. V. Karman, Z. Angew. Math. Mech. 1, 233 (1921).
32. S.S. Chawla, A.K. Verna, Proc. R. Soc. Lond. A386, 163 (1983).
33. J. Newman, Electrochemical Systems, Prentice Hall, Inc., Englewoods Cliffs, NJ (1973).
34. J. Newman, Ind. Eng. Chem. Fund. 7, 514 (1968).
35. W.G. Cochran, Proc. Camb. Phil. Soc. 30, 365 (1934).
36. E.M. Sparrow, J.L. Gregg, J. Aerospace Sc. 27, 252 (1960).
37. V.P. Sharma, Acta Mechanica 32, 19 (1979).
38. C. Deslouis, C. Gabrielli, B. Tribollet, J. Electrochem. Soc. 130, 2044 (1983).
39. C. Deslouis, B. Tribollet, J. Electroanal. Chem. 185, 171 (1985).
40. E. Levart, D. Schuhmann, J. Electroanal. Chem. 28, 45 (1970).
41. B. Tribollet, J. Newman, J. Electrochem. Soc. 130, 822 (1983).
42. I. Epelboin, C. Gabrielli, M. Keddam, H. Takenouti, Electrochimica Acta. 20, 913 (1975).
43. S.A. Martem'Yanov, B.M. Grafov, Soviet Electrochemistry 24, 94 (1988).
44. R. Landsberg, R. Thiele, Electrochimica Acta 11, 1243 (1966).
45. F. Scheller, S. Muller, R. Landsberg, H.J. Spitzer, J. Electroanal. Chem. 19, 187 (1968).
46. F. Scheller, R. Landsberg, S. Muller, J. Electroanal. Chem. 20, 375 (1969).
47. W.R. Smythe, J. Appl. Phys. 24, 70 (1953).
48. E. Levart, D. Schuhmann, M. Etman, O. Contamin, J. Electroanal. Chem. 70, 117 (1976).
49. V. YU. Filinovsky, Electrochimica Acta 25, 309 (1980).
50. D.A. Gough, J.K. Leypoldt, Anal. Chem. 51, 439 (1979).
51. J. Lindemann, R. Landsberg, J. Electroanal. Chem. 31, 107 (1971).
52. T. Gueshi, K. Tokuda, H. Matsuda, J. Electroanal. Chem. 89, 247 (1978).
53. T. Gueshi, K. Tokuda, H. Matsuda, J. Electroanal. Chem. 101, 29 (1979).
54. M. Etman, D. Schuhmann, E. Levart, J. Electroanal. Chem. 101, 141 (1979).
55. A. Caprani, C. Deslouis, M. Keddam, Ph. Morel, B. Tribollet, Electrochimica Acta 22, 1231 (1977).
56. A. Caprani, C. Deslouis, S. Robin, B. Tribollet, J. Electroanal. Chem. 238, 67 (1987).
57. C. Deslouis, O. Gil, B. Tribollet, J. Fluid Mech. 215, 85 (1990).
58. C. Deslouis, S. Robin, B. Tribollet, PCH Journal 9, 53 (1987).
59. C. Deslouis, B. Tribollet, M. Duprat, F. Moran, J. Electrochem. Soc. 134, 2496 (1987).
60. D.D. MacDonald, M.C.H. McKubre, Modern aspects of electrochemistry, n° 14, J.O'M. Bockris, B.E. Conway, R.E. White (Eds.), Plenum Press, New York (1982), Chap. 2, p. 61.
61. E.R. Benton, J. Fluid Mech. 24, Part. 4, 781 (1966).
62. B. Robertson, B. Tribollet, C. Deslouis, J. Electrochem. Soc. 135, 2279 (1988).
63. C. Deslouis, B. Tribollet, J. Electroanal. Chem. 142, 95 (1982).
64. C. Deslouis, B. Tribollet, Rheologica Acta 26, 336 (1987).
65. W.H. Smyrl, J. Electrochem. Soc. 132, 1555 (1985).
66. B. Tribollet, J. Newman, W.H. Smyrl, J. Electrochem. Soc. 135, 134 (1988).
67. B. Miller, S. Bruckenstein, Anal. Chem. 46, 2026 (1974).
68. B. Miller, S. Bruckenstein, An. Chem. 13, 2033 (1974).
69. K. Tokuda, S. Bruckenstein, J. Electrochem. Soc. 126, 431 (1979).
70. Y. Kanzaki, S. Bruckenstein, J. Electrochem. Soc. 126, 437 (1979).
71. J.M. Rosamilia, B. Miller, J. Electroanal. Chem. 160, 131 (1984).
72. J.M. Rosamilia, B. Miller, An. Chem. 55, 1142 (1983).
73. B. Miller, J.M. Rosamilia, An. Chem. 55, 1281 (1983).
74. A. Bonnel, F. Dabosi, C. Deslouis, M. Duprat, M. Keddam, B. Tribollet, J. Electrochem. Soc. 130, 753 (1983).
75. C. Deslouis, M. Duprat, C. Tulet-Tournillon, J. Electroanal. Chem. 181, 119 (1984).
76. C. Deslouis, M. Duprat, C. Tulet-Tournillon, Corrosion Science 29, 13 (1989).

77. C. Deslouis, B. Tribollet, G. Mengoli, M. M. Musiani, J. Applied Electrochem. 18, 384 (1988).
78. F. Dabosi, C. Deslouis, M. Duprat, M. Keddam, J. Electrochem. Soc. 130, 761 (1983).
79. C. Deslouis, M. Duprat, Pitture e Vernici 7, 16 (1984).
80. F. Dabosi, C. Deslouis, M. Duprat, F. Moran, Fundamental aspects of corrosion protection by surface modification, M. Cafferty (ed.), Electrochem. Soc. PV 84-3 (1984), pp. 260–268.
81. C. Deslouis, M. Duprat, F. Moran, C. Tulet-Tournillon, in 6th European Symposium on Corrosion inhibitors (1985), Vol. 2, pp. 845–858.
82. D. Bernard, C. Deslouis, F. Olivier, T. E. Pou, B. Tribollet, in: Transient techniques in Corrosion Science and Engineering, Electrochem. Soc. N. J. (1989), pp. 327–337.
83. C. Deslouis, G. Maurin, N. Pebere, B. Tribollet, J. Applied Electrochem. 18, 745 (1988).
84. C. Deslouis, G. Maurin, N. Pebere, B. Tribollet, Electrochimica Acta, 34, 1229 (1989).
85. C. Deslouis, M. M. Musiani, B. Tribollet, J. Electroanal. Chem. 264, 35 (1989).
86. J. F. Cassidy, J. G. Vos, J. Electroanal. Chem. 218, 341 (1987).
87. J. F. Cassidy, J. G. Vos, J. Electrochem. Soc. 135, 863 (1988).
88. C. Gabrielli, O. Haas, H. Takenouti, J. Applied Electrochem. 17, 82 (1987).
89. C. P. Andrieux, J. M. Saveant, J. Electroanal. Chem. 111, 377 (1980).
90. J. E. Frommer, R. R. Chance, in: Encyclopedia of Polymer Sciene and Engineering, Wiley, N. Y. (1986), Vol. 5, p. 462.
91. C. E. D. Chidsey, R. W. Murray, J. Phys. Chem. 90, 1479 (1986).
92. J. C. Chiang, A. G. MacDiarmid, Synthetic Metals 13, 193 (1986).
93. C. Deslouis, M. M. Musiani, B. Tribollet, J. Electroanal. Chem. 264, 57 (1989).
94. C. Deslouis, M. M. Musiani, B. Tribollet, Synthetics Metals 38, 195 (1990).
95. C. Deslouis, C. Gabrielli, M. M. Musiani, B. Tribollet, J. F. Equey, O. Haas, J. Electroanal. Chem. 244, 325 (1988).
96. A. Caprani, Bioelectrochemistry and Bioenergetics, 6, 413 (1979).
97. C. Deslouis, M. Keddam, C. Pallotta, B. Tribollet, in: Electrochemical Methods in Corrosion research, M. Duprat (ed.), Materials Science Forum (1986), Vol. 8, pp. 69–80.
98. O. Aaboubi, J. P. Chopart, J. Douglade, A. Olivier, C. Gabrielli, B. Tribollet, J. Electrochem. Soc. 137, 1796 (1990).
99. B. Miller, S. Menezes, A. Heller, J. Electrochem. Soc. 126, 1487 (1979).
100. S. Bruckenstein, B. Miller, J. Electrochem. Soc. 129, 2029 (1982).
101. V. Cohen, K. R. Walton, R. Sard, J. Electrochem. Soc. 131, 2489 (1984).
102. D. T. Schwartz, P. Stroeve, B. L. Higgins, AIChE Journal 35, 1315 (1989).
103. B. Miller, S. Bruckenstein, Anal. Chem. 46, 2026 (1974).

Advances in Electrochemical Science and Engineering
Edited by Heinz Gerischer and Charles W. Tobias

Index